THEORETICAL MODELS FOR THE ELECTROCHEMICAL REDUCTION OF CO2 ON COPPER CATALYSTS UNDER WORKING CONDITIONS

Federico Dattila

UNIVERSITAT ROVIRA i VIRGILI

THEORETICAL MODELS FOR THE ELECTROCHEMICAL REDUCTION OF CO_2 ON COPPER CATALYSTS UNDER WORKING CONDITIONS

Federico Dattila

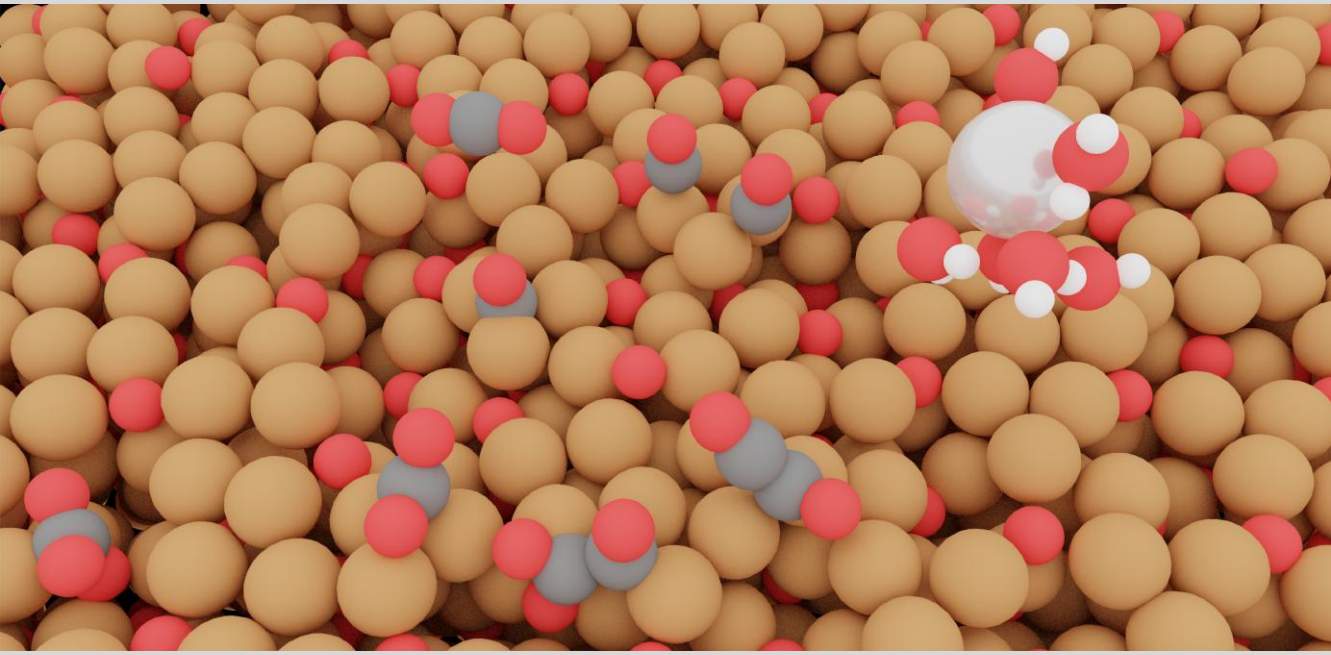

DOCTORAL THESIS
2020

UNIVERSITAT ROVIRA I VIRGILI
THEORETICAL MODELS FOR THE ELECTROCHEMICAL REDUCTION OF CO2 ON COPPER CATALYSTS UNDER WORKING CONDITIONS
Federico Dattila

UNIVERSITAT ROVIRA I VIRGILI
THEORETICAL MODELS FOR THE ELECTROCHEMICAL REDUCTION OF CO2 ON COPPER CATALYSTS UNDER WORKING CONDITIONS
Federico Dattila

Federico Dattila

Theoretical Models for the Electrochemical Reduction of CO_2 on Copper Catalysts under Working Conditions

DOCTORAL THESIS

Supervised by
Prof. Núria López Alonso and
Dr. Rodrigo Antonio García Muelas

Institute of Chemical Research of Catalonia (ICIQ)
and Rovira i Virgili University (URV)

UNIVERSITAT ROVIRA I VIRGILI

Tarragona
2020

UNIVERSITAT ROVIRA I VIRGILI
THEORETICAL MODELS FOR THE ELECTROCHEMICAL REDUCTION OF CO2 ON COPPER CATALYSTS UNDER WORKING CONDITIONS
Federico Dattila

Institut Català d'Investigació Química
Av. Països Catalans, 16
43007 Tarragona. Spain

Prof. Núria López Alonso, group leader at the Institute of Chemical Research of Catalonia, and Dr. Rodrigo Antonio García Muelas, group scientific coordinator at the Institute of Chemical Research of Catalonia

WE STATE that the present study, entitled "**Theoretical Models for the Electrochemical Reduction of CO_2 on Copper Catalysts under Working Conditions**", presented by Federico Dattila for the award of the degree of Doctor in Chemical Science and Technology, has been carried out under our joint supervision at the Institute of Chemical Research of Catalonia and that it fulfills all the requirements to be eligible for the International Doctorate Award.

Tarragona, November 3rd, 2020

Prof. Núria López Alonso Dr. Rodrigo Antonio García Muelas

UNIVERSITAT ROVIRA I VIRGILI
THEORETICAL MODELS FOR THE ELECTROCHEMICAL REDUCTION OF CO2 ON COPPER CATALYSTS UNDER WORKING CONDITIONS
Federico Dattila

Sponsors

The work presented in this Ph.D. thesis has been funded by the European Commission (EC) under the Innovative Training Network (ITN) project ELCOREL-722614 within the Marie Skłodowska-Curie Actions (MSCA) in the framework of the European Research Program Horizon 2020. The generous computer resources provided by the Barcelona Supercomputing Centre (MareNostrum) and the Spanish Supercomputing Network are also acknowledged.

UNIVERSITAT ROVIRA I VIRGILI

Barcelona Institute of Science and Technology

Barcelona Supercomputing Center
Centro Nacional de Supercomputación

Acknowledgments

It is hard to thank whoever I am grateful to for this thesis, as I wrote three years ago in the acknowledgments for my Master Thesis. Of course, there are few relevant people who catalyze my Ph.D. "reaction" and I will acknowledge their contribution later. Yet, given my idea of society, I should start from a broader perspective.

I am a son of two public servants and of public education. Thus, the very first people I will thank are the Italian citizens who paid my education through their taxes. In fact, I could get primary and secondary school education besides a high school diploma in humanistic studies. For my Master of Science in Physics I will acknowledge the 10 million Swedish citizens as well for my year at Chalmers University of Technology in Göteborg between 2015 and 2017. That was my first experience abroad and it was possible thanks to the Erasmus program. Hence, I must mention the whole European Union citizenship. I should thank European taxpayers twice, since they also funded this Ph.D. within ELCoREL, as one of the Marie Skłodowska-Curie Actions in the Research Program Horizon 2020. Finally, the biggest mention goes to the 47 million Spanish citizens, including 7.5 million Catalans, who fund the Institute of Chemical Research of Catalonia (ICIQ), where I carried out this thesis. As a final remark, thanks also to the Dutch citizens to host me twice for my mobilities, first at the University of Leiden and later at Avantium Chemicals BV.

After this needed preamble, I now move on with specific acknowledgments. The first one to highlight is Prof. Núria López for evident reasons. She never gave up with me, even when my scientific dedication was in doubt. As an exceptionally good mentor, she got a Master student with messy slides and unclear prose and she modeled a scientist out of him. I do not think I could ever return to her all the support, dedication, and patience received in these three years. At least, I can guarantee a never-ending feeling of respect and gratitude. Thanks to her, I learnt how to focus and pay attention to each detail. These skills will help me no matter what my future will be. The second active and selective catalyst was Dr. Rodrigo García Muelas, my co-supervisor. Even if when I started this journey, he was a fresh doc-

tor, he contributed to shape my personality with wise scientific and personal advices. He always stood by my side and understood my difficulties. Even in the worst scientific moments, he was always there, as during the evening when we shared a pizza at ICIQ since I needed fresh energy to finish an important task. Again, I hope to have given back at least a part of what Rodrigo invested in me. Although sometimes we had strong scientific and personal discussions (I am not an easy dude unfortunately), Núria, Rodrigo, and I never lost faith and respect in each other.

It is now the turn of the outstanding people that I met during my staying abroad. In the figure of Prof. Marc Koper I found an extraordinary scientist, with the unique ability of modeling electrochemical processes with a piece of paper and a pencil. The fruitful discussions with him and the members of his group, like Mariana, Chunmiao, Akansha, Giulia, Matias, Stefan, Arthur, Allison, Ian, affected my scientific path. The Leiden memories end with José, the lovely person who organized every detail of my staying, and Ann, my extraordinary landlady. As for the time at Avantium, a special mention goes to Dr. Klaas Jan Schouten, who convinced me that CO_2 reduction is industrially possible. Together with him, I thank Davide, my extraordinary experimental-theoretical collaborator. He had the special merit of having taught a physicist to synthesize chemicals. Additionally, I hope to have soon new interesting discussions on GDEs and beers with Matt, and to see again Julia, Mariana, and Gil. A last memory goes to the people who shared the Amsterdam COVID19 period with me: Natalie, Martina, Enrique, Ella, and Jelena. You were my family in a moment where my biological family was in danger.

Now, it comes the ELCoREL family: Vlad, Riccardo, DJ, Noor, Rebecca, Paula, Daniel, Spyros, Tuğçe, and Chunmiao, Mariana, Davide and Matt who I already mentioned before. As the most important outcome of this Ph.D., I got their friendship. I will miss forever my ELCoREL conferences' roommate, Spyros, and Paula. We started together our research path at ICIQ. She has always been and will always be a special friend, always there when needed. We have different characters, so I had even more to learn. As a second family, I must mention all the folks passing through the ICIQ theoretical lab: Nathan, Bob, Jordi, Sergio, Andrea, Julian, Javier, Rostislav, Enric, Diego, Alba, Joan, Mireia, Bruna, Sara, Raúl, Lucía, Adiran, Núria V., Prof. Carles Bo, Prof. Feliu Maseras, and all the others. Though, some people deserve a specific mention. For instance, the Serbian triangle, Kosta, Edvin (and Pavle now), for being so affine to me: I hope we will stay connected and we will soon visit Belgrade together. I will miss Albert's joder. I am so glad to have met Moisés and Martin, Master of Computer skills but still so human. Thanks Manu and Franzis for being so different but able to influence me so much. Thanks, Yecheng, for keeping

our friendship even now that we are so far away. Last, but not least, thanks to Marcos, who will soon deliver a much better project than my thesis. Every time I was stressed, he always managed to make me smile.

Ending with the ICIQ family, I acknowledge the influence of current and former members of the ICIQ workers committee: Marta G. (the president!), Marta M., Irene (our super-secre), Jandro (our new super-secre), Xavi, Jesús, Raúl, Ilario, Albert, Vanesa, Catherine, Laia, Pablo, Javi, Isra, Joe, etc. We started a long journey to improve ICIQ, and we are still here fighting. Gràcies a Laia dues vegades, for being the core of ICIQ outreach and thanks to the friends of divulgaTGN: Fran, Maria, Victor, Carlos, Lydia, Gerard, Albert, Ximena, etc. Thanks Fernando for introducing me to such an amazing team! Of course, old friends are the core of our life, so I must remember here good mates from high school (Eugenio, Cristina, Zoltan, Chiara, Carlotta, Lara, Andrea D., ...); from the Master (Giorgio, Luca G., Luca P. Lucio, Eugenio D., Giacomo), who constituted the legendary group *Da Pino*, from the name of the owner of the trattoria where we used to eat before every lab experience; my (beach)volleyball friends (Primavera, Juanjo, Enrico, Alessandro, Ludovico, Andrea C., ...); my ERASMUS friends (Federico B., Roberto, Alessandra, Ludovica, Fabian, Michelle, ...). Finally, thanks to all the special people who made these three years in Spain among the best of my life (and taught me Spanish): Albert, Guillem, Joan S. G., Joan G. M., Anna, Júlia, Mabel.

Here it comes the most important part, my roots. I owe everything I am to my mother Isabella, a former school employee, and my father Francesco, a former high school teacher of Chemistry. I hope he is proud that I have finally pursued a similar path. My *Babbo* taught me to be rational and scientific; my *Mamma* taught me to be empathic; together, they taught me that diversity is always a plus. Thank as well to my sister Francesca, who is taking care of granny, *babbo*, and *mamma* while I am abroad. She is such a volcano, and I am so proud of her as of her husband Peter. Again, diversity rules it all!

Finally, I dedicate this Ph.D. thesis to my grandparents, who could have never expected their grandson to be a Ph.D. candidate one day. To my 93-years old, still living maternal grandma, Caterina, and to my paternal grandma, Giuseppina†: *Nonna Pina*, I hope this study gives you back the secondary and university education which you were not entitled to get 80 years ago since you were born woman. A last dedication to three key mentors in my life: my secondary school Math teacher, Luigia Ferrero, my high school Math and Physics teacher, Maria Rosa Toscano, and Prof. Dinko Chakarov, for being the first to believe that a physicist can contribute to the beautiful field of Chemistry.

Contents

Abbreviations

GDP	Gross Domestic Product
OECD	Organization for Economic Co-operation and Development
IPCC	Intergovernmental Panel on Climate Change
IEA	International Energy Agency
PHS	Pumped Hydroelectric Storage
CAES	Compressed Air Energy Storage
VRB	Vanadium Redox flow Battery
SMES	Superconducting Magnetic Energy Storage
AL-TES	Aquiferous Low-temperature Thermal Energy Storage
HT-TES	High-Temperature Thermal Energy Storage
eCO_2RR	Electrochemical CO_2 Reduction Reaction
HER	Hydrogen Evolution Reaction
OER	Oxygen Evolution Reaction
ORR	Oxygen Reduction reaction
FE	Faradaic Efficiency
DFT	Density Functional Theory
CHE	Computational Hydrogen Electrode
SHE	Standard Hydrogen Electrode
NHE	Normal Hydrogen Electrode
RHE	Reversible Hydrogen Electrode
U^0	Equilibrium potential
η	Overpotential
R	Reactant
P	Product
$C_{R,P}$	Concentration of reactant / product
r	Reaction rate
ν	Heteregeneous reaction rate
k	Heterogeneous reaction rate per mole
k^0	Standard heterogeneous rate constant

α	Charge transfer coefficient
E_{a}	Activation energy
IPE	Ideal Polarizable Electrode
EDL	Electrical Double Layer
IHP/L	Inner Helmholtz Plane / Layer
OHP/L	Outer Helmholtz Plane / Layer
C_{d}	Electrical double layer capacitance
$J_i(x)$	x-directional flux of chemical species i
D_i	Mass diffusivity coefficient for chemical species i
δ_i	Diffusion layer thickness for chemical species i
ω	Angular Velocity
LDA	Local-Density Approximation
GGA	Generalized Gradient Approximation
AIMD	Ab Initio Molecular Dynamics
BOMD	Born-Oppenheimer Molecular Dynamics
CPMD	Car-Parinello Molecular Dynamics
VASP	Vienna Ab Initio Simulation Package
NPs	Nanoparticles
p-Cu	Polycrystalline copper
g-Cu	Graphene-covered copper
GDE	Gas Diffusion Electrode
GDL	Gas Diffusion Layer
U_{pzc}	Potential of zero charge
EC-AFM	Electrochemical Atomic Force Microscopy
EC-STM	Electrochemical Scanning Tunneling Miscroscopy
SEM	Scanning Electron Microscopy
XRD	X-ray diffraction spectroscopy
OD-Cu	Oxide-derived copper
Cu_2O-red	Cu_2O reduction models
Cu-oxi	Cu oxidation models
Cu_{ad}	Copper adatom
$O_{\mathrm{n,s}}$	Near-surface oxygen
ERD-Cu	Electro-redeposited Cu
Oxi-Cu	Oxidized Cu
PT	Plasma-treated Cu
Lig-Cu	Ligand-modified Cu
CV-Cu	Cyclic Voltammetry-treated Cu
MOF	Metal-Organic framework
NCs	Nanocrystals
LDH	Layered Double Hydroxides
ED-Cu	Electrodeposited Cu
NF	Nanoflowers

List of publications

1. **Origin of the selective electroreduction of carbon dioxide to formate by chalcogen modified copper**. *R. García-Muelas, F. Dattila, T. Shinagawa, A. J. Martín, J. Pérez-Ramírez, and N. López*, J. Phys. Chem. Lett. **2018**, 9, 24, 7153–7159.

2. **Active and selective ensembles in oxide-derived copper catalysts for CO_2 reduction**. *F. Dattila, R. García-Muelas, and N. López*, ACS Energy Lett. **2020**, 5, 10, 3176–3184.

Federico Dattila wrote the first draft and did all the Density Functional Theory calculations of publication 2. He did part of the calculations and actively participated in writing publication 1.

Furthermore, the author has contributed to the following submitted publication.

- **Tracking the potential-controlled synthesis of Cu-nanocuboids and graphene-covered Cu-nanocuboids under *Operando* CO_2 electro-reduction**. *T. H. Phan, K. Banjac, F. P. Cometto, F. Dattila, R. García-Muelas, N. López, and M. Lingenfelder*, ChemRxiv **2020**, Preprint, DOI: 10.26434/chemrxiv.13198481.v1.

Abstract

Climate change has a clear human origin due to anthropogenic CO_2 emissions. In the next decades, the struggle to access energy and electricity will cause even stronger social and economic crises, since climate change will affect more severely developing countries. By 2100, an estimated global warming of at least 1.5°C will drastically impact our life and reduce our welfare. Since an industrial model based on fossil fuels has evident limitations toward the creation of open and democratic societies, the use of renewable energy is the key for a sustainable and fair development. However, due to the intermittency of renewable sources, their use requires energy storage and fuels are the only candidates which offer long-term energy supply due to their high energy density. These chemicals can be produced through CO_2 reduction and this process concurs in lessening CO_2 atmospheric concentration since it uses captured carbon dioxide as reactant. This reaction is properly characterized for well-defined metallic catalysts. Yet its understanding is still very minimal for more complex copper-based materials which can generate the high valuable C_{2+} products. Therefore, theory must deal with this complexity to untangle mutual influences and provide guidelines to experimental synthesis.

This thesis aims at modeling copper catalysts under reaction conditions through Density Functional Theory (DFT) simulations. In Chapter 1, I introduced the motivation and the objectives of this study. An accurate description of a real catalyst under CO_2 reduction conditions requires the study of factors which interact reciprocally, such as polarization, surface modifiers, and electrolyte. In Chapter 2, I described the computational and methodological tools employed throughout the manuscript, thus I introduced basic concepts of electrochemistry, Density Functional Theory, and Ab Initio Molecular Dynamics. Chapter 3 describes the advances in the correlation of copper product distribution with its local morphology: close-packed facets are selective toward CH_4, (100) domains toward C_2H_4, and defects toward oxygenates. In Chapter 4, I investigated the reconstruction of polycrystalline copper at high negative potential. Local surface polarization drives the experimentally detected evolution of polycrystalline copper

toward open domains and defective sites. (100) facets are selective to ethylene, thus I applied theoretical guidelines to synthesize a catalyst with high Faradaic efficiency to C_2H_4. In Chapter 5, I devised a first order approximation to characterize surface reconstruction processes for oxide-derived copper and correlate these structural properties with the enhanced CO_2 activity and C_{2+} selectivity of this family of catalysts. By applying Ab Initio Molecular Dynamics, I investigated the thermodynamic stability of residual oxygens and their influence in copper speciation and formation of recurrent surface ensembles. By assessing the reactivity of these ensembles, I decoupled the roles of surface polarization and large surface area on CO_2 reaction activity. Furthermore, I suggested C_{2+} selectivity on oxide-derived copper to be driven by polarization and metastable near-surface oxygens, which stabilize the CO-CO dimer through the formation of a new reaction intermediate, a deprotonated glyoxylate species. Chapter 6 focuses on the impact of surface modifiers on copper reactivity, such as the enhancement of formate production on sulfur modified copper nanoparticles. A sulfur adatom acts as a strong tethering center for CO_2 and H, opening two new direct reaction pathways to $HCOO^-$. As a needed Appendix, I suggested similar chemical interactions to rule cation effect on CO_2 activity. Positively charged dehydrated cations stabilize negatively polarized reaction intermediates close to the surface, thus promoting reduction processes. Finally, Chapter 7 accounts for the main conclusions of this work.

This theoretical study sheds light on the complexity of electrochemical CO_2 reduction on copper under working conditions and proposes complementary methods to describe polarization-driven surface reconstruction and the action of surface modifiers. Only by accounting for all these mutual interactions, it will be possible to devise new theoretical guidelines for experimental synthesis of catalysts selective to the sought-after C_{2+} products. As required by the FAIR principles of findability, accessibility, interoperability, and reusability of scientific data, all structures and all the publications resulting from this work are stored in open access databases.

Chapter 1

Introduction

Fossil fuels exploitation have caused several economic, energetic, and social crises since the last century. The increasing CO_2 emissions due to human activities alter the natural cycles occurring in our planet, leading to the well-known phenomenon of climate change. Several studies have confirmed the human-driven alteration of our climate in the last century,[1] and policy makers are now acting to face this existential thread.[2] Renewable sources such as sun, wind, and hydropower provide a sustainable alternative to fossil fuels exploitation. Yet, they need an effective energy storage due to their intermittent nature. State-of-the-art storage devices such as Li-ion batteries are massive due to their low energy density. Thus, their application to energy-demanding technologies, such as vehicles, is intrinsically hindered. Energetic storage via chemical bonds is a good alternative and, coupled with CO_2 reduction, it provides negative CO_2 emissions. The direct conversion of sunlight and carbon dioxide to chemical products is still limited to laboratory scales due to the complexity of photoelectrochemical processes,[3] hence electrochemical CO_2 reduction is the preferential option in the short term. Pioneered by the Italian chemist Ciamician in 1912,[4] this chemical reaction was first demonstrated on mercury electrodes in 1954.[5] Since then, the systematic work on Hori set the basis for a rapid development of the field.[6] Thanks to a huge joint theoretical and experimental effort,[7–11] industrial CO_2 reduction toward CO and formate is now getting close to applications,[12,13] but production of valuable C_{2+} chemicals such as ethylene, ethanol and propanol is still economically unfavorable.[14] Copper has been employed as a CO_2 reduction catalyst due to its unique selectivity toward a wide range of products including hydrocarbons,[10,15] . Theoretical and experimental studies have rationalized the catalytic properties of well-defined copper systems such as single crystals or polycrystalline.[7,11] Yet, the understanding of catalyst' evolution under working conditions is not

yet achieved. A better assessment of reconstruction processes,[16] electrolyte effect,[17,18] surface polarization, surface pH,[19–21] and mass transfer[22,23] for CO_2 reduction on copper paves the way toward a theoretical-driven synthesis of materials selective to the desired chemicals. Thus, such investigation concurs in devising a more sustainable future for the whole humankind.

1.1 Anthropogenic CO_2 emissions

The anthropogenic CO_2 fingerprint in the Earth atmosphere increased significantly since industrial revolution, accounting for more than 30 billion ton CO_2 emissions released in 2019.[24] This alternation of the carbon cycle is due to human activity. In fact, CO_2 emission scales with both world population, **Figure 1.1a**, and world gross domestic product per capita, **Figure 1.1b**. Recent studies have proved that the consequent modification of the Earth climate affects ecosystems and seasonal turnover. Meta-analysis on more than 1700 animal and vegetal species showed that on average their natural ecosystems shifted toward the poles by 6.1 ± 2.4 km per decade and spring events occur on average 2.3 days in advance per decade.[1] Among 74% and 91% of the species considered exhibited changes in agreement with climate change predictions.[1]

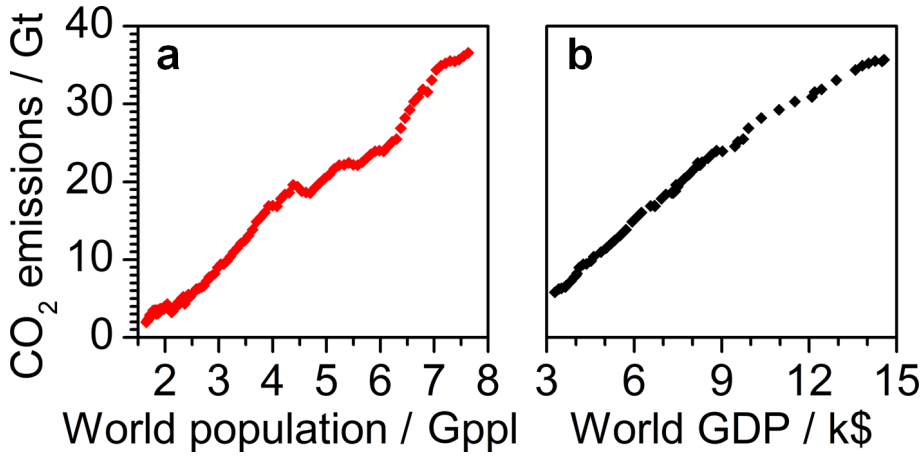

Figure 1.1: Estimates of annual CO_2 emissions[25] versus **a**, world population (1900-2018)[26] and **b**, average world Gross Domestic Product (GDP) per capita (1950-2018).[27]

1.2 Economic, social, and political consequences

Even though a clear correlation between industrial activities, CO_2 emissions, and climate change can be drawn, there is a lack of common actions to fight this existential thread. This general passivity is embedded in the present economic model, unable to move from a linear to a circular economy. Furthermore, the wild and quick development of Asian, South American, and African countries affects every global decision. In the last 20 years, whilst OECD* countries energy consumption exhibits a limited increment from 3 Gtoe to 3.6 Gtoe, non-OECD countries almost doubled their energy consumption, from 3 Gtoe to 6 Gtoe.[28] China alone moved from an energy consumption below 0.75 Gtoe in 1990 to more than 2 Gtoe in 2020, whereas India almost tripled its energetic demand, from less than 0.25 Gtoe to 0.6 Gtoe.

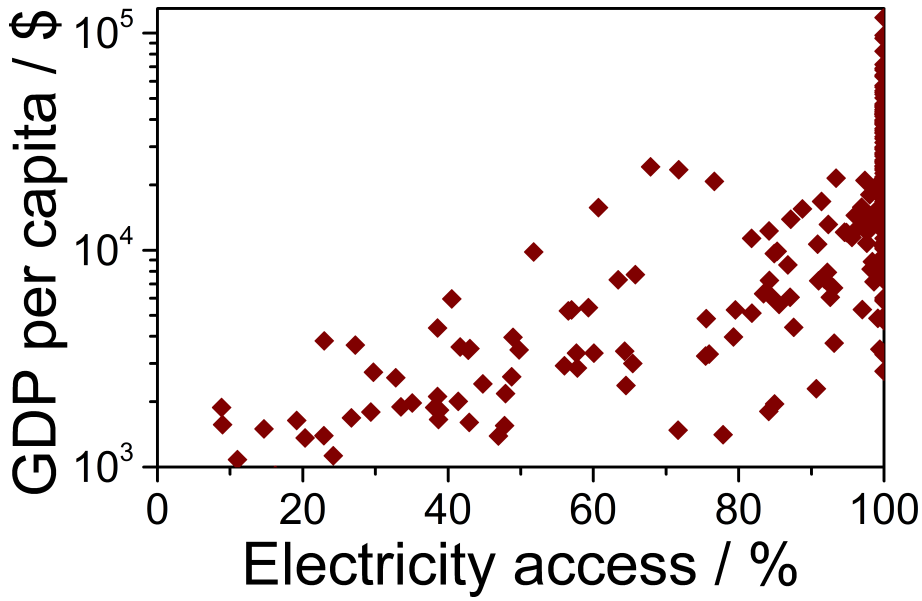

Figure 1.2: Gross domestic product per capita per country in 2016[27] versus estimated share of electricity access per country in 2016.[29]

As shown in **Figure 1.2**, energy supply is a key factor for the development of a country. The gross domestic product per capita, which we can assume as an indicator of the welfare, increases exponentially depending on the access to electricity. Richer countries provide access to electricity to the entire population, whereas poorer countries fulfill energy demand only for capitals and large cities. Thus, the economic and social progresses

*Organisation for Economic Co-operation and Development.

in developing countries need a stable and continuous energy supply, which is currently provided with fossil fuels. Science must provide a sustainable alternative to guarantee a fair and sustainable development to the whole humankind.

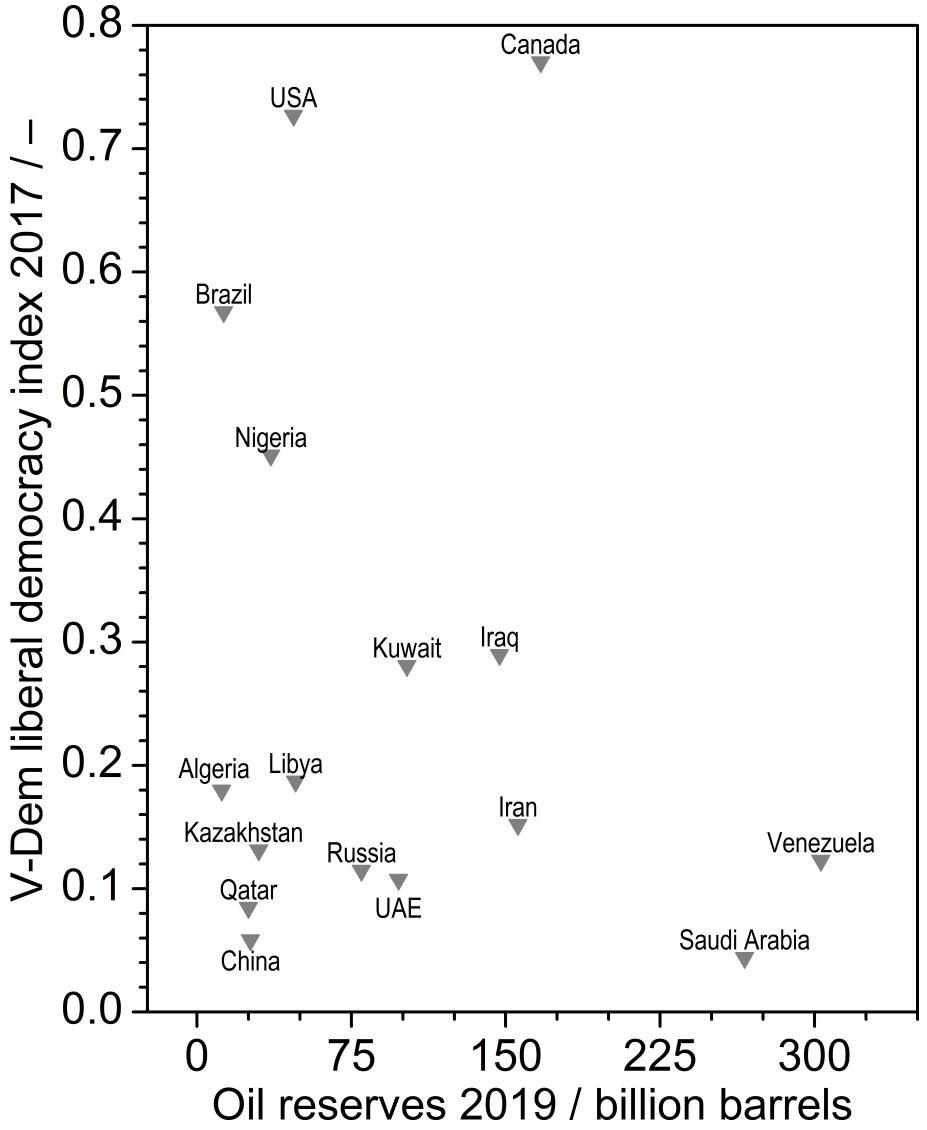

Figure 1.3: V-Dem[30] liberal democracy index 2017[31] versus oil reserves per country in billion barrels as estimated in 2019.[32]

As mentioned above, access to energy is fundamental for future social developments. However, the current use of fossil fuels to meet this energetic demand has intrinsic limitations for the creation of more open and

democratic societies. Besides their negative impact in the mid term due to climate changes, fossil fuels affect humanity as well in the short term. Since they are a limited and localized energy source, oligarchies can control fossil fuels reserves and establish despotic institutions. Among the countries with large oil reserves, well-established democracies such as Canada and United States of America are the only exceptions to oppressive regimes, **Figure 1.3**. Thus, the progress of humanity implies a strong change of economic and energetic paradigms.

Apart from energy supply, new generations will face the social and economic consequences of climate changes. Even though the short-term impact of global warming cannot be easily determined, we can quantify its long-term effects from economic models. Warm countries are going to be severely affected with GDP loss between 0.5% and 1.5% for global warming between 1.5°C and 2.0°C (target of the Paris Agreement).[33] Instead, cold continents such as North America, Asia, and Europe could have a partial benefit due to increments in agricultural production. Yet, for higher temperature anomalies the global impact on welfare would be severe for the entire world population.

Taking European Union as a reference,[34] all the regions apart from Northern Europe would experience a welfare loss between 0.2% and 1.7%, **Figure 1.4**. Southern countries such as Spain, Italy, and Greece would suffer a significant reduction of their agricultural potential due to desertification and reduction of coastal areas. Touristic flow would shift toward Central and Northern Europe, favoring the touristic sector in these regions. River flood and other extreme weather phenomena would damage South-central Europe and British Isles. Northern Europe would instead have a positive return from climate change, mostly due to agricultural development. Overall, a global warming from 2.5 to 5.4°C would reduce European Union citizenship welfare from 0.3 to 1.1% due to coastal deterioration and extreme weather phenomena. According to the Intergovernmental Panel on Climate Change (IPCC),[35] global temperature could increase from 0.3°C to 4.8°C relative to 1850-1900 values by 2100. Temperature alteration is likely to exceed 1.5°C for three scenarios over the four employed in the IPCC study, thus global and European predictions of welfare and GDP loss are likely to occur. For this reason, global and local initiatives toward sustainable development such as the European Green Deal[2] are necessary and should involve the largest possible numbers of stakeholder.

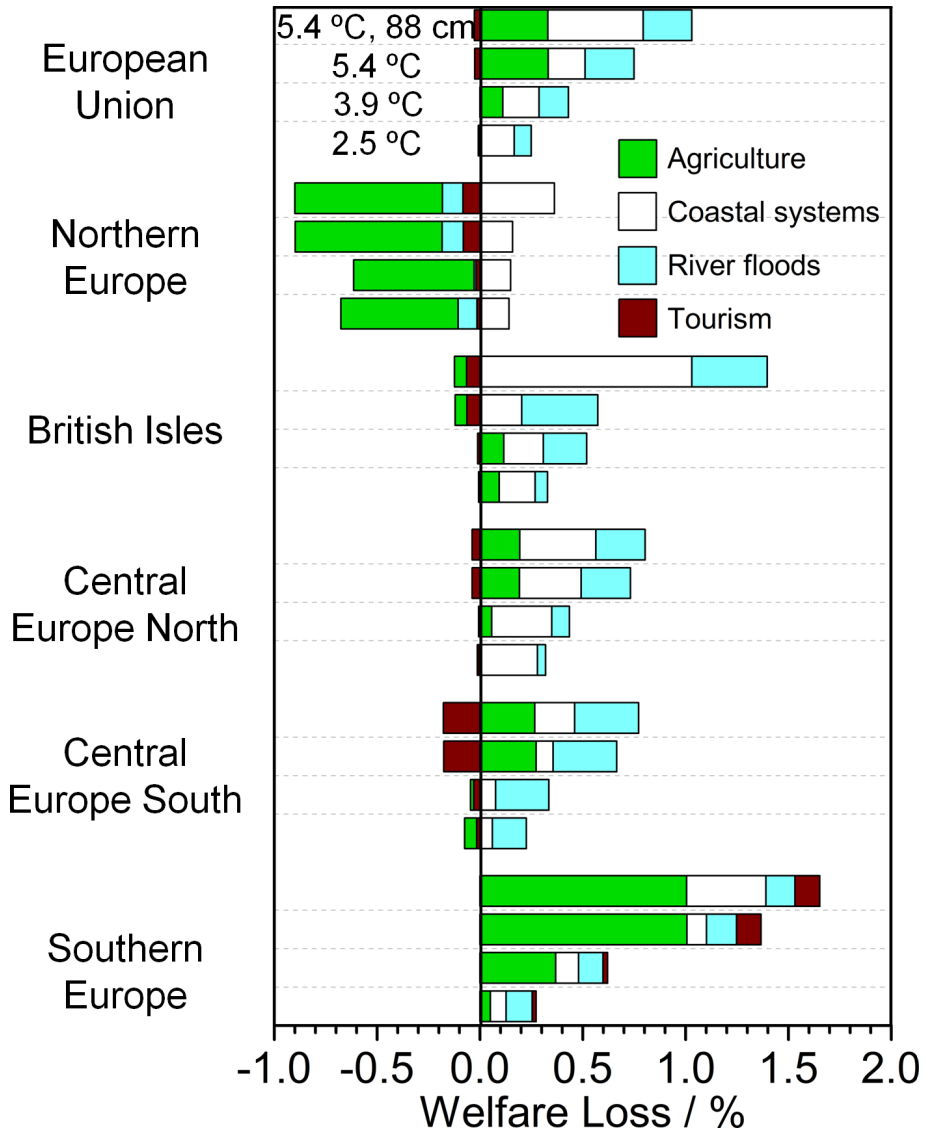

Figure 1.4: Effects of climate changes in European economy for four different scenarios in 2080. Adapted from Ref.[34].

1.3 Low-carbon energy sources

Power generation from low-carbon energy sources, such as renewables and nuclear, had a significant increase in the last twenty years, moving from a 35% share in 2000 (18% renewable) to a 37% share in 2019 (27% renewable). Predictions from the International Energy Agency (IEA) based on a sustainable development scenario suggest that 49% of the global power

could be generate by renewable energies by 2030, accounting for an overall low-carbon production of 59%.[36] These positive expectations on renewable energies are possible because of the exponential decrease of photovoltaic devices cost during the last forty years,[37] which makes solar energy the cheapest electricity source in the history[38] with a cost per unit of power lower than 0.38 \$ W^{-1}.[37] However, technological progress in renewable energy production must goes hand in hand with ideation and production of better devices for energy storage, since wind power, photovoltaic, and hydropower are intermittent energy sources.[39]

1.4 Energy storage

The introduction of energy storage dates to the beginning of the 20th century to provide energy when the power stations were not active.[40] The first systems were based on potential energy storage such as Pumped Hydroelectric Storage (PHS) and Compressed Air Energy Storage (CAES). Even though both infrastructures allow for long lifetime so they are among the most employed technologies nowadays, the scarcity of suitable sites limits their future implementation. Hydroelectric storage requires the construction of two large reservoirs or two dawns at different altitudes, whereas Compresses Air Storage involves the presence of a large cave or artificial container underground. Furthermore, due to the large investments necessary for their installation, these complexes only respond to commodity energy management.

Other forms of mechanical and electrical storage such as capacitors, supercapacitors, flywheels, and superconducting magnets have different issues which hinder their large-scale application. Capacitors, supercapacitors, and flywheels provide high power density. Hence, they are suitable for short duration powering. However, they suffer of huge energy losses due to windage and self-discharge, thus they are unable to respond to high duration needs. Instead, superconducting magnets present a high energy storage efficiency (around 97%) and long lifetime per cycle. Nevertheless, their industrial scale up is hampered by the high production and maintenance cost and the negative environmental impacts due to the high magnetic field created.

Developed technologies such as redox flow batteries, Li-ion batteries, and thermal energy storage are good candidates for application due to their low capital cost and their medium energy density, **Figure 1.5**. Li-ion batteries are currently the most employed energetic storage for portable devices and automotive sector thanks to their energy density. Even so, the high demand for lithium and its extraction cost will affect this technology in the future.[41] An ultimate solution to energy storage would be to produce chemical fuels

such as hydrogen and methanol from abundant feedstocks as water and carbon dioxide. Thanks to their high energy density, more than 0.5 kWh l^{-1},[40] these sustainable fuels would be good alternatives to fossil fuels.

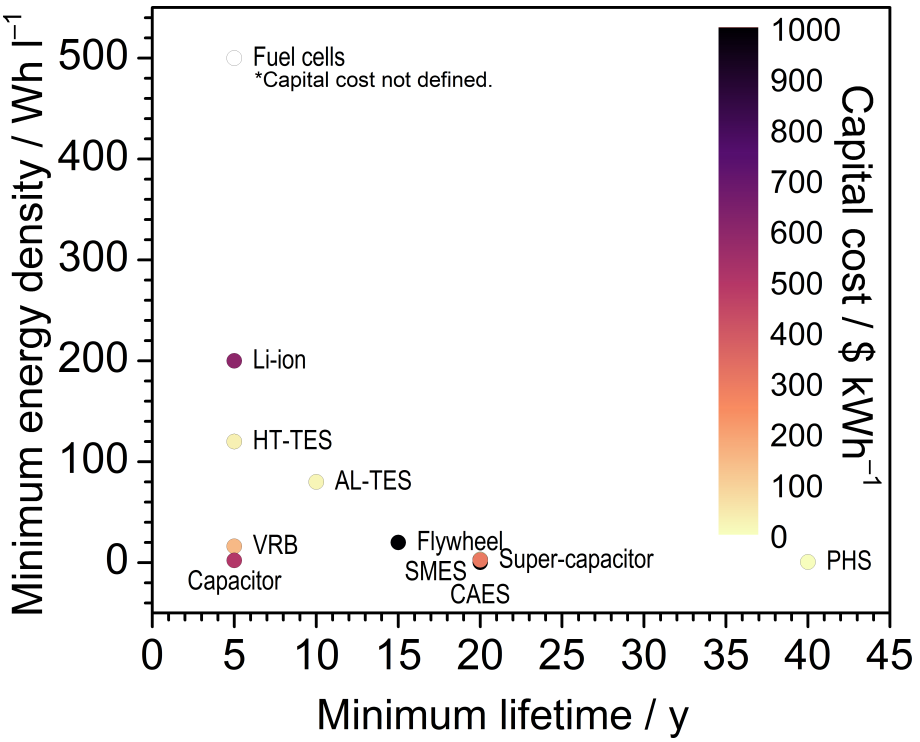

Figure 1.5: Energy storage classified by minimum lifetime in years, minimum volumetric energy density, and capital cost in \$ kWh^{-1}. PHS: Pumped Hydroelectric Storage, CAES: Compressed Air Energy Storage, VRB: Vanadium Redox flow Battery, SMES: Superconducting Magnetic Energy Storage, AL-TES: Aquiferous Low-temperature Thermal Energy Storage, HT-TES: High-Temperature Thermal Energy Storage. Adapted from Ref.[40].

1.5 Electrochemical CO_2 reduction

In comparison to Hydrogen production, electrochemical CO_2 reduction has the benefit of being able to produce green fuels with net negative impact on CO_2 emissions,[42] **Figure 1.6**.

Carbon is the basic molecule for the development of life and biological metabolism is based on the capability of organisms to convert this element between its different oxidation state.[12] Since C in CO_2 has the highest possible oxidation state, +4, the conversion of this molecule into chemical

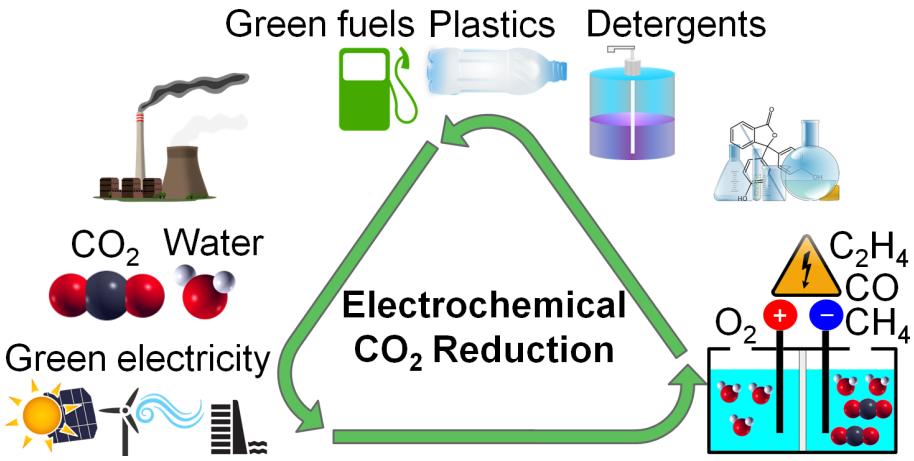

Figure 1.6: Scheme for electrochemical CO_2 reaction. Green electricity can be stored in chemical bonds by converting carbon dioxide and water into basic carbon feedstocks at the cathodic section of an electrochemical cell, whilst oxygen is produced at the anode. These basic carbon components can be converted into more valuable organic molecules employed as fuels or to produce plastics or detergents. By combustion of these fuels, the carbon dioxide initially stored is released, therefore allowing for the closure of the carbon cycle.

products requires the transfer of electrons, **Table 1.1**. The energetic cost of a specific reaction product depends on the number of electrons needed, thus the production of C_2 and C_3 chemicals such as ethylene, ethanol, and propanol is more energetically demanding. Since the anodic reaction, Oxygen Evolution Reaction, exhibits a thermodynamic equilibrium potential of 1.23 V vs RHE, the potential applied to the electrochemical cell to enable CO_2 reduction is always larger than 1 V due to the positive equilibrium potential for carbon products.

In general, the CO_2 reduction process presents an initial base cost due to the capture of carbon dioxide from air, which is at least 200 $ per ton of carbon.[12,43] Hence, the electrochemical production of chemicals which can be obtained from natural gas, as coal, syngas, and methane, is industrially unfavorable. Same applies for the production of methanol in the short term. Even though this compound is promising due to its high energy content, its electrochemical synthesis may be competitive with production by other chemical processes only for low electricity cost, **Figure 1.7**. Carbon monoxide and formic acid are the two CO_2 reduction products which currently provide the best industrial revenue.[12,14] Although they have a limited market share, specific future applications, such as the usage of formic

Table 1.1: **Main CO_2 reduction products with equilibrium potential E^0 in V vs RHE.** Adapted from Ref.[12].

Reaction	E^0	Product
$2H^+ + 2e^- \rightarrow H_2$	0	Hydrogen
$CO_2 + 2H^+ + 2e^- \rightarrow HCOOH_{(aq)}$	–0.12	Formic acid
$CO_2 + 2H^+ + 2e^- \rightarrow CO_{(g)} + H_2O$	–0.10	Carbon monoxide
$CO_2 + 6H^+ + 6e^- \rightarrow CH_3OH_{(aq)} + H_2O$	+0.03	Methanol
$CO_2 + 8H^+ + 8e^- \rightarrow CH_{4(g)} + 2H_2O$	+0.17	Methane
$2CO_2 + 2H^+ + 2e^- \rightarrow (COOH)_{2(s)}$	–0.47	Oxalic acid
$2CO_2 + 8H^+ + 8e^- \rightarrow CH_3COOH_{(aq)} + 2H_2O$	+0.11	Acetic acid
$2CO_2 + 10H^+ + 10e^- \rightarrow CH_3CHO_{(g)} + 3H_2O$	+0.06	Acetaldehyde
$2CO_2 + 12H^+ + 12e^- \rightarrow C_2H_5OH_{(aq)} + 3H_2O$	+0.09	Ethanol
$2CO_2 + 12H^+ + 12e^- \rightarrow C_2H_{4(g)} + 4H_2O$	+0.08	Ethylene
$2CO_2 + 14H^+ + 14e^- \rightarrow C_2H_{6(g)} + 4H_2O$	+0.14	Ethane
$3CO_2 + 16H^+ + 16e^- \rightarrow C_2H_5CHO_{(aq)} + 5H_2O$	+0.09	Propionaldehyde
$3CO_2 + 18H^+ + 18e^- \rightarrow C_3H_7OH_{(aq)} + 5H_2O$	+0.10	Propanol

acid as a hydrogen carrier, could boost their future industrial relevance. In the mid to long term scenario ethylene and ethanol production from CO_2 could also be suitable for industrial scale up. The annual global production of ethylene is around 120-150 Mt[12,14] since it is employed as precursor for fabrication of plastics, such as polyethylene (116 Mt/year), polyvinyl chloride (38 Mt/year) and polystyrene (25 Mt/year).[14,44] The current technology involves repeated cycles of steam cracking at high temperature with consequent quenching, distillation, and recompression, thus this process is energy-demanding and has huge impact on the environment.[12,45] Instead, ethanol is already sold at a higher price that the potential cost of its electrochemical production from CO_2,[12] thus this synthetic route is open as well.

From the pioneering studies of Teeter and Van Rysselberghe,[5] the field of electrochemical CO_2 reduction has developed quickly. Several metals are good catalysts for this reaction, since they adsorb carbon dioxide good enough to enable the electron transfer needed for its reduction.[18] The systematic study of Hori on polycrystalline[6,15] and single crystals metallic electrodes[7] permitted to classify these systems based on their ability to adsorb hydrogen or carbon monoxide,[10] **Figure 1.8**. Metals which adsorb CO and H too strongly, such as Ni, Pd, Pt, etc. are subjected to CO poisoning, thus they are unselective toward CO_2 reduction and they evolve hydrogen if a negative potential is applied. On the other side, metals like Sn, Ti, Hg, Cd, and Pd exhibit a very poor catalytic activity, hence they are unable

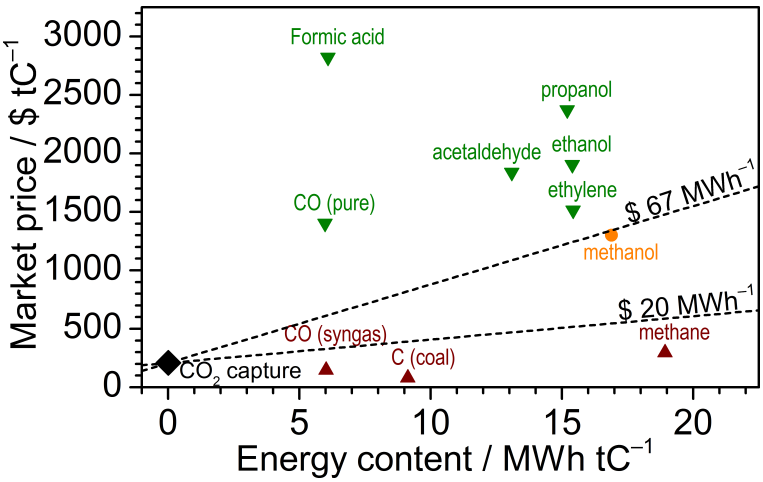

Figure 1.7: Market price for specific CO_2 reduction products versus their energy content. 20 \$ MWh^{-1} is the industrial electricity price assumed for a massive photovoltaic generation,[12] whereas 67 \$ MWh^{-1} accounts for the industrial USA electricity price in 2020.[46] In red prohibitive CO_2 reduction products, in orange scalable technologies for low electricity price, in green chemical production possible at the current electricity price. Adapted from Ref.[12].

to adsorb hydrogen. As a consequence, at negative potential they reduce CO_2 to formate or formic acid. Metals with a higher affinity to hydrogen, such as gold, silver, and zinc are instead selective to CO, since they have a thermoneutral adsorption energy for this intermediate. Copper has instead the unique ability of producing hydrocarbons,[15] thus copper-based catalysts are usually investigated for ethylene and ethanol production. CO_2 reduction selectivity depends on Cu local morphology.[7,11] (100) facets are expected to be active toward ethylene productions, whilst (110) defects enhance ethanol production. Close-packed domains such as Cu(111) are instead preferential sites for methane production.

1.6 Challenges of electrochemical CO_2 reduction on copper

Even though modeling of well-defined copper surfaces[9–11] provided good predictions of experimental results,[6,7,15] non-conventional synthetic procedures and more accurate characterization techniques have generated new theoretical challenges. Surface reconstruction of polycrystalline copper under CO_2 reduction conditions has been detected.[16] Either polarization ef-

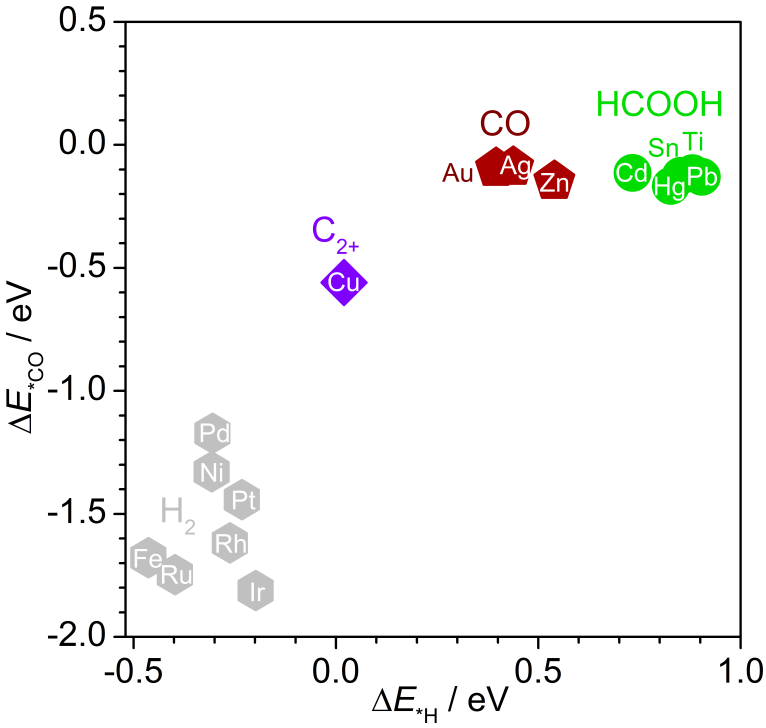

Figure 1.8: Theoretical classification of selective metallic electrodes for CO_2 reduction toward formic acid (green), carbon monoxide (red), C_{2+} (purple), and hydrogen (gray) based on *H and *CO binding energy. Adapted from Ref.[10].

fects[16] or interactions with reaction intermediates[47,48] have been suggested as the driving force. Oxide-derived copper exhibits a very different CO_2 product distribution from metallic copper[49,50] and moreover its selectivity changes over reduction time.[51] These experimental evidences led to a never-ending debate on the presence and influence of residual oxygen on the chemical process. Chemical modification of copper by insertion of tiny amount of *p*-block elements[52–54] can enhance its selectivity toward desired products such as formate[55] and carbon monoxide.[56,57] Cation is expected to stabilize relevant reaction intermediates such as CO_2^- and $OCCO^-$,[17,58] yet so far theoretical simulations only rationalized this effect by assuming cation concentration gradients[21,59] and consequent variations of the surface electric field.[20] All these effects influence each other mutually, thus increasing even more the overall complexity. Nevertheless, an accurate description of the copper electrode under working conditions must include all these contributions.

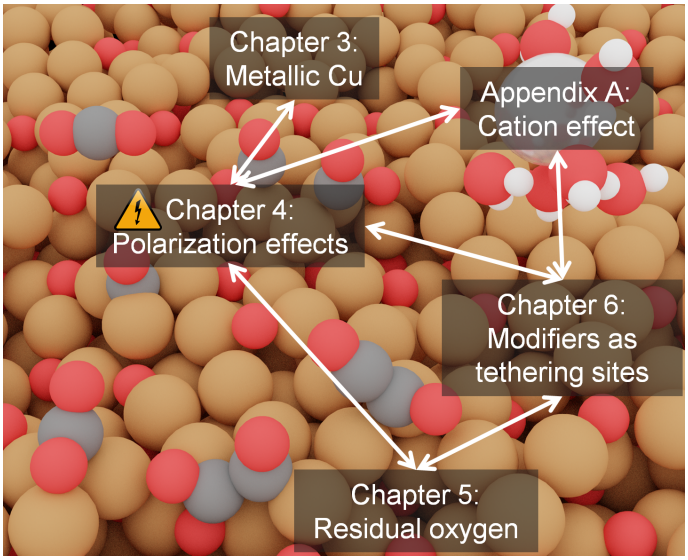

Figure 1.9: Main challenges in theoretical modeling of electrochemical CO_2 reduction. Basic models on crystalline copper cannot entirely explain copper selectivity under working conditions. Theory must explicitly consider potential-driven surface reconstruction, surface modifiers, cation, and residual oxygen to achieve a more accurate understanding of the processes occurring at the electrode surface.

1.7 Objectives

The target of this thesis is to model the electrochemical CO_2 reduction on copper-based catalysts under working conditions. Thus, this work has aimed at suggesting methodological concepts to address two main aspects: (i) the reconstruction at the cathode surface due to high surface polarization and (ii) the influence of surface modifiers on the catalytic performance of copper. Since CO_2 reduction on copper catalysts is a rapidly evolving field, a proper sharing of results to the scientific community helps its progress. Following the FAIR principles, which means to make our results Findable, Accessible, Interoperable, and Reusable, all the structures generated for this study where uploaded in a public online database, ioChem-BD.[60] Furthermore, the two publications (Refs.[61, 62]) resulting from this work were granted open access.

Summary of the objectives by chapter

Chapter 3 Metallic Cu

As a first introduction to the topic, I investigate two simple systems, copper nanoparticles and Cu(100), and I confirm the experimental observations about their preferential reactivity towards methane and C_{2+}, from both kinetic and thermodynamic perspectives.

Chapter 4 Surface reconstruction under reaction conditions.

I address the influence of applied potential on copper surface reconstruction by developing a Density Functional Theory model which explains this structural phenomenon on a thermodynamic basis. Furthermore, I relate the expected reconstruction toward Cu(100) to a higher selectivity of copper-based catalysts toward ethylene, by synthesizing a CuO-derived catalyst during my secondment at Avantium Chemicals BV.

Chapter 5 C_{2+} selectivity and activity of oxide-derived copper

Oxide-derived copper has been reported experimentally highly active and selective towards C_{2+} products. I decouple the contributions of polarized copper sites, residual oxygen, and surface alkaline pH to the strong reconstruction happening at the electrolyte-electrode interface and to the consequent time-dependent product distribution under reduction conditions. Initially, I characterize the system, assessing the chemical speciation of copper, its local coordination, and the thermodynamic stability of residual oxygen. Secondly, I investigate the main factors which contribute to the enhanced activity and selectivity to C_{2+} products of oxide-derived copper. Thirdly, I characterize the active surface area of the system and the atomic surface roughness, as well as assess the influence of surface polarization and ensembles on the catalyst's performance.

Chapter 6 CO_2 reduction to formate on chalcogen modified copper

State-of-the-art reports highlight the promotion of formate production on sulfur modified catalysts. Copper is itself poorly selective to formate with Faradaic efficiency (FE) lower than 20%. However, tiny amounts of sulfur promote formate or formic acid up to 80% FE. Even though many experimental studies have been carried out, they do not provide evidences on the chemical species of the active site, whether Cu or S, neither a rational behind this improvement in selectivity. The goal of this chapter is to model the experimental system and to explain the significant influence of sulfur on CO_2 reduction to formate on copper catalysts.

Chapter 2

Theoretical background

Modeling of CO_2 reduction reaction requires a deep understanding of both electrochemical processes and Density Functional Theory (DFT) formalism. First, this reaction involves the transfer of the reactant, carbon dioxide, all the way from the bulk electrolyte to the cathodic surface. At this stage, mass transfer limitations play a relevant role. Upon adsorption, an electron transfer to CO_2 is required to enable the reduction, therefore the kinetics of charge transfer has a additional influence on the process. Evolution of reactants to reaction intermediates and eventually products imply electrochemical steps, such as electron transfers, or chemical steps without charge transfer, which can happen both at the electrode surface (heterogeneous reaction) or in solution (homogeneous reaction). Concurrently, electrochemical conditions affect the electrode surface in real time, thus polarization-driven surface reconstruction or interaction with reaction intermediates and electrolyte are relevant parameters as well. Density Functional Theory, being a theory at the atomistic scale, provide useful insights into the ease of electrochemical and chemical steps, therefore all the other factors mentioned before must be assessed through analytical electrochemical equations.

Whereas the DFT formalism can describe accurately well-defined atomic systems such as single crystals, its application to catalysts under working conditions must be coupled to hybrid models to account for electrochemical processes. DFT is employed to study catalytic activity of atomic ensembles, and analytical models and electrostatic corrections through Poisson-Boltzmann theory are generally applied to describe mass transfer processes[63] or the influence of local electrostatic field.[21,64] The kinetics of charge transfer is not usually considered in DFT calculations, whereas charge transfer and influence of the applied negative potential are included in the simulations through the Computational Hydrogen Electrode approach.[9,65] According to this model, charge transfer is assumed to occur as proton-coupled

electron transfers and the Gibbs free energy of a charged reaction intermediate is stabilized by a linear correction which depends on number of electrons transferred and applied potential.

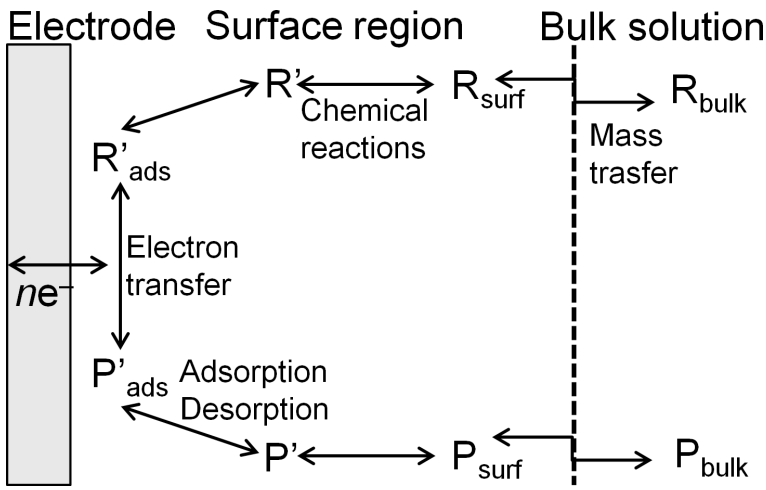

Figure 2.1: Reactions and processes on an electrode (cathode or anode). Here, R is the reactant and P the product. Adapted from Ref.[66].

2.1 Electrochemistry

Allen J. Bard and Larry R. Faulkner describe electrochemistry as "the branch of chemistry concerned with the interrelation of electrical and chemical effects" in the so-called "Bible" of electrochemistry.[66] Electrochemistry indeed focuses on the interaction between electrons and chemical compounds between a electrochemical cell, a black box composed by a positively polarized electrode, the anode, and a negatively polarized one, the cathode.

2.1.1 Electrochemical cells

Electrochemical cells are typical electrochemical systems composed by two electrodes separated by at least one electrolyte, **Figure 2.2**. By establishing an electrical connection between the two electrodes, charge transport starts occurring between the different chemical phases composing the cell. In the electrodes charge transport happens through the motion of electrons and holes. In the electrolyte, charge is carried by the motion of the ions contained in the solution. As a consequence, one half-reaction takes place at each electrode, so that an overall chemical reaction occurs within the cell. Since a given reaction such as CO_2 reduction occurs at one electrode,

called working electrode, the reaction taking place at the opposite electrode, named reference electrode, is standardized, so that the change in the interfacial potential difference depends only on the reaction of interest.

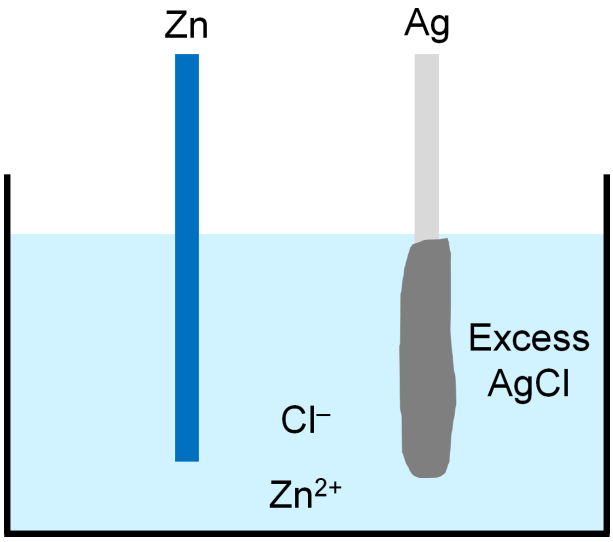

Figure 2.2: An example of electrochemical cell: $Zn/Zn^{2+},Cl^{-}/AgCl/Ag$. According to Bard/Faulkner notation, slashes represent a phase boundary (solid electrode/liquid electrolyte) whilst the comma separates two components at the same phase. In the depicted system, Zn and Ag are the metallic electrodes (anode and cathode) in the solid phases, whereas Zn^{2+} and Cl^{-} diffuse between them in a $ZnCl_2$ solution. The overall chemical reaction happening in the cell, $Zn_{(s)} + 2Ag^{+}_{(aq)} \rightarrow Zn^{2+}_{(aq)} + 2Ag_{(s)}$, is constituted by two half-reaction: the oxidation of Zinc at the anode, $Zn_{(s)} \rightarrow Zn^{2+}_{(aq)} + 2e^{-}$, and the reduction of silver at the cathode, $Ag^{+}_{(aq)} + e^{-} \rightarrow Ag_{(s)}$. Adapted from Ref.[66].

The references electrodes employed throughout this thesis are:

- Standard Hydrogen Electrode, SHE, also called Normal Hydrogen Electrode (NHE), described by the following half reaction, hydrogen evolution reaction at unit activity (pH = 0), **Equation 2.1**.

$$Pt/H_2(a = 1)/H^{+}(a = 1, \text{ aqueous}) \tag{2.1}$$

- Reversible Hydrogen Electrode, a subtype of the SHE. The electrode is in contact with the electrolyte solution, therefore the measured potential is corrected to account for the electrolyte pH, **Equation 2.2**.

$$U(\text{V vs RHE}) = U(\text{V vs SHE}) + k_B T \cdot \ln 10 \cdot \text{pH} \tag{2.2}$$

Without an external bias, the potential across the electrochemical cell is called open circuit potential and it depends on the standards potentials of the half-reactions involved at both cathode and anode. Connecting the cathode to a power supply, the energy of the electrons at the electrode surface is raised and they can transfer to vacant electronic sites of the electrolyte species (reduction current). Applying a positive potential to the anode, the energy of the electrons is lowered and a oxidation current occurs from the solutes in the electrolyte to the anode (oxidation current). The potentials U which enable these charge transfer processes are related to the standard potentials U^0 of reduction or oxidation of a specific chemical species. The flow of electrons through an electrode correlates with the rate of the chemical reaction occurring, according to the Faraday's law:

A charge transfer of 96485 C (Faradaic constant) causes 1 equivalent of the chemical reaction, which leads to the consumption of 1 mole of reactant and the production of 1 mole of product in the case of a single-electron process.

Chemical reactions which occur through an electron transfer are described as Faradaic processes. Non Faradaic processes do not imply charge transfer, therefore they consists of intermediate adsorption, desorption, changes in the electrolyte, etc.

2.1.2 Faradaic processes

When Faradaic processes occur inside an electrochemical cell by connecting cathode and anode, this system is named galvanic or voltaic cell and it is used to generate electrical energy from redox reactions happening within the device, as the Zn-Ag cell shown in **Figure 2.2**. Instead, when an external potential greater than the open circuit potential is applied to the cell to convert reactants into products, this technology is called electrolytic cell, **Figure 2.3**. These are the typical cells used for electrochemical CO_2 reduction. For instance, CO_2 can reduce to CO on gold and silver cathodes at mild potentials, whilst oxygen evolution reaction is performed at the anode as the other half-reaction to close the circuit. Following Faraday's law, the rate of this chemical reaction can be expressed as **Equation 2.3**, with the Faradaic constant F, the moles of CO produced N, the reduction current i, and the number of electrons transferred n, in this case 2. For chemical reactions occurring at the electrode surface, named heterogeneous processes, **Equation 2.3** is commonly normalized by the electrode area, **Equation 2.4**, so that j is the current density. Since to enable a chemical reaction the external bias must be higher than the open circuit potential,

the degree of polarization of the electrode is defined through the concept of overpotential η, difference between the applied external potential and the cell equilibrium potential, U_{eq}, equivalent to its open circuit potential if the contributions of liquid junctions are neglected.

$$r\ (\text{mol s}^{-1}) = \frac{\mathrm{d}N}{\mathrm{d}t} = \frac{i}{nF} \tag{2.3}$$

$$\nu\ (\text{mol s}^{-1}\ \text{cm}^{-2}) = \frac{i}{nFA} = \frac{j}{nF} \tag{2.4}$$

$$\eta = U - U_{\text{eq}} \tag{2.5}$$

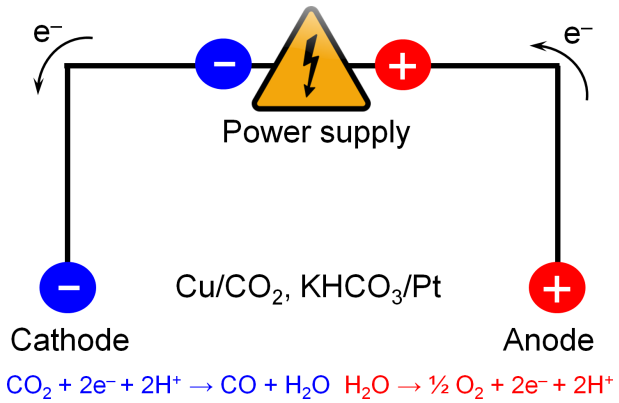

Figure 2.3: An example of electrolytic cell: CO_2 is reduced at the cathode to CO (blue), whilst oxygen evolution reaction occurs at the anode (red) upon application of an external potential. Adapted from Ref.[66].

2.1.3 Butler-Volmer model of electrode kinetics

The rate constant k normalized by the concentration of reactant C_R for a specific chemical reaction is defined by the experimental relationship known as Arrhenius equation, **Equation 2.6**. This experimental formula states the dependency of reaction rate constant on temperature T, reaction activation energy E_{a}, and frequency factor A. Chemical reactions can present both a forward and reverse path. Taking for instance **Reaction 2.7**, the reactant R reduces to the product P through n electron transfers at a rate constant k_{f}. However, P can oxidized back to the reactant R at a rate constant k_{b}. Upon reduction reaction, the forward pathway increases the surface concentration of the product C_P, whilst the concentration of the reactant C_R decreases. For the reverse process, the opposite holds true. The

forward reaction leads to a cathodic current, i_c, whilst the reverse process creates an anodic current, i_a, which depends on the reaction rates and the concentration of R and P species, **Equation 2.8**. The overall current at the electrode is given by the difference between cathodic and anodic current, **Equation 2.9**.

$$k\ (\mathrm{mol}^{-1}\ ) = Ae^{\frac{-E_a}{RT}} \tag{2.6}$$

$$R + n\mathrm{e}^- \underset{k_b}{\overset{k_f}{\rightleftharpoons}} P \tag{2.7}$$

$$\begin{aligned} i_c =& nFA\nu_f = nFAk_fC_R(0,t) \\ i_a =& nFA\nu_b = nFAk_bC_P(0,t) \end{aligned} \tag{2.8}$$

$$i = i_c - i_a = nFA[k_fC_R(0,t) - k_bC_P(0,t)] \tag{2.9}$$

If the potential applied to the electrolytic cell is equal to the equilibrium potential, the system is at equilibrium, thus the bulk concentrations of R and P species are equal due to Nerst equation, **Equation 2.10**, and the net reaction rate between forward and reverse reactions must be null, $k_fC_R(0,t) = k_bC_P(0,t) \Longrightarrow k_f = k_b$. Hence, k_f and k_b can be expressed as a function of a unique parameter, the standard rate constant k^0, **Equation 2.11**, where transfer coefficient α quantifies the ease of electron transfer. **Equation 2.9** can then be rewritten as the Butler-Volmer equation, **Equation 2.12**. This equation has different approximated forms depending on the electrochemical regimes. At high overpotential, it leads to the definition of the well-known Tafel equation, **Equation 2.13**. The parameter b, defined as the Tafel slope, provides an estimation of the number of electrons transferred for a chemical reaction. Thus, this current versus overpotential plot is employed in electrochemistry to shed light on charge transfers processes.[61,67]

$$U = U^0 + \frac{RT}{nF}\ln\frac{C_R}{C_P} \tag{2.10}$$

$$\begin{aligned} k_f =& k^0e^{-\frac{n\alpha F}{RT}(U-U^0)} \\ k_b =& k^0e^{-\frac{n(1-\alpha)F}{RT}(U-U^0)} \end{aligned} \tag{2.11}$$

$$i = nFAk^0\left[C_R(0,t)e^{-\frac{n\alpha F}{RT}(U-U^0)} - C_P(0,t)e^{-\frac{n(1-\alpha)F}{RT}(U-U^0)}\right] \tag{2.12}$$

$$\begin{aligned} i =& a'e^{\frac{\eta}{b'}} \\ \eta =& a + b\log i \end{aligned} \tag{2.13}$$

2.1.4 Electrical double layer

Under certain potential ranges, no charge transfer takes place between electrodes and electrolyte, therefore the Faradaic current which occurs upon application of an external bias is only due to electrochemical conversion of the reactant toward a given product. Under these working conditions, an electrode is defined Ideal polarizable Electrode (IPE) and the electrode-electrolyte interface can be modeled as a capacitor, a system constituted by two conductors, in this case the electrodes, separated by a dielectric material, the electrolyte. If polarized, an electrode will accumulate charge, q^{M}, which is balanced by an opposite charge of the electrolyte solution, $q^{\mathrm{S}} = -q^{\mathrm{M}}$. q^{M} resides in the external layer of the electrode within < 0.1 Å from its termination, whilst q^{S} builds up from the excess of ions, respectively anions in the vicinity of the anode and cations in the vicinity of the cathode. The accumulation of these charged species at the metal-electrolyte interface creates the so-called electrical double layer. This concept is experimentally characterized by the double layer capacitance, C_{d}.

Current models for the electrical double layer account for regions. In the proximity of the electrode, the inner layer, also named compact, Helmholtz, or Stern layer, is constituted by solvent molecules and, under specific conditions, unsolvated cations and anions which specifically interact with the electrode surface.[68–70] The center of those charges species accounts for the inner Helmholtz plane (IHP), distant x_1 from the electrode surface, **Figure 2.4**. The outer Helmholtz layer (OHP) resides at a distance x_2, where solvated ions begin to appear. These solvated species extend for the whole diffusion layer, region ranging from the OHP to the bulk electrolyte. Thus, the excess charge density of the electrolyte solution, σ^{S} comprehends the charge density concentrated in the inner Helmholtz plane, σ^{i}, and the charge density within the diffuse layer, σ^{d}, **Figure 2.4**.

$$\sigma^{\mathrm{S}} = \frac{q^{\mathrm{S}}}{A} = \sigma^{\mathrm{i}} + \sigma^{\mathrm{d}} = -\sigma^{\mathrm{M}} \tag{2.14}$$

Higher the ionic concentration in the bulk electrolyte, lower the diffuse layer thickness, which accounts for less than 100 Å for ionic concentrations higher than 10^{-2} M.[66] Furthermore, the potential drop across the diffuse layer caused by cation and anions, $\phi_2 - \phi^{\mathrm{S}}$, in V, diminishes the gradient of potential at the electrode-electrolyte interface, $\Delta\phi = \phi^{\mathrm{M}} - \phi_2$, instead of a $\Delta\phi = \phi^{\mathrm{M}} - \phi^{\mathrm{S}}$, expression valid for an ideal system.

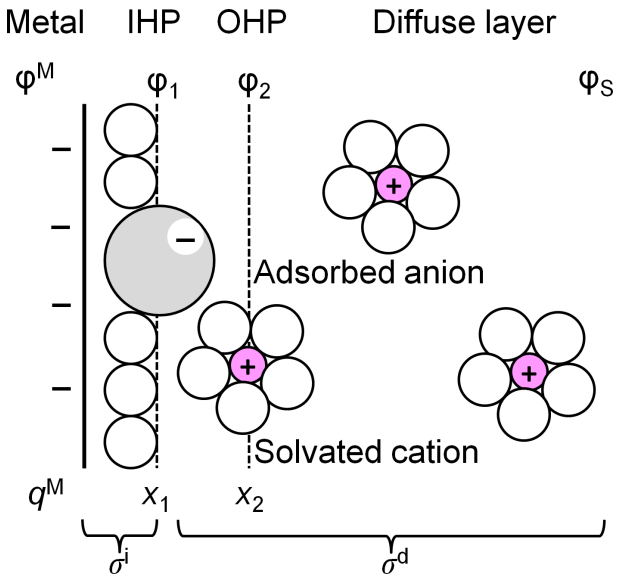

Figure 2.4: Graphical representation of the electrical double layer under specific interaction between charged anion and cathodic surface.[70] Adapted from Ref.[66].

2.1.5 Mass transfer

Introduction

Gradients of chemical and electrical potentials influence the motion of an element in solution. Three main factors affect mass transfer. First, effects due to different concentrations of chemical species in solution are classified under the concept of diffusion. Secondly, influences of local variations of the electric field on the motion are defined as migration phenomena. Finally, convection plays a role when motion is affected by hydrodynamic transport due to natural convection, such as density gradients, or forced convection, such as stirring. All the three phenomena are described by the Nernst-Planck equation: at a distance x from the electrode, the unidimensional flux of a chemical species i, $J_i(x)$, measured in mol s^{-1} cm^{-2}, is modeled through **Equation 2.15**. Diffusion depends on the mass diffusivity coefficient D, in cm^2 s^{-1}, and the gradient of the concentration of the chemical specie, C, measured in mol cm^{-3}. Migration effects correlate with concentration, diffusion coefficient, charge, and gradient of the electric potential ϕ. Convection phenomena scale with the velocity of a differential volume of solution, $v(x)$, and the concentration of the chemical species. If the employed electrolyte is inert, so that it can be described as a supporting electrolyte, and convection is controlled, migration and convection effects are negligi-

ble. Therefore, **Equation 2.15** simplifies to the Fick's first law, **Equation 2.16**. If no chemical reaction is occurring, mass conservation applies: any local variation of the concentration of a chemical species over time determines a spatial concentration gradient of the same magnitude. Therefore, Fick's second law can be derived from the first law, **Equation 2.17**. A numerical solution of this equation allows to estimate the evolution of the concentration of specific elements over time.

$$J_i(x) = \underbrace{-D_i \frac{\partial C_i(x)}{\partial x}}_{\text{diffusion}} \underbrace{- \frac{z_i F}{RT} D_i C_i \frac{\partial \phi(x)}{\partial x}}_{\text{migration}} + \underbrace{C_i v(x)}_{\text{convection}} \tag{2.15}$$

$$J_i = -D_i \nabla C_i(x) \tag{2.16}$$

$$\frac{\partial C_i}{\partial t} = D_i \nabla^2 C_i \tag{2.17}$$

Influence of mass transfer on the reaction rate

If a given chemical reaction presents a low energy barrier, its rate of reaction can be mass transfer limited, which means that the net rate of reaction, ν, is completely controlled by reactant concentration at the electrode surface, $C_R(x = 0)$. Within the diffusion layer thickness of the reactant, δ_R, both migration and convection do not play a relevant role if the cell is static and the electrolyte is inert. Therefore, the mass transfer rate for the reactant, ν_{mt}, is described by Fick's first law, **Equation 2.16**. Upon reaction, $C_R(x = 0)$ will decrease, whilst reactant bulk concentration dooes not suffer local variation if the electrolyte is stirred and constant reactant supply is provided. Thus, it is possible to approximate the variation of reactant concentration as a linear gradient from its maximum value at the bulk and minimum value close to the electrode surface, so that the mass transfer rate reads as **Equation 2.18**. Hence, for steady-state conditions and mass-transfer limited chemical reactions, the current density can be defined as a function of the gradient of concentrations of reactant R and product P and their respective diffusion coefficients and diffusion layer thicknesses, **Equation 2.19**. This analytical equation allows to quantify the effect of mass transfer on the chemical reaction. The diffusion layer thickness of a given chemical species can be estimated under specific experimental conditions. For instance, the Rotating Disk Electrode (RDE) geometry permits the explicit derivation of δ from the angular velocity ω of the electrode through the so called Levich equation, **Equation 2.20**. Influence of the solvent is taken into account through its kinematic viscosity ν, measured in $\text{cm}^2\ \text{s}^{-1}$.

$$\nu_{\mathrm{mt}} = D_R \frac{[C_R - C_R(x=0)]}{\delta_R} \tag{2.18}$$

$$j = nF\left(\frac{D_{\mathrm{R}}}{\delta_{\mathrm{R}}}[C_R - C_R(x=0)] + \frac{D_{\mathrm{P}}}{\delta_{\mathrm{P}}}[C_P(x=0) - C_P]\right) \tag{2.19}$$

$$\delta = \frac{1.61 \cdot \sqrt[3]{D}\sqrt[6]{\nu}}{\sqrt{\omega}} \tag{2.20}$$

2.2 Modeling at the atomic scale

In science, every model has a certain range of validity. In the case of mechanics, Newton's second law can be applied to a physical system to relate its position and momentum to an external force $\vec{F}$ applied to the system, **Equation 2.21**.[71] Thus, it is possible to define the status of a physical system from the forces applied, predicting its evolution over time.[71] However, the Newton's model of classical mechanics fails when it comes to predict the status of a physical system in the atomic scale, such as a molecule, an atom or one of its constituents (proton, neutron, electron, etc.).

$$\vec{F} = m \cdot \vec{a} \tag{2.21}$$

2.2.1 Schrödinger equation

A revolutionary theory, quantum mechanics,[72] was introduced at the beginning of the 20th century. Seeking to solve the experimental and theoretical evidences of the wave-particles dualism, such as the scattering of X-rays (M. Von Laue,[73] A. H. Compton[74]) and the photoelectric effect (A. Einstein[75]), the Austrian physicist Erwin Schrödinger proposed to describe the status of a physical system by mean of wave functions.[76] According to this formalism, the time-independent Schrödinger equation is an eigenvalues equation, **Equation 2.22**, where $\hat{H}$ is the Hamiltonian operator and Ψ is the state vector of the quantum systems. The Ψ_n eigenstates of the Hamiltonian are the solutions of the previous equation and have n associated eigenvalues E_n, which are real numbers. The expansion in term of the positions eigenvector of the state vector is the position-space wave function of the system, **Equation 2.23**.

$$\begin{aligned} \hat{H}\,|\Psi\rangle &= E\,|\Psi\rangle \\ \hat{H}\Psi_n &= E_n\Psi_n \end{aligned} \tag{2.22}$$

$$\Psi(\vec{r}) = \langle \vec{r} | \Psi \rangle \tag{2.23}$$

The definition of the Hamiltonian depends on the system. In chemical systems such as molecules and atoms, atomic nuclei are much heavier than electrons, since the masses of proton and neutron, the constituents of atomic nuclei, are around 1800 times the mass of an electron. Therefore, electrons' response to external excitation is faster, whereas the nuclear motion is slower due to their higher mass. Following these considerations, the Born-Oppenheimer approximation allows to decouple the contributions of nuclei and electrons to calculate the ground state of the system.[77] Thus, the Hamiltonian, **Equation 2.22**, of a non-relativistic system with multiple nuclei and N electrons can be expressed as **Equation 2.24**. The ground state energy E of the electrons depends on their kinetic energy K, the potential V generated by the "fixed" nuclei and the interaction U between electrons. The all-electron wave function is here represented as **Equation 2.25**. For a simple chemical system such as a CO_2 molecule, the all-electron wave function is a 66-dimensional function (22 electrons with 3 spatial coordinates each) so the analytical solution of **Equation 2.24** for molecular systems is not possible.

$$\left[\underbrace{-\frac{\hbar^2}{2m_e}\sum_{i=1}^{N}\nabla_i^2}_{\hat{K}}+\underbrace{\sum_{i=1}^{N}V(\vec{r}_i)}_{\hat{V}}+\underbrace{\sum_{i=1}^{N}\sum_{j<1}U(\vec{r}_i,\vec{r}_j)}_{\hat{U}}\right]\Psi=E\Psi \tag{2.24}$$

$$\langle\vec{r}|\Psi\rangle=\Psi(\vec{r}_1,...,\vec{r}_N) \tag{2.25}$$

A further approximation allows to decouple the all-electron wave function as a product of single-electron wave function, where **Equation 2.26** is defined as the Hartree product. Yet, even under this simplification, **Equation 2.24** cannot be solved for real physical systems due to its many-body problem's nature. Decoupling the all-electron wave function for each of its component, the determination of each single-electron wave function depends on U, the interaction between electrons, **Equation 2.24**, therefore it requires the simultaneous determination of all the other components. The U term is needed for solving Schrödinger equation, but it is defined by the solutions of the equation itself.

$$\Psi(\vec{r}_1,...,\vec{r}_N)=\Psi_1(\vec{r})\Psi_2(\vec{r}),...,\Psi_N(\vec{r}) \tag{2.26}$$

An exact estimation of the all-electron wave function is not of physical interest since it is a mathematical formalism and not a physical observable. Instead, the relevant theoretical variable is the probability for N electrons to be localized in a certain set of coordinates, $(\vec{r}_1,...,\vec{r}_N)$. In fact, electrons'

probability can be related to an experimental observable, the electronic density $n(\vec{r})$, as shown in **Equation 2.27**, where $\hat{n}$ is the density operator, δ the Dirac function, N is the number of electrons in the system, and the second summation accounts for the spin s of each electron i. According to Pauli's exclusion principle, each electronic state can be occupied by two electrons only if they have different spin state since these particles are fermions. Finally, to refer to electronic density, $n(\vec{r}) = n(r_x, r_y, r_z)$, instead of the position wave function, $\Psi(\vec{r}_1, ..., \vec{r}_{3N})$, reduces the complexity of the solution from a 3N-dimensional theoretical function to a 3-dimensional physical observable.

$$\begin{aligned} n(\vec{r}) &= \langle \Psi | \, \hat{n}(\vec{r}) \, | \Psi \rangle \\ \hat{n}(\vec{r}) &= \sum_{i=1}^{N} \sum_{s_i} \delta(\vec{r} - \vec{r}_i) \end{aligned} \tag{2.27}$$

2.2.2 Hohenberg-Kohn theorems

In 1964 Hohenberg and Kohn introduced the concept of a universal functional F of the electronic density $n(\vec{r})$,[78] thus they established the basis for the Density Functional Theory (DFT) formalism. By demonstrating two basic properties of this functional, they provided basic concepts toward a solution of the all-electron Schrödinger equation, **Equation 2.24**.

Theorem 1 *The external potential $V(\vec{r})$ is a unique functional of the electronic density: $V(\vec{r}) = F[n(\vec{r})]$. As a consequence, the full many-body ground state is a unique functional of $n(\vec{r})$ since the external potential defines the Hamiltonian of the system.*

Theorem 2 *The electronic density which minimizes the energy of $F[n(\vec{r})]$ corresponds to the electronic density of the ground state resulting from the solution of the many-body Schrödinger equation.*

Thus, it is possible to determine the ground-state energy of a physical system from its ground-state electronic density (3-D function) instead of the all-electron position wave function ($3N$-D function). Moreover, the ground-state electronic density of the physical system is the one that minimizes the energy of the functional. Through a suitable definition of this unique functional, $n(\vec{r})$ can be estimated by solving the many-body Schrödinger equation. By iteration, it is then possible to determine the ground-state electronic density and consequently the ground-state energy of the system.

2.2.3 Kohn-Sham equations

To define this unique functional, it is convenient to decouple the N-electron Schrödinger equation into N single-electron Schrödinger equations. Thus,

the space wave function now reads as a product of the wave function for each electron, **Equation 2.26**. Hence, the resulting Schrödinger equations for each i single-electron wave function reads as **Equations 2.28**, the so-called Kohn-Sham equations.[79] K and V_{N} account respectively for the kinetic energy of the single electron and the potential resulting from the electronic interaction with the atomic nuclei. Both terms follow from **Equation 2.24**.

$$\left[\underbrace{-\frac{\hbar^2}{2m_{\mathrm{e}}}\nabla_i^2}_{\hat{K}} + \underbrace{V_{\mathrm{N}}(\vec{r})}_{\hat{V}_{\mathrm{N}}(\vec{r})} + \underbrace{e^2\int\frac{n(\vec{r}')}{|\vec{r}-\vec{r}'|}d^3\vec{r}'}_{\hat{V}_{\mathrm{H}}(\vec{r})} + \underbrace{\frac{\delta E_{\mathrm{XC}}}{\delta n(\vec{r})}}_{\hat{V}_{\mathrm{XC}}(\vec{r})}\right]\Psi_i(\vec{r}) = E_i\Psi_i(\vec{r}) \quad (2.28)$$

V_{H}, the Hartree potential, **Equation 2.29**, describes the repulsion between the single electron considered and all the other electrons, represented by $n(\vec{r})$. Since each specific electron contributes twice, both as a single-electron and in the electronic density term, the Hartree potential is affected by a non-physical self-interaction effect. Correction to the self-interaction effect as well as contributions by exchange and correlation are included in the last term, the exchange-correlation potential, which is defined for consistency as a functional derivative, **Equation 2.30**. E_{XC} is the only unknown variable in **Equations 2.30** and it can be estimated via different approximations which are discussed in the following section.

$$V_{\mathrm{H}} = e^2\int\frac{n(\vec{r}')}{|\vec{r}-\vec{r}'|}d^3\vec{r}' \quad (2.29)$$

$$V_{\mathrm{XC}} = \frac{\delta E_{\mathrm{XC}}}{\delta n(\vec{r})} \quad (2.30)$$

Given a convenient approximation of the exchange-correlation term, the ground-state energy for a specific system can be calculated solving self-consistently the Kohn-Sham equations,[79] **Equations 2.28**.

1. An initial electron density $n_0(\vec{r})$ is defined.
2. Kohn-Sham equations are solved and the single-electron wave functions $\Psi_{i,0}(\vec{r})$ are determined.
3. A new electronic density $n_1(\vec{r})$ is calculated applying the density operator $\hat{n}(r)$ (**Equation 2.27**) to the single-electron wave functions, **Equation 2.31**.

$$n_1(\vec{r}) = 2\sum_i \Psi_{i,0}^*(\vec{r})\Psi_{i,0}(\vec{r}) \quad (2.31)$$

4. $n_1(\vec{r})$ and $n_0(\vec{r})$ are compared. If they fall within the same tolerance range, then $n_1(\vec{r})$ is defined as the ground-state electronic density and the ground-state energy of the system is computed. Otherwise, $\Psi_{i,1}(\vec{r})$ are calculated and the cycle is repeated from step 3.

Exchange-correlation functionals

According to Pauli's exclusion principle, a specific electronic state can contain two electrons only if they have opposite spin. Therefore, electrons with the same spin must be spatially separated and this leads to a reduction of the Coulomb energy of the system,[80] called exchange energy. Additionally, since the Hartree-Fock approach approximates the all-electron wave function into several single-electron wave function, the energy of the single-electron system needs to be corrected by a factor, named correlation energy. Both exchange and correlation energies are included in the exchange-correlation energy, **Equation 2.30**. This term has to be approximated to allow the solution of the Kohn-Sham equations. Several approximations are possible and their hierarchy in term of accuracy has been defined by John Perdew as "the Jacobs ladder of DFT",[72,81] **Figure 2.5**.

Local-Density Approximation The simplest approximation is the Local-Density Approximation (LDA), introduced by Kohn and Sham in 1965.[79] The exchange-correlation energy of an electronic system is here derived assuming that the exchange-correlation energy per electron at coordinates $\vec{r}$, $\epsilon_{\mathrm{XC}}(\vec{r})$, is the same as in a homogeneous electron gas with the same local electronic density, $\epsilon_{\mathrm{XC}}^{\mathrm{homo}}(\vec{r})$ **Equation 2.32**. The exchange-correlation energy function is treated as a local phenomenon and it is calculated by stochastic methods (Ref.[82]) for high-density electron gases and then interpolated for intermediate and low-density electron gases. Therefore, the LDA approximation guarantees reliable results for bulk solid or any other material with almost constant valence electron density. For atoms, molecules, and other interesting systems the electron density varies locally, thus more complete approaches are needed, since this approximation overestimates bond energies, with error bars of around 2 eV.[83]

$$\begin{aligned} E_{\mathrm{XC,LDA}}[n(\vec{r})] &= \int n(\vec{r})\epsilon_{\mathrm{XC}}^{\mathrm{homo}}(\vec{r})d^3\vec{r'} \\ \frac{\delta E_{\mathrm{XC,LDA}}}{\delta n(\vec{r})} &= \frac{\partial \epsilon_{\mathrm{XC}}^{\mathrm{homo}}(\vec{r})n(\vec{r})}{\partial n(\vec{r})} \end{aligned} \tag{2.32}$$

Generalized Gradient Approximation The Generalized Gradient Approximation (GGA) includes the spatial variation of the electronic density

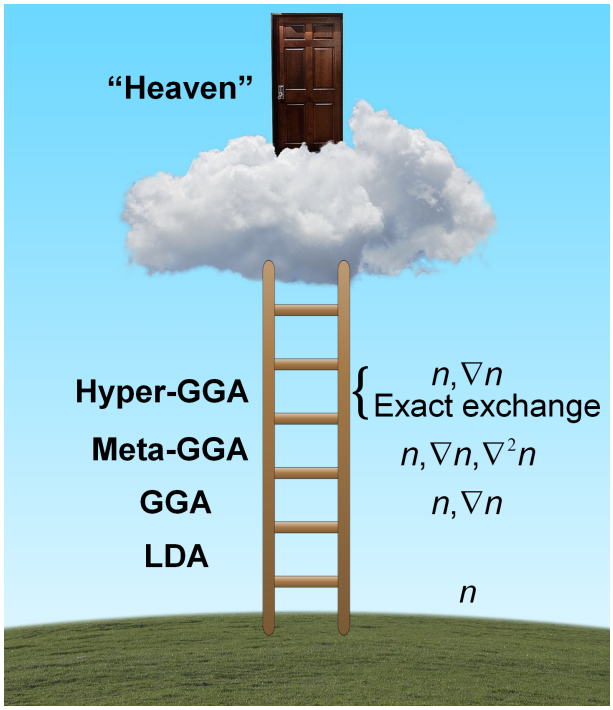

Figure 2.5: Perdew classification of DFT functional from the simplest approximation, the Local-Density approximation, to hybrid functionals which explicitly account for exchange. Adapted from Ref.[72].

of a physical system by accounting for both the local electron density $n(\vec{r})$ and its gradient $\nabla n(\vec{r})$, **Equation 2.33**. In this way, this approximation accounts as well for systems which have slowly varying electronic densities. As LDA, nonempirical GGA functionals satisfy the uniform density limit: at the limit of uniform density, the exchange-correlation energy reproduces the uniform electron gas energy at that electronic density. Among nonempirical GGA functionals, Perdew-Wang 91 (PW91)[84] and Perdew-Burke-Ernzerhof (PBE)[85] functional are widely employed. Since GGA functionals do not account for the London dispersion forces, their application leads to an underestimation of physisorption of molecules on metal surfaces.[86,87] Many corrections such as the Grimme's empirical methods,[88–91] vdw-DF,[92] vdw-DF2,[93] and the Tkatchenko-Scheffler method[94] are usually included to improve the accuracy of the calculation of adsorption energies.

$$E_{\mathrm{XC,GGA}}[n(\vec{r})] = \int n(\vec{r})\epsilon_{\mathrm{XC}}[n(\vec{r}), \nabla n(\vec{r})]d^3\vec{r} \tag{2.33}$$

Meta-GGA functionals Meta-GGA functionals extend the GGA approach by including second order derivatives of the electronic density of a physical systems,[95] **Equation 2.34**.

$$E_{\mathrm{XC,GGA}}[n(\vec{r})] = \int n(\vec{r})\epsilon_{\mathrm{XC}}[n(\vec{r}), \nabla n(\vec{r}), \nabla^2 n(\vec{r})]d^3\vec{r'} \tag{2.34}$$

Hybrid-GGA functionals Hybrid-GGA functionals describe exchange-correlation energy by including contributions from both exact exchange and GGA exchange functionals. For instance, B3LYP[96–98] functional is defined as **Equation 2.35**, where $E_{\mathrm{C}}^{\mathrm{LDA}}$ is the LDA contribution,[99] $E_{\mathrm{X}}^{\mathrm{GGA}}$ is the Becke 88 exchange functional,[100] $E_{\mathrm{C}}^{\mathrm{GGA}}$ is the Lee-Yang-Parr correlation functional,[96] α_1, α_2, α_3 are numerical parameters, and E^{exchange} is the exact exchange energy calculated over the occupied orbitals ϕ_i by **Equation 2.36**. Hybrid functionals are convenient for DFT calculations based on localized basis sets, whilst they increase the complexity of solving Kohn-Shan equations in a plane-wave basis set. Therefore, these functionals are hardly employed for simulations of supercells which require periodic boundary conditions. Furthermore, the explicit calculation of the exact exchange term prevents hybrid functionals from satisfying the uniform density limit, which make them unsuitable for metals. Hence, functionals developed under the Generalized Gradient Approximation, such as the Perdew-Burke-Ernzerhof (PBE),[85] are used for investigating metallic surfaces.

$$\begin{aligned} E_{\mathrm{XC}}^{\mathrm{B3LYP}} =& E_{\mathrm{XC}}^{\mathrm{LDA}} + \alpha_1(E^{\mathrm{exchange}} - E_{\mathrm{X}}^{\mathrm{LDA}}) + \alpha_2(E_{\mathrm{X}}^{\mathrm{GGA}} - E_{\mathrm{X}}^{\mathrm{LDA}}) + \\ & \alpha_3(E_{\mathrm{C}}^{\mathrm{GGA}} - E_{\mathrm{C}}^{\mathrm{LDA}}) \end{aligned} \tag{2.35}$$

$$E^{\mathrm{exchange}}(\vec{r}) = \frac{1}{2n(\vec{r})} \int d^3\vec{r'} \frac{|\sum_i \phi_i^*(\vec{r'})\phi_i(\vec{r})|}{|\vec{r} - \vec{r'}|} \tag{2.36}$$

Periodic systems

Heterogeneous catalysis involves catalysts with a different phase from products and reactants. For electrochemical CO_2 reactions, heterogeneous catalysts are usually solid materials. In this study, I focused on copper, a crystal which is solid at standard conditions. A crystal is defined as a three-dimensional periodic structure of identical building blocks of atoms.[101] The identical building block is defined basis and the set of points which describes the periodicity is called Bravais lattice. The lattice is usually composed by three linearly independent translation vectors, $\vec{a}_1$, $\vec{a}_2$, and $\vec{a}_3$, whose directions determine the crystal axes as well. If the periodicity of each basis satisfies **Equation 2.37** for every arbitrary integers n_1, n_2, and n_3, these lattice vectors are named primitive translation vectors. The geometric

block defined by the primitives axes $\vec{a_1}$, $\vec{a_2}$, and $\vec{a_3}$ is called primitive cell or Wigner-Seitz cell. It is the basis or building block which contains the fewer atoms possible. Overall, the periodicity of crystals is described by 14 different lattice types. In the case of copper, at room temperature its periodicity accounts for a face-centered cubic lattice (fcc).

$$\vec{R} = n_1\vec{a_1} + n_2\vec{a_2} + n_3\vec{a_3} \tag{2.37}$$

From the Bravais lattice it is useful to derive the reciprocal lattice, constructed by the reciprocal cell vectors $\vec{b_1}$, $\vec{b_2}$, and $\vec{b_3}$ defined as **Equations 2.38**. The reciprocal lattice relative to the primitive cell is named Brillouin zone. The three primitive vectors of the reciprocal lattice combine into the reciprocal lattice vector $\vec{G}$, **Equation 2.39**, with u_1, u_2 and u_3 as integer numbers. Whilst the lattice vectors $\vec{a_j}$ are measured in Å, the reciprocal lattice vectors have $Å^{-1}$ as unit.

$$\begin{aligned}
\vec{b_1} &= 2\pi\frac{\vec{a_2}\times\vec{a_3}}{\vec{a_1}\cdot\vec{a_2}\times\vec{a_3}} \\
\vec{b_2} &= 2\pi\frac{\vec{a_3}\times\vec{a_1}}{\vec{a_1}\cdot\vec{a_2}\times\vec{a_3}} \\
\vec{b_3} &= 2\pi\frac{\vec{a_1}\times\vec{a_2}}{\vec{a_1}\cdot\vec{a_2}\times\vec{a_3}}
\end{aligned} \tag{2.38}$$

$$\vec{G} = v_1\vec{b_1} + v_2\vec{b_2} + v_3\vec{b_3} \tag{2.39}$$

A bulk crystal can be cleaved to produce crystal planes. The orientation of these crystal facets is represented by its Miller indices, which are defined from the lattice vectors according to a specific methodology. The intercepts (i_1,i_2,i_3) between the crystal axes and the crystal plane are defined in term of $\vec{a}_1$, $\vec{a}_2$, $\vec{a}_3$. The surface orientation of a given facet is then determined by the reciprocals of the intercepts ($i_1{}^{-1}$,$i_2{}^{-1}$,i_3^{-1}). If a plane does not intercept an axis, then the corresponding index is 0. In case of a negative intercept $-i$, then the Miller index is written as $\bar{h} = i^{-1}$. Planes which are equivalent by symmetry as denoted by curly brackets, as for instance $\{h_1h_2h_3\}$. For fcc metals as copper the most stable orientation is the (111) cut.

Bloch's Theorem

The single-electron Schrödinger equation can be solved numerically for different basis sets. Basis sets composed of atomic orbitals are usually employed in quantum chemistry for simulating the properties of isolated molecules and chemical compounds. For solid state systems, a better choice is the plane-waves basis set, which employs the periodicity of the simulated

structure to significantly decrease the computing time. This formalism is based on the Bloch's theorem.[102]

The potential energy of an electron in a periodic system is invariant under a crystal lattice translation $\vec{R}$, which is a linear combination of the lattice vectors $\vec{a}_1$, $\vec{a}_2$, and $\vec{a}_3$, **Equation 2.40**. Thus, Bloch's theorem states that the eigenstates of the single-electron wave function, **Equation 2.28**, can be written as a product of a cell periodic part, **Equation 2.41**, and a wave-like part dependent on the the wave vectors $\vec{k}$, called k-points, **Equation 2.42**. For each wave vector $\vec{k}$, the exact definition of the eigenstate Ψ_j would require a infinite summation over the plane waves. Yet, since contributions of high kinetic energies plane waves are minor, we can limit their number by setting a kinetic energy cutoff. Additionally, the single-electron wave function is composed by the eigenstates calculated for each k point. Thus, the k-points sampling defines the integration grid in the first Brillouin zone and a high k-points density leads to an increase of accuracy at the expenses of computational time. Nevertheless, since electronic wave function for similar k-points are almost identical, their sampling can be reduced, following as well considerations on symmetry.[103]

$$U(\vec{r}) = U(\vec{r} + \vec{T}) \tag{2.40}$$

$$u_j(\vec{r}) = u_j(\vec{r} + \vec{T}) = \sum_{\vec{G}} C(\vec{k} + \vec{G}) e^{+i\vec{G}\cdot\vec{r}} \tag{2.41}$$

$$\Psi_j(\vec{r}) = u_j(\vec{r}) e^{i\vec{k}\cdot\vec{r}} \tag{2.42}$$

Pseudopotentials

Bloch's theorem allows for a reduction of simulation time due to a proper choice of k-points sampling and energy cutoff. However, a plane-waves basis expansion over both core and valence electrons would dramatically increase the computational burden, due to the high numbers of plane waves required to account for the rapid oscillations of the valence electrons wave functions in the core region. Usually, valence electrons determine the chemical properties of physical systems more significantly than core electrons, since core electrons are strongly bound to the nuclei and interact with the surrounding to a lower extent. Therefore, the pseudopotential approximation allows to replace the core electrons and the strong ionic potential between nucleus and core electrons with a weaker pseudopotential based on a set of pseudo wave functions, **Figure 2.6**. Only valence electrons are explicitly assessed for the numerical solution of Kohn-Sham Equations, **Equations 2.28**. From a cut-off radius r_c all electron and pseudopotential wave functions overlap. Key

properties of the so-defined pseudopotentials are their transferability and softness. To have transferable pseudopotentials means that they reproduce inner electrons properties irrespectively from the atomic valence electrons. To have soft pseudopotentials implies that the plane-waves expansion of the valence electrons wave functions must be limited to the lowest energy cutoff possible to decrease simulation time. A high cutoff radius implies an increase of pseudopotentials softness at the detriment of transferability, whilst the opposite holds true as well. The most employed pseudopotentials are the Vanderbilt ultrasoft (US-PP)[104] and the Projector-Augmented Wave pseudopotentials (PAW).[105] For the entire study, I employed PAW pseudopotentials since they perform better for transition metals.[106]

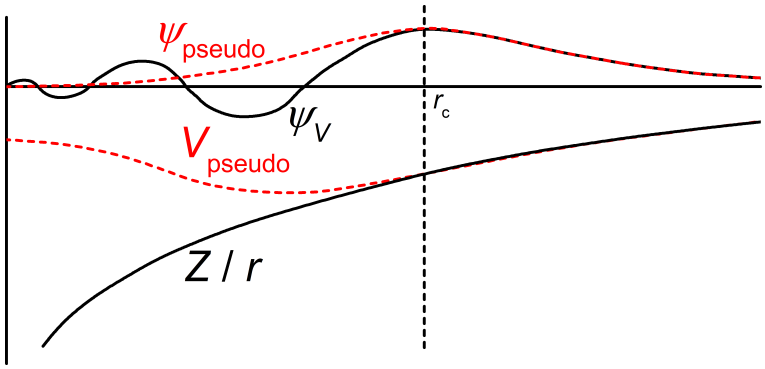

Figure 2.6: All electron (black line) and pseudoelectron (red line) wave functions and corresponding potentials. Pseudoelectron wave functions and potentials overlap with all electron values from the cutoff radius r_c. Adapted from Ref.[80].

2.3 The Computational Hydrogen Electrode

DFT methodologies based on periodic boundaries conditions cannot account for charged cells. Thus, basic electrochemical phenomena, such as electron transfer, pH, and electric potential, are hard to model. A simple model which has been applied to electrocatalysis is the Computational Hydrogen Electrode (CHE).[65] This methodology was proposed for the Oxygen Reduction Reaction (ORR),[65] however it was soon extended to additional chemical reactions, akin electrochemical CO_2 reduction.[9] It allows to calculate intermediate adsorption energy including electron transfer, electric potential, and pH. This approach is based on the following hypotheses.

1. Taking as reference potential the Standard Hydrogen Electrode (SHE), the chemical potential for the reaction $H^+ + e^-$ can be related

to the Gibbs free energy of $\frac{1}{2}H_2$. Therefore, at standard conditions (298 K, 1 bar of gas phase H_2), **Equation 2.43** is valid.

$$G_{H^+} = \frac{1}{2} G_{H_2,\mathrm{DFT}} \tag{2.43}$$

2. The effect of the electric potential is included adding to a thermodynamic state the energy of each transferred electron, ne^-U, where U is the applied potential. **Figure 2.7** shows a practical example for CO_2 reduction to CO.

3. The effect on the intermediates of the electrostatic field caused by the electrical double layer is neglected since calculated within DFT intrinsic error (0.01 eV). In case of intermediates with large electric dipole moments $\vec{\mu}$, the stabilization is estimated as $\mu_z \cdot E_z$.[65,107]

4. Proton Gibbs free energy is corrected for pH > 0 by the entropy related to H^+ concentration, **Equation 2.44**.

$$G(\mathrm{pH}) = -k_B T \ln H^+ = k_B T \cdot \ln(10) \cdot \mathrm{pH} \tag{2.44}$$

5. Solvation contribution must be included either through explicit insertion of water molecules in the simulation box[65] or implicit model based on solvent dielectric permittivity.[108,109]

6. The DFT energies for the reaction intermediates must be corrected by their zero point energies and the influence of entropy at the reaction temperature T, **Equation 2.45**.

$$\Delta G = \Delta E_{\mathrm{DFT}} + \Delta E_{\mathrm{ZPE}} - T\Delta S \tag{2.45}$$

The CHE model assumes for simplicity every electron transfer as a proton-coupled electron transfer. Therefore, its application to decoupled proton-electron transfers, such as CO_2 adsorption, has intrinsic limitations.[18] An alternative model derived from Marcus theory (Ref.[110]) has been proposed to account for the transition between sequential and concerted proton-electron transfer.[111–113]

2.4 Molecular Dynamics

As explained in **Section 2.2**, the application of Density Functional Theory is limited to steady states systems since this theory is based on the solution of the time-independent Schrödinger equation. However, to assess interesting phenomena such as reconstruction of complex materials or *Operando*

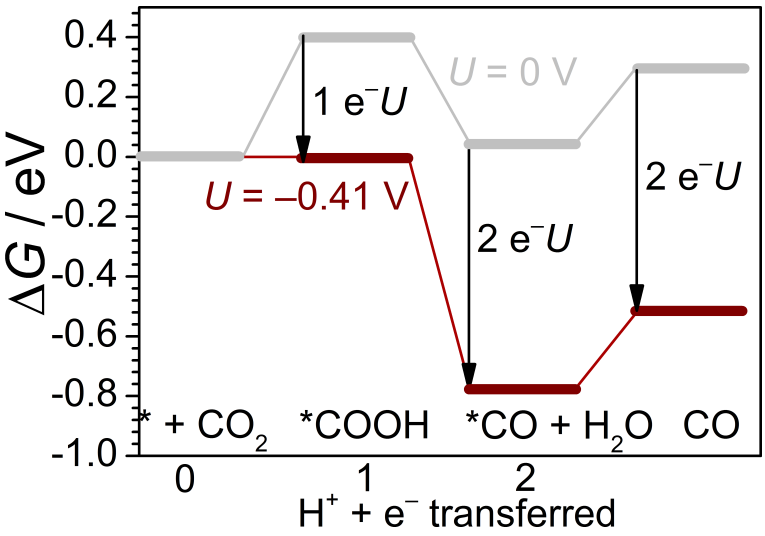

Figure 2.7: Application of the CHE approach to the modeling of CO_2 reduction toward CO. For every proton-coupled electron transfer, the Gibbs free energy of the reaction intermediate is corrected by a $e^{-}U$ factor. Adapted from Ref.[9].

catalysts the atomic motions need to be simulated. Thus, another useful tool for a theoretical electrochemist is the formalism of Ab Initio Molecular Dynamics.[72,114]

2.4.1 Classical Molecular Dynamics

Microcanonical ensemble

In classical mechanics, the status of a system with N components having mass m_i in a volume V, is defined by their $3N$ coordinates, $\{r_1, ...r_{3N}\}$, and the components of their velocities, $\{v_1, ..., v_{3N}\}$. Due to the law of conservation of energy, the overall energy of the system E does not change over time, **Equation 2.46**. Thus, E is given by the sum of kinetic and potential energy, respectively K and U. In statistical dynamics this system of components is called microcanonical ensemble, since the number of components N, its volume V, and the overall energy is constant. Recalling the Newton's law of motion, **Equation 2.21**, and since the force applied to the system is the negative gradient of the total potential energy, **Equation 2.47**, the time evolution of all the components is described by the solution of a system of $6N$ first-order differential equations, **Equation 2.48**. Given the number of atoms contained in a physical system, these equations cannot be solved analytically for a realistic material. However, applying Taylor expansion,

the time evolution of an atom can be derived by its previous position and the resulting force through the Verlet algorithm, **Equation 2.49**, if the time step Δt is small. The velocities of the atoms of a real system depend on its temperature T and follow Maxwell-Boltzmann distribution. According to this distribution, the average kinetic energy of each degree of freedom scales with its temperature, **Equation 2.50**, therefore the velocities of the atoms correlate with the kinetic energy of the system and consequently with its temperature.

$$E = K - U = \frac{1}{2}\sum_{i=1}^{3N} m_i v_i^2 - U(r_1, ..., r_{3N}) \tag{2.46}$$

$$\vec{F_i} = m_i \cdot \vec{a_i} = m_i \frac{\mathrm{d}\vec{v_i}}{\mathrm{d}t} = -\frac{\partial U}{\partial \vec{r_i}} \tag{2.47}$$

$$\begin{aligned} \frac{\mathrm{d}r_i}{\mathrm{d}t} &= v_i \\ \frac{\mathrm{d}v_i}{\mathrm{d}t} &= -\frac{1}{m_i}\frac{\partial U(r_1, ..., r_{3N})}{\partial r_i} \end{aligned} \tag{2.48}$$

$$\vec{r_i}(t + \Delta t) \cong 2\vec{r_i}(t) - \vec{r_i}(t - \Delta t) + \frac{\vec{F_i}}{m_i}\Delta t^2 \tag{2.49}$$

$$\frac{1}{2}m\overline{v^2} = \frac{k_\mathrm{B}T}{2} \tag{2.50}$$

Canonical ensemble

A real system exchanges heat with the environment, thus experimental conditions are better described by a canonical ensemble, which is a system where the number of atoms N, the volume V, and the temperature T are constant. To adapt the equations of motion of a microcanonical ensemble to a canonical ensemble, Nosé introduced a fictitious heat reservoir through an additional degree of freedom s.[115] Hence, the Lagrangian of the system, a mathematical function which describes its dynamics, reads as **Equation 2.51**. The parameter g, equal to the overall number of the degrees of freedom, is chosen to satisfy the canonical distribution at the equilibrium. Q is a factor which behaves as the effective mass of s and T is the temperature set for the system. If $s(t) = 1$, **Equation 2.51** simplifies to **Equation 2.52**, which is the Lagrangian of a microcanonical ensemble. The Lagrangian formalism allows to determine the equations of motion of every single constituent of the system as **Equations 2.53** for each of the $3N$ degrees of freedom.

$$L = K - U = \frac{1}{2}\sum_{i=1}^{3N} m_i v_i^2 s^2 - U(r_1, ..., r_{3N}) + \frac{Q}{2}\left(\frac{\partial s}{\partial t}\right)^2 - g k_{\mathrm{B}} T \ln s \quad (2.51)$$

$$L = K - U = \frac{1}{2}\sum_{i=1}^{3N} m_i v_i^2 - U(r_1, ..., r_{3N}) \quad (2.52)$$

$$\frac{\mathrm{d}}{\mathrm{d}t}\left(\frac{\partial L}{\partial v_i}\right) = \frac{\partial L}{\partial r_i} \quad (2.53)$$

After the pioneering work of Nosé, Hoover derived the equations of motion for the extended Lagrangian as **Equations 2.54**,.[116] The parameter ζ acts as a feedback term which increases or decreases the velocities of the atom depending on its sign and it is controlled by the instantaneous temperature of the atoms in the system, T_{inst}. According to Maxwell-Boltzmann distribution, each degree of freedom accounts for a kinetic energy of $\frac{k_B T}{2}$, **Equation 2.50**, therefore the feedback loop is explicit, **Equation 2.55**. If the temperature of the system, T_{inst} is beyond the chosen value T, ζ increases, thus lessening the velocities of each constituent. Otherwise, if the instantaneous temperature is low, ζ is diminished, leading to an increase of the kinetic energy of the system. The Q, defined before as the mass of s, controls the speed of the feedback loop. **Equations 2.54** can be solved numerically through an extension of the Verlet algorithm, **Equation 2.49**. Therefore, this derivation, so-called Nosé-Hoover thermostat,[117] allows to study the time evolution of a system at a constant temperature T. From position $\vec{r}_i$, friction ζ, and forces $\vec{F}_i$ at time t, it is possible to calculate the positions at time $t + \Delta t$, **Equation 2.56**. Since the forces applied to the system need to be determined at every time step, bigger is the investigated system, larger is the computational cost of a Molecular Dynamics simulation. Additionally, the Verlet algorithm is valid only for small times steps, due to its derivation through a Taylor series of Δt. By definition, a Molecular Dynamics simulation should describe fast motions as atomic vibrational frequencies, thus a suitable time step should be set in the order of the fs.

$$\begin{aligned}
\frac{\mathrm{d}r_i}{\mathrm{d}t} &= v_i \\
\frac{\mathrm{d}v_i}{\mathrm{d}t} &= -\frac{1}{m_i}\frac{\partial U(r_1, ..., r_{3N})}{\partial r_i} - \zeta v_i \\
\frac{\mathrm{d}\zeta}{\mathrm{d}t} &= \frac{1}{Q}\left[\sum_{i=1}^{3N} m_i v_i^2 - 3N k_{\mathrm{B}} T\right] \\
\frac{\mathrm{d}\ln s}{\mathrm{d}t} &= \zeta
\end{aligned} \quad (2.54)$$

$$\frac{\mathrm{d}\zeta}{\mathrm{d}t} = \frac{1}{Q}\left[\sum_{i=1}^{3N} m_i v_i^2 - 3Nk_\mathrm{B}T\right] = \frac{3Nk_\mathrm{B}}{Q}[T_\mathrm{inst} - T] \tag{2.55}$$

$$\vec{r_i}(t+\Delta t) \cong 2\vec{r_i}(t) - \vec{r_i}(t-\Delta t) + (\frac{\vec{F_i}}{m_i} - \zeta\vec{v_i})\Delta t^2 \tag{2.56}$$

2.4.2 Ab Initio Molecular Dynamics

Classical molecular dynamics allows to describe the dynamics of N atoms provided the estimation of their potential energy as a function of their spatial coordinates, $U(r_1, ..., r_{3N})$. As demonstrated in **Section 2.2**, Density Functional Theory can be applied for this purpose. The Lagrangian for a molecular system can then be expressed as **Equation 2.57**. $\Psi(r_1, ..., r_{3N})$ are the Kohn-Sham one-electron wave functions which represent the electronic ground state for the $3N$ degrees of freedom of the complex. This Lagrangian is valid for a microcanonical ensemble, thus at constant N, V and E.

$$L = K - U = \frac{1}{2}\sum_{i=1}^{3N} m_i v_i^2 - E[\Psi(r_1, ..., r_{3N})] \tag{2.57}$$

The workflow for an Ab Initio Molecular Dynamics starts with the determination of the ground-state energy from the initial coordinates of the atoms of system. Then Classical Molecular Dynamics (**Section 2.4.1**) is applied and the nuclear positions of the atoms are updated depending on the applied forces. Finally, the ground-state energy of the updated configurations is calculated through DFT and the resulting forces are determined from the potential energy. If the Kohn-Shan equations are explicitly solved, this methodology is described as Born-Oppenheimer Molecular Dynamics (BOMD). The determination of the ground-state energy of the updated configuration is expedited using the electronic properties of the system for the previous molecular dynamics steps, thus making BOMD simulations computationally viable. An alternative methodology by Car and Parinello, the Car-Parinello Molecular Dynamics (CPMD),[118] is based on the parallel calculation of the dynamics of the atomic nuclei and the ground-state energy. The equations of motions for both the nuclear and electronic degrees of freedom are described by a generalized Lagrangian, which includes the electronic degrees of freedom as fictitious dynamical variables. However, this approximation makes CPMD less accurate than BOMD.

2.5 General computational details

Throughout the whole thesis, I carried out Density Functional Theory simulations of surfaces, adsorbates, and reference molecules in gas phase following some general guidelines.

I employed the Vienna Ab Initio Simulation Package (VASP)[119,120] and used the PBE as the density functional.[85] Inner electrons were always represented by PAW pseudopotentials[105,106] and a kinetic energy cutoff of 450 eV was chosen for the expansion as plane waves of the monoelectronic states for the valence electrons. I sampled the Brillouin zone with a Γ-centered k-points mesh from the Monkhorst-Pack method,[103] large enough to provide a reciprocal grid size smaller than 0.03 $Å^{-1}$. In the case of surfaces, I followed the supercell approximation, thus building a 2D-periodic surface of several atomic layers with an upper vacuum thickness large enough to avoid interactions in the z-directions. As for the molecules, they were simulated in box of 10-20 Å size to circumvent spurious interactions given by periodic boundary conditions. I included dispersion through the DFT-D2 method[88,121] with the C_6 coefficients for the metals reparametrized as in Ref.[89] to assess the adsorption of reaction intermediates. I included solvation effects through implicit models based on the VASP-MGCM framework (Refs.[108, 109]) and the VASPsol code (Refs.[122, 123]). When I employed asymmetric simulation cells, I applied a dipole correction to remove artifacts generated by asymmetry.[124] Upon estimation of solvent effects, dipole correction was deactivated.

If specific computational parameters were needed, I highlighted the different choice of set chapter by chapter.

Chapter 3

An ideal system: metallic Cu

Copper has been widely employed as a CO_2 reduction catalyst after Hori's pioneering reports of its selectivity towards many different products,[6] including hydrocarbons,[15] and formate among others.[125] Theoretical modeling has rationalized the dependence of copper catalytic performance on its local morphology.[9,11,126] Different crystal facets present different product distribution. Cu(111) reduces CO_2 to methane and hydrogen, whilst Cu(100) opens the pathway to ethylene.[7] Ethanol and *n*-propanol form on defective sites. Polycrystalline Cu exhibits a selectivity in agreement with the performance of its most stable crystalline facet, Cu(111).[127,128] Small Cu nanoparticles (NPs) are selective towards CO (around 20% FE), whereas particles with larger diameter catalyze the production of CH_4 and C_2H_4.[129] As a result of this accurate understanding, general reaction schemes have been proposed for CO_2 reduction on copper.[130]

In this chapter, I performed two benchmark studies to provide good agreement with the state-of-the-art. I modeled two simple Cu systems, Cu(111) and Cu(100) slabs. The Cu(111) model was employed to explain the production of formate and carbon monoxide on solvothermally synthesized Cu nanoparticles at $U = -0.6$ V vs RHE.[55,61] The (100) slab was simulated to confirm experimental evidences of open domains as preferential sites for CO_2 reduction toward C_{2+} products.

3.1 Copper as an ideal catalyst for CO_2 reduction

Copper is a highly conductive transition metal due to its unpaired $4s$ electrons. It has an estimated concentration in Earth's crust in the range of 0.005-0.007%.[131] Due to its occurrence as a native metal,[131] it has been known to humankind since 8000 years B.C. and it identified one of the civilization eras, Chalcolithic or Copper age (4500 B.C. – 3300 B.C.).[132] Even

if the increasing demand for copper is reducing natural reserves and led to a peak price of $2.61 per pound in November 2019,[133] recycling protocols guarantee the availability of this metal for future human generations. Thus, this metal is a suitable candidate for catalyzing electrochemical CO_2 reduction toward a wide spectrum of chemical products.[6,7,15]

CO_2 reduction has been investigated experimentally on several different Cu morphologies. Following a bottom-up approach, I first consider the simplest experimental configurations, copper single crystals,[7] to set the basis for rationalizing more complex systems. In fact, polycrystalline Cu[8] and copper nanoparticles[129] exhibit catalytic properties which are a convolution of the features of the most stable crystalline domains.[128]

3.2 Copper single crystals

To correlate product distribution and copper local morphology, Hori *et al.* carried out electrochemical CO_2 reduction on a wide range of crystalline facets derived from stepped (100) and (111) planes: Cu(S)-[n(100)×(110)], Cu(S)-[n(100)×(111)], and Cu(S)-[n(111)×(100)],[7] from top to bottom in **Figure 3.1**. The authors assessed product distribution for all the systems with a CO_2-saturated electrolyte 0.1 M $KHCO_3$ at constant current density of 5 mA cm^{-2} and applied potential U between −1.34 and −1.55 V vs SHE. As a result, Cu(100) facet catalyzed ethylene (40.4% FE) and methane (30.4%) production. Cu(111) opens the pathway to formic acid (11.5%) and CO (6.4%), keeping a high selectivity toward methane (46.3%). (110) defects on Cu(100) facets are responsible for ethanol production, **Figure 3.1**.

Copper ability to produce ethylene and ethanol has been explained by its mild *H adsorption and strong CO adsorption,[10,126] see **Section 1.5**. The first property limits hydrogen coverage of the catalytic surface, whereas the second factor determines the high CO coverage needed to enable the CO-CO dimerization step. As for C_2 product distribution, Cu coordination number has been employed as descriptor to explain the thermodynamics of ethylene and ethanol production.[11] Ethylene is favored on active sites which have average Cu-Cu coordination number 8, such as Cu(100) surface atoms, whilst low-coordinated sites such as n(100)×(110) steps with $\overline{N}_{\text{Cu-Cu}} = 6$ promote ethanol formation,[7] **Figure 3.1**.

To benchmark these experimental and theoretical evidences, I compared hydrogen evolution and CO_2 reduction reaction pathways. At mild potential, hydrogen evolution reaction is more favorable than CO_2 reduction since it presents only a low energy barrier for hydrogen desorption, $\Delta G_{\text{H}_2\text{-des}} = +0.23$ eV at $U = -0.6$ V vs RHE, **Figure 3.2**. However, CO

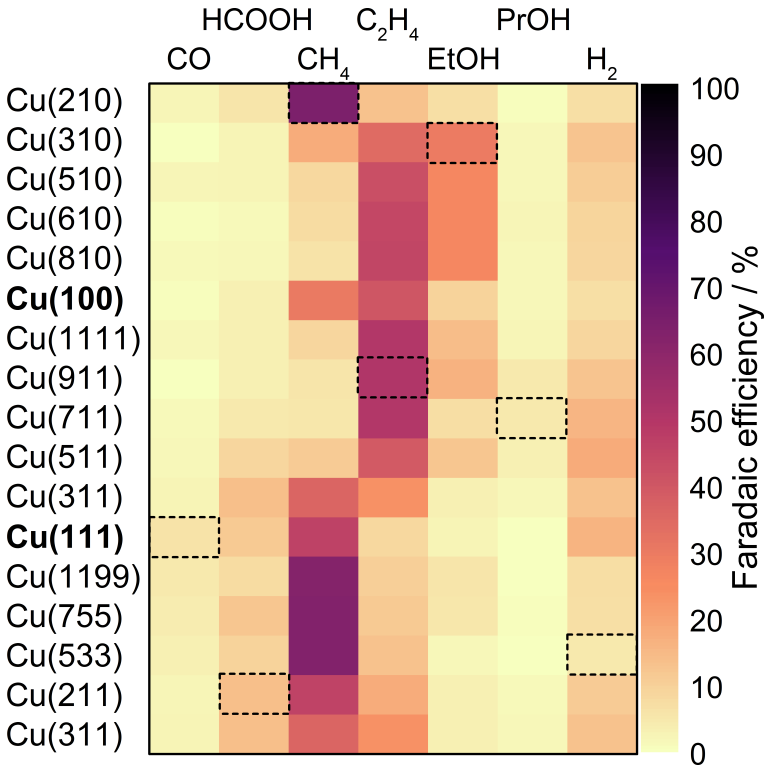

Figure 3.1: Faradaic efficiencies toward CO_2 reduction products on copper single crystals. Dashed boxes highlight the facets with highest FE toward each CO_2R product and lowest FE in case of H_2. Adapted from Ref.[7].

is strongly bound to the surface, leading to an energy barrier for CO desorption as high as +0.75 eV. Since CO cannot desorb, CO coverage on the surface increases, thus creating the conditions for enabling C–C coupling. At the high potential needed for producing ethylene, mass transfer limitations and high alkaline surface pH hinder hydrogen evolution.[18,19,21,134] Instead, the high surface polarization promotes CO coverage, thus benefiting the CO-CO dimerization step due to the high CO surface concentration.[135] Upon high surface coverage of CO, CO-CO dimerization leads to the formation of the *$OCCO^-$ intermediate, assumed as the key intermediate toward C_{2+} production.[18,136] The formation of this species from two neighboring CO presents a thermodynamic barrier higher that 1 eV due to the strong CO adsorption on Cu(100) surface sites and the borderline-stability of the CO-CO dimer. In addition, a kinetic barrier of more than 0.5 eV further limits *$OCCO^-$ formation, **Figure 3.3a**. However, further stabilization of this elusive intermediate has been attributed to interaction with unsolvated

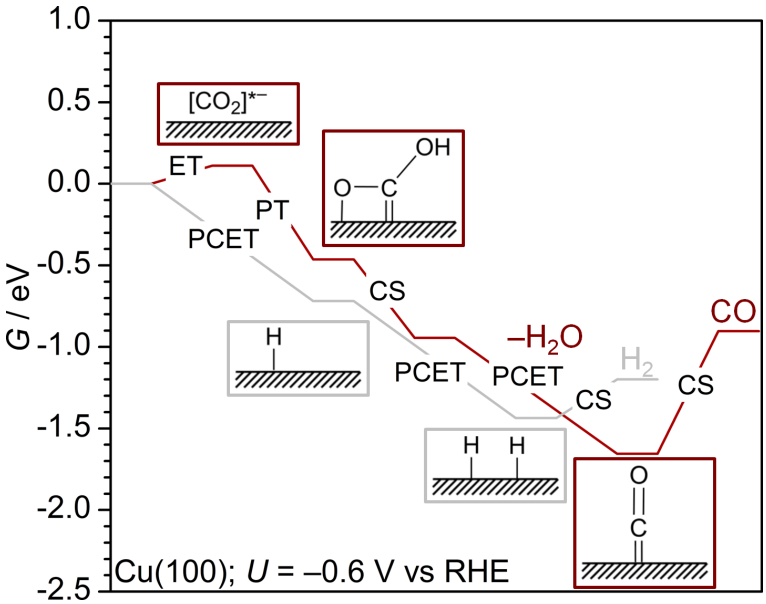

Figure 3.2: Gibbs free energy diagram and main reaction intermediates for Hydrogen Evoluton Reaction (gray) and CO_2 reduction to CO (red) on Cu(100) at $U = -0.6$ V vs RHE. ET: electron transfer; PCET: proton-coupled electron transfer; PT: proton transfer; CS: chemical step. Adapted from Ref.[61]

cations[17] and dipole effects due to the electrostatic field within the electrical double layer.[107] In particular, the effect of electric field on $OCCO^-$ dipole is suggested to provide a stabilization of more than 1 eV for Cu(100), thus making the CO-CO dimerization process thermoneutral at electrostatic potential of $\vec{E} = -1.0$ V Å^{-1}, **Figure 3.3b**. Thus, production of ethylene and ethanol on copper-based catalysts is assumed to happen through this chemical route.[18]

3.3 Polycrystalline copper

Polycrystalline copper is composed of well-defined single crystals, where surface energy rules the relative extension of these domains.[127,128] Their catalytic performance is a convolution of the contribution of each component, thus this system exhibits similar catalytic properties as copper single crystal.[6–8,15,125] At low negative potentials, the main reaction products are H_2 and CO, which account for a maximum Faradaic efficiency around 75% and 20% respectively, **Figure 3.4**. Formate production starts from $U = -0.7$ V vs RHE, reaching a maximum selectivity of more than 20% FE.

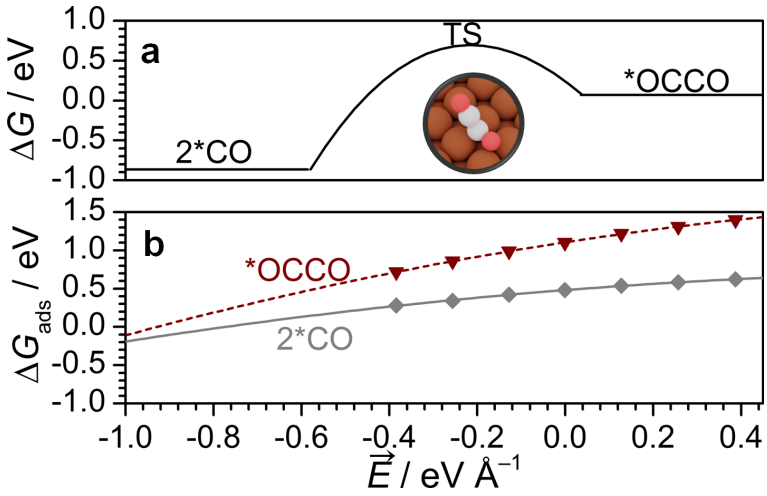

Figure 3.3: **a**, Thermodynamic and kinetic barrier for CO-CO dimerization step on Cu(100) at $U = -0.6$ V vs RHE (CO_2 as energy reference) and **b**, effect of electric field on CO (gray line) and $*OCCO^-$ (red dashed line) adsorption on Cu(100) (CO as energy reference). Adapted from Ref.[62] and Ref.[107] respectively.

Therefore, polycrystalline copper acts similarly to Cu(111). At potentials lower than -1.0 V vs RHE, C_{2+} are formed with similar product distribution to (100) planes: initially *n*-propanol (4% FE), followed by ethanol and ethylene (around 10 and 25% FE). Electrochemical-STM characterization detected surface reconstruction of polycrystalline copper to Cu(100) under CO_2 reduction conditions.[16] This experimental observation explains the occurrence of C_{2+} for polycrystalline copper at negative potentials.[11] Methane is generated as well in this potential window and it reaches a maximum Faradaic efficiency around 40% around -1.2 V vs RHE.[8]

Experimental onset potentials for specific CO_2 reduction products on polycrystalline copper[125] were first reproduced on simple Cu(211) models through the Computational Hydrogen Electrode methodology.[65] By defining the Gibbs free energies diagrams for hydrogen, formic acid, carbon monoxide, and methane production, the authors determined the theoretical onset potential for each of the products.[9] Hydrogen Evolution Reaction starts from -0.03 V vs RHE. HCOOH and CO reaction pathways are open from $U < -0.41$ V vs RHE. Finally, methane production exhibits a theoretical onset potential of -0.74 V vs RHE, needed to achieve strong binding of CO and its protonations to form this hydrocarbon.

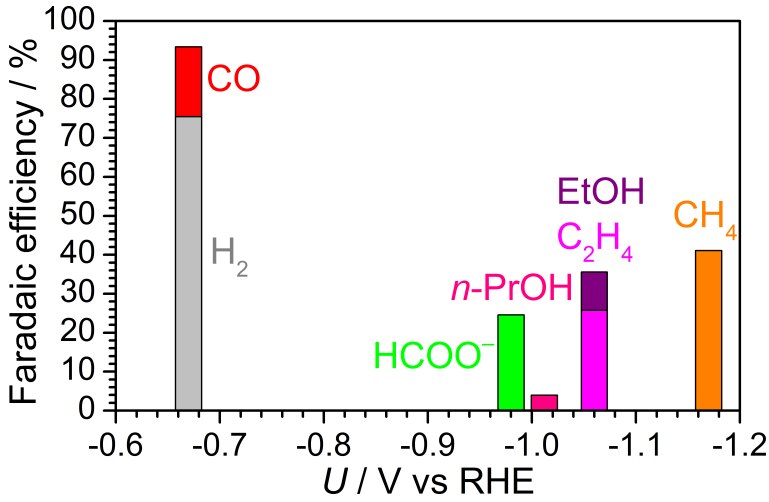

Figure 3.4: Maximum Faradaic efficiencies for CO_2 reduction and Hydrogen Evolution Reaction products on polycrystalline copper. Electrolyte: 0.1 M $KHCO_3$; pH = 6.8. Adapted from Ref.[8].

3.4 Copper nanoparticles

Copper nanoparticles present high abundance of undercoordinated sites due to their (110) edges between (100) and (111) planes: smaller the copper nanoparticle, higher the areal ratio between (110) plane and (111) or (100) facets.[128] As a consequence, nanoparticles with diameter smaller than 15 nm have been reported selective to CO (20%) and methane (15%).[129] Being highly defective, these systems generate equivalent products to (100) steps on (111) planes and (110) steps on (100) planes, **Figure 3.1**. Yet, product distribution depends on nanoparticle size[129] and chemical synthesis. Copper nanoparticles produced by solvothermal route[55,61] present poor selectivity to CO_2 reduction products: around 12% formate and 12% CO.

Copper nanoparticles reactivity can be modeled by assessing the catalytic properties of the facets which present lower surface energy. According to the Wulff theorem,[127] a lower surface energy corresponds to a larger extension of a specific crystalline domain. Since Cu is a fcc metal, its most stable surface configuration is Cu(111). Therefore, I compared the Gibbs free energy of the main intermediates for Hydrogen Evolution Reaction and CO_2 reduction to formate and CO, **Figure 3.5**. HER is exothermic until the H_2 desorption step, which presents a low thermodynamic barrier of 0.28 eV. On the contrary, CO_2 reduction is limited by the stabilization of the CO_2^- intermediate, exothermic by 0.13 eV at $U = -0.6$ V vs RHE. If CO_2 is effectively bonded, the formate pathway is downhill in Gibbs free

energy, whilst the production of carbon monoxide is still hindered by an endothermic desorption barrier of 0.46 eV. These theoretical results motivate the experimental product distribution for Cu nanoparticles synthesized through solvothermal route:[61] these systems evolve hydrogen with FE larger than 70%, since they are unselective toward CO_2 reduction. However, the neutral pH characteristic of a CO_2-saturated $KHCO_3$ electrolyte hinders H_2 production due to diffusion limitations. Thus, the exothermic CO_2 reaction to formate and CO can occur and determine the low Faradaic efficiencies reported for both products.

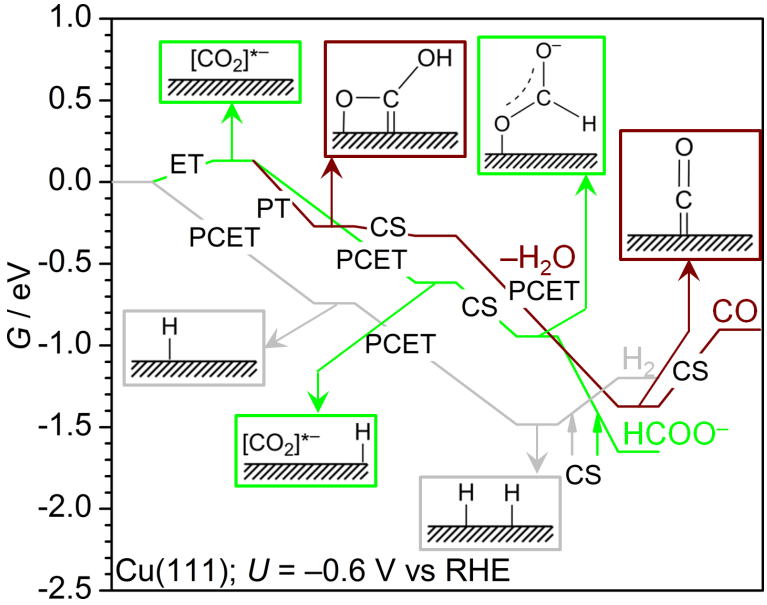

Figure 3.5: Gibbs free energy diagram and main reaction intermediates for Hydrogen Evolution Reaction (gray) and CO_2 reduction to formate (Green) and CO (red) on Cu(111) at $U = -0.6$ V vs RHE. ET: electron transfer; PCET: proton-coupled electron transfer; PT: proton transfer; CS: chemical step. Adapted from Ref.[61].

3.5 CO_2 reduction reaction network on copper

Fundamental experimental and theoretical studies contributed to define a simple CO_2 reduction scheme for copper,[130] **Figure 3.6**. The stabilization of the CO_2^- intermediate is considered the rate determining step for CO_2 reduction reaction,[18] RDS_1. This step competes with the adsorption of CO_2 as COOH through a proton-coupled electron transfer and hydrogen

adsorption. Depending on the configuration of adsorbed CO_2^-, either formate (O-bound intermediate) or CO (C-bound intermediate) are formed.[137] If CO desorption is hindered due to a strong CO binding energy, the pathways toward methane, methanol, and C_{2+} products open. Methane and methanol are normally favored to C_{2+} production, since this process requires the stabilization of the $*OCCO^-$ dimer, RDS_2,[17,18] which has a high thermodynamic and kinetic barrier, **Figure 3.3**. $*OCHCH_2$ is assumed as the common intermediate toward ethanol and ethylene, thus it motivates their analogous onset potential**Figure 3.4**.

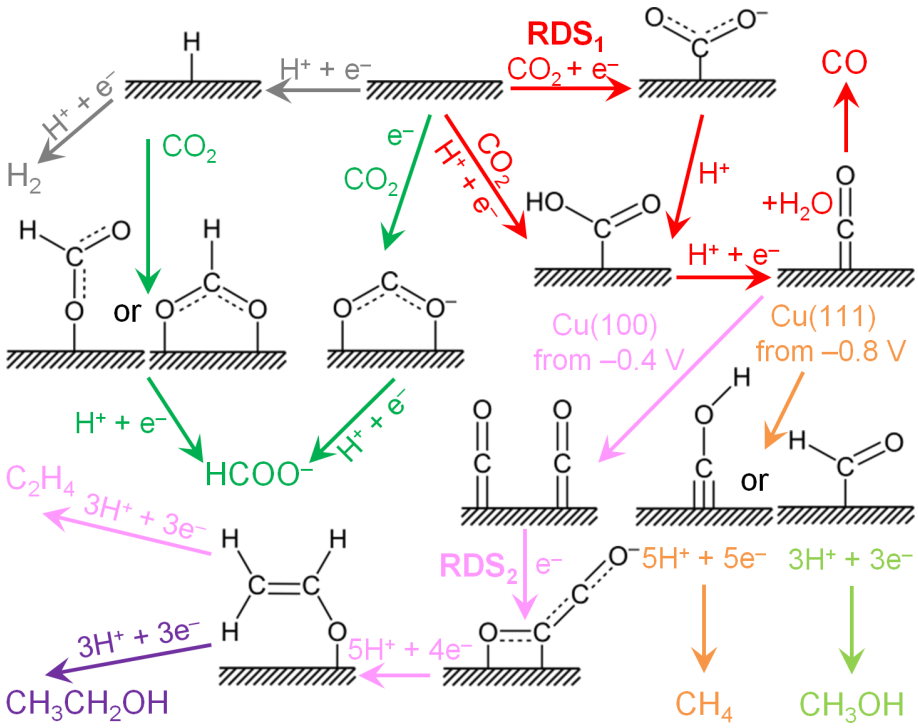

Figure 3.6: Proposed reaction network for electrochemical CO_2 reduction on copper at neutral pH toward CO (red), methane (orange), methanol (light green), formate (dark green), ethylene (magenta), and ethanol (purple). Hydrogen Evolution is highlighted in gray. Potentials: vs RHE; RDS: rate determining steps. Adapted from Ref.[130].

3.6 Conclusions

In this chapter I reviewed experimental and theoretical investigations of copper-based catalysts for electrochemical CO_2 reduction. Cu foils and nanoparticles are selective to a wide range of products due to the presence of either specific crystalline domains or surface defects. Cu(111) sites are selective to methane due to their mild adsorption of the *CO intermediate. Instead, Cu(100) opens the pathway to ethylene and ethanol due to its strong CO binding energy and thermoneutral hydrogen adsorption. The strong CO adsorption allows for a high CO coverage, whilst a mild interaction with hydrogen limits hydrogen evolution on this facet. Even though CO_2 reduction to C_{2+} is impeded by a thermodynamic and kinetic barrier of more than 1.5 eV for the CO-CO dimerization step, cation or local electric field can stabilize the $OCCO^-$ intermediate, thus enabling this reaction. Finally, ethylene and ethanol selectivity can be related to Cu coordination numbers: Cu(100) surface sites are responsible for generating the hydrocarbon, whilst (110) steps for producing the alcohol. Copper foil does not catalyze carbon monoxide production due to the high barrier for CO desorption. Copper nanoparticles exhibit a CO_2 reduction selectivity which depends on their size and their synthesis. In the case of solvothermally synthesized Cu nanoparticles, they are characterized by low selectivity toward formate and carbon monoxide,[55,61] due to the strong *H binding energy of Cu(111), the most extended surface facet for these nanostructures. Thus, Hydrogen Evolution Reaction is favored, accounting for more than 70% FE.

Chapter 4

Surface reconstruction under CO_2 reduction conditions

Due to their specific capability to produce C_{2+} products,[10,15] copper-based catalysts have been studied for CO_2 reduction toward ethylene.[138–144] Experimental and theoretical reports have demonstrated that open facets such as Cu(100)[11] and defective (110) and (111) sites (Ref.[7]) are responsible for the enhanced catalytic performance toward ethylene and ethanol, see **Section 3.2**, **Figure 3.1**. Since copper undergoes surface reconstruction toward Cu(100) due to polarization[16] and interaction with reaction intermediates,[48] nanocubic features are often synthesized through colloidal chemistry,[47] electrodeposition,[145] electrochemical cycling,[146] thermally-grown,[147] or electrochemically-grown Cu oxides and halides[148] to maximize ethylene selectivity.

The reconstruction process of polycrystalline copper toward Cu(111) and eventually Cu(100) has been characterized via *Operando* techniques,[149,150] such as Electrochemical Scanning Tunneling Microscopy (EC-STM).[16,151,152] Nevertheless, the influence of polarization and reaction intermediates on the reconstruction process has not been untangled yet neither experimental control on the surface faceting has been achieved so far. In this chapter, I prove the key role of surface polarization on the growth of copper nanocuboids under CO_2 reduction conditions. According to the developed model, higher polarization leads to a larger abundance of surface defects. Thus, the reconstruction process may be controlled to maximize the presence of defective sites and the catalyst's selectivity toward ethylene. I proved these assumptions in collaboration with Davide Pavesi during my experimental internship at Avantium Chemical BV through the synthesis of CuO-derived copper and its reduction to metallic copper at high negative potential. By applying this catalyst on a Gas

Diffusion Electrode (GDE) configuration,[153] the fuel cell generated ethylene with nearly 60% FE and partial current density higher than 200 mA cm^{-2} on a 10.5 cm^{-2} cell.

4.1 Polycrystalline copper reconstruction toward Cu(100)

To assess polarization effects on copper reconstruction, our collaborators from the Max Planck-EPFL Center for Molecular Nanoscience and Technology utilized both pristine (p-Cu) and a graphene-covered (g-Cu) polycrystalline copper. Graphene is an effective barrier to prevent Cu diffusion in the electrolyte and cation-surface interaction.[154] Hence, no electrolyte effect is expected for the g-Cu system. Furthermore, surface characterization of p-Cu and g-Cu at $U = -1$ V vs Pt was carried out for both CO_2- and N_2-saturated $KHCO_3$ to rule out any potential influence of CO_2 reduction intermediates, **Figure 4.1a**.[152]

Both p-Cu and g-Cu systems underwent similar surface reconstruction, irrespectively of the presence of CO_2 in the electrolyte. Initially, polycrystalline copper evolved toward dynamic mesocrystals, **Figure 4.1b-c**, which later reconstructed toward (100) facets, **Figure 4.1d**. After 4 hours of polarization, our collaborators detected the growth of nanocuboids on top of the (100), **Figure 4.1e**. The size and the kinetic of formation of these nanostructures depended on the polarization time and the magnitude of the potential applied. *Operando* EC-Raman spectroscopy and EC-STM confirmed the stability of the graphene layer for the g-Cu system, thus neglecting any noteworthy influence of this coverage on the reconstruction process. Experimental results suggested a univocal potential-dependent reconstruction process toward nanostructures, ruling out any influence of reaction intermediates or cation under the applied experimental conditions.

Polarization-driven copper nanostructuring The Gouy-Chapman-Stern (GCS) model[66] describes the capacitance of the Electrical Double Layer (EDL) at the electrode-electrolyte interface, C_{d}, as a series network of Outer Helmholtz layer capacitance, C_{H}, and the diffuse layer capacitance, C_{D}. At the large electrolyte concentration and large polarization characteristic of CO_2 reduction conditions, the main contribution to the EDL capacitance is due to the Helmholtz layer capacitance. The EDL is then equivalent to a parallel plate capacitor with capacitance C_{d}, which can be approximated by the Helmholtz capacitance C_{H}. Thus, the EDL capacitance depends on the dielectric thickness d (the Outer Helmholtz Layer distance), the dielectric permittivity of the medium (electrolyte) ϵ, and the

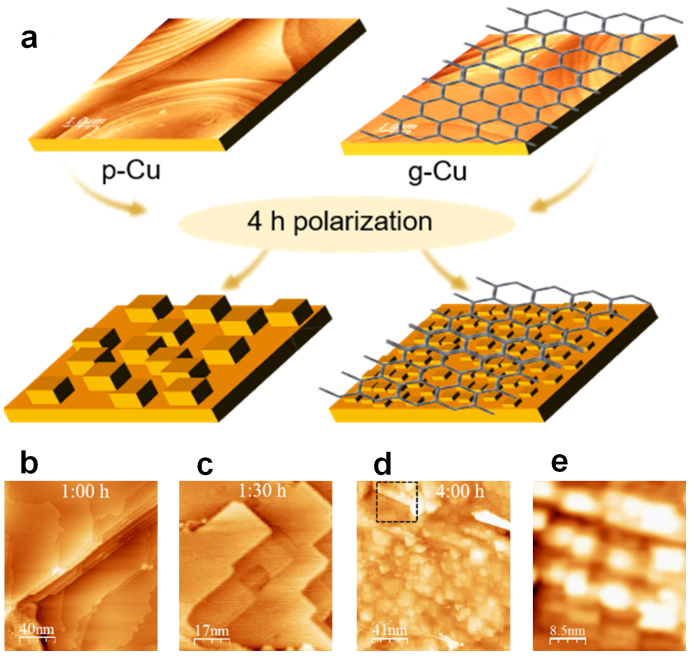

Figure 4.1: **a**, Scheme of the experimental process. **b**, pristine polycrystalline and graphene-covered polycrystalline copper were polarized at −1 V vs Pt and underwent surface reconstruction toward **c**, mesocrystals, **d**, Cu(100), and eventually **e**, nanocuboids depending on the polarization time, as characterized by EC-STM, $U_b = 328$ mV, $I = 1.75$ nA. Adapted from Ref.[152].

electrode surface A, **Equation 4.1**.

$$C_d \sim C_H = \frac{\epsilon \cdot A}{d} \tag{4.1}$$

When a negative potential is applied to p-Cu and g-Cu, copper surface atoms get negatively polarized. Depending on their local coordination, they present different polarizability,[89] therefore open domains can store the increased electronic density more effectively. By accepting electronic density on the Cu-Cu bonds, the outermost layers act as a parallel plate capacitor. The electrostatic energy E_{el} stored in the plate of this device depends on the applied electric field $\vec{E}$, the dielectric permittivity ϵ at the gap, the capacitor area A, and the dielectric thickness d, **Equation 4.2**. For the copper system, the high surface electronic density strengthens the Cu-Cu atomic bonds. The electric field stabilizes the system through electrostatic interaction, thus the overall energy increases. Density Functional Theory simulations (see **Section B.2** in **Appendix B** for details) on 1×1 Cu(100)

and 1×1 Cu(111) symmetric slabs confirm this model, since the energy for both systems becomes more negative for more negative electric field, **Figure 4.2a-b**. The electrostatic contribution derived by DFT results is reproduced by the analytical **Equation 4.2** for a capacitor area A equivalent to the extension of (100) and (111) facets, dielectric thickness equal to the vacuum (30 Å), and dielectric permittivity ϵ_0. ϵ_r is here equal to 1 since the simulations were performed under vacuum (see **Section B.2** in **Appendix B**).

$$E(\vec{E}) = E(\vec{E}=0) + E_{el} = E(\vec{E}=0) - \frac{1}{2} \cdot \epsilon \cdot A \cdot d \cdot \vec{E}^2 \qquad (4.2)$$

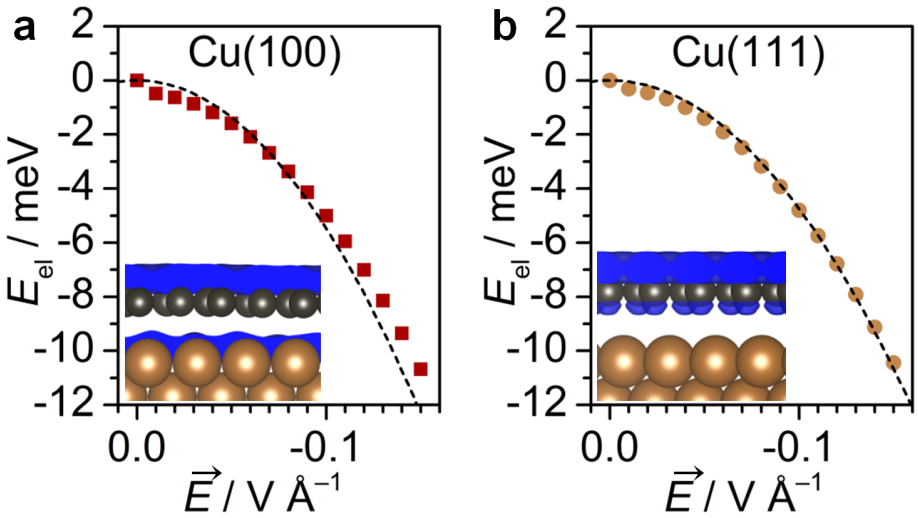

Figure 4.2: Electrostatic energy stored in **a**, Cu(100) (dark brown squares) and **b**, Cu(111) (light brown circles) symmetric slabs at increasing applied electric field. The analytic model (dashed lines) agrees with DFT data. Charge polarization is higher for Cu(100) (electronic density for $\vec{E} = -0.3$ V Å^{-1} in blue, Cu in brown, C in black, inset). Adapted from Ref.[152].

After having validated our analytical model through DFT simulations for a simple Cu system under vacuum, I changed its input parameter to reproduce the experimental system. The solvent employed was water, which has a relative dielectric permittivity ϵ_r of 78.4. However, a recent theoretical study estimated a dielectric permittivity at the Outer Helmholtz layer of 50.0 under CO_2 reduction conditions.[21] Thus, I assumed ϵ_r to range between these two values. Due to the protective action of the graphene layer, cation intercalation and diffusion toward the copper surface can be neglected. Hence, the Outer Helmholtz Layer thickness, which here acts as

the dielectric thickness, can be approximated by the copper-graphene distance. Upon DFT optimization of graphene-covered 5×5 Cu(100) and 1×1 Cu(111) systems (see Computational Details in **Section B.2**, **Appendix B**), an optimal copper-graphene distance of 3.11 Å and 3.40 Å was calculated for the (100) and (111) facets, respectively. Instead, a value of 3 Å was assumed for Cu(110) OHL thickness, as suggested by previous models of the EDL.[155] As a consequence, the analytical model allows to evaluate the magnitude of the electrostatic contribution to the thermodynamic stability of the experimental system, **Equation 4.2**, by calculating the surface energies of the specific copper facets, **Equation 4.3**.[156] I estimated the energy of the slab, the energy of bulk copper, and surface relaxation energy ΔE_{rel} under no electric field from DFT simulations on each crystalline domain, with n equal to the number of copper atoms in the system. I calculated the effective electric potential U_{eff} from the electrostatic field through **Equation 4.4**. To report the stability of each facet vs a given reference potential, I corrected the effective electric potential by the potential of zero charge U_{pzc} for Cu(111), Cu(100), and Cu(110) respectively -0.2 V vs SHE, -0.54 V vs SHE, and -0.69 V vs SHE through **Equation 4.5**.[20,157,158]

$$\gamma_{\text{rel}} = \frac{1}{A}\left\{\frac{1}{2}\left[E(\vec{E}=0) - \frac{1}{2}\cdot\frac{\epsilon_{\text{r}}\cdot\epsilon_0\cdot A}{d_{\text{Cu-graphene}}}\cdot U_{\text{eff}}^2 - n\cdot E_{\text{Cu-bulk-DFT}}\right] + \frac{1}{2}\Delta E_{\text{rel-DFT}}\right\} \tag{4.3}$$

$$U_{\text{eff}} = \vec{E}\cdot d_{\text{Cu-graphene}} \tag{4.4}$$

$$U = U_{\text{eff}} + U_{\text{PZC}} \tag{4.5}$$

Cu(111) is expected to be the most abundant facet on p-Cu,[127,128] due to its lower surface energy,[159] However at high negative potential the bonds between Cu atoms on closed-packed surfaces become saturated. Therefore, the local electrostatic repulsion between the outermost atoms increases, making the (111) unstable and not detectable experimentally. Instead, the polycrystalline copper reconstructs toward open facets, such as Cu(100), which allows a better distribution of the high electronic density due to the lower coordination of its surface atoms,[89] **Figure 4.3**. At even higher negative potential, (110) defects may occur on the surface to further relax the electrostatic stress among the charged atoms. The thermodynamic stability of these open domains explains the experimental detection of nanocuboids, whose structures are characterized by (100) and (110) edges. A recent experimental work confirmed the correlation between line defect densities and ap-

plied negative potential through *in-situ* EC-AFM (Electrochemical Atomic Force Microscopy).[160]

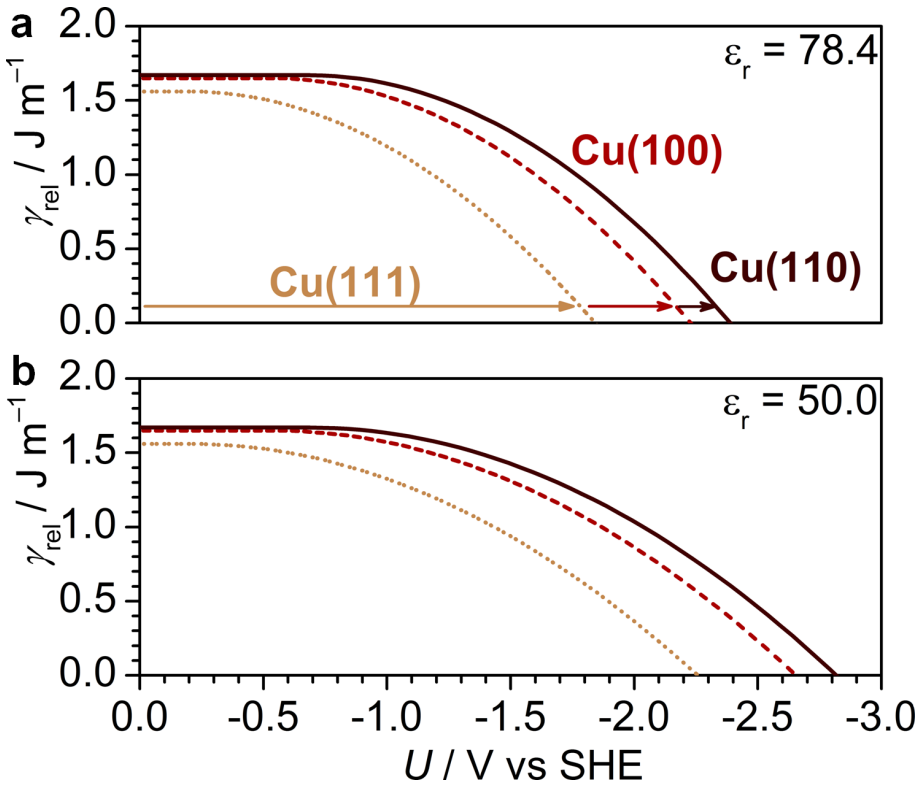

Figure 4.3: Modeled surface energies for Cu(110) (dark brown), Cu(100) (dashed brown), and Cu(111) (dotted light brown) facets for a solvent relative dielectric permittivity of **a**, 78.4 (water) and **b**, 50 (reported for CO_2 reduction, Ref.[21]), as calculated through **Equation 4.3**. The potential has been corrected by the potential of zero charge of Cu(110), Cu(100), and Cu(111).[20,157] Adapted from Ref.[152].

The link between the dynamic nanostructuring detected and the suggested thermodynamic driving force is given by the local variation of the electric field along the electrode. For a conductor, the electric potential across the conducting surface depends on the accumulated charge density, ρ, and its principal radii of curvature, R and R': smaller features experience a higher local electric potential, **Equation 4.6**. Kinetics processes such as Cu diffusion and interactions with the cations can alter surface morphology and local electric field. Hence, the electrode surface experiences a non-homogeneous polarization, with higher values for smaller, more curved features. When the local electric field is beyond a certain thermodynamic

threshold, **Figure 4.3**, the reconstruction process starts occurring.

$$\frac{d^2U}{dw^2} = 4\pi\rho \cdot \left(\frac{1}{R} + \frac{1}{R'}\right) \tag{4.6}$$

Thus, under the steady application of electric field, smaller features originated by dynamic processes at the surface experience a higher electric potential than average, which leads to the growth of nanocubic domains, characterized by low coordinated (110) edges. Since it has a lower surface coordination than the (100) facet, Cu(110) is more stable than Cu(100) at high surface electric potentials.

4.2 CuO-derived catalysts for selective ethylene production

As reported in **Section 3.2**, defective sites in (100) planes are active for CO_2 reduction to ethylene. Thus, according to the theoretical results mentioned above, a strong polarization should lead to copper-based catalysts selective to C_2H_4. During my staying at Avantium Chemical BV I tested this assumption by synthesizing an oxide-derived copper catalyst and assessing its catalytic performance together with Davide Pavesi.

The synthetic process consisted of a simple water-based precipitation,[161] followed by calcination.[50,162] I dissolved $CuCl_2$ precursor in deionized water and mixed this solution with NaOH under continuous magnetic stirring. I centrifuged the resulting $Cu(OH)_2$ precipitate and cleaned it with deionized water, before carrying out calcination to CuO during 2 h at 200°C (see **Section B.3.1**, **Appendix B** for further experimental details). X-ray diffraction spectroscopy (XRD) performed by Davide Pavesi confirmed the synthesis of CuO.[163] The characteristic (002) and (111) diffraction peaks were detected and a crystallite size in the range 2.6-3.3 nm was calculated through Scherrer equation (Copper K-α employed as X-ray energy source), **Figure 4.4a**. We observed CuO nanocrystallites clusters with sizes in the order of 50 μm through Scanning Electron Microscopy (SEM), **Figure 4.4b**. Even though the initial system is a copper(II) oxide, the oxidic phase is expected to reduce to metallic Cu^0 at the high current densities usually applied on a Gas Diffusion Electrode.[164] Thus, given the polarization effect explained in **Section 4.1**, under operation the catalyst should be metallic copper with (100) domains and abundant surface defects. Thus, this system should be a good potential catalyst for CO_2 reduction to ethylene (see **Section 3.2**).

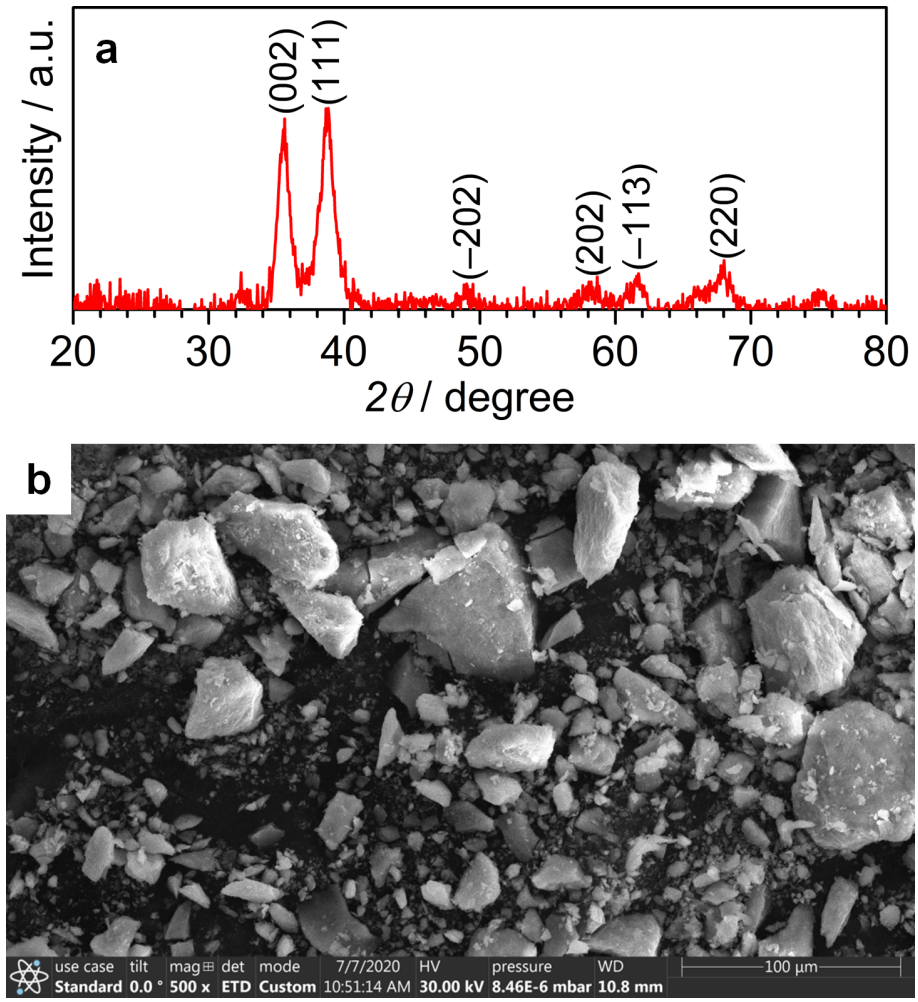

Figure 4.4: **a**, XRD patterns of CuO nanoparticles. The crystallite size was calculated to range between 2.6 and 3.3 nm through Scherrer equation.**b**, Scanning Electron Microscopy (SEM) of CuO clusters.

CO_2 electroreduction to ethylene I investigated the performance of the synthesized catalyst on a GDE configuration with an electrode geometrical area of 10.5 cm^2. I prepared a catalytic ink by suspending CuO powder in isopropyl alcohol and mixing it with an amount of Nafion^{TM} equal to 20 wt% on the final weight. I airbrushed the ink on a GDE prepared at Avantium Chemical BV through a patented procedure.[165] Finally, I performed galvanostatic electrolysis on a 10.5 cm^2 GDE flow cell (ElectroCell Micro Flow Cell) operated in a flow-through configuration. Anode and cathode were separated by a Nafion^{TM} membrane N324 with 0.5 M H_2SO_4 as anolyte

and 0.5 M $KHCO_3$ as catholyte. The anodic half-reaction was Oxygen Evolution Reaction on a Ir/RuO_2 catalyst, whilst CO_2 reduction occurred at the cathode where a continuous CO_2 flow of 50 ml min^{-1} was supplied through the GDE. Electrolysis was carried out at four current densities, 100, 200, 300, and 400 mA cm^{-2}, which inhibited a proper estimation of the electrode potential due to significant ohmic drops. Gaseous products were detected by a Gas chromatograph connected to the catholyte column, whilst liquid products were collected from the catholyte and further analyzed (see **Section B.3.1**, **Appendix B** for further details).

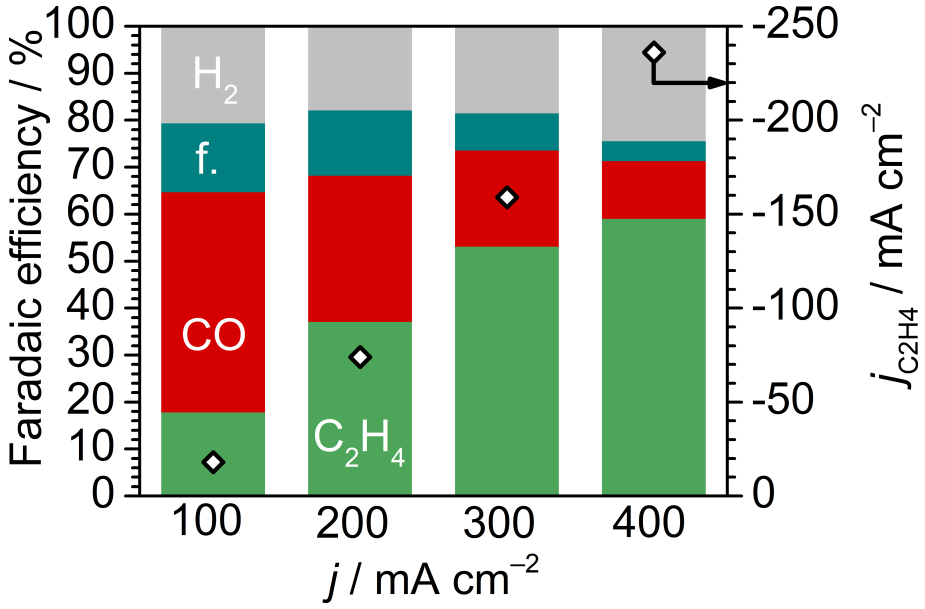

Figure 4.5: Product distribution for CuO-derived catalysts on a GDE configuration on a CO_2-saturated 0.5 $KHCO_3$ electrolyte (bulk pH = 7.4) with CO_2 flow equal to 50 ml min^{-1} and a catalyst loading of 0.67 mg cm^{-2}. Faradaic efficiency calculated as averages values after 1 h continuous electrolysis at each specific current. The product abbreviated as f. is formate.

The catalyst confirmed the performance suggested by theoretical predictions, **Figure 4.5**. Upon continuous electrolysis at constant CO_2 flow and fixed current densities, raised every 1 h by steps of 100 mA cm^{-2}, CO_2 selectivity toward ethylene evolves from an initial 20% FE at 100 mA cm^{-2} to around 60% FE at 400 mA cm^{-2}. The competing Hydrogen Evolution Reaction is limited to 20-25% Faradaic efficiency at any applied current density and tiny amounts of formate were detected as well (10-5% FE). CO is the main reaction product at 100 mA cm^{-2} with more than 40% FE, yet at high polarization its production diminishes in favor of ethylene. CO and

C_2H_4 together account for a constant 60-70% FE. At low current density, carbon monoxide can desorb from the cathode due to mild CO adsorption. From 200 mA cm^{-2}, high cathodic polarization enables a strong CO binding energy and a consequent high CO surface coverage. Thus, CO-CO dimerization, the rate determining step for C_{2+} formation,[18] is promoted and ethylene production is boosted.[135] Current densities higher than 400 mA cm^{-2} lead to a significant increase of hydrogen production to the detriment of CO_2 reduction activity. Indeed, the GDE after electrolysis showed cracks and further evidences of physical damage due to the long exposition at harsh conditions (between 100 and 400 mA cm^{-2} for more than 4h).

These results agree with previous studies on similar catalytic systems. Lee and co-workers reported a stable CO_2 reduction to ethylene at 40% FE for 40 h on a $Cu(OH)_2$-derived catalyst[140] and C_2H_4 production on a CO-fed copper-based GDE has been suggested to be independent from Cu oxidation states.[166] Finally, pasma-activated copper foils catalyze CO_2 reduction to ethylene (60% FE), whilst traces amount of ethanol were detected only for oxidized samples.[167] Consequently, ethanol conversion pathway seems inhibited for copper-based materials in absence of polarized copper sites or residual oxygen.

As a needed remark, I highlight that the total measured Faradaic efficiency accounted for less than 90% (see **Table B.3**, **Appendix B**) because of the elevated temperature of the electrode due to Joule effect. Hence, Faradaic efficiencies have been normalized to 100% throughout this study under the assumption that no further undetected product was formed. Very minor amount of CH_4 ($< 1\%$) were measured as well, whilst no liquid products apart from formate were reported.

Effects of mass transfer and surface pH After having assessed the CO_2 reduction performance of the CuO-derived catalyst, I investigated the influence of CO_2 mass transfer since benchmark experiments suggested this parameter to affect product distribution. Thus, a newly prepared CuO-coated GDE with a similar catalyst loading (0.84 mg cm^{-2}) was tested for different CO_2 flows through the GDE, from 50 ml min^{-1} to 100 ml min^{-1} by steps of 25 ml min^{-1}. A higher CO_2 flow is expected to increase CO_2 mass transfer by increasing local availability of carbon dioxide at the catalyst layer.

The colormaps reported in **Figure 4.6** allow to untangle the effect of surface pH,[19,20,23,145,147] CO_2 / bicarbonate chemical equilibrium,[22] and surface polarization on ethylene formation. Faradaic efficiency toward ethylene is maximum at high current densities due to the strong CO binding enabled by the resulting high negative potential, **Figure 4.6a**. A higher

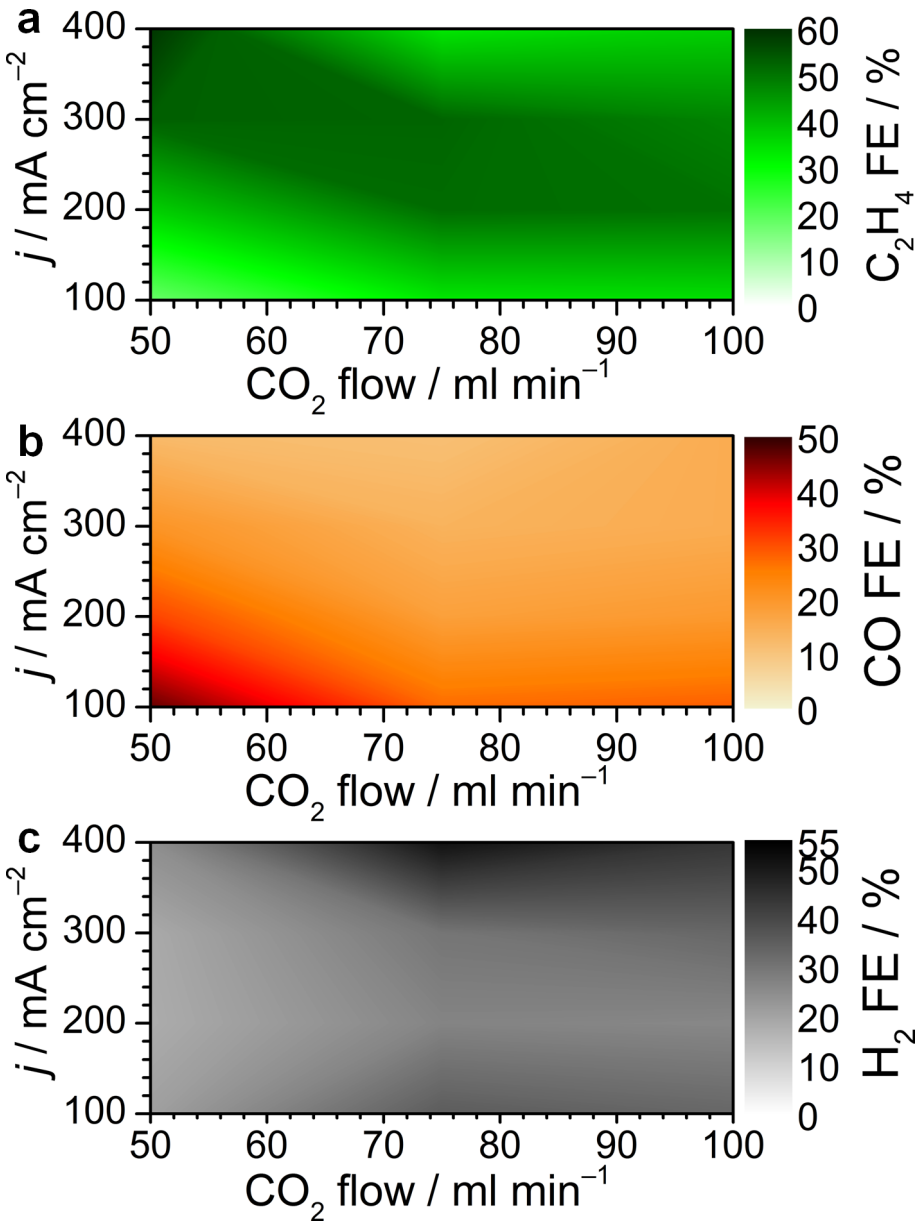

Figure 4.6: Faradaic effiencies toward **a**, ethylene, **b**, carbon monoxide, and **c**, hydrogen for different applied currents and CO_2 flow for CuO-coated GDE in CO_2-saturated 0.5 M $KHCO_3$ electrolyte (bulk pH = 7.4).

CO_2 flow should imply a higher CO_2 concentration at the cathode, thus enhancing ethylene production. Indeed, CO_2 reduction to ethylene is favored for CO_2 flow of 75 and 100 ml min^{-1} until current densities of 300

mA cm^{-2}, however it is hindered when a current of 400 mA cm^{-2} is applied across the cell. The key to understand this unexpected phenomenon lies in the carbon dioxide / bicarbonate chemical equilibrium at neutral pH. A CO_2 molecule can react with a OH^- at the catalyst layer to form bicarbonate, **Reaction 4.7**, with high equilibrium and kinetic constants, $K = 4.27 \times 10^7$ and $k_f = 2.2 \times 10^3$ M^{-1} s^{-1}.[22,63] Hence, at 400 mA cm^{-2} bias the high alkaline surface pH caused by water reduction (Refs.[18–21,134,145]) reduce the surface CO_2 concentration, causing a big drop in CO_2 reduction activity due to mass transfer limitations.

$$CO_2 + OH^- \rightleftharpoons HCO_3^- \tag{4.7}$$

CO_2 flow does not affect CO production, **Figure 4.6b**. In fact, carbon monoxide is formed at low current densities where the alteration of surface pH due to water reduction is lower and does not influence CO_2 mass transfer. Higher CO_2 flow rates unbalance the CO / C_2H_4 equilibrium in favor of the hydrocarbon, as expected by the larger availability of reactants and the consequent increase of CO coverage.[135] Instead, mild and high CO_2 flows enhance hydrogen production at low and high current densities, **Figure 4.6c**. In those two regions, water reduction wins the competition against CO_2 reduction due to either a weak adsorption of CO_2R intermediates (j = 100 mA cm^{-2}) or mass transfer limitation on CO_2R caused by the buffering mechanism proposed above (j = 400 mA cm^{-2}). Finally, the effect of cations is not here considered, however they could play an important role since they affect CO_2 reduction activity and selectivity (see **Section A.2**, **Appendix A**)[17,20] as well as water reduction dynamics.[23]

4.3 Conclusions

In this chapter, I developed a model for explaining the polarization-driven surface reconstruction of polycrystalline Cu under electrochemical conditions toward open facets and defects. The consequential reconstruction from polycrystalline Cu to Cu(100) and nanocuboids is due to surface polarization and thermodynamic instability of close-packed domains. For fcc metals, open facets have a higher surface energy since they are less coordinated than (111) domains, thus they can effectively store the increased electronic density. The devised model suggests that under strong and prolonged polarization open facets should evolve toward defective sites, as (110) edges, characterized by lower surface coordination and better polarizability. Hence, this joint experimental-theoretical characterization predicts that CO_2 reduction to ethylene is enhanced on copper materials treated with

strong negative biases, due to formation of surface sites active for C_2H_4 production.

I tested experimentally the correctness of this hypothesis by carrying out CO_2 reduction on CuO-coated Gas Diffusion Electrode configuration. At the high polarization caused by the high current density applied to the cell, the resulting highly defective metallic copper electrode generated ethylene with 60% FE and partial current density around 240 mA cm^{-2}. The competition between C_2H_4, CO, and H_2 is affected by CO_2 mass transfer, which is controlled by CO_2 flow through the GDE and surface pH.

Chapter 5

Oxide-derived copper

Oxide-derived copper (OD-Cu) is a family of Cu-based catalysts which exhibits high selectivity toward C_{2+} products, such as ethylene, ethanol, and *n*-propanol. Many factors have been deemed responsible to their performance: polarized sites due to residual oxygen,[51,138–140,167–169] surface defects,[129,150,170–172] grain boundaries,[50,51,173] alkaline pH at the electrode-electrolyte interface,[19,20,145,147,174,175] open facets,[47,51,145] surface roughness,[150,167] etc. However, most of the theoretical studies modeled this class of catalysts through ordered crystalline facets, thus they were unable to reproduce their high complexity under reaction conditions.

In this chapter, I modeled oxide-derive copper catalysts starting with oxygen-depleted structures obtained from pristine Cu_2O/Cu supercells. Born-Oppenheimer Ab initio Molecular Dynamics was carried out on the systems to allow surface reconstruction. I characterized the final structures to assess the stability of residual oxides, the chemical speciation of copper, and the presence of relevant ensembles near the surface. Through this analysis I classified the key factors which promote CO_2 reduction on OD-Cu and I quantified their relative contribution toward C_{2+} production. The results of the present project are reported in Ref.[62] and the generated structures are available at the ioChem-BD platform[60] at Ref.[176].

5.1 Background

Oxide-derived copper catalysts can reduce CO_2 into C_{2+} products, which have high industrial value and energy density.[14] Depending on their synthesis, OD-Cu are selective toward ethylene,[49,50,138–140,142,167,171,177] ethanol[50] and *n*-propanol,[50,178] with traces of *n*-butanol,[179] acetate, and ethane,[50,143] see **Tables B.1-B.2**, **Appendix B**. Some studies suggest surface reconstruction to open facets as the main contributor to C_{2+} pro-

duction on OD-Cu,[155,180] since the same product distribution is reported on polycrystalline Cu,[8] and CO-CO coupling is expected to be promoted on Cu(100),[7,11,47,51,145] see **Section 3.2**.

Additional reports propose the importance of residual oxygen for OD-Cu performance.[51,138–140,167–169,181] Yet, the role of residual oxygen is debated in literature,[18,182] since oxidic phases are thermodynamically unstable under CO_2 reduction conditions.[164] Oxygen was not detected during CO_2 reduction for copper-derived catalysts which underwent air oxidation or mild anodic polarization,[164,183,184] and isotopic labeling on Cu nanocubes confirmed an oxygen content lower than 1.0 at.% upon operation.[185] Further studies highlighted the full conversion of Cu_2O phases to metallic Cu during CO_2 reduction.[164,171,183,186] The use of Cu_xO_y precursors or a deep oxidation of the catalyst before operation lead instead to different results, which suggest the presence of oxygen under reduction conditions.[51,140,169,187] Cavities formed upon surface reconstruction at negative potential (Refs.[16,48,51,150,169,188]) may permit the kinetic trapping of near-surface oxygens,[189] further stabilized by configurational entropy.[190]

5.2 Structural characterization

I employed two classes of models to reproduce the morphology evolution of OD-Cu catalysts under operation,[62] following experimental evidences of the absence of oxygen at the surface[164] and low residual O content (10-20 at.%).[142,167,191] On the one hand, I constructed $2\sqrt{3} \times 2\sqrt{3} - R30°$ $Cu_2O(111)$-derived supercells by removing the outermost O layer and part of the subsurface according to different depletion patterns. This first family of models was named Cu_2O-red.[62] On the other hand, Cu_2O/Cu models were characterized by 3 $Cu_2O(111)$ layers on top of $5\sqrt{3} \times 5\sqrt{3} - R30°$ bulk Cu(111) and the outermost oxygen layers depleted as for the previous class. Due to the interphase between metallic and oxidic copper, these models were assumed as a proxy of oxidation conditions, thus they were called Cu-oxi.[62] The systems which constituted the Cu_2O-derived class presented a O percent between 31 and 30 at.%, whilst the Cu_2O/Cu models had a lower oxygen content (11 at.%), **Table 5.1**. Within both classes, the suboxides formation energy by Cu atom differed by 0.01 eV, thus within intrinsic Density Functional Theory uncertainty.

Ab Initio Molecular Dynamics with the PBE functional[85] was applied to the system for 1 + 10 ps at 700 K (3 fs time step). We investigated three main factors: the thermodynamic stability of the modeled suboxides, structural and chemical fingerprints of copper, and the presence of surface ensembles.

Table 5.1: **Copper oxide formation energies by Cu atom for pristine and reconstructed OD-Cu models.** Oxygen atomic percentage, $\frac{N_O}{N_{Cu}+N_O} \cdot 100$, and copper-oxide formation energy per Cu atom, $E_{Cu_2O}\ N_{Cu}^{-1}$ / eV, for the modeled systems. Trajectories at $t = 0$ ps correspond to the pristine structures relaxed before equilibration, whilst trajectories at $t = 11$ ps stand for final structures relaxed after Ab Initio Molecular Dynamics. Red and oxi subscript labels respectively Cu_2O and Cu oxidation models, whereas nS accounts for the initial of the geometric depletion pattern, S, and the number of depleted subsurface oxygens n. R stands for Rhomboidal, T for Triangular, and L for linear. Adapted from Ref.[62].

System	O %	$E_{Cu_2O}\ N_{Cu}^{-1}$ (0 ps) / eV	$E_{Cu_2O}\ N_{Cu}^{-1}$ (11 ps) / eV
$4R_{red}$	31	0.60	0.60
$4T_{red}$	31	0.59	0.60
$6L_{red}$	30	0.60	0.59
SY_{ox}	13	0.35	0.34
$4R_{oxi}$	11	0.21	0.18
$4T_{oxi}$	11	0.21	0.18
$6L_{oxi}$	11	0.22	0.18

Thermodynamics of residual subodixic phases For a bulk material, the stability of its phases is addressed from its Pourbaix diagram.[192] For Cu-O, only three phases are thermodynamically stable at neutral pH and mild potential: Cu, Cu_2O, and CuO. Since both Cu_2O-red and Cu-oxi models exhibit formation energy higher than Cu_2O by at most 0.1 eV, they are thermodynamically metastable[193] as experimental suboxides,[194,195] **Figure 5.1a**. Configurational entropy is expected to have a stabilization effect by at least 0.2 eV on oxidic formation energies in disordered materials,[190] furthermore interaction with reaction intermediates influences surface reconstruction.[48,196] Residual oxygen may be kinetically trapped in surface cavities or stabilized by reaction intermediates, thus some metastable suboxidic features may be present under CO_2 reduction conditions. Overall, these conclusions on suboxides stability should be taken as a lower threshold, since more accurate methods to assess entropic effects and the explicit insertion of reaction intermediates upon AIMD reconstruction may better describe the stability window.

Residual oxygens desorb from the electrode as water under CO_2 reduction conditions. Hence, to sample the thermodynamics of this process for the simulated suboxides, I randomly selected 21 near-surface oxygen configurations and calculated the thermodynamic driving force for their detachment from the surface. Due to water reduction, the pH close to the cathode is

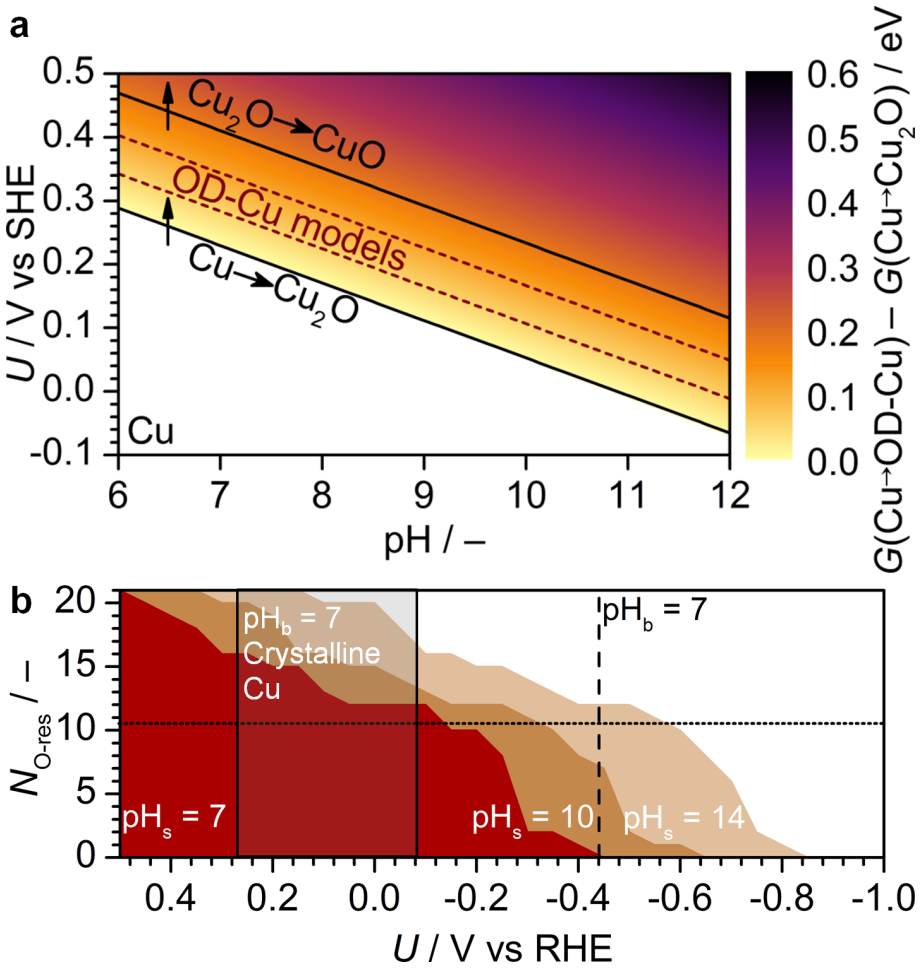

Figure 5.1: **a**, The OD-Cu modeled systems (dashed red lines) present formation energies 0.05-0.10 eV higher than Cu_2O formation energy (black line), thus they are metastable[193] akin suboxides detected experimentally.[194,195] **b**, Simulations of O desorption at alkaline surface pHs for 21 O configurations suggest residual oxygens to be stable until −0.84 V vs RHE for $pH_s = 14$, in good agreement with recent experimental evidences.[51,140,191,197,198] Dark gray area represents DFT-estimated O stability window on crystalline copper at neutral bulk pH. Adapted from Ref.[62].

higher than bulk pH,[19,21,23,134] therefore I estimated the window of stability of residual oxygen considering a surface pH between 7 and 14,[65] **Figure 5.1b**. 50% of oxygen configurations are stable until −0.1, −0.3 and −0.5 V vs RHE depending on the assumed pH and their stability extended until −0.44, −0.64 and −0.84 V vs RHE respectively. These results are indepen-

dent from the dielectric permittivity of the electrolyte,[62] which can change significantly under operation.[21] Remarkably, the stability window that resulted from this study agrees with the experimental detection of residual oxygen until −1 vs RHE for $Cu(OH)_2$-derived catalyst[197] and is compatible with the low overpotential needed for ethanol production on OD-Cu catalysts.[50]

Copper speciation I assessed the local coordination of Cu atoms by the Cu-Cu and Cu-O radial distribution functions, $g_{\text{Cu-Cu}}$ and $g_{\text{Cu-O}}$, which exhibited analogous features for both Cu_2O-red and Cu-oxi classes of models and independently from Cu/O stoichiometry. $g_{\text{Cu-O}}$ highlighted a Cu-O first coordination shell extended until $d_{\text{Cu-O}} = 2.50$ Å.[62] Assuming this value as threshold for oxygen coordination, three main Cu species were identified depending on the number of neighboring oxygen atoms, either 0, 1 or 2, **Figure 5.2a**. To relate structural and electronic properties, I assessed the oxidation state of the three Cu species by calculating their Bader charges. Depending on its oxygen coordination, Cu presents three well-defined oxidation states: metallic Cu^0, suboxidic $Cu^{\delta+}$, and oxidic Cu^+, respectively ccoordinated to 0, 1 and 2 oxygens, **Figure 5.2b**. Metallic and oxidic fingerprints are analogous to bulk materials, instead suboxidic Cu exhibits an intermediate polarization, which can be considered as a $\delta+$ charge characteristic of polarized copper[187,197,199] coordinated to 1 oxygen atom as observed experimentally ($\overline{N}_{\text{Cu}^{\delta+}\text{-O(exp)}} = 1.1$, Ref.[197]). Overall, the OD-Cu models exhibit undercoordinated sites in comparison to crystalline copper, **Figure 5.2b**. Metallic Cu presents $\overline{N}_{\text{Cu}^0\text{-Cu(theo)}} = 4.9$, in line with experimental reports of $\overline{N}_{\text{Cu}^0\text{-Cu(exp)}} = 6.6$.[197] $Cu^{\delta+}$ loses 1 Cu bond upon coordination to oxygen, thus the average Cu-Cu coordination number is lowered by around 1 unit, $\overline{N}_{\text{Cu}^{\delta+}\text{-Cu(theo)}} = 3.6$ vs $\overline{N}_{\text{Cu}^{\delta+}\text{-Cu(exp)}} = 3.08$.[200] Finally, its double oxygen coordination saturates Cu^+ species, hence average Cu-Cu coordination number further decreases to $\overline{N}_{\text{Cu}^+\text{-Cu(theo)}} = 2.0$ as experimentally reported ($\overline{N}_{\text{Cu}^+\text{-Cu(exp)}} = 2.21$, 1.84, Ref.[200]).

Near-surface ensembles Moving from averaged to local properties, I characterized the coordination of each species detected on OD-Cu models by relating interatomic angles within Cu and O coordination shells at a given z. I then identified recurrent atomic ensembles through the repeated occurrence of specific angles for Cu^+, $Cu^{\delta+}$, Cu^0, and O neighbors, **Figure 5.3**.

Both metallic and suboxidic copper form specific patterns close to the surface. Few low coordinated metallic copper adatoms were identified, either 4-coordinated, Cu_{4Cu}, or 6-coordinated Cu_{6Cu}, **Figure 5.3a,d**. OD-Cu

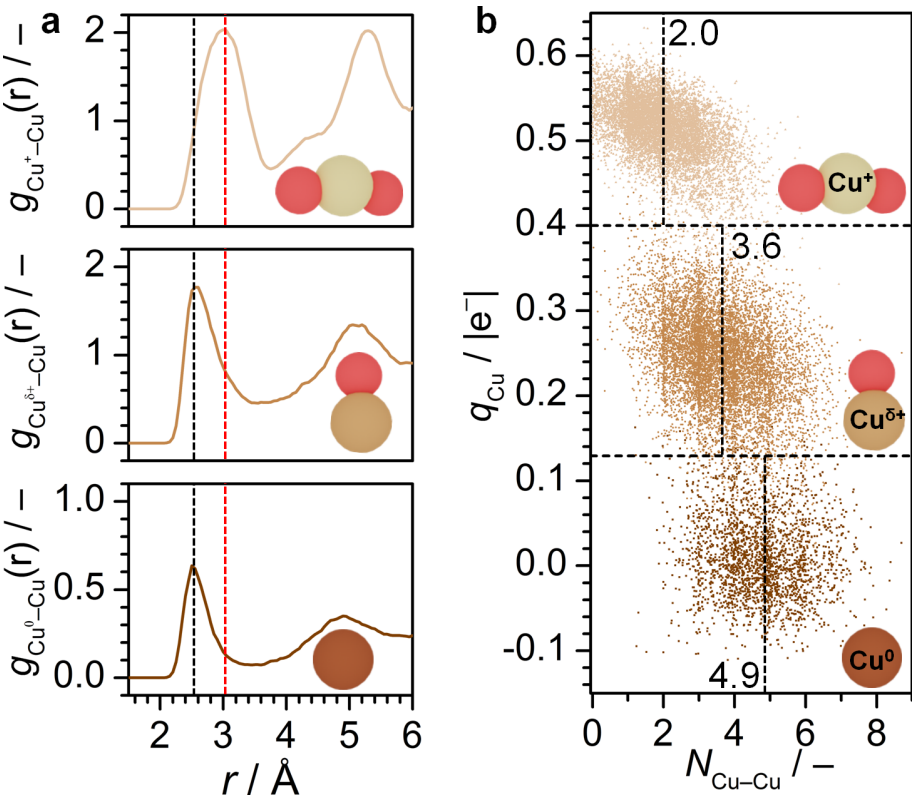

Figure 5.2: **a**, Cu-Cu radial distribution functions for the three Cu coordination environments detected: 0 (bottom), 1 (middle) and 2 (top) oxygens. The first and second coordination shells of bulk Cu and Cu_2O are shown as black and red dashed lines, respectively. **b**, Each copper species is characterized by a specific range of Bader charges, therefore the three coordination environments correspond to Cu^0 (bottom), $Cu^{\delta+}$, and Cu^+. Dashed lines indicate average $\overline{N}_{Cu\text{-}Cu}$. Adapted from Ref.[62].

surface reconstructs as well toward distorted crystalline domains, such as Cu(100), Cu(110), and Cu(111), as reported by *Operando* EC-STM characterization.[16,183] These facets can be either constituted only by metallic Cu sites or they can include $Cu^{\delta+}$, **Figure 5.3b,d**. Additionally, $Cu^{\delta+}$ aggregates as well into triangular $Cu_3^{\delta+}O_3$ clusters, **Figure 5.3b,d**, compatible with EXAFS signals on OD-Cu systems.[199] Oxidic Cu^+ species are not abundant in the outermost layers in good agreement with experimental evidences of the absence of oxidic phases at the catalyst surface.[164]

Oxygen adatoms coordinate to three or four Cu atoms, $O_{3Cu,ad}$ and $O_{4Cu,ad}$, and they are responsible for the diffuse signal nearby the surface layer, **Figure 5.3c**. However, surface oxygens are less abundant than near-

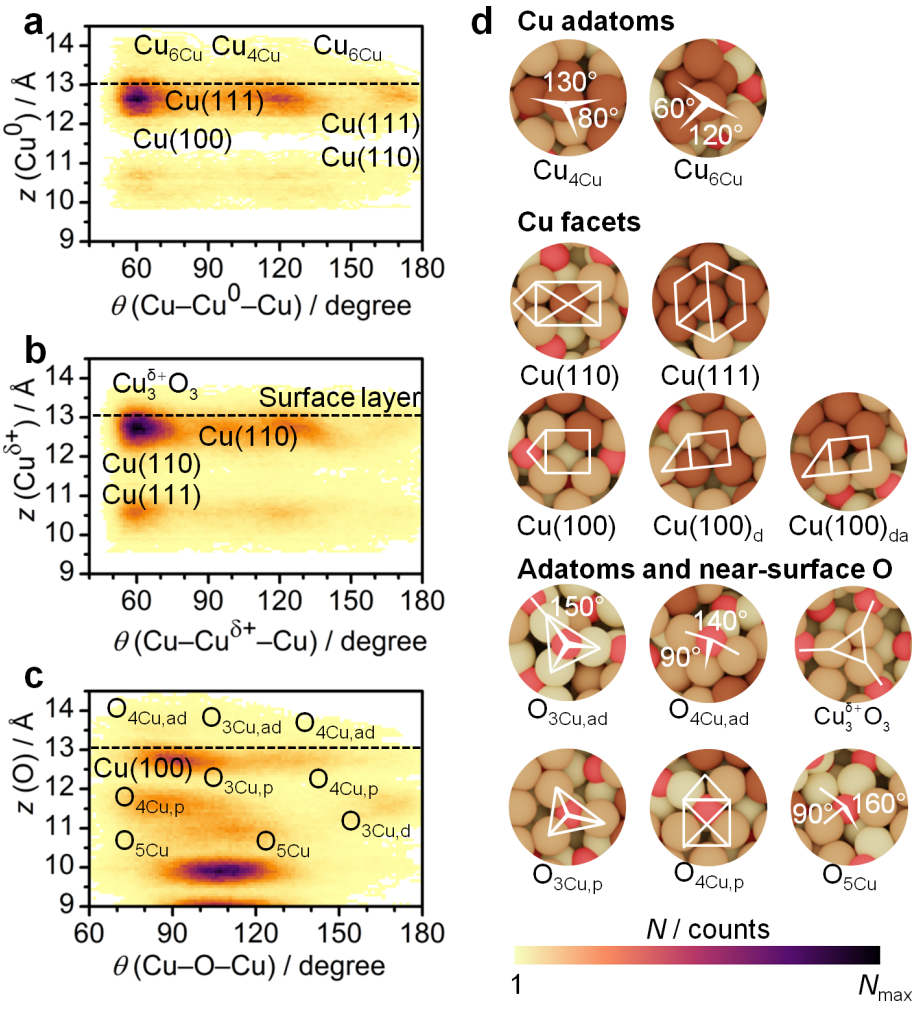

Figure 5.3: Histograms for angles **a**, $\theta(\mathrm{Cu}-\mathrm{Cu}^0-\mathrm{Cu})$, **b**, $\theta(\mathrm{Cu}-\mathrm{Cu}^{\delta+}-\mathrm{Cu})$, and **c**, $\theta(\mathrm{Cu}-\mathrm{O}-\mathrm{Cu})$ measured between neighboring atoms within the first coordination shell of a central atom at a specific height z. **d**, Near-surface ensembles were identified upon surface reconstruction: tetra- and hexa-coordinated Cu adatoms, $\mathrm{Cu}_{3\mathrm{Cu}}$ and $\mathrm{Cu}_{4\mathrm{Cu}}$; crystalline domains: Cu(100)-like facets, either metallic or asymmetric in charge (subscripts "d" and "da"), Cu(110) and Cu(111) facets; tri- and tetra-coordinated O adatoms: $\mathrm{O}_{3\mathrm{Cu,ad}}$ and $\mathrm{O}_{4\mathrm{Cu,ad}}$; a $\mathrm{Cu}_3^{\delta+}\mathrm{O}_3$ cluster; tri- and tetra-coordinated planar O: $\mathrm{O}_{3\mathrm{Cu,p}}$ and $\mathrm{O}_{4\mathrm{Cu,p}}$, and penta-coordinated near-surface O: $\mathrm{O}_{5\mathrm{Cu}}$. $N_{\max}$: 1600 (**a**), 3600 (**b**), 1200 (**c**). Here I only reported the analysis for a single OD-Cu model. Yet, the results hold for any other oxygen depletion pattern. Adapted from Ref.[62].

surface configurations. These near-surface oxygens, O_{ns}, adopt planar coordination, such as $O_{3Cu,p}$ and $O_{4Cu,p}$, **Figure 5.3 d**, and have been detected and characterized in $Cu_2O_{0.5}$ stoichiometry for OD-Cu system until -1.0 V vs RHE.[197] 5-fold coordination, O_{5Cu}, is identified as well in inner layers.

5.3 CO_2 reduction activity and C_{2+} selectivity

After having modeled and characterized OD-Cu, I related the structural and electronic properties detected to the outstanding performance of oxide-derived copper catalysts for CO_2 reduction. In literature, two main properties are highlighted for OD-Cu: the increased CO_2 reduction activity[18,150,167,199] and the high C_{2+} selectivity. The high electrochemically active surface area and a strong CO_2 binding energy due to surface polarization have been suggested as descriptors for the enhanced activity,[18,150] whilst C_{2+} selectivity has been related to the capability of catalyst or catalytic environment to promote the CO-CO dimerization step by stabilizing the volatile $*OCCO^-$ intermediate.[17,18,130]

As an initial step to decouple the contributions of both high electrochemically active surface area[18,150,167,199] and surface polarization[51,138–140,167–169] on CO_2 reduction activity, I estimated atomic surface roughness and the number of surface sites. Afterwards, I assessed CO_2 adsorption on the near-surface ensembles detected previously. To rationalizing the enhanced C_{2+} selectivity, I estimated the thermodynamics and kinetics of the CO-CO dimerization step on the reconstructed surfaces.

Electrochemically active surface area Upon AIMD simulations, the oxygen-depleted models reconstructed and cavities, adatoms, defects, and grain boundaries appeared at the surface,[201] **Figure 5.4a**. For all the employed models, the atomic surface roughness is higher than values reported for crystalline Cu,[202] **Figure 5.4b**. Upon reconstruction, Cu surface sites are between 20% and 40% more abundant than surface sites for pristine Cu_2O crystalline surfaces, in agreement with roughness factors larger than 1 reported for OD-Cu.[51,167] Assuming the ratio between the surface density of Cu sites for OD-Cu models and pristine Cu_2O as a proxy for the electrochemical surface area, A_{Cu}, experimental evidences of higher surface areas for OD-Cu systems are here confirmed, **Figure 5.4c**. A higher abundance of surface sites leads to an higher activity per unit of geometrical area, thus it explains the impact of surface roughness on CO_2 reduction for oxide-derived copper catalysts.

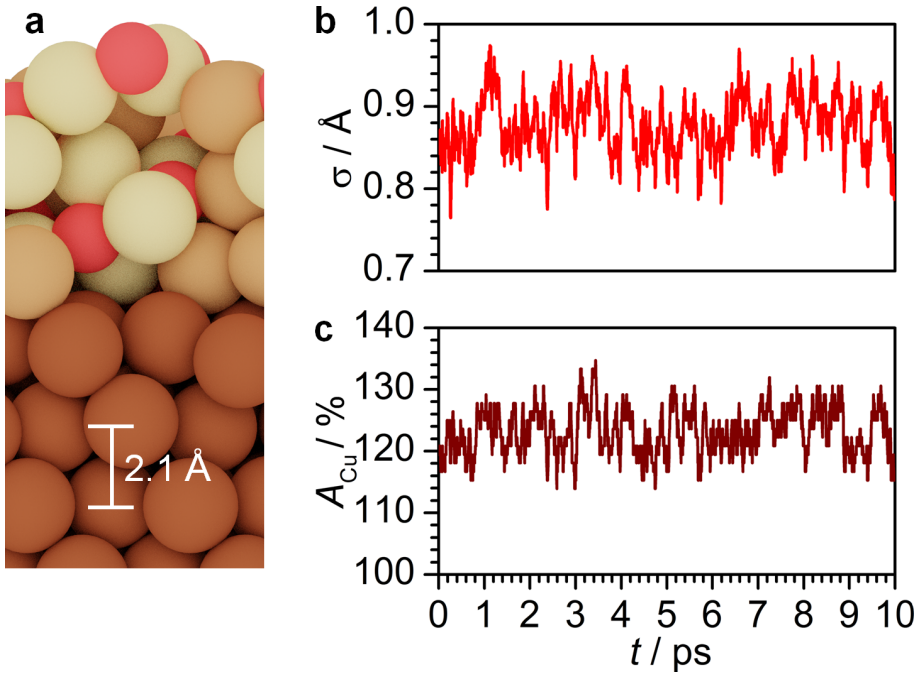

Figure 5.4: **a**, All the employed models exhibit similar surface reconstruction upon AIMD simulation.[201] **b**, For every OD-Cu model, theoretical atomic surface roughness is higher than crystalline Cu values, 0.32 Å.[202] **c**, The number of Cu surface sites after reconstruction is at least 20% higher than crystalline oxide surface sites. A_{Cu}, the ratio between OD-Cu and Cu_2O surface sites, is here defined as a proxy for surface activity. Adapted from Ref.[62].

Surface polarization effects on activity Surface polarization has been suggested as a key parameter to drive CO_2 reduction activity. On both Cu_2O-red and Cu-oxi classes, CO_2 can adsorb on the reconstructed surface either as a $\eta^2_{C,O}$ configuration on Cu sites or as a carbonate via a C-O_{ns} bond, **Figure 5.5**. In both cases, CO_2 binding energy scales with the polarization of the binding sites X(C) and Y(O) approximated by Q, sum of their Bader charges with respect to neutral atoms, **Equation 5.1**. Presenting low polarization, metallic Cu sites are unable to tether CO_2 strongly and thus to permit its reduction at low overpotential. Instead, asymmetric surface sites such as Cu_{4Cu}, Cu_{6Cu}, and $Cu_3^{\delta+}O_3$ account for a strong CO_2 binding energy of 0.2 eV, thus they can open the reduction pathway. For strongly polarized active sites such as near-surface oxygens, their high local electronic density saturates the bond between carbon and surface oxygen. As a consequence, CO_2 adsorption becomes an exothermic process, and the formation of car-

bonate is promoted. In fact, this specie has been detected *via in situ* and real-time surface-enhanced infrared absorption spectroscopy (SEIRAs) under CO_2 reduction conditions.[203,204] By passivating the surface, carbonate blocks the activity of near-oxygen sites.[168] In general, polarized sites such as Cu^0-$Cu^{\delta+}$ or $Cu^{\delta+}$-$Cu^{\delta+}$ lead to a lower overpotential for CO_2 adsorption due to their strong CO_2 binding energy. This result have been confirmed experimentally by detecting CO_2 adsorption with lower overpotentials when suboxidic and oxidic sites were present.[138]

$$Q = \frac{1}{N_{X(\mathrm{C})}} \left| \sum_{i=1}^{N_{X(\mathrm{C})}} q_{X_i(\mathrm{C})} \right| + \frac{1}{N_{Y(\mathrm{O})}} \left| \sum_{i=1}^{N_{Y(\mathrm{O})}} q_{Y_i(\mathrm{O})} \right| \tag{5.1}$$

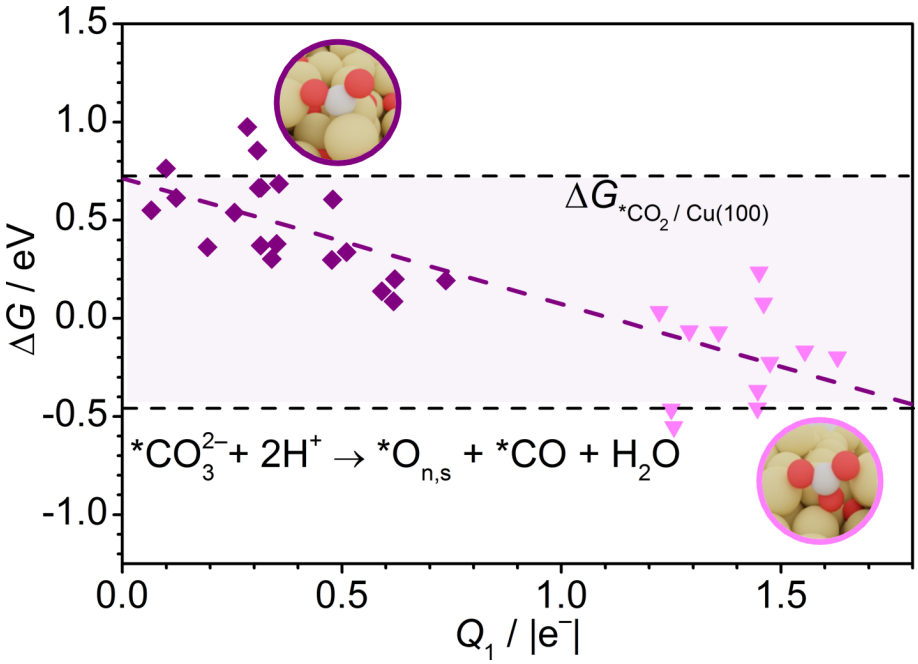

Figure 5.5: CO_2 adsorbs on OD-Cu models either on Cu sites (purple) or on a near-surface oxygens as a carbonate (magenta). In both cases, CO_2 binding energy scales with active sites polarization, Q_1: $\Delta G_{*\mathrm{CO}_2} = +0.7(\pm 0.1) - 0.6(\pm 0.1)Q_1$. Cu^0-$Cu^{\delta+}$ and $Cu^{\delta+}$-$Cu^{\delta+}$ pairs strongly tether CO_2, thus increasing OD-Cu catalytic activity, purple area. Adapted from Ref.[62].

Surface polarization effects on C_{2+} selectivity Since the CO-CO stabilization step is assumed to be the rate determining step toward C_{2+}

production,[17,18,136] I calculated the adsorption energy of the initial and final states for this process: 2*CO and *OCCO$^-$. Both CO and CO dimer binding energies scale with the polarization of the active sites, approximated by the sum of the absolute values of their Bader charges, **Equation 5.1**. High surface polarization hinders the adsorption of two neighboring CO, whilst it promotes the CO-CO dimer, **Figure 5.6a**. Metallic domains present a high thermodynamic and kinetic barrier for forming the *OCCO intermediate, **Figure 5.6a-b**, thus they show similar product distribution to copper foil and copper nanoparticles: H_2, CO, CH_4. Instead, polarized Cu^0-$Cu^{\delta+}$(100)-(110) facets presents similar reactivity as crystalline Cu(100), ΔG_{*OCCO} = 0.07 eV, thus reconstructed domains exhibits similar product distribution as open facets as suggested in literature.[47,205]

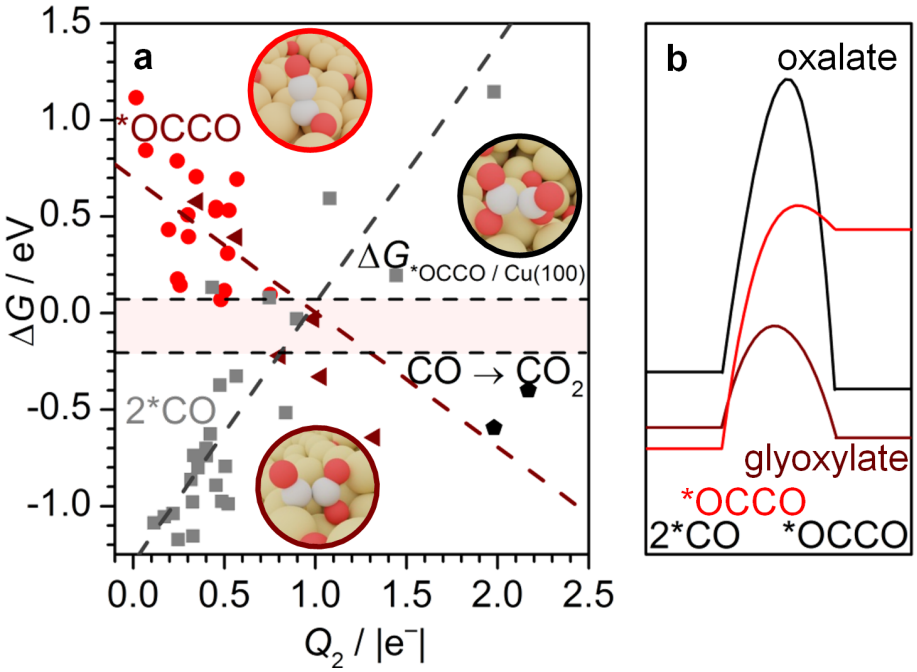

Figure 5.6: **a**, Surface polarization drives the thermodynamics of the CO-CO dimer: $\Delta G_{*OCCO} = +0.7(\pm0.1) - 0.7(\pm0.1)Q_2$. Polarized Cu and near-surface oxygens stabilize the CO-CO dimer as a deprotonated glyoxylate intermediate (dark red area). In contrast, low polarized metallic Cu sites (red) adsorb CO too strongly, $\Delta G_{2*CO} = -1.3(\pm0.1) + 1.3(\pm0.1)Q_2$. Oxalates formation on highly polarizes surface sites (black) is hindered by a high kinetic barrier. **b**, Kinetic barriers for CO-CO dimerization steps as *OCCO (red), deprotonated glyoxylate (dark red), and oxalate (black) on OD-Cu. Adapted from Ref.[62].

By further increasing polarization, the $Cu^{\delta+}$-O_{ns} pair is the main active site which generate C_{2+} products by making the dimerization reaction thermoneutral. This ensemble stabilizes the CO-CO dimer as a deprotonated glyoxylate intermediate, OC*CO(O_{ns}),[176] whose formation presents a low kinetic barrier of 0.53 eV. The presence of this elusive chemical species, so far never reported for electrochemical CO_2 reduction,[130,206] is well-known in prebiotic CO_2 reduction.[207] Besides, its role is further suggested by the compatibility of its higher vibrational frequencies, 1630, 1479 and 1145 cm^{-1}, with SEIRAS and IR spectroscopy signals detected during CO_2 reduction on OD-Cu.[17,203,204] Due to its facile formation, this species may be the intermediate which opens the CO_2 reduction pathway toward ethanol at potential as low as -0.25 V vs RHE for oxide-derived copper.[50]

At high surface polarization oxalates can form on a O_{ns}-O_{ns} pair. As for the case of the carbonate, the formation of this strongly bond intermediate would lead to surface passivation and eventually to surface dissolution due to the strong C-O_{ns} bonds. However, oxalate formation is hindered by the high kinetic barrier associated to this process, $E_a = 1.51$ eV, **Figure 5.6b**.

C_{2+} product distribution on copper-based catalysts Oxide-derived copper catalysts can be obtained either by anodizing pristine Cu or from oxides precursors. Anodization processes return materials which are selective toward ethylene,[138–144] whereas the oxide precursors lead to production of oxygenates, such as ethanol[50,171,177] and *n*-propanol,[177,178] **Table B.1** in **Appendix B**. Plasma-treatment on pristine Cu foils or nanoparticles increases surface defects, hence making the catalyst selective to ethylene.[167] Bimetallic catalysts such as Cu-Ag systems exhibit outstanding CO_2 conversion to oxygenates such as ethanol,[208–210] and *n*-propanol.[205] Instead, when copper is modified with a element with higher oxygen affinity, as Zinc, ethylene production is favored.[211] This bimetal effect cannot be entirely explained by changes in the local copper morphology, thus a joint effect of both metals is expected. Cu modified with electron acceptors or ligands presents good selectivity towards each of the C_{2+} products previously mentioned and the specific Faradic efficiency depends on the modifier.

Ethylene and ethanol are expected to originate from a common intermediate which follows the CO-CO dimerization step,[130] see **Figure 3.6, Section 3.5**. Their production at low overpotentials on oxide-derived Cu can be explained by the low energetic barrier associated to the deprotonated glyoxylate intermediate. Yet, this theoretical evidence does not provide any further insights on the chemical differences which lead to different production rates for ethylene, ethanol and *n*-propanol depending on OD-Cu synthetic process, **Table B.1** in **Appendix B**. Three specific sites have been

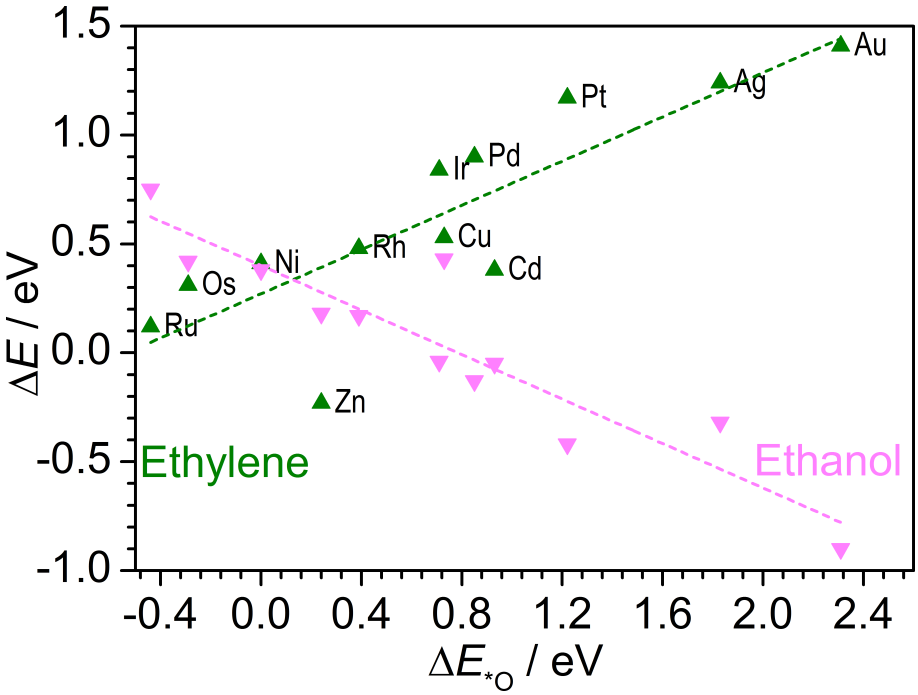

Figure 5.7: Ethanol (magenta) and ethylene (green) formation energy on selected metals versus adsorbed oxygen stability calculated with respect to water and hydrogen according to the reaction scheme described in **Figure 3.6, Section 3.5**.

associated to each product via isotopic labeling by Lum *et al.*[212] According to the structural analysis previously exposed, the reactivity of the ensembles detected for the OD-Cu models is subject to their local polarization and their O or Cu coordination. Low coordinated Cu^0 site are strong binding sites, whilst $Cu^{\delta+}$ adsorption properties depends on their coordination. Cu^0, $Cu^{\delta+}$, and Cu^+ are less oxophilic than crystalline Cu and their oxygen affinity further decreases upon increment of the oxidation state.[62] Since O-bound reaction intermediates have been suggested to promote ethanol production, whilst C-bound would account for ethylene formation,[137] O affinity and Cu coordination could be applied together as proper descriptors to understand C_{2+} product distribution of OD-Cu catalysts.

Oxygen affinity has already been introduced to describe CO_2 reduction selectivity toward alcohols,[137] such as 1-butanol.[179] Following this approach, it is possible to plot ethylene and ethanol formation energy for specific metals versus oxygen affinity, **Figure 5.7**. Copper-based catalysts modified with elements which exhibit low oxygen affinity, such as Ag, pro-

mote ethanol production.[205,208–210] On the contrary, bimetallic systems composed by copper and metals with high oxygen affinity, such as Zinc, have been reported as effective catalysts for ethylene production.[211]

5.4 Conclusions

In this project I applied Ab Initio Molecular Dynamics on oxygen-depleted Cu_2O and Cu_2O/Cu systems to model the morphological changes which happen to oxide-derived copper catalysts under reaction conditions.[62] Experimental evidences highlight high CO_2 reduction activity and C_{2+} selectivity for this class of materials.[18] Ethylene, ethanol, and *n*-propanol are expected to form at different active sites.[185] Whilst the large electrochemically active surface area due to cathodic reconstruction determines the high CO_2 activity,[18,150,167,199] some studies suggest residual oxygen as an additional contributor to the high reduction current densities and C_{2+} selectivity.[51,138–140,167–169]

The resulting subodixic phases resulting from AIMD presented metastable features as experimental reports suggest.[194,195] The proposed window of stability for residual oxygen extends until -0.84 V vs RHE since oxygen is stabilized by alkaline surface pH and kinetic trapping on surface cavities. Depending on its coordination to these residual oxygens, Cu differentiates into three main species with well-defined oxidation state: metallic Cu^0, suboxidic (single oxygen coordination) $Cu^{\delta+}$, and oxidic Cu^+ (double oxygen coordination). Cu and O combine into surface ensembles, among which Cu adatoms, O adatoms, reconstructed crystalline domains, a $Cu_3^{\delta+}O_3$ suboxide, and near-surface oxygens. Their presence explains OD-Cu performance for CO_2 reduction together with the high electrochemical active surface area characterized for the oxygen-depleted models. Due to their polarization, $Cu^{\delta+}$ and Cu^0-$Cu^{\delta+}$ active sites present strong CO_2 binding energy, hence they are responsible for the high activity of OD-Cu. Presenting mild polarization, Cu-O_{ns} pair stabilizes C–C coupling by forming a deprotonated glyoxylate intermediate, which opens the reduction pathway toward C_{2+} products.

To summarize, I here developed a simplified method to mimic surface reconstruction on oxide-derived copper. Even without including reaction intermediates, solvent, electrolyte, and electric field, I reproduced some of the structural patterns characteristic of OD-Cu. I rationalized CO_2 reduction activity and selectivity through a general model based on active sites polarization and a new reaction intermediate, a deprotonated glyoxylate. New synthetic protocols can now focus on reproducing the active ensembles here classified and produce more active and selective copper-based catalysts.

Chapter 6

Chalcogen modified copper

Copper can catalyze electrochemical CO_2 reduction toward many liquid and gaseous products.[7,8,42] A common strategy to improve Cu selectivity toward a specific reaction product is to modify it with different chemical elements.[49,50,52,54,167,188] In this Chapter, I consider the case of copper materials modified by elements of the *p*-block of the periodic table, the chalcogen group: O, S, Se, and Te. This study resulted in the publication Ref.[61] and the output of the simulations are available at Ref.[213] in the ioChem-BD repository.[60]

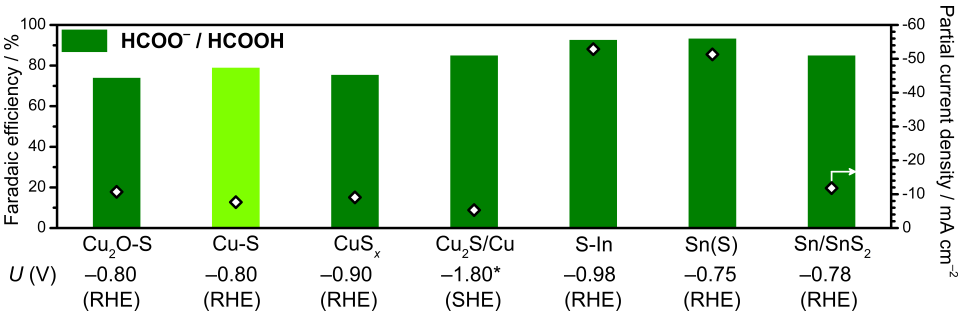

Figure 6.1: Experimental reports on electrochemical CO_2 reduction toward formate and formic acid on S modified metal catalysts. From left to right: Refs.[214],[55],[215–219]. *Organic electrolyte: acetonitrile (MeCN) with 0.5 mol l^{-1} 1-butyl-3-methylimidazolium tetrafluoroborate.[216]

Experimental reports highlighted the promotion of CO_2 electroreduction to formate (or formic acid) by sulfur modification of metallic catalysts, accounting for Faradaic efficiencies higher than 70%, **Figure 6.1**.[55,214–219] Our experimental collaborators from the group of Prof. Pérez-Ramírez at ETH Zürich reported a Faradaic efficiency toward formate as high as 80% at −0.8 V vs RHE on oxide-derived copper modified by sulfur,[55] **Figure**

6.2. Our investigation focuses on the understanding of the role of sulfur on the catalytic performance of the system. The theoretical studies here were carried out in collaboration with Dr. Rodrigo Antonio García Muelas.

6.1 Formate production on sulfur modified copper

Our coworkers synthesized S modified Cu nanoparticles by a solvothermal route, with 42 nm averaged size, and S content measured by XPS spectroscopy of 3.4 ± 1.0 at.% and 1.1 ± 1.1 at.% respectively before and after electrochemical testing.[55] No Cu-S crystalline phases were detected prior to CO_2 reduction,[55,61] as expected from the thermodynamic instability of copper sulfides at negative potentials.[220] The same results held for the other chalcogens, such as O, Se and Te modified Cu. Nanoparticles can be modeled as the most stable crystal facets for the bulk material, predicting the relative abundance from their surface energy.[81,128,221] The lowest energy surface domains present the largest extensions,[127] thus the reactivity of nanostructures can be assessed by analyzing the contribution of each facet. Explicit nanoparticles models are also possible,[181] yet the computation cost of these simulations increases. Due to the instability of chalcogenides phases,[220] we modeled the experimental system as the most stable crystalline copper facets[222–224] modified by a chalcogen adatom on a fcc site. The theoretical chalcogen / copper ratio was set in agreement with experimental values:[55] 1 adatom for 36 surface atoms, accounting for 2.7 at.%. The adatom configuration was the only stable motif for the modifier under reaction conditions: the removal of S adatom as H_2S was endothermic until -0.92 V vs RHE.[61]

Copper nanoparticles have been reported selective toward methane, CO, and hydrogen.[129] O, Se, and Te modified systems account for similar product distributions (FE $>$ 60% H_2, $<$ 30% CO), however the S modified copper catalyst presents an outstanding production of formate to the detriment of other CO_2 reduction products and hydrogen. O and Se modified systems have higher selectivity to formate than Cu foils: 25% Faradaic efficiency instead of 15%,[7] yet they are far from optimal. The instability of oxygen (Refs.[183, 185, 225]) and tellurium at negative potentials explains the detection of ethylene, which is promoted by open facets generated upon copper surface reconstruction, see **Section 4.1**.[16] Finally, a volcano trend for chalcogen modified Cu selectivity toward formate appears, showing a peak for the Cu-S sample, **Figure 6.2**.

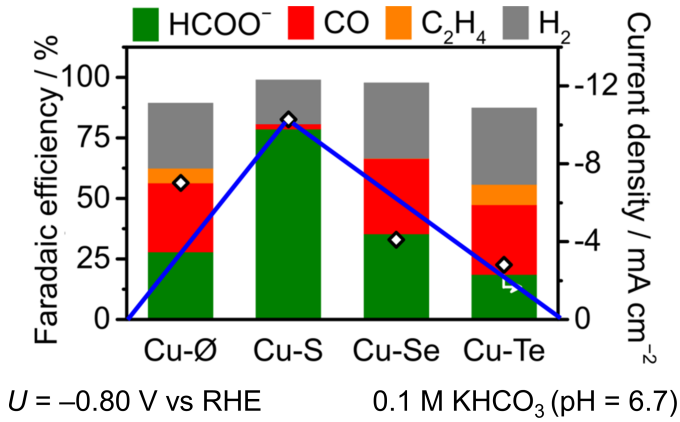

Figure 6.2: Product distribution for the copper-chalcogen systems with O, S, Se, and Te as the surface modifiers. The blue line highlights the volcano trend toward formate production. The O modified system is here labeled as Cu-Ø since O is expected to be reduced for chemically synthesized copper oxide nanoparticles.[164,183,185,225] Adapted from Ref.[61].

6.2 CO_2 activation

CO_2 adsorption is considered the rate determining step for electrochemical CO_2 reduction reaction on metallic catalysts.[18,130,226,227] An electron transfer to CO_2 LUMO stabilizes this intermediate on the catalytic surface,[228] however this process requires more than 1 eV to happen, **Figure 6.3a**. Upon electron transfer, the CO_2^- intermediate presents different conformations depending on the active site[130] and each CO_2 conformation generates a different reaction product. This explains the lack of selectivity of polycrystalline copper, since it is characterized by a large variety of active sites, which generate different reaction products, such as methane, carbon monoxide, hydrogen or formate.[6,7,9,129,130]

When a modifier is inserted in a copper material, it can help in lowering CO_2 adsorption barrier and tethering carbon dioxide in a specific conformation. Since chemisorbed CO_2 exhibits a bending of the O-C-O angle because of CO_2 activation, we can assume the energy to bend CO_2 as a proxy of its activation energy. In our case, S helps CO_2 activation by strongly binding this intermediate in a $\eta^2_{C,O}$ conformation together with a neighboring Cu site. As shown in **Figure6.3b**, the usually endothermic bending of CO_2 is promoted by S and the process becomes exothermic by more than 1 eV without electron transfers. The chalcogen acts as a donor due to its partial negative charge, confirmed by Bader charge analysis[229–232] ($\delta = -0.59 \mid e^- \mid$ for a S adatom on a Cu(111)).

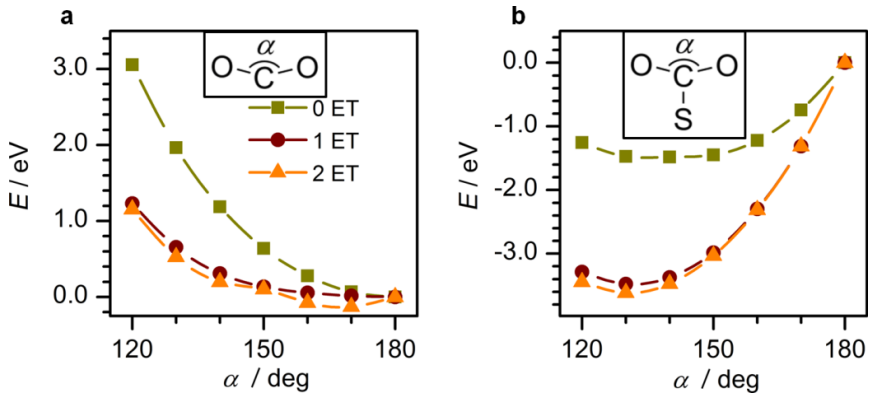

Figure 6.3: DFT energies for gas phase **a**, CO_2 and **b**, thiocarbonate (SCO_2) vs CO_2 activation angle, α. CO_2 activation is promoted by electron transfers (ET) (dark red and orange) as well as negatively charged tethering sites, such as S. Adapted from Ref.[61].

6.3 CO_2- and H-mediated pathways to formate

By tethering CO_2, sulfur opens a new reaction pathway which is uniquely selective toward formate, **Figure 6.4a**. If a proton adsorbs on a vicinal Cu site *via* a proton-coupled electron transfer, it can further react with the CO_2 tethered by the chalcogen through a transition state. The C-S bond breaking and the consequent C-H formation presents an activation barrier of 1.02 eV, which leads to the production of formate. The strong tethering action of the chalcogen inhibits CO formation as well, since this product would need the simultaneous breaking of C-S and C-O bonds. Furthermore, since the electronic density is localized on the chalcogen adatoms, CO_2 adsorption on vicinal Cu atom is destabilized by 0.53 (first neighboring), 0.27 (second neighboring) and 0.12 eV (third neighboring).[61] Hence, chalcogen adatoms hinder the unselective reduction pathways on copper caused by multiple CO_2 adsorption conformations discussed earlier.

Secondly, $S^{\delta-}$ sites can as well adsorb protons, thus leading to the formation of surface hydrosulfides $S^{\delta-}H$, **Figure 6.4b**. These surface hydrides can react either with a proton or a CO_2 molecule in solution *via* Heyrovský-like mechanisms. The first chemical reaction accounts for Hydrogen Evolution Reaction, but at high overpotential mass transfer limits hydrogen formation.[18,20,147,233–235] The second chemical reaction leads to the direct formation of formate, thus it justifies the outstanding performance of Cu-S catalyst through a second selective path toward the desired product.

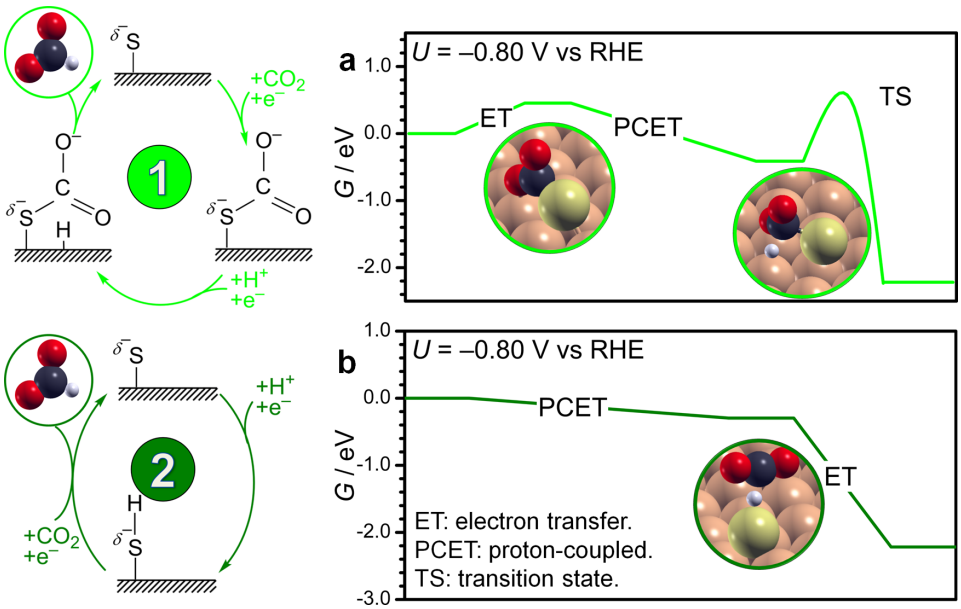

Figure 6.4: Sulfur opens two selective paths toward formate, **a**, tethering CO_2 (light green) and **b**, through a hydride (dark green) which mediates an Heyrovský-like mechanism. Sulfur acts as a promotor due to his partial negative charge, δ^-, which scales with the applied potential U. These energy diagrams account for S adatom on the most stable Cu facet, Cu(111).[222–224] Adsorption energies on Cu(100), Cu(110), Cu(211) scale accordingly. Adapted from Ref.[61].

6.4 Surface basicity drives formate production

The preeminence of sulfur among the chalcogens assessed is motivated by its intermediate basicity, property which can be described by the p band center of the atom, **Figure 6.5**.[236] More basic chalcogen adatoms bind both the CO_2 and H strongly (blue), thus they promote the formation of adsorbed HCO_2^- through the two reaction pathways reported in **Figure 6.4**. Moreover, HCO_2^- binding energy decreases for higher basicity (green), thus formate production is enhanced. Chalcogen basicity influences as well its stability on the Cu surfaces (brown shadow in **Figure 6.5**): more basic chalcogen modifiers, as oxygen, present lower covalency of the adatom-Cu bond, thus lower stability on the surface. Thus, the best performing chalcogen is sulfur, since it exhibits intermediate CO_2 / H adsorption and formate desorption energies and it is stable under reaction conditions. Hydrogen Evolution Reaction on vicinal Cu sites is not promoted by chalcogen basicity as described by a constant *H adsorption (gray), result which explains

the almost constant Faradaic efficiency toward H_2 production, **Figure 6.2**.

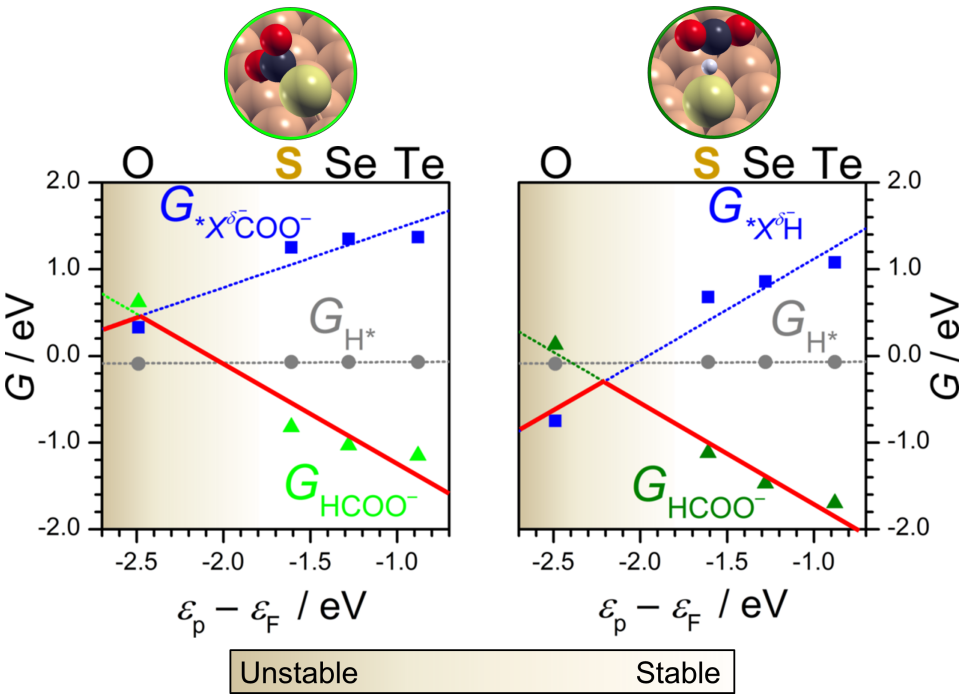

Figure 6.5: The experimental volcano trend reported in **Figure 6.2** is rationalized by the influence of chalcogen basicity (p band center) on the thermodynamics of the main reaction intermediates: $*X^{\delta-}CO_2$ (blue, left), $*X^{\delta-}H$ (blue, right), *H (hydrogen on a neighboring Cu, gray) adsorption energies and $HCOO^-$ formation energy (green, left and right), where X stands for the chalcogen adatom. Adapted from Ref.[61].

6.5 Conclusions

In this project I applied Density Functional Theory to explain the outstanding performance of sulfur in the electrochemical conversion of CO_2 toward formate on chalcogen modified copper catalysts. Since experimental results indicate that tiny amounts of sulfur change completely the product distribution on copper surfaces, I employed as models the most stable system: Cu facets with the chalcogen as an adatom. Subsurface configurations and substitution of copper vacancies were assessed and found not stable at the negative potential employed. Given its partial negative charge, the chalcogen atom acts as a tethering center for CO_2 and H, hence it promotes two alternative reaction pathways. Formate can be produced *via* protonation of

the adsorbed CO_2 or by an Heyrovský-like coupling of surface hydride and a CO_2 molecule from solution, **Figure 6.3**. Chalcogens hinder CO_2 adsorption on the vicinal Cu sites as well, thus they inhibit reaction pathways toward CO or methane, whilst mass transfer phenomena limits hydrogen evolution. The preeminence of sulfur among the chalcogens group is determined by its p band center, which is a proxy for its basicity. This element exhibits a strong tethering of the main reaction intermediates, such as CO_2 and H, however it yet allows an exothermic desorption of the final product, formate. Additionally, sulfur intermediate basicity makes Cu-S bond more covalent, thus stabilizing the adatom under working conditions. H adsorption on Cu sites is independent from chalcogen basicity, thus it leads to a constant H_2 production among the series of chalcogens modifiers.

To summarize, I developed a chemical descriptor, the modifier basicity, to model the performance of chalcogen modified copper. Following the guidelines developed in this chapter, experimental syntheses which employ alternatives modifiers could lead to catalysts with higher selectivity to a desired product.

Chapter 7

Conclusions

In this thesis I modeled electrochemical CO_2 reduction on copper catalysts with a bottom-up approach. This chemical process is basic for a sustainable development, since CO_2 and electricity are converted to high valuable chemicals used for energy storage and as feedstock for plastics (**Chapter 1**). Through state-of-the-art DFT simulations and basic electrochemical concepts (**Chapter 2**), I investigated systems with an increasing degree of complexity. I started employing simple models such as crystalline copper facets (**Chapter 3**), which were then improved by applying a negative electrostatic field at the electrode surface and studying the surface reconstruction (**Chapter 4**). An alternative approach for assessing the polarization-driven surface nanostructuring was proposed through the application of Ab Initio Molecular Dynamics simulations on oxide-derived copper catalysts (**Chapter 5**). Finally, I unraveled the role of a chalcogen modifier as a tethering site to promote formate production on copper-based materials (**Chapter 6**). Overall, this work investigated and highlighted the effect of reduction potential, surface polarization, modifiers, cation, and solvation.

- In **Chapter 3** I reported the state-of-the-art experimental results for CO_2 reduction on copper foils and copper nanoparticles. These results were reproduced following the current theoretical understanding and methods. Polycrystalline Cu accounts for different CO_2 reduction products, which depend on the most stable facets as reported by Hori.[7] Cu(111) is selective toward methane, whilst Cu(100) allows the production of C_{2+} products, mostly ethylene. Small copper nanoparticles generate methane, whilst larger diameter leads to an increase in CO production. Formate and formic acid usually account for 10-20% of the total Faradaic efficiency. Assessing Cu(111) and Cu(100) facets, I confirmed that methane production is thermodynamically favored on the close-packed domains, whereas the (100) facet enable the CO-CO

dimerization step and it opens the pathway to C_{2+} products.

- In **Chapter 4** I developed a model for assessing polycrystalline Cu surface reconstruction under electrochemical conditions and in absence of reaction intermediates. Electrostatic surface polarization at high negative potential drives the sequential evolution of polycrystalline Cu to Cu(100) and eventually to nanocuboids. For fcc metals, open facets have high surface energy since they are less coordinated than the (111) surface. Under negative potentials, close-packed facets experience repulsion between surface atoms, which lead to their destabilization and consequential reconstruction toward open configurations. Under prolonged polarization, the abundance of defective sites increases. Following the theoretical guidelines developed, I built an electrochemical fuel cell with a Gas Diffusion Electrode which employed a CuO-derived catalyst. This cell accounted for a stable electrochemical CO_2 reduction to ethylene with partial current density higher than 200 mA cm^{-2} and FE around 60%.

- In **Chapter 5** I modeled oxide-derived copper catalysts with oxygen-depleted systems derived from pristine $Cu_2O(111)/Cu(111)$ structures and I studied surface reconstruction upon Ab Initio Molecular Dynamics. The main Cu species detected were classified as metallic Cu^0, polarized $Cu^{\delta+}$, and oxidic Cu^+ depending on their coordination to residual oxygen, respectively 0, 1, and 2. The local structural configurations of these species lead to recurrent surface ensembles, reconstructed crystalline Cu facets, defects, and near-surface oxygens. Finally, I demonstrated that polarized $Cu^{\delta+}$ sites and large active surface area upon reconstruction promote CO_2 activity, whereas oxygen triggers C_{2+} production. In fact, near-surface oxygens stabilize the CO-CO dimer as a deprotonated glyoxylate, whose formation is thermodynamically and kinetically favorable. This chemical species is here proposed for the first time as the key intermediate for ethylene and C_{2+} oxygenates production on OD-Cu.

- In **Chapter 6** I unraveled the promotion of CO_2 electroreduction to formate via sulfur modification of copper nanoparticles. Sulfur, modeled as an adatom on the Cu surface, promotes two direct pathways toward formate through either a CO_2 or a H intermediate. As for the CO_2-mediated pathway, sulfur tethers CO_2, which then, together with a proton, evolves as formate through a transition state. As for the hydride-mediated mechanism, given its localized negative charge, the adatom can adsorb a proton, which evolves to formate upon coupling with a CO_2 molecule from the solution *via* a Heyrosvký-like

mechanism. Among the chalcogen group, sulfur present the best performance due to its intermediate basicity, which we propose as a good descriptor for formate selectivity.

Appendices

UNIVERSITAT ROVIRA I VIRGILI
THEORETICAL MODELS FOR THE ELECTROCHEMICAL REDUCTION OF CO2 ON COPPER CATALYSTS UNDER WORKING CONDITIONS
Federico Dattila

Appendix A

Supplementary Methods

A.1 Estimation of $HCOO^-$ Gibbs free energy from Density Functional Theory principles

Since formate is a charged species, the direct estimation of G_{HCOO^-} from DFT is ill-defined. Thus, I obtained it from the DFT-calculated Gibbs free energies of formic acid, carbon dioxide, and hydrogen through the direct relation between K_{eq} and ΔG^0, **Equation A.4**, at equilibrium. G_{HCOO^-} can be calculated as a function of G_{HCOOH}, G_{H_2}, K_{eq}, and the applied potential, **Equation A.11**, introduced through the Computational Hydrogen Electrode approach,[65] **Equation A.9**. The scheme employed is reported in **Figure A.1**.

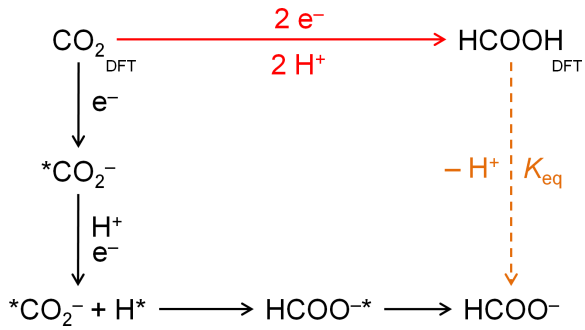

Figure A.1: Thermodynamic cycle to estimate formate Gibbs free energy from formate / formic acid equilibrium. In black the reaction pathway for CO_2 reduction to formate. In red the reaction pathway for CO_2 reduction to formic acid, which can be applied to evaluate G_{HCOOH}. In orange the chemical equilibrium reaction employed to derive G_{HCOO^-} from K_{eq}.

Formic acid / formate equilibrium Formic acid and formate are in equilibrium in aqueous solution, **Equation A.1**, and this reaction presents an equilibrium constant, K_{eq}, given by the reaction quotient, **Equation A.2**. The thermodynamics of this reaction is described by the reaction Gibbs free energy under standard conditions, ΔG^0, the equilibrium constant, and the temperature of the system T (in K), **Equation A.3**. By definition, the Gibbs free energy of a reaction at equilibrium is zero. Hence, the Gibbs free energy under standard conditions, ΔG^0, can be calculated from the reaction quotient, given by the reaction equilibrium constant, K_{eq}, **Equation A.4**. Therefore ΔG^0 can be expresses as a function of the Gibbs free energies of formate, formic acid, and proton, **Equation A.5**. By reversing **Equation A.5**, the Gibbs free energy for formate under standard conditions can be determined from formic acid and proton Gibbs free energies, **Equation A.6**.

$$\text{HCOOH} \rightleftharpoons \text{HCOO}^- + \text{H}^+ \tag{A.1}$$

$$K_{\text{eq}} = \frac{[\text{HCOO}^-][\text{H}^+]}{[\text{HCOOH}]} \tag{A.2}$$

$$\Delta G = \Delta G^0 + RT \ln\left(\frac{C_{\text{products}}}{C_{\text{reactants}}}\right) = \Delta G^0 + RT \ln(K_{\text{eq}}) \tag{A.3}$$

$$\text{At equilibrium } \Delta G = 0 \Longrightarrow \Delta G^0 = -RT \ln(K_{\text{eq}}) \tag{A.4}$$

$$\Delta G^0 = G^0_{\text{HCOO}^-} + G^0_{\text{H}^+} - G^0_{\text{HCOOH}} \tag{A.5}$$

$$\begin{aligned} -RT \ln(K_{\text{eq}}) &= G^0_{\text{HCOO}^-} + G^0_{\text{H}^+} - G^0_{\text{HCOOH}} \\ G^0_{\text{HCOO}^-} &= G^0_{\text{HCOOH}} - G^0_{\text{H}^+} - RT \ln(K_{\text{eq}}) \end{aligned} \tag{A.6}$$

Formate Gibbs free energy Given the electrochemical reduction of CO_2 to formic acid, **Equation A.7**, the Gibbs free energy to generate formic acid, G_{HCOOH}, can be calculated as **Equation A.8** from the Gibbs free energy of carbon dioxide, formic acid ($\bar{G}_{\text{HCOOH}}$), and proton. By applying the CHE approach,[65] it is possible to evaluate the Gibbs free energy under standard conditions of a proton in solution from the hydrogen Gibbs free energy calculated by DFT, $G_{\text{H}_2,\text{DFT}}$, **Equation A.9**. Thus, the Gibbs free energy to produce formic acid from CO_2 can be estimated by Density

Functional Theory calculations, so that **Equation A.8** can be rewritten as **Equation A.10**, where $G_{i,\mathrm{DFT}}$ is the Gibbs free energy of the molecule i in gas phase. Thus, it is possible to obtain formate Gibbs free energy under standard conditions by replacing the formic acid Gibbs free energy term of **Equation A.6** by its DFT definition, **Equation A.10**. The result allows to calculate formate Gibbs free energy as a function of CO_2, H_2 and HCOOH DFT Gibbs free energies, applied potential U, and equilibrium constant K_{eq}, **Equation A.11**.

$$\mathrm{CO_2} + 2\,\mathrm{H^+} + 2\,\mathrm{e^-} \rightleftharpoons \mathrm{HCOOH} \tag{A.7}$$

$$G_{\mathrm{HCOOH}} = \bar{G}_{\mathrm{HCOOH}} - G_{\mathrm{CO_2}} - 2G_{\mathrm{H^+}} \tag{A.8}$$

$$G_{\mathrm{H^+}} = \frac{1}{2} G_{\mathrm{H_2,DFT}} \tag{A.9}$$

$$G^0_{\mathrm{HCOOH}} = \bar{G}^0_{\mathrm{HCOOH,DFT}} - G^0_{\mathrm{CO_2,DFT}} - G^0_{\mathrm{H_2,DFT}} + 2|e^-|U \tag{A.10}$$

$$G^0_{\mathrm{HCOO^-}} = \bar{G}^0_{\mathrm{HCOOH,DFT}} - G^0_{\mathrm{CO_2,DFT}} - \frac{3}{2} G^0_{\mathrm{H_2,DFT}} - RT\ln(K_{\mathrm{eq}}) + 2|e^-|U \tag{A.11}$$

A.2 Cation effect

Larger alkali cations promote CO_2 reduction to formate on sulfur modified copper, **Figure A.2a**.[61] Whilst for the $LiHCO_3$ electrolyte hydrogen is the main reaction product, the use of Cesium allows to revert the trend and leads to a more than double partial current density toward formate. The so-called cation effect is well-known in literature,[237] and it has been related to modification of surface pH due to local hydrolysis of cation solvation shell[238] or local induced electrostatic field on the surface.[20,59,155] Our calculations support the electrostatic effects hypothesis. However, they suggest that the stabilization is driven by chemical bonds between cation and key reaction intermediates (Ref.[17]) rather than effect of average electrostatic field. By being partially desolvated, cation species can interact with negatively charged intermediates, therefore stabilizing them close to the electrode surface and enabling the reduction reaction. Since smaller alkali cations present a larger solvation energy, their interaction with HCO_2^-

is hindered, therefore causing the low CO_2 reduction selectivity detected, **Figure A.2b**. Instead, larger cations akin Cs^+ are more prone to decoordinate water molecules and consequent chemical interaction, thus motivating the selectivity shift toward CO_2 reduction products.

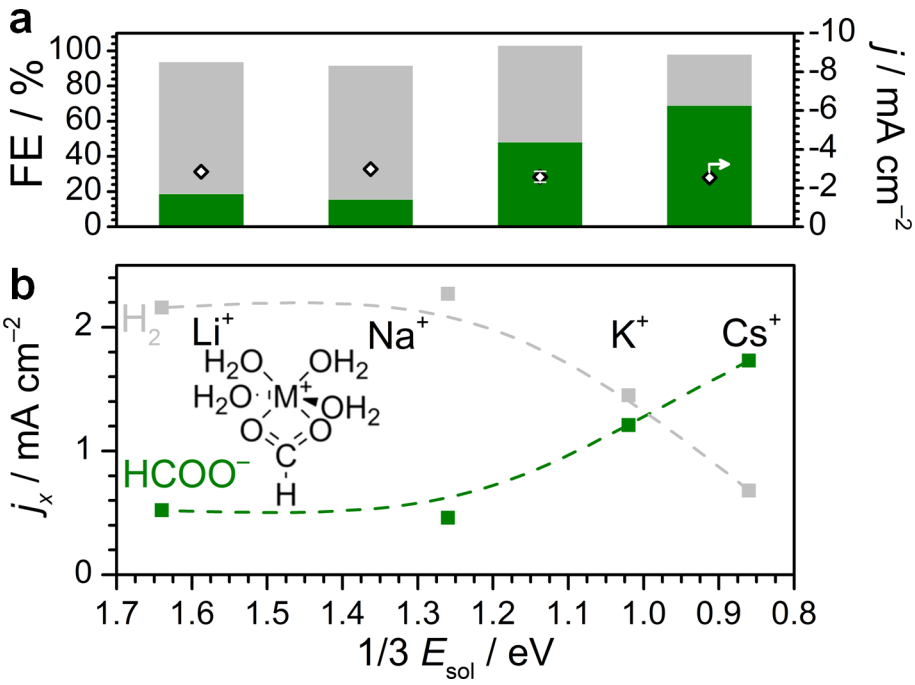

Figure A.2: Cation effect on formate selectivity for sulfur modified copper catalysts.[61] **a**, Competition between Hydrogen Evolution Reaction and CO_2 reduction to formate characterized by chronoamperometry at -0.6 V vs RHE for 1.5 h in CO_2-saturared MHCO$_3$ electrolyte with M= Li, Na, K, and Cs. **b**, H_2 (gray) and $HCOO^-$ (green) partial current density versus cation Gibbs free energy of solvation. As a first order approximation, solvated cation is considered coordinated to six water molecules, thus it can stabilize HCO_2^- intermediate by decoordinating two water molecules from its first solvation shell.

Appendix B

Supplementary Data

B.1 CO_2 reduction to C_{2+} on copper-based catalysts

Table B.1: **Main C_{2+} products for CO_2 reduction on copper-based catalysts.** Faradaic efficiencies toward ethylene, ethanol, and *n*-propanol for different classes of copper-based catalysts. CV-treated: anodized and/or reduced Cu; Cu_xO_y: pristine oxide-derived catalysts. Plasma: O_2/H_2 plasma-treated Cu; Cu-Ag: bimetallic Cu-Ag catalysts; p-doped: Cu catalysts modified with an electron acceptor; Ligands: ligands-modified Cu. More details are provided in **Table B.2**, **Appendix B.1**.

	Ethylene	EtOH	*n*-PrOH
CV-treated	45%;[138] 40%;[139] 38%;[140] 28%;[141] 25%;[142] 20%;[143]	–	8%;[144]
Cu_xO_y	72%;[239] 70%;[198] 59%;[240] 50%;[241] 48%;[242] 45%;[197] 43%;[177] 39%;[171] 36%;[243] 32%;[244] 20%;[245]	45%;[50] 19%;[171] 12%[177]	23%;[178] 5%;[177]
Plasma	60%;[167]	–	–
Cu-Ag	15%[210]	41%;[208] 35%;[209] 17%;[210]	33%;[205]
p-doped	80%;[246] 51%;[247] 50%;[248]	91%;[200] 52%;[249] 29%;[250] 14%[247]	20%;[251]
Ligands	72%;[252]	41%;[253]	5%;[254]

Table B.2: Experimental studies on copper-based catalysts. U / V_{RHE}, where V_{RHE} = V vs RHE; observation: product (Faradaic efficiency). ERD-Cu: electro-redeposited Cu; Oxi-Cu: oxidized Cu; OD-Cu: oxide-derived Cu; PT: Plasma-treated Cu; Lig-Cu: ligand-modified Cu; NPs: nanoparticles; CV-Cu: cyclic voltammetry-treated Cu; MOF: Metal-organic framework; NCs: nanocrystals; LDH: layered double hydroxides; ED-Cu: electrodeposited Cu; NF: nanoflowers.

Ref.	Catalyst	U (V_{RHE})	Observation
145	Cu-CO_2 ERD	−0.70	C_{2+} (90%)
255	CuO_x	−0.90	C_{2+} (80%).
51	Oxi-Cu	−1.00	C_{2+} (76%)
256	Au/Cu_2O	−0.50	C_{2+} (70%)
257	CuO on Cu_3N	−0.95	C_{2+} (64%)
185	OD-Cu	−1.00	C_{2+} (60%)
225	OD-Cu	−0.40	C_{2+} (50%)
258	Cu_2S	−0.95	C_{2+} (32%)
259	PT Cu	−1.00	C_2 (69%)
246	Cu-B	−1.10	C_2H_4 (80%)
239	Cu_2O	−0.52	C_2H_4 (72%)
252	Lig-Cu	−0.84	C_2H_4 (72%)
260	Cu	−0.65	C_2H_4 (70%)
198	Cu/Cu_2O	−1.70	C_2H_4 (70%)
167	PT Cu	−0.90	C_2H_4 (60%)
240	Cu_2O NPs	−1.10	C_2H_4 (59%)
247	Cu-Br	−1.10	C_2H_4 (51%)
241	OD-Cu	−1.00	C_2H_4 (50%)
261	Cu	−1.30	C_2H_4 (50%)
248	Cu-Cl	−1.80	C_2H_4 (50%)
242	Cu_m-CeO_x	−1.10	C_2H_4 (48%)
197	Cu_4O	−1.00	C_2H_4 (45%)
138	CV-Cu	−1.00	C_2H_4 (45%)
262	Cu on MOF	−1.07	C_2H_4 (45%)
177	OD-Cu	−0.98	C_2H_4 (43%)
47	Cu NCs	−1.10	C_2H_4 (41%)
139	ERD-Cu	−1.20	C_2H_4 (40%)
171	CuO	−0.99	C_2H_4 (39%)
140	OD-Cu	−1.08	C_2H_4 (38%)
243	Cu-Cu_2O LDH	−1.10	C_2H_4 (36%)
244	OD-Cu	−0.98	C_2H_4 (32%)
141	ED-Cu	−1.10	C_2H_4 (28%)

Ref.	Catalyst	U / V_{RHE}	Observation
142	ED-Cu_2O	−1.20	C_2H_4 (25%)
143	ED-Cu	−1.00	C_2H_4 (20%)
245	OD-Cu	−1.10	C_2H_4 (20%)
129	Cu	−1.10	C_2H_4 (20%)
210	OD-Cu/Ag	−1.10	C_2H_4 (15%)
200	Cu/C	−0.70	C_2H_5OH (91%)
263	NF Cu	−0.33	C_2H_5OH (60%)
249	N-C/Cu	−0.68	C_2H_5OH (52%)
50	OD-Cu NPs	−0.30	C_2H_5OH (45%)
208	Cu-Ag	−0.67	C_2H_5OH (41%)
253	Lig-Cu	−0.82	C_2H_5OH (41%)
209	Cu-Ag	−1.20	C_2H_5OH (35%)
250	Cu-N	−0.50	C_2H_5OH (29%)
171	CuO	−0.99	C_2H_5OH (19%)
210	OD-Cu/Ag	−1.10	C_2H_5OH (17%)
247	Cu-I	−1.09	C_2H_5OH (14%)
177	OD-Cu	−0.98	C_2H_5OH (12%)
205	Cu-Ag	−0.46	n-PrOH (33%)
178	OD-Cu	−0.47	n-PrOH (23%)
251	Cu-I	−0.45	n-PrOH (20%)
144	ED-Cu	−0.95	n-PrOH (8%)
254	Lig-Cu	−0.83	n-PrOH (5%)
177	OD-Cu	−0.98	n-PrOH (5%)
261	Cu	−1.30	C_2H_6 (60%)
143	ED-Cu	−0.60	C_2H_6 (40%)
250	Cu-N	−0.50	Acetate (35%)
129	Cu	−1.10	CH_4 (57%)
138	CV-Cu	−1.00	CH_4 (40%)
138	ED-Cu	−1.00	CH_4 (30%)
129	Cu NPs	−1.10	CO (25%)
264	GO-Cu_xO	−0.80	HCOOH (81%)
129	Cu NPs	−1.10	H_2 (65%)
138	ED-Cu	−1.00	H_2 (55%)
138	Cu	−1.00	H_2 (50%)

B.2 Polarization-driven surface reconstruction

To investigate polycrystalline copper reconstruction, three models were employed, respectively Cu(110) 1×1, Cu(100) 1×1, and Cu(111) 1×1. To improve the accuracy in the determination of the surface energy of each

system, 17 valence electrons were considered for the copper atoms ($3p^6$ orbitals included). I modeled copper facets as symmetric slabs, presenting 13 Cu layers, whose 2 outermost per each side were relaxed. I chose a vacuum between surface terminations of 30 Å to ensure the lack of periodic interaction in the z-direction. By construction, the slabs were equivalent to parallel plate capacitors, with area A, dielectric thickness $d = 30$ Å, and dielectric permittivity ϵ_0. A electric field was applied between the surfaces by including an artificial dipole correction.[89,265]

To simulate graphene-covered copper, a graphene layer was deposited on 5×1 Cu(100) and 1×1 Cu(111) asymmetric systems, composed of 7 Cu layers with the 2 outermost relaxed. I included dispersion through the DFT-D2 method[88,121] and a dipole correction was applied to remove artifacts generated by the asymmetry of these models.[124]

B.3 Ethylene production on oxide-derived copper catalysts

B.3.1 Experimental details

Catalyst synthesis. The synthesis was a simple water-based precipitation,[161] followed by calcination.[162] We added 2 mmol of $CuCl_2 \cdot 2H_2O$ to 200 mL of deionized water under vigorous magnetic stirring. After this, we added 4 mL of 1M NaOH solution dropwise, until a light blue copper hydroxide precipitate appeared. The $Cu(OH)_2$ precipitate was then centrifuged and cleaned with deionized water for 5 times before being transferred to an oven at 200 °C for 2 hours to enable hydroxide decomposition to CuO.

Ink formulation. The as prepared CuO catalyst was suspended in isopropyl alcohol and an amount of Nafion^{TM} solution corresponding to 20 wt% of the final weight was added to the dispersion. In both cases we initially suspended CuO powder in the solvent by sonication, then we added the ionomer solution under magnetic stirring, and we sonicated again the ink until homogeneity was not obtained. We then airbrushed the ink on a Gas Diffusion Layer (GDL) suitable for flow-through operation, made in house following a patented procedure.[165]

Electrolysis. The galvanostatic electrolysis was carried out in a commercial, two-compartment, 10.5 cm^2 GDE flow cell (ElectroCell Micro Flow Cell) operated in a flow-through configuration. Anode and cathode were

separated by a reinforced Nafion^{TM} membrane N324. A 0.5M H_2SO_4 solution was employed as anolyte and Oxygen Evolution Reaction occurred at the anode catalyst on a Ti current collector coated with Ir/RuO_2. 0.5M $KHCO_3$ was used as catholyte and the cathode consisted of the CuO-coated GDE. The electrolyte solutions were circulated in both anodic and cathodic compartments at a flow rate of 50 ml min^{-1} with a peristaltic pump, and CO_2 was fed through the GDE. Before use, $KHCO_3$ was pre-electrolyzed for several hours with a graphite rod as the anode and carbon felt as the cathode at a current density of 2 mA cm^{-2} to remove metallic impurities. The resulting cell was powered and operated at different geometrical current densities. Gas chromatography was performed on a Varian 4900 micro GC connected to the catholyte column and equipped with four modules: CO_x module, MS5 (mol. sieve) module, PPQ (poraplotQ) module and 52C WAX module. Liquid samples were analyzed with an Agilent 1260 HPLC with aqueous 5 mM H_2SO_4 as eluent.

B.3.2 Product distribution on CuO-derived catalysts

Table B.3: **Faradaic efficiencies for CuO-based catalyst.** CO_2-saturated 0.5 $KHCO_3$ eletrolyte, catalyst loading: 0.67 mg cm^{-2}, CO_2 flow: 50 ml min^{-1}.

j / mA cm^{-2}	C_2H_4	CO	$HCOO^-$	H_2	Total
100	16	42	15	19	92
200	32	27	14	15	88
300	44	17	8	16	85
400	50	11	4	21	86

Table B.4: **Faradaic efficiencies for CuO-based catalyst.** CO_2-saturated 0.5 $KHCO_3$ eletrolyte, catalyst loading: 0.84 mg cm^{-2}, CO_2 flow: 75 ml min^{-1}.

j / mA cm^{-2}	C_2H_4	CO	$HCOO^-$	H_2	Total
100	26	22	4	28	80
200	42	15	4	21	82
300	41	11	4	23	79
400	29	10	4	44	87

Table B.5: **Faradaic efficiencies for CuO-based catalyst.** CO_2-saturated 0.5 $KHCO_3$ eletrolyte, catalyst loading: 0.84 mg cm^{-2}, CO_2 flow: 100 ml min^{-1}.

j / mA cm^{-2}	C_2H_4	CO	$HCOO^-$	H_2	Total
100	33	27	4	31	95
200	43	16	4	22	85
300	45	15	4	31	95
400	35	15	4	41	95

Bibliography

[1] Parmesan, C.; Yohe, G. A globally coherent fingerprint of climate change impacts across natural systems, *Nature* **2003,** *421,* 37–42.

[2] European Commission, *A European Green Deal*, `https://ec.europa.eu/info/strategy/priorities-2019-2024/european-green-deal_en`, 2020 Online; accessed 25 October 2020.

[3] He, J.; Janáky, C. Recent advances in solar-driven carbon dioxide conversion: Expectations versus reality, *ACS Energy Lett.* **2020,** *5,* 1996–2014.

[4] Ciamician, G. The photochemistry of the future, *Science* **1912,** *36,* 385–394.

[5] Teeter, T. E.; Van Rysselberghe, P. Reduction of carbon dioxide on mercury cathodes, *J. Chem. Phys.* **1954,** *22,* 759–760.

[6] Hori, Y.; Kikuchi, K.; Suzuki, S. Production of CO and CH_4 in electrochemical reduction of CO_2 at metal electrodes in aqueous hydrogencarbonate solution, *Chem. Lett.* **1985,** *14,* 1695–1698.

[7] Hori, Y.; Takahashi, I.; Koga, O.; Hoshi, N. Electrochemical reduction of carbon dioxide at various series of copper single crystal electrodes, *J. Mol. Catal. Chem.* **2003,** *199,* 39–47.

[8] Kuhl, K. P.; Cave, E. R.; Abram, D. N.; Jaramillo, T. F. New insights into the electrochemical reduction of carbon dioxide on metallic copper surfaces, *Energy Environ. Sci.* **2012,** *5,* 7050–7059.

[9] Peterson, A. A.; Abild-Pedersen, F.; Studt, F.; Rossmeisl, J.; Nørskov, J. K. How copper catalyzes the electroreduction of carbon dioxide into hydrocarbon fuels, *Energy Environ. Sci.* **2010,** *3,* 1311–1315.

[10] Bagger, A.; Ju, W.; Varela, A. S.; Strasser, P.; Rossmeisl, J. Electrochemical CO_2 reduction: A classification problem, *ChemPhysChem* **2017,** *18,* 3266–3273.

[11] Bagger, A.; Ju, W.; Varela, A. S.; Strasser, P.; Rossmeisl, J. Electrochemical CO_2 reduction: Classifying Cu facets, *ACS Catal.* **2019,** *9,* 7894–7899.

[12] Nitopi, S.; Bertheussen, E.; Scott, S. B.; Liu, X.; Engstfeld, A. K.; Horch, S.; Seger, B.; Stephens, I. E. L.; Chan, K.; Hahn, C.; Nørskov, J. K.; Jaramillo, T. F.; Chorkendorff, I. Progress and perspectives of electrochemical CO_2 reduction on copper in aqueous electrolyte, *Chem. Rev.* **2019,** *119,* 7610–7672.

[13] Chen, C.; Kotyk, J. F. K.; Sheehan, S. W. Progress toward commercial application of electrochemical carbon dioxide reduction, *Chem* **2018,** *4,* 2571–2586.

[14] De Luna, P.; Hahn, C.; Higgins, D.; Jaffer, S. A.; Jaramillo, T. F.; Sargent, E. H. What would it take for renewably powered electrosynthesis to displace petrochemical processes?, *Science* **2019,** *364,* eaav3506.

[15] Hori, Y.; Kikuchi, K.; Murata, A.; Suzuki, S. Production of methane and ethylene in electrochemical reduction of carbon dioxide at copper electrode in aqueous hydrogencarbonate solution, *Chem. Lett.* **1986,** *15,* 897–898.

[16] Kim, Y. G.; Baricuatro, J. H.; Javier, A.; Gregoire, J. M.; Soriaga, M. P. The evolution of the polycrystalline copper surface, first to Cu(111) and then to Cu(100), at a fixed CO_2RR potential: A study by *Operando* EC-STM, *Langmuir* **2014,** *30,* 15053–15056.

[17] Pérez-Gallent, E.; Figueiredo, M. C.; Calle-Vallejo, F.; Koper, M. T. M. Spectroscopic observation of a hydrogenated CO dimer intermediate during CO reduction on Cu(100) electrodes, *Angew. Chem. Int. Ed.* **2017,** *56,* 3621–3624.

[18] Birdja, Y. Y.; Pérez-Gallent, E.; Figueiredo, M. C.; Göttle, A. J.; Calle-Vallejo, F.; Koper, M. T. M. Advances and challenges in understanding the electrocatalytic conversion of carbon dioxide to fuels, *Nat. Energy* **2019,** *4,* 732–745.

[19] Veenstra, F. L. P.; Ackerl, N.; Martín, A. J.; Pérez-Ramírez, J. Laser-microstructured copper reveals selectivity patterns in the electrocatalytic reduction of CO_2, *Chem* **2020,** *6,* 1707–1722.

[20] Ringe, S.; Morales-Guio, C. G.; Chen, L. D.; Fields, M.; Jaramillo, T. F.; Hahn, C.; Chan, K. Double layer charging driven carbon dioxide adsorption limits the rate of electrochemical carbon dioxide reduction on Gold, *Nat. Commun.* **2020,** *11,* 33.

[21] Bohra, D.; Chaudhry, J. H.; Burdyny, T.; Pidko, E. A.; Smith, W. A. Modeling the electrical double layer to understand the reaction environment in a CO_2 electrocatalytic system, *Energy Environ. Sci.* **2019,** *12,* 3380–3389.

[22] Zhang, B. A.; Ozel, T.; Elias, J. S.; Costentin, C.; Nocera, D. G. Interplay of homogeneous reactions, mass transport, and kinetics in determining selectivity of the reduction of CO_2 on gold electrodes, *ACS Cent. Sci.* **2019,** *5,* 1097–1105.

[23] Goyal, A.; Marcandalli, G.; Mints, V. A.; Koper, M. T. M. Competition between CO_2 reduction and hydrogen evolution on a gold electrode under well-defined mass transport conditions, *J. Am. Chem. Soc.* **2020,** *142,* 4154–4161.

[24] International Energy Agency, *Global energy-related CO_2 emissions, 1900-2020, IEA, Paris*, `https://www.iea.org/data-and-statistics/charts/global-energy-related-co2-emissions-1900-2020`, 2020 Online; accessed 25 October 2020.

[25] Our World in Data, *Annual CO_2 emissions*, `https://ourworldindata.org/grapher/annual-co2-emissions-per-country`, 2020 Online; accessed 25 October 2020.

[26] Our World in Data, *Population, 1800 to 2019*, `https://ourworldindata.org/grapher/population`, 2020 Online; accessed 25 October 2020.

[27] Our World in Data, *GDP per capita, 1870 to 2016*, `https://ourworldindata.org/grapher/average-real-gdp-per-capita-across-countries-and-regions`, 2020 Online; accessed 25 October 2020.

[28] International Energy Agency, *Data and statistics*, `https://www.iea.org/data-and-statistics`, 2020 Online; accessed 25 October 2020.

[29] Our World in Data, *Access to electricity vs. GDP per capita, 2016*, `https://ourworldindata.org/grapher/access-to-electricity-vs-gdp-per-capita`, 2020 Online; accessed 25 October 2020.

[30] V-Dem Institute, *About V-Dem*, https://www.v-dem.net/en/about/about-v-dem/, 2020 Online; accessed 25 October 2020.

[31] Our World in Data, *V-Dem Liberal democracy index, 2017*, https://ourworldindata.org/grapher/v-dem-liberal-democracy-index, 2020 Online; accessed 25 October 2020.

[32] U.S. Energy Information Administration, *Petroleum and other liquids*, https://www.eia.gov/international/data/world/petroleum-and-other-liquids/annual-crude-and-lease-condensate-reserves, 2020 Online; accessed 25 October 2020.

[33] Pretis, F.; Schwarz, M.; Tang, K.; Haustein, K.; Allen, M. R. Uncertain impacts on economic growth when stabilizing global temperatures at 1.5°C or 2°C warming, *Phil. Trans. R. Soc. A* **2018,** *376,* 20160460.

[34] Ciscar, J. C.; Iglesias, A.; Feyen, L.; Szabó, L.; Van Regemorter, D.; Amelung, B.; Nicholls, R.; Watkiss, P.; Christensen, O. B.; Dankers, R.; Garrote, L.; Goodess, C. M.; Hunt, A.; Moreno, A.; Richards, J.; Soria, A. Physical and economic consequences of climate change in Europe, *Proc. Natl. Acad. Sci. U.S.A.* **2011,** *108,* 2678–2683.

[35] Intergovernmental Panel on Climate Change, *IPCC, 2014: Climate Change 2014: Synthesis Report. Contribution of Working Groups I, II and III to the Fifth Assessment Report of the Intergovernmental Panel on Climate Change;* IPCC, Geneva, Switzerland: 2014.

[36] International Energy Agency, *Share of renewables in power generation in the Sustainable Development Scenario, 2000-2030*, https://www.iea.org/data-and-statistics/charts, 2020 Online; accessed 25 October 2020.

[37] Our World in Data, *Solar PV module prices*, https://ourworldindata.org/grapher/solar-pv-prices, 2020 Online; accessed 25 October 2020.

[38] International Energy Agency, *World Energy Outlook 2020;* IEA, Paris, France: 2020.

[39] Jurasz, J.; Canales, F. A.; Kies, A.; Guezgouz, M.; Beluco, A. A review on the complementarity of renewable energy sources: Concept, metrics, application and future research directions, *Sol. Energy* **2020,** *195,* 703–724.

[40] Chen, H.; Cong, T. N.; Yang, W.; Tan, C.; Li, Y.; Ding, Y. Progress in electrical energy storage system: A critical review, *Prog. Nat. Sci.* **2009,** *19,* 291–312.

[41] Ambrose, H.; Kendall, A. Understanding the future of lithium: Part 1, resource model, *J. Ind. Ecol.* **2020,** *24,* 80–89.

[42] Raciti, D.; Wang, C. Recent advances in CO_2 reduction electrocatalysis on copper, *ACS Energy Lett.* **2018,** *3,* 1545–1556.

[43] Majumdar, A.; Deutch, J. Research opportunities for CO_2 utilization and negative emissions at the gigatonne scale, *Joule* **2018,** *2,* 805–809.

[44] Geyer, R.; Jambeck, J. R.; Law, K. L. Production, use, and fate of all plastics ever made, *Sci. Adv.* **2017,** *3,* e1700782.

[45] Kniel, L.; Winter, O.; Stork, K. *Ethylene - A keystone to the petrochemical industry;* M. Dekker, New York: 1980.

[46] U.S. Energy Information Administration, *Short-term energy outlook*, https://www.eia.gov/outlooks/steo/report/electricity.php, 2020 Online; accessed 25 October 2020.

[47] Loiudice, A.; Lobaccaro, P.; Kamali, E. A.; Thao, T.; Huang, B. H.; Ager, J. W.; Buonsanti, R. Tailoring copper nanocrystals towards C_2 products in electrochemical CO_2 reduction, *Angew. Chem. Int. Ed.* **2016,** *55,* 5789–5792.

[48] Huang, J.; Hörmann, N.; Oveisi, E.; Loiudice, A.; De Gregorio, G. L.; Andreussi, O.; Marzari, N.; Buonsanti, R. Potential-induced nanoclustering of metallic catalysts during electrochemical CO_2 reduction, *Nat. Commun.* **2018,** *9,* 3117.

[49] Li, C. W.; Kanan, M. W. CO_2 reduction at low overpotential on Cu electrodes resulting from the reduction of thick Cu_2O films, *J. Am. Chem. Soc.* **2012,** *134,* 7231–7234.

[50] Li, C. W.; Ciston, J.; Kanan, M. W. Electroreduction of carbon monoxide to liquid fuel on oxide-derived nanocrystalline copper, *Nature* **2014,** *508,* 504–507.

[51] Arán-Ais, R. M.; Scholten, F.; Kunze, S.; Rizo, R.; Roldan Cuenya, B. The role of in situ generated morphological motifs and Cu(I) species in C_{2+} product selectivity during CO_2 pulsed electroreduction, *Nat. Energy* **2020,** *5,* 317–325.

[52] Larrazábal, G. O.; Martín, A. J.; Pérez-Ramírez, J. Building blocks for high performance in electrocatalytic CO_2 reduction: Materials, optimization strategies, and device engineering, *J. Phys. Chem. Lett.* **2017,** *8,* 3933–3944.

[53] Larrazábal, G. O.; Martín, A. J.; Krumeich, F.; Hauert, R.; Pérez-Ramírez, J. Solvothermally-prepared Cu_2O electrocatalysts for CO_2 reduction with tunable selectivity by the introduction of p-block elements, *ChemSusChem* **2017,** *10,* 1255–1265.

[54] Zeng, J.; Bejtka, K.; Ju, W.; Castellino, M.; Chiodoni, A.; Sacco, A.; Farkhondehfal, M. A.; Hernández, S.; Rentsch, D.; Battaglia, C.; Pirri, C. F. Advanced Cu-Sn foam for selectively converting CO_2 to CO in aqueous solution, *Appl. Catal. B Environ.* **2018,** *236,* 475–482.

[55] Shinagawa, T.; Larrazábal, G. O.; Martín, A. J.; Krumeich, F.; Pérez-Ramírez, J. Sulfur-modified copper catalysts for the electrochemical reduction of carbon dioxide to formate, *ACS Catal.* **2018,** *8,* 837–844.

[56] Larrazábal, G. O.; Martín, A. J.; Mitchell, S.; Hauert, R.; Pérez-Ramírez, J. Enhanced reduction of CO_2 to CO over Cu-In electrocatalysts: Catalyst evolution is the key, *ACS Catal.* **2016,** *6,* 6265–6274.

[57] Veenstra, F. L. P.; Martín, A. J.; Pérez-Ramírez, J. Nitride-derived Copper modified with indium as a selective and highly stable catalyst for the electroreduction of carbon dioxide, *ChemSusChem* **2019,** *12,* 3501–3508.

[58] Pérez-Gallent, E.; Marcandalli, G.; Figueiredo, M. C.; Calle-Vallejo, F.; Koper, M. T. M. Structure-and potential-dependent cation effects on CO reduction at copper single-crystal electrodes, *J. Am. Chem. Soc.* **2017,** *139,* 16412–16419.

[59] Resasco, J.; Chen, L. D.; Clark, E.; Tsai, C.; Hahn, C.; Jaramillo, T. F.; Chan, K.; Bell, A. T. Promoter effects of alkali metal cations on the electrochemical reduction of carbon dioxide, *J. Am. Chem. Soc.* **2017,** *139,* 11277–11287.

[60] Álvarez-Moreno, M.; de Graaf, C.; López, N.; Maseras, F.; Poblet, J. M.; Bo, C. Managing the computational chemistry big data problem: The ioChem-BD Platform, *J. Chem. Inf. Model.* **2015,** *55,* 95–103.

[61] García-Muelas, R.; Dattila, F.; Shinagawa, T.; Martín, A. J.; Pérez-Ramírez, J.; López, N. Origin of the selective electroreduction of carbon dioxide to formate by chalcogen modified copper, *J. Phys. Chem. Lett.* **2018,** *9,* 7153–7159.

[62] Dattila, F.; García-Muelas, R.; López, N. Active and selective ensembles in oxide-derived copper catalysts for CO_2 reduction, *ACS Energy Lett.* **2020,** *5,* 3176–3184.

[63] Gupta, N.; Gattrell, M.; MacDougall, B. Calculation for the cathode surface concentrations in the electrochemical reduction of CO_2 in $KHCO_3$ solutions, *J. Appl. Electrochem.* **2006,** *36,* 161–172.

[64] Ringe, S.; Clark, E. L.; Resasco, J.; Walton, A.; Seger, B.; Bell, A. T.; Chan, K. Understanding cation effects in electrochemical CO_2 reduction, *Energy Environ. Sci.* **2019,** *12,* 3001–3014.

[65] Nørskov, J. K.; Rossmeisl, J.; Logadottir, A.; Lindqvist, L.; Kitchin, J. R.; Bligaard, T.; Jónsson, H. Origin of the overpotential for oxygen reduction at a fuel-cell cathode, *J. Phys. Chem. B* **2004,** *108,* 17886–17892.

[66] Bard, A. J.; Faulkner, L. R. *Electrochemical methods: Fundamentals and applications, 2^{nd} edition;* John Wiley & Sons, Inc.: 2001.

[67] Shinagawa, T.; Garcia-Esparza, A. T.; Takanabe, K. Insight on Tafel slopes from a microkinetic analysis of aqueous electrocatalysis for energy conversion, *Sci. Rep.* **2015,** *5,* 13801.

[68] Mills, J. N.; McCrum, I. T.; Janik, M. J. Alkali cation specific adsorption onto fcc(111) transition metal electrodes, *Phys. Chem. Chem. Phys.* **2014,** *16,* 13699–13707.

[69] Rudnev, A. V.; Kiran, K.; Broekmann, P. Specific cation adsorption: Exploring synergistic effects on CO_2 electroreduction in ionic liquids, *ChemElectroChem* **2020,** *7,* 1897–1903.

[70] Bagger, A.; Arnarson, L.; Hansen, M. H.; Spohr, E.; Rossmeisl, J. Electrochemical CO reduction: A property of the electrochemical interface, *J. Am. Chem. Soc.* **2019,** *141,* 1506–1514.

[71] Newton, I. *The Principia: Mathematical principles of natural philosophy;* University of California Press: 1999.

[72] Sholl, D.; Steckel, J. A. *Density functional theory: A practical introduction;* John Wiley & Sons: 2009.

[73] von Laue, M. *Concerning the detection of X-ray interferences*, `https://www.nobelprize.org/prizes/physics/1914/laue/lecture/`, 1920 Online; accessed 13 July 2020.

[74] Compton, A. H. *X-rays as a branch of optics*, `https://www.nobelprize.org/prizes/physics/1927/compton/lecture/`, 1927 Online; accessed 13 July 2020.

[75] Einstein, A. Über einen die erzeugung und verwandlung des lichtes betreffenden heuristischen gesichtspunkt, *Ann. Phys.* **1905,** *322,* 132–148.

[76] Schrödinger, E. Quantisierung als eigenwertproblem, *Ann. Phys.* **1926,** *384,* 361–376.

[77] Born, M.; Oppenheimer, R. Zur quantentheorie der molekeln, *Ann. d. Phys.* **1927,** *389,* 457–484.

[78] Hohenberg, P.; Kohn, W. Inhomogeneous electron gas, *Phys. Rev.* **1964,** *136,* B864.

[79] Kohn, W.; Sham, L. J. Self-consistent equations including exchange and correlation effects, *Phys. Rev.* **1965,** *140,* A1133.

[80] Payne, M. C.; Teter, M. P.; Allan, D. C.; Arias, T. A.; Joannopoulos, J. D. Iterative minimization techniques for *ab initio* total-energy calculations: Molecular dynamics and conjugate gradients, *Rev. Mod. Phys.* **1992,** *64,* 1045.

[81] López, N.; Almora-Barrios, N.; Carchini, G.; Błoński, P.; Bellarosa, L.; García-Muelas, R.; Novell-Leruth, G.; García-Mota, M. State-of-the-art and challenges in theoretical simulations of heterogeneous catalysis at the microscopic level, *Catal. Sci. Technol.* **2012,** *2,* 2405–2417.

[82] Ceperley, D. M.; Alder, B. J. Ground state of the electron gas by a stochastic method, *Phys. Rev. Lett.* **1980,** *45,* 566.

[83] Jones, R. O.; Gunnarsson, O. The density functional formalism, its applications and prospects, *Rev. Mod. Phys.* **1989,** *61,* 689.

[84] Perdew, J. P.; Wang, Y. Accurate and simple analytic representation of the electron-gas correlation energy, *Phys. Rev. B* **1992,** *45,* 13244.

[85] Perdew, J. P.; Burke, K.; Ernzerhof, M. Generalized gradient approximation made simple, *Phys. Rev. Lett.* **1996,** *77,* 3865-3868.

[86] Carrasco, J.; Santra, B.; Klimeš, J.; Michaelides, A. To wet or not to wet? Dispersion forces tip the balance for water ice on metals, *Phys. Rev. Lett.* **2011,** *106,* 026101.

[87] Błonski, P.; López, N. On the adsorption of formaldehyde and methanol on a water-covered Pt(111): A DFT-D study, *J. Phys. Chem. C* **2012,** *116,* 15484–15492.

[88] Grimme, S. Semiempirical GGA-type density functional constructed with a long-range dispersion correction, *J. Comput. Chem.* **2006,** *27,* 1787–1799.

[89] Almora-Barrios, N.; Carchini, G.; Błoński, P.; López, N. Costless derivation of dispersion coefficients for metal surfaces, *J. Chem. Theory Comput.* **2014,** *10,* 5002–5009.

[90] Grimme, S. Accurate description of van der Waals complexes by density functional theory including empirical corrections, *J. Comput. Chem.* **2004,** *25,* 1463–1473.

[91] Grimme, S.; Antony, J.; Ehrlich, S.; Krieg, H. A consistent and accurate *ab initio* parametrization of density functional dispersion correction (DFT-D) for the 94 elements H-Pu, *J. Chem. Phys.* **2010,** *132,* 154104.

[92] Dion, M.; Rydberg, H.; Schröder, E.; Langreth, D. C.; Lundqvist, B. I. Van der Waals density functional for general geometries, *Phys. Rev. Lett.* **2004,** *92,* 246401.

[93] Lee, K.; Murray, É. D.; Kong, L.; Lundqvist, B. I.; Langreth, D. C. Higher-accuracy van der Waals density functional, *Phys. Rev. B* **2010,** *82,* 081101.

[94] Tkatchenko, A.; Scheffler, M. Accurate molecular van der Waals interactions from ground-state electron density and free-atom reference data, *Phys. Rev. Lett.* **2009,** *102,* 073005.

[95] Tao, J.; Perdew, J. P.; Staroverov, V. N.; Scuseria, G. E. Climbing the density functional ladder: Nonempirical meta–generalized gradient approximation designed for molecules and solids, *Phys. Rev. Lett.* **2003,** *91,* 146401.

[96] Lee, C.; Yang, W.; Parr, R. G. Development of the Colle-Salvetti correlation-energy formula into a functional of the electron density, *Phys. Rev. B* **1988,** *37,* 785.

[97] Becke, A. D. Density-functional thermochemistry. III. The role of exact exchange, *J. Chem. Phys.* **1993,** *98,* 5648.

[98] Stephens, P. J.; Devlin, F. J.; Chabalowski, C. F.; Frisch, M. J. Ab initio calculation of vibrational absorption and circular dichroism spectra using density functional force fields, *J. Phys. Chem.* **1994,** *98,* 11623–11627.

[99] Vosko, S. H.; Wilk, L.; Nusair, M. Accurate spin-dependent electron liquid correlation energies for local spin density calculations: critical analysis, *Can. J. Phys.* **1980,** *58,* 1200–1211.

[100] Becke, A. D. Density-functional exchange-energy approximation with correct asymptotic behavior, *Phys. Rev. A* **1988,** *38,* 3098.

[101] Kittel, C. *Introduction to solid state physics, 8th edition;* John Wiley & Sons, Inc.: 2005.

[102] Bloch, F. Über die quantenmechanik der elektronen in kristallgittern, *Z. Phys.* **1929,** *52,* 555–600.

[103] Monkhorst, H. J.; Pack, J. D. Special points for Brillouin-zone integrations, *Phys. Rev. B* **1976,** *13,* 5188.

[104] Vanderbilt, D. Soft self-consistent pseudopotentials in a generalized eigenvalue formalism, *Phys. Rev. B* **1990,** *41,* 7892.

[105] Blöchl, P. E. Projector augmented-wave method, *Phys. Rev. B* **1994,** *50,* 17953.

[106] Kresse, G.; Joubert, D. From ultrasoft pseudopotentials to the projector augmented-wave method, *Phys. Rev. B* **1999,** *59,* 1758.

[107] Jiang, K.; Sandberg, R. B.; Akey, A. J.; Liu, X.; Bell, D. C.; Nørskov, J. K.; Chan, K.; Wang, H. Metal ion cycling of Cu foil for selective C–C coupling in electrochemical CO_2 reduction, *Nat. Catal.* **2018,** *1,* 111–119.

[108] Garcia-Ratés, M.; López, N. Multigrid-based methodology for implicit solvation models in periodic DFT, *J. Chem. Theory Comput.* **2016,** *12,* 1331–1341.

[109] Garcia-Ratés, M.; García-Muelas, R.; López, N. Solvation effects on methanol decomposition on Pd(111), Pt(111), and Ru(0001), *J. Phys. Chem. C* **2017,** *121,* 13803–13809.

[110] Marcus, R. A. On the theory of electron-transfer reactions. VI. Unified treatment for homogeneous and electrode reactions, *J. Chem. Phys.* **1965,** *43,* 679–701.

[111] Koper, M. T. M. Theory of the transition from sequential to concerted electrochemical proton-electron transfer, *Phys. Chem. Chem. Phys.* **2013,** *15,* 1399–1407.

[112] Koper, M. T. M. Theory of multiple proton-electron transfer reactions and its implications for electrocatalysis, *Chem. Sci.* **2013,** *4,* 2710–2723.

[113] Göttle, A. J.; Koper, M. T. M. Proton-coupled electron transfer in the electrocatalysis of CO_2 reduction: Prediction of sequential *vs.* concerted pathways using DFT, *Chem. Sci.* **2017,** *8,* 458–465.

[114] Marx, D.; Hutter, J. *Ab initio molecular dynamics: Basic theory and advanced methods;* Cambridge University Press: 2009.

[115] Nosé, S. A unified formulation of the constant temperature molecular dynamics methods, *J. Chem. Phys.* **1984,** *81,* 511–519.

[116] Hoover, W. G. Canonical dynamics: Equilibrium phase-space distributions, *Phys. Rev. A* **1985,** *31,* 1695.

[117] Evans, D. J.; Holian, B. L. The Nose-Hoover thermostat, *J. Chem. Phys.* **1985,** *83,* 4069.

[118] Car, R.; Parinello, M. Unified approach for molecular dynamics and density-functional theory, *Phys. Rev. Lett.* **1985,** *55,* 2471.

[119] Kresse, G.; Furthmüller, J. Efficient iterative schemes for *ab initio* total-energy calculations using a plane-wave basis set, *Phys. Rev. B* **1996,** *54,* 11169.

[120] Kresse, G.; Furthmüller, J. Efficiency of ab-initio total energy calculations for metals and semiconductors using a plane-wave basis set, *Computat. Mater. Sci.* **1996,** *6,* 15–50.

[121] Bučko, T.; Hafner, J.; Lebègue, S.; Angyán, J. G. Improved description of the structure of molecular and layered crystals: Ab initio DFT calculations with van der Waals corrections, *J. Phys. Chem. A* **2010,** *114,* 11814–11824.

[122] Fishman, M.; Zhuang, H. L.; Mathew, K.; Dirschka, W.; Hennig, R. G. Accuracy of exchange-correlation functionals and effect of solvation on the surface energy of copper, *Phys. Rev. B* **2013,** *87,* 245402.

[123] Mathew, K.; Sundararaman, R.; Letchworth-Weaver, K.; Arias, T. A.; Hennig, R. G. Implicit solvation model for density-functional study of nanocrystal surfaces and reaction pathways, *J. Chem. Phys.* **2014,** *140,* 084106.

[124] Makov, G.; Payne, M. C. Periodic boundary conditions in ab initio calculations, *Phys. Rev. B* **1995,** *51,* 4014–4022.

[125] Hori, Y.; Murata, A.; Takahashi, R. Formation of hydrocarbons in the electrochemical reduction of carbon dioxide at a copper electrode in aqueous solution, *J. Chem. Soc., Faraday Trans. 1* **1989,** *85,* 2309–2326.

[126] Hussain, J.; Jónsson, H.; Skúlason, E. Calculations of product selectivity in electrochemical CO_2 reduction, *ACS Catal.* **2018,** *8,* 5240–5249.

[127] Wulff, G. Zur frage der geschwindigkeit des wachsthums und der auflösung der krystallflächen., *Z. Kristallog.* **1901,** *34,* 449–530.

[128] Carchini, G.; Almora-Barrios, N.; Revilla-López, G.; Bellarosa, L.; García-Muelas, R.; García-Melchor, M.; Pogodin, S.; Błoński, P.; López, N. How theoretical simulations can address the structure and activity of nanoparticles, *Top. Catal.* **2013,** *56,* 1262–1272.

[129] Reske, R.; Mistry, H.; Behafarid, F.; Roldan Cuenya, B.; Strasser, P. Particle size effects in the catalytic electroreduction of CO_2 on Cu nanoparticles, *J. Am. Chem. Soc.* **2014,** *136,* 6978–6986.

[130] Kortlever, R.; Shen, J.; Schouten, K. J. P.; Calle-Vallejo, F.; Koper, M. T. M. Catalysts and reaction pathways for the electrochemical reduction of carbon dioxide, *J. Phys. Chem. Lett.* **2015,** *6,* 4073–4082.

[131] Emsley, J. *Nature's building blocks: An A–Z guide to the elements;* Oxford University Press: 2011.

[132] *The New Encyclopaedia Britannica;* Encyclopaedia Britannica, Inc.: 1998.

[133] U.S. Department of the Interior, U.S Geological Survey, *Copper in November 2019*, `https://prd-wret.s3.us-west-2.amazonaws.com/assets/palladium/production/atoms/files/mis-201911-coppe.pdf`, 2020 Online; accessed 24 July 2020.

[134] Zhang, F.; Co, A. C. Direct evidence of local pH change and the role of alkali cation during CO_2 electroreduction in aqueous media, *Angew. Chem. Int. Ed.* **2020,** *59,* 1674–1681.

[135] Wang, X.; de Araújo, J. F.; Ju, W.; Bagger, A.; Schmies, H.; Kühl, S.; Rossmeisl, J.; Strasser, P. Mechanistic reaction pathways of enhanced ethylene yields during electroreduction of CO_2–CO co-feeds on Cu and Cu-tandem electrocatalysts, *Nat. Nanotechnol.* **2019,** *14,* 1063–1070.

[136] Calle-Vallejo, F.; Koper, M. T. M. Theoretical considerations on the electroreduction of CO to C_2 species on Cu(100) electrodes, *Angew. Chem. Int. Ed.* **2013,** *52,* 7282–7285.

[137] Katayama, Y.; Nattino, F.; Giordano, L.; Hwang, J.; Rao, R. R.; Andreussi, O.; Marzari, N.; Shao-Horn, Y. An *In Situ* surface-enhanced infrared absorption spectroscopy study of electrochemical CO_2 reduction: Selectivity dependence on surface C-bound and O-bound reaction intermediates, *J. Phys. Chem. C* **2019,** *123,* 5951–5963.

[138] Chou, T.-C.; Chang, C.-C.; Yu, H.-L.; Yu, W.-Y.; Dong, C.-L.; Velasco-Vélez, J.-J.; Chuang, C.-H.; Chen, L.-C.; Lee, J.-F.; Chen, J.-M.; Wu, H.-L. Controlling the oxidation state of Cu electrode and reaction intermediates for electrochemical CO_2 reduction to ethylene, *J. Am. Chem. Soc.* **2020,** *142,* 2857–2867.

[139] De Luna, P.; Quintero-Bermudez, R.; Dinh, C.-T.; Ross, M. B.; Bushuyev, O. S.; Todorović, P.; Regier, T.; Kelley, S. O.; Yang, P.; Sargent, E. H. Catalyst electroredeposition controls morphology and oxidation state for selective carbon dioxide reduction, *Nat. Catal.* **2018,** *1,* 103–110.

[140] Lee, S. Y.; Jung, H.; Kim, N.-K.; Oh, H.-S.; Min, B. K.; Hwang, Y. J. Mixed copper states in anodized Cu electrocatalyst for stable and selective ethylene production from CO_2 reduction, *J. Am. Chem. Soc.* **2018,** *140,* 8681–8689.

[141] Jeon, H. S.; Kunze, S.; Scholten, F.; Roldan Cuenya, B. Prism-shaped Cu nanocatalysts for electrochemical CO_2 reduction to ethylene, *ACS Catal.* **2018,** *8,* 531–535.

[142] Kim, D.; Lee, S.; Ocon, J. D.; Jeong, B.; Lee, J. K.; Lee, J. Insights into an autonomously formed oxygen-evacuated Cu_2O electrode for the selective production of C_2H_4 from CO_2, *Phys. Chem. Chem. Phys.* **2015,** *17,* 824–830.

[143] Dutta, A.; Rahaman, M.; Luedi, N. C.; Mohos, M.; Broekmann, P. Morphology matters: Tuning the product distribution of CO_2 electroreduction on oxide-derived Cu foam catalysts, *ACS Catal.* **2016,** *6,* 3804–3814.

[144] Ren, D.; Wong, N. T.; Handoko, A. D.; Huang, Y.; Yeo, B. S. Mechanistic insights into the enhanced activity and stability of agglomerated Cu nanocrystals for the electrochemical reduction of carbon dioxide to *n*-Propanol, *J. Phys. Chem. Lett.* **2016,** *7,* 20–24.

[145] Wang, Y.; Wang, Z.; Dinh, C.-T.; Li, J.; Ozden, A.; Kibria, M. G.; Seifitokaldani, A.; Tan, C.-S.; Gabardo, C. M.; Luo, M.; Zhou, H.; Li, F.; Lum, Y.; McCallum, C.; Xu, Y.; Liu, M.; Proppe, A.; Johnston, A.; Todorović, P.; Zhuang, T.-T.; Sinton, D.; Kelley, S. O.; Sargent, E. H. Catalyst synthesis under CO_2 electroreduction favours faceting and promotes renewable fuels electrosynthesis, *Nat. Catal.* **2020,** *3,* 98-106.

[146] Kwon, Y.; Lum, Y.; Clark, E. L.; Ager, J. W.; Bell, A. T. CO_2 electroreduction with enhanced ethylene and ethanol selectivity by nanostructuring polycrystalline copper, *ChemElectroChem* **2016,** *3,* 1012–1019.

[147] Kas, R.; Kortlever, R.; Yılmaz, H.; Koper, M. T. M.; Mul, G. Manipulating the hydrocarbon selectivity of copper nanoparticles in CO_2 electroreduction by process conditions, *ChemElectroChem* **2015,** *2,* 354–358.

[148] Chen, C. S.; Handoko, A. D.; Wan, J. H.; Ma, L.; Ren, D.; Yeo, B. S. Stable and selective electrochemical reduction of carbon dioxide to ethylene on copper mesocrystals, *Catal. Sci. Technol.* **2015,** *5,* 161–168.

[149] Choi, Y.-W.; Mistry, H.; Roldan Cuenya, B. New insights into working nanostructured electrocatalysts through operando spectroscopy and microscopy, *Curr. Opin. Electrochem.* **2017,** *1,* 95–103.

[150] Gao, D.; Arán-Ais, R. M.; Jeon, H. S.; Roldan Cuenya, B. Rational catalyst and electrolyte design for CO_2 electroreduction towards multicarbon products, *Nat. Catal.* **2019,** *2,* 198–210.

[151] Kim, Y.-G.; Baricuatro, J. H.; Soriaga, M. P. Surface reconstruction of polycrystalline Cu electrodes in aqueous $KHCO_3$ electrolyte at potentials in the early stages of CO_2 reduction, *Electrocatalysis* **2018,** *9,* 526–530.

[152] Phan, T. H.; Banjac, K.; Cometto, F. P.; Dattila, F.; García-Muelas, R.; López, N.; Lingenfelder, M. Tracking the potential-controlled synthesis of Cu-nanocuboids and graphene-covered Cu-nanocuboids under *Operando* CO_2 electroreduction, *ChemRxiv* **2020,** DOI: 10.26434/chemrxiv.13198481.v1.

[153] Philips, M. F.; Gruter, G.-J. M.; Koper, M. T. M.; Schouten, K. J. P. Optimizing the electrochemical reduction of CO_2 to formate: A state-of-the-art analysis, *ACS Sustainable Chem. Eng.* **2020,** *8,* 15430–15444.

[154] Hong, J.; Lee, S.; Lee, S.; Han, H.; Mahata, C.; Yeon, H.-W.; Koo, B.; Kim, S.-I.; Nam, T.; Byun, K.; Min, B.-W.; Kim, Y.-W.; Kim, H.; Joob, Y.-C.; Lee, T. Graphene as an atomically thin barrier to Cu diffusion into Si, *Nanoscale* **2014,** *6,* 7503–7511.

[155] Fields, M.; Hong, X.; Nørskov, J. K.; Chan, K. Role of subsurface oxygen on Cu surfaces for CO_2 electrochemical reduction, *J. Phys. Chem. C* **2018,** *122,* 16209–16215.

[156] Łodziana, Z.; Topsøe, N.-Y.; Nørskov, J. K. A negative surface energy for alumina, *Nat. Mater.* **2004,** *3,* 289–293.

[157] White, R. E.; Bockris, J. O.; Conway, B. E. *Modern aspects of electrochemistry No. 33;* Springer US: 1999.

[158] Tripkovic, V.; Björketun, M. E.; Skúlason, E.; Rossmeisl, J. Standard hydrogen electrode and potential of zero charge in density functional calculations, *Phys. Rev. B* **2011,** *84,* 115452.

[159] Vitos, L.; Ruban, A. V.; Skriver, H. L.; Kollár, J. The surface energy of metals, *Surf. Sci.* **1998,** *411,* 186–202.

[160] Simon, G. H.; Kley, C. S.; Roldan Cuenya, B. Potential–dependent morphology of copper catalysts during CO_2 electroreduction revealed by *In Situ* Atomic Force Microscopy, *Angew. Chem. Int. Ed.* **2020,** DOI: 10.1002/anie.202010449.

[161] Griffin, G. L.; Bugayong, J. Electrochemical reduction of CO_2 using copper oxide nanoparticles supported on glassy carbon electrodes, *Mater. Res. Soc. Symp. Proc.* **2014,** *1677,* DOI: 10.1557/opl.2014.557.

[162] Cudennec, Y.; Lecerf, A. The transformation of $Cu(OH)_2$ into CuO, revisited, *Solid State Sci.* **2003,** *5,* 1471–1474.

[163] Su, D.; Xie, X.; Dou, S.; Wang, G. CuO single crystal with exposed {001} facets - A highly efficient material for gas sensing and Li-ion battery applications, *Sci. Rep.* **2014,** *4,* 5753.

[164] Scott, S. B.; Hogg, T. V.; Landers, A. T.; Maagaard, T.; Bertheussen, E.; Lin, J. C.; Davis, R. C.; Beeman, J. W.; Higgins, D.; Drisdell, W. S.; Hahn, C.; Mehta, A.; Seger, B.; Jaramillo, T. F.; Chorkendorff, I. Absence of oxidized phases in Cu under CO reduction conditions, *ACS Energy Lett.* **2019,** *4,* 803–804.

[165] Gulla, A. F.; Krasovic, J. *Gas-Diffusion Electrode, US 2014/0227634 A1*, 2014.

[166] Lee, S. H.; Sullivan, I.; Larson, D. M.; Liu, G.; Toma, F. M.; Xiang, C.; Drisdell, W. S. Correlating oxidation state and surface area to activity from *Operando* studies of copper CO electroreduction catalysts in a gas-fed device, *ACS Catal.* **2020,** *10,* 8000–8011.

[167] Mistry, H.; Varela, A. S.; Bonifacio, C. S.; Zegkinoglou, I.; Sinev, I.; Choi, Y.-W.; Kisslinger, K.; Stach, E. A.; Yang, J. C.; Strasser, P.; Roldan Cuenya, B. Highly selective plasma-activated copper catalysts for carbon dioxide reduction to ethylene, *Nat. Commun.* **2016,** *7,* 12123.

[168] Velasco-Vélez, J.-J.; Jones, T.; Gao, D.; Carbonio, E.; Arrigo, R.; Hsu, C.-J.; Huang, Y.-C.; Dong, C.-L.; Chen, J.-M.; Lee, J.-F.; Strasser, P.; Roldan Cuenya, B.; Schlögl, R.; Knop-Gericke, A.; Chuang, C.-H. The role of the copper oxidation state in the electrocatalytic reduction of CO_2 into valuable hydrocarbons, *ACS Sustain. Chem. Eng.* **2019,** *7,* 1485–1492.

[169] Favaro, M.; Xiao, H.; Cheng, T.; Goddard III, W. A.; Yano, J.; Crumlin, E. J. Subsurface oxide plays a critical role in CO_2 activation by Cu(111) surfaces to form chemisorbed CO_2, the first step in reduction of CO_2, *Proc. Natl. Acad. Sci. USA* **2017,** *114,* 6706–6711.

[170] Auer, A.; Andersen, M.; Wernig, E.-M.; Hörmann, N. G.; Buller, N.; Reuter, K.; Kunze-Liebhäuser, J. Self-activation of copper electrodes during CO electrooxidation in alkaline electrolyte, *Nat. Catal.* **2020,** *3,* 797–803.

[171] Ren, D.; Deng, Y.; Handoko, A. D.; Chen, C. S.; Malkhandi, S.; Yeo, B. S. Selective electrochemical reduction of carbon dioxide to ethylene and ethanol on copper(I) oxide catalysts, *ACS Catal.* **2015,** *5,* 2814–2821.

[172] Cheng, T.; Xiao, H.; Goddard III, W. A. Nature of the active sites for CO reduction on copper nanoparticles; Suggestions for optimizing performance, *J. Am. Chem. Soc.* **2017,** *139,* 11642–11645.

[173] Feng, X.; Jiang, K.; Fan, S.; Kanan, M. W. A direct grain-boundary-activity correlation for CO electroreduction on Cu nanoparticles, *ACS Cent. Sci.* **2016,** *2,* 169–174.

[174] Schouten, K. J. P.; Qin, Z.; Pérez Gallent, E.; Koper, M. T. M. Two pathways for the formation of ethylene in CO reduction on single-crystal copper electrodes, *J. Am. Chem. Soc.* **2012,** *134,* 9864–9867.

[175] Schouten, K. J. P.; Pérez Gallent, E.; Koper, M. T. M. The influence of pH on the reduction of CO and CO_2 to hydrocarbons on copper electrodes, *J. Electroanal. Chem.* **2014,** *716,* 53–57.

[176] Dattila, F. *Glyoxylate-like configurations: (O_{ss})OCCO, sites 1-9*, `https://doi.org/10.19061/iochem-bd-1-165`, 2020 Online; accessed 24 July 2020.

[177] Handoko, A. D.; Ong, C. W.; Huang, Y.; Lee, Z. G.; Lin, L.; Panetti, G. B.; Yeo, B. S. Mechanistic insights into the selective electroreduction of carbon dioxide to ethylene on Cu_2O-derived copper catalysts, *J. Phys. Chem. C* **2016,** *120,* 20058–20067.

[178] Li, J.; Che, F.; Pang, Y.; Zou, C.; Howe, J. Y.; Burdyny, T.; Edwards, J. P.; Wang, Y.; Li, F.; Wang, Z.; De Luna, P.; Dihn, C.-T.; Zuang, T.-T.; Saidaminov, M. I.; Cheng, S.; Wu, T.; Finfrock, Y. Z.; Ma, L.; Hsieh, S.-H.; Liu, Y.-S.; Botton, G. A.; Pong, W.-F.; Du, X.; Guo, J.; Sham, T.-K.; Sargent, E. H.; Sinton, D. Copper adparticle enabled selective electrosynthesis of *n*-propanol, *Nat. Commun.* **2018,** *9,* 4614.

[179] Ting, L. R. L.; García-Muelas, R.; Martin, A. J.; Veenstra, F. L. P.; Chen, S. T.-J.; Peng, Y.; Per, E. Y. X.; Pablo-García, S.; López, N.; Pérez-Ramírez, J.; Yeo, B. S. Electrochemical reduction of carbon dioxide to 1-butanol on oxide-derived copper, *Angew. Chem. Int. Ed.* **2020,** *59,* 21072–21079.

[180] Garza, A. J.; Bell, A. T.; Head-Gordon, M. Is subsurface oxygen necessary for the electrochemical reduction of CO_2 on copper?, *J. Phys. Chem. Lett.* **2018,** *9,* 601–606.

[181] Liu, C.; Lourenço, M. P.; Hedström, S.; Cavalca, F.; Diaz-Morales, O.; Duarte, H. A.; Nilsson, A.; Pettersson, L. G. M. Stability and effects of subsurface oxygen in oxide-derived Cu catalyst for CO_2 reduction, *J. Phys. Chem. C* **2017,** *121,* 25010–25017.

[182] Tomboc, G. M.; Choi, S.; Kwon, T.; Hwang, Y. J.; Lee, K. Potential link between Cu surface and selective CO_2 electroreduction: Perspective on future electrocatalyst designs, *Adv. Mater.* **2020,** *32,* 1908398.

[183] Kim, Y. G.; Soriaga, M. P. Cathodic regeneration of a clean and ordered Cu(100)-(1×1) surface from an air-oxidized and disordered electrode: An *operando* STM study, *J. Electroanal. Chem.* **2014,** *734,* 7–9.

[184] Velasco-Vélez, J.-J.; Mom, R. V.; Sandoval-Diaz, L.-E.; Falling, L. J.; Chuang, C.-h.; Gao, D.; Jones, T. E.; Zhu, Q.; Arrigo, R.; Roldan Cuenya, B.; Knop-Gericke, A.; Lunkenbein, T.; Schlögl, R. Revealing the active phase of copper during the electroreduction of CO_2 in aqueous electrolyte by correlating *In Situ* X-ray spectroscopy and *In Situ* electron microscopy, *ACS Energy Lett.* **2020,** *5,* 2106–2111.

[185] Lum, Y.; Ager, J. W. Stability of residual oxides in oxide-derived copper catalysts for electrochemical CO_2 reduction investigated with ^{18}O labeling, *Angew. Chem. Int. Ed.* **2018,** *57,* 551–554.

[186] Mandal, L.; Yang, K. R.; Motapothula, M. R.; Ren, D.; Lobaccaro, P.; Patra, A.; Sherburne, M.; Batista, V. S.; Yeo, B. S.; Ager, J. W.; Martin, J.; Venkatesan, T. Investigating the role of copper oxide in electrochemical CO_2 reduction in real time, *ACS Appl. Mater. Interfaces* **2018,** *10,* 8574–8584.

[187] Schedel-Niedrig, T.; Neisius, T.; Böttger, I.; Kitzelmann, E.; Weinberg, G.; Demuth, D.; Schlögl, R. Copper (sub)oxide formation: A surface sensitive characterization of model catalysts, *Phys. Chem. Chem. Phys.* **2000,** *2,* 2407–2417.

[188] Eilert, A.; Cavalca, F.; Roberts, F. S.; Osterwalder, J.; Liu, C.; Favaro, M.; Crumlin, E. J.; Ogasawara, H.; Friebel, D.; Pettersson, L. G. M.; Nilsson, A. Subsurface oxygen in oxide-derived copper electrocatalysts for carbon dioxide reduction, *J. Phys. Chem. Lett.* **2017,** *8,* 285–290.

[189] Jung, H.; Lee, S. Y.; Lee, C. W.; Cho, M. K.; Won, D. H.; Kim, C.; Oh, H.-S.; Min, B. K.; Hwang, Y. J. Electrochemical fragmentation of Cu_2O nanoparticles enhancing selective C–C coupling from CO_2 reduction reaction, *J. Am. Chem. Soc.* **2019,** *141,* 4624–4633.

[190] Rost, C. M.; Sachet, E.; Borman, T.; Moballegh, A.; Dickey, E. C.; Hou, D.; Jones, J. L.; Curtarolo, S.; Maria, J.-P. Entropy-stabilized oxides, *Nat. Commun.* **2015,** *6,* 8485.

[191] Möller, T.; Scholten, F.; Thanh, T. N.; Sinev, I.; Timoshenko, J.; Wang, X.; Jovanov, Z.; Gliech, M.; Roldan Cuenya, B.; Varela, A. S.; Strasser, P. Electrocatalytic CO_2 reduction on CuO_x nanocubes: Tracking the evolution of chemical state, geometric structure, and catalytic selectivity using Operando Spectroscopy, *Angew. Chem. Int. Ed.* **2020,** *59,* 17974–17983.

[192] Persson, K. A.; Waldwick, B.; Lazic, P.; Ceder, G. Prediction of solid-aqueous equilibria: Scheme to combine first-principles calculations of solids with experimental aqueous states, *Phys. Rev. B* **2012,** *85,* 235438.

[193] Singh, A. K.; Zhou, L.; Shinde, A.; Suram, S. K.; Montoya, J. H.; Winston, D.; Gregoire, J. M.; Persson, K. A. Electrochemical stability of metastable materials, *Chem. Mater.* **2017,** *29,* 10159–10167.

[194] Guan, R.; Hashimoto, H.; Kuo, K. H. Electron-microscopic study of the structure of metastable oxides formed in the initial stage of copper oxidation. II. Cu_8O, *Acta Cryst.* **1984,** *B40,* 560–566.

[195] Guan, R.; Hashimoto, H.; Kuo, K. H. Electron-microscopic study of the structure of metastable oxides formed in the initial stage of copper oxidation. III. $Cu_{64}O$, *Acta Cryst.* **1985,** *B41,* 219–225.

[196] Hersbach, T. J. P.; McCrum, I. T.; Anastasiadou, D.; Wever, R.; Calle-Vallejo, F.; Koper, M. T. M. Alkali metal cation effects in structuring Pt, Rh, and Au surfaces through cathodic corrosion, *ACS Appl. Mater. Interfaces* **2018,** *10,* 39363–39379.

[197] Zhang, W.; Huang, C.; Xiao, Q.; Yu, L.; Shuai, L.; An, P.; Zhang, J.; Qiu, M.; Ren, Z.; Yu, Y. Atypical oxygen-bearing copper boosts ethylene selectivity toward electrocatalytic CO_2 reduction, *J. Am. Chem. Soc.* **2020,** *142,* 11417–11427.

[198] Bai, H.; Cheng, T.; Li, S.; Zhou, Z.; Yang, H.; Li, J.; Xie, M.; Ye, J.; Ji, Y.; Li, Y.; Zhou, Z.; Sun, S.; Zhang, B.; Peng, H. Controllable CO adsorption determines ethylene and methane productions from CO_2 electroreduction, *Sci. Bull.* **2020,** DOI: 10.1016/j.scib.2020.06.023.

[199] Lin, S.-C.; Chang, C.-C.; Chiu, S.-Y.; Pai, H.-T.; Liao, T.-Y.; Hsu, C.-S.; Chiang, W.-H.; Tsai, M.-K.; Chen, H. M. Operando time-resolved X-ray absorption spectroscopy reveals the chemical nature enabling highly selective CO_2 reduction, *Nat. Commun.* **2020,** *11,* 3525.

[200] Xu, H.; Rebollar, D.; He, H.; Chong, L.; Liu, Y.; Liu, C.; Sun, C.-J.; Li, T.; Muntean, J. V.; Winans, R. E.; Liu, D.-J.; Xu, T. Highly selective electrocatalytic CO_2 reduction to ethanol by metallic clusters dynamically formed from atomically dispersed copper, *Nat. Energy* **2020,** *5,* 623–632.

[201] Dattila, F. *Supporting Videos 1-7*, `https://iochem-bd.iciq.es/browse/handle/100/26145`, 2020 Online; accessed 24 July 2020.

[202] Yu, J.; Namba, Y. Atomic surface roughness, *Appl. Phys. Lett.* **1998,** *73,* 3607.

[203] Zhu, S.; Jiang, B.; Cai, W.-B.; Shao, M. Direct observation on reaction intermediates and the role of bicarbonate anions in CO_2 electrochemical reduction reaction on Cu surfaces, *J. Am. Chem. Soc.* **2017,** *139,* 15664–15667.

[204] Heyes, J.; Dunwell, M.; Xu, B. CO_2 reduction on Cu at low overpotentials with surface-enhanced in Situ spectroscopy, *J. Phys. Chem. C* **2016,** *120,* 17334–17341.

[205] Wang, X.; Wang, Z.; Zhuang, T.-T.; Dinh, C.-T.; Li, J.; Nam, D.-H.; Li, F.; Huang, C.-W.; Tan, C.-S.; Chen, Z.; Chi, M.; Gabardo, C. M.; Seifitokaldani, A.; Todorović, P.; Proppe, A.; Panfg, Y.; Kirmani, A. R.; Wang, Y.; Ip, A. H.; Richter, L. J.; Scheffel, B.; Xu, A.; Lo, S.-C.; Kelley, S. O.; Sinton, D.; Sargent, E. H. Efficient upgrading of CO to C_3 fuel using asymmetric C–C coupling active sites, *Nat. Commun.* **2019,** *10,* 5186.

[206] Handoko, A. D.; Wei, F.; Jenndy,; Yeo, B. S.; Seh, Z. W. Understanding heterogeneous electrocatalytic carbon dioxide reduction through operando techniques, *Nat. Catal.* **2018,** *1,* 922–934.

[207] Muchowska, K. B.; Varma, S. J.; Moran, J. Synthesis and breakdown of universal metabolic precursors promoted by iron, *Nature* **2019,** *569,* 104–107.

[208] Li, Y. C.; Wang, Z.; Yuan, T.; Nam, D.-H.; Luo, M.; Wicks, J.; Chen, B.; Li, J.; Li, F.; García de Arquer, F. P.; Wang, Y.; Dinh, C.-T.; Voznyy, O.; Sinton, D.; Sargent, E. H. Binding site diversity promotes CO_2 electroreduction to ethanol, *J. Am. Chem. Soc.* **2019,** *141,* 8584–8591.

[209] Lee, S.; Park, G.; Lee, J. Importance of Ag–Cu biphasic boundaries for selective electrochemical reduction of CO_2 to ethanol, *ACS Catal.* **2017,** *7,* 8594–8604.

[210] Ting, L. R. L.; Piqué, O.; Lim, S. Y.; Tanhaei, M.; Calle-Vallejo, F.; Yeo, B. S. Enhancing CO_2 electroreduction to ethanol on copper-silver composites by opening an alternative catalytic pathway, *ACS Catal.* **2020,** *10,* 4059–4069.

[211] da Silva, A. H. M.; Raaijaman, S. J.; Santana, C. S.; Assaf, J. M.; Gomes, J. F.; Koper, M. T. M. Electrocatalytic CO_2 reduction to C_{2+} products on Cu and Cu_xZn_y electrodes: Effects of chemical composition and surface morphology, *J. Electroanal. Chem.* **2020,** DOI: 10.1016/j.jelechem.2020.114750.

[212] Lum, Y.; Ager, J. W. Evidence for product-specific active sites on oxide-derived Cu catalysts for electrochemical CO_2 reduction, *Nat. Catal.* **2019,** *2,* 86–93.

[213] García-Muelas, R. *Structures for "Origin of the selective electroreduction of carbon dioxide to formate by chalcogen modified copper"*, `https://www.doi.org/10.19061/iochem-bd-1-92`, 2018.

[214] Huang, Y.; Deng, Y.; Handoko, A. D.; Goh, G. K. L.; Yeo, B. S. Rational design of sulfur-doped copper catalysts for the selective electroreduction of carbon dioxide to formate, *ChemSusChem* **2018,** *11,* 320–326.

[215] Deng, Y.; Huang, Y.; Ren, D.; Handoko, A. D.; Seh, Z. W.; Hirunsit, P.; Yeo, B. S. On the role of sulfur for the selective electrochemical reduction of CO_2 to formate on CuS_x catalysts, *ACS Appl. Mater. Interfaces* **2018,** *10,* 28572–28581.

[216] Zhu, Q.-G.; Sun, X.-F.; Kang, X.-C.; MA, J.; Qian, Q.-L.; Han, B.-X. Cu_2S on Cu foam as highly efficient electrocatalyst for reduction of CO_2 to formic acid, *Acta Phys. - Chim. Sin.* **2016,** *32,* 261–266.

[217] Ma, W.; Xie, S.; Zhang, X.-G.; Sun, F.; Kang, J.; Jiang, Z.; Zhang, Q.; Wu, D.-Y.; Wang, Y. Promoting electrocatalytic CO_2 reduction to formate via sulfur-boosting water activation on indium surfaces, *Nat. Commun.* **2019,** *10,* 892.

[218] Zheng, X.; De Luna, P.; García de Arquer, F. P.; Zhang, B.; Becknell, N.; Ross, M. B.; Li, Y.; Banis, M. N.; Li, Y.; Liu, M.; Voznyy, O.; Dinh, C. T.; Zhuang, T.; Stadler, P.; Cui, Y.; Du, X.; Yang, P.; Sargent, E. H. Sulfur-modulated tin sites enable highly selective electrochemical reduction of CO_2 to formate, *Joule* **2017,** *1,* 794–805.

[219] Li, F.; Chen, L.; Xue, M.; Williams, T.; Zhang, Y.; MacFarlane, D. R.; Zhang, J. Towards a better Sn: Efficient electrocatalytic reduction of CO_2 to formate by Sn/SnS_2 derived from SnS_2 nanosheets, *Nano Energy* **2017,** *31,* 270–277.

[220] Lide, D. R. *Handbook of Chemistry and Physics, 84^{th} edition;* CRC press: 2003.

[221] Marks, L. D.; Peng, L. Nanoparticle shape, thermodynamics and kinetics, *J. Phys. Condens. Matter* **2016,** *28,* 053001.

[222] Tyson, W. R.; Miller, W. A. . Surface free energies of solid metals: Estimation from liquid surface tension measurements, *Surf. Sci.* **1977,** *62,* 267–276.

[223] De Boer, F. R.; Mattens, W. C. M.; Boom, R.; Miedema, A. R.; Niessen, A. K. *Cohesion in metals;* North-Holland: 1988.

[224] Skriver, H. L.; Rosengaard, N. M. Surface energy and work function of elemental metals, *Phys. Rev. B* **1992,** *46,* 7157.

[225] Verdaguer-Casadevall, A.; Li, C. W.; Johansson, T. P.; Scott, S. B.; McKeown, J. T.; Kumar, M.; Stephens, I. E. L.; Kanan, M. W.; Chorkendorff, I. Probing the active surface sites for CO reduction on oxide-derived copper electrocatalysts, *J. Am. Chem. Soc.* **2015,** *137,* 9808–9811.

[226] Gattrell, M.; Gupta, N.; Co, A. A review of the aqueous electrochemical reduction of CO_2 to hydrocarbons at copper, *J. Electroanal. Chem.* **2006,** *594,* 1–19.

[227] Chernyshova, I. V.; Somasundaran, P.; Ponnurangam, S. On the origin of the elusive first intermediate of CO_2 electroreduction, *Proc. Natl. Acad. Sci. U.S.A.* **2018,** *115,* E9261–E9270.

[228] Taifan, W.; Boily, J.-F.; Baltrusaitis, J. Surface chemistry of carbon dioxide revisited, *Surf. Sci. Rep.* **2016,** *71,* 595–671.

[229] Henkelman, G.; Arnaldsson, A.; Jónsson, H. A fast and robust algorithm for Bader decomposition of charge density, *Comput. Mater Sci.* **2006,** *36,* 354–360.

[230] Sanville, E.; Kenny, S. D.; Smith, R.; Henkelman, G. Improved grid-based algorithm for Bader charge allocation, *J. Comput. Chem.* **2007,** *28,* 899–908.

[231] Tang, W.; Sanville, E.; Henkelman, G. A grid-based Bader analysis algorithm without lattice bias, *J. Phys. Condens. Matter* **2009,** *21,* 084204.

[232] Yu, M.; Trinkle, D. R. Accurate and efficient algorithm for Bader charge integration, *J. Chem. Phys.* **2011,** *134,* 064111.

[233] Roberts, F. S.; Kuhl, K. P.; Nilsson, A. Electroreduction of carbon monoxide over a copper nanocube catalyst: Surface structure and pH dependence on selectivity, *ChemCatChem* **2016,** *8,* 1119–1124.

[234] Varela, A. S.; Kroschel, M.; Reier, T.; Strasser, P. Controlling the selectivity of CO_2 electroreduction on copper: The effect of the electrolyte concentration and the importance of the local pH, *Catal. Today* **2016,** *260,* 8–13.

[235] Ooka, H.; Figueiredo, M. C.; Koper, M. T. M. Competition between hydrogen evolution and carbon dioxide reduction on copper electrodes in mildly acidic media, *Langmuir* **2017,** *33,* 9307–9313.

[236] Torres, D.; López, N.; Illas, F.; Lambert, R. M. Low-basicity oxygen atoms: A key in the search for propylene epoxidation catalysts, *Angew. Chem. Int. Ed.* **2007,** *46,* 2055–2058.

[237] Murata, A.; Hori, Y. Product selectivity affected by cationic species in electrochemical reduction of CO_2 and CO at a Cu electrode, *Bull. Chem. Soc. Jpn.* **1991,** *64,* 123–127.

[238] Singh, M. R.; Kwon, Y.; Lum, Y.; Ager III, J. W.; Bell, A. T. Hydrolysis of electrolyte cations enhances the electrochemical reduction of CO_2 over Ag and Cu, *J. Am. Chem. Soc.* **2016,** *138,* 13006–13012.

[239] Li, J.; Wang, Z.; McCallum, C.; Xu, Y.; Li, F.; Wang, Y.; Gabardo, C. M.; Dinh, C.-T.; Zhuang, T.-T.; Wang, L.; Howe, J. Y.; Ren, Y.; Sargent, E. H.; Sinton, D. Constraining CO coverage on copper promotes high-efficiency ethylene electroproduction, *Nat. Catal.* **2019,** *2,* 1124–1131.

[240] Gao, Y.; Wu, Q.; Liang, X.; Wang, Z.; Zheng, Z.; Wang, P.; Liu, Y.; Dai, Y.; Whangbo, M.-H.; Huang, B. Cu_2O nanoparticles with both {100} and {111} facets for enhancing the selectivity and activity of CO_2 electroreduction to ethylene, *Adv. Sci.* **2020,** *7,* 1902820.

[241] Shang, L.; Lv, X.; Shen, H.; Shao, Z.; Zheng, G. Selective carbon dioxide electroreduction to ethylene and ethanol by core-shell copper/cuprous oxide, *J. Colloid. Interface Sci.* **2019,** *552,* 426–431.

[242] Wu, D.; Dong, C.; Wu, D.; Fu, J.; Liu, H.; Hu, S.; Jiang, Z.; Qiao, S. Z.; Du, X.-W. Cuprous ions embedded in ceria lattice for selective and stable electrochemical reduction of carbon dioxide to ethylene, *J. Mater. Chem. A* **2018,** *6,* 9373–9377.

[243] Altaf, N.; Liang, S.; Huang, L.; Wang, Q. Electro-derived Cu-Cu_2O nanocluster from LDH for stable and selective C_2 hydrocarbons production from CO_2 electrochemical reduction, *J. Energy Chem.* **2020,** *48,* 169–180.

[244] Huang, Y.; Handoko, A. D.; Hirunsit, P.; Yeo, B. S. Electrochemical reduction of CO_2 using copper single-crystal surfaces: Effects of CO* coverage on the selective formation of ethylene, *ACS Catal.* **2017,** *7,* 1749–1756.

[245] Ma, M.; Djanashvili, K.; Smith, W. A. Controllable hydrocarbon formation from the electrochemical reduction of CO_2 over Cu nanowire arrays, *Angew. Chem. Int. Ed.* **2016,** *55,* 6680–6684.

[246] Zhou, Y.; Che, F.; Liu, M.; Zou, C.; Liang, Z.; De Luna, P.; Yuan, H.; Li, J.; Wang, Z.; Xie, H.; Li, H.; Chen, P.; Bladt, E.; Quintero-Bermudez, R.; Sham, T.-K.; Bals, S.; Hofkens, J.; Sinton, D.; Chen, G.; Sargent, E. H. Dopant-induced electron localization drives CO_2 reduction to C_2 hydrocarbons, *Nat. Chem.* **2018,** *10,* 974–980.

[247] Kim, T.; Palmore, G. T. R. A scalable method for preparing Cu electrocatalysts that convert CO_2 into C_{2+} products, *Nat. Commun.* **2020,** *11,* 3622.

[248] Kibria, M. G.; Dinh, C.-T.; Seifitokaldani, A.; De Luna, P.; Burdyny, T.; Quintero-Bermudez, R.; Ross, M. B.; Bushuyev, O. S.; García de Arquer, F. P.; Yang, P.; Sinton, D.; Sargent, E. H. A surface reconstruction route to high productivity and selectivity in CO_2 electroreduction toward C_{2+} hydrocarbons, *Adv. Mater.* **2018,** *30,* 1804867.

[249] Wang, X.; Wang, Z.; García de Arquer, F. P.; Dinh, C.-T.; Ozden, A.; Li, Y. C.; Nam, D.-H.; Li, J.; Liu, Y.-S.; Wicks, J.; Chen, Z.; Chi, M.; Chen, B.; Wang, Y.; Tam, J.; Howe, J. Y.; Proppe, A.; Todorović, P.; Li, F.; Zhuang, T.-T.; Gabardo, C. M.; Kirmani, A. R.; McCallum, C.; Hung, S.-F.; Lum, Y.; Luo, M.; Min, Y.; Xu, A.; O'Brien, C. P.; Stephen, B.; Sun, B.; Ip, A. H.; Richter, L. J.; Kelley, S. O.; Sinton, D.; Sargent, E. H. Efficient electrically powered CO_2-to-ethanol via suppression of deoxygenation, *Nat. Energy* **2020,** *5,* 478–486.

[250] Wang, H.; Tzeng, Y.-K.; Ji, Y.; Li, Y.; Li, J.; Zheng, X.; Yang, A.; Liu, Y.; Gong, Y.; Cai, L.; Li, Y.; Zhang, X.; Chen, W.; Liu, B.; Lu, H.; Melosh, N. A.; Shen, Z.-X.; Chan, K.; Tan, T.; Chu, S.; Cui, Y. Synergistic enhancement of electrocatalytic CO_2 reduction to C_2 oxygenates at nitrogen-doped nanodiamonds/Cu interface, *Nat. Nanotechnol.* **2020,** *15,* 131–137.

[251] Pang, Y.; Li, J.; Wang, Z.; Tan, C.-S.; Hsieh, P.-L.; Zhuang, T.-T.; Liang, Z.-Q.; Zou, C.; Wang, X.; De Luna, P.; Edwards, J. P.; Xu, Y.; Li, F.; Dihn, C.-T.; Zhong, M.; Lou, Y.; Wu, D.; Chen, L.-J.; Sargent, E. H.; Sinton, D. Efficient electrocatalytic conversion of carbon monoxide to propanol using fragmented copper, *Nat. Catal.* **2019,** *2,* 251–258.

[252] Li, F.; Thevenon, A.; Rosas-Hernández, A.; Wang, Z.; Li, Y.; Gabardo, C. M.; Adnan, O.; Cao, T. D.; Li, J.; Wang, Y.; Edwards, J. P.; Xu, Y.; McCallum, C.; Tao, L.; Liang, Z.-Q.; Luo, M.; Wang, X.; Li, H.; O'Brien, C. P.; Tan, C.-S.; Nam, D.-H.; Quintero-Bermudez, R.; Zhuang, T.-T.; Li, Y. C.; Han, Z.;

Britt, R. D.; Sinton, D.; Agapie, T.; Peters, J. C.; Sargent, E. H. Molecular tuning of CO_2-to-ethylene conversion, *Nature* **2019,** *577,* 509-513.

[253] Li, F.; Li, Y. C.; Wang, Z.; Li, J.; Nam, D.-H.; Lum, Y.; Luo, M.; Wang, X.; Ozden, A.; Hung, S.-F.; Chen, B.; Wang, Y.; Wicks, J.; Xu, Y.; Li, Y.; Gabardo, C. M.; Dinh, C.-T.; Wang, Y.; Zhuang, T.-T.; Sinton, D.; Sargent, E. H. Cooperative CO_2-to-ethanol conversion via enriched intermediates at molecule–metal catalyst interfaces, *Nat. Catal.* **2020,** *3,* 75-82.

[254] Rudd, J. A.; Kazimierska, E.; Hamdy, L. B.; Bain, O. J. E.; Ahn, S.; Barron, A. R.; Andreoli, E. CO_2 reduction to propanol by copper foams: A pre- and post-catalysis study, *ChemRxiv* **2020,** DOI: 10.26434/chemrxiv.12022623.v1.

[255] Jeong, H. M.; Kwon, Y.; Won, J. H.; Lum, Y.; Cheng, M.-J.; Kim, K. H.; Head-Gordon, M.; Kang, J. K. Atomic-scale spacing between copper facets for the electrochemical reduction of carbon dioxide, *Adv. Energy Mater.* **2020,** *10,* 1903423.

[256] Gao, J.; Ren, D.; Guo, X.; Zakeeruddin, S. M.; Grätzel, M. Sequential catalysis enables enhanced C–C coupling towards multi-carbon alkenes and alcohols in carbon dioxide reduction: A study on bifunctional Cu/Au electrocatalysts, *Faraday Discuss.* **2019,** *215,* 282–296.

[257] Liang, Z.-Q.; Zhuang, T.-T.; Seifitokaldani, A.; Li, J.; Huang, C.-W.; Tan, C.-S.; Li, Y.; De Luna, P.; Dinh, C. T.; Hu, Y.; Xiao, Q.; Hsieh, P.-L.; Wang, Y.; Li, F.; Quintero-Bermudez, R.; Zhou, Y.; Chen, P.; Pang, Y.; Lo, S.-C.; Chen, L.-J.; Tan, H.; Xu, Z.; Zhao, S.; Sinton, D.; Sargent, E. H. Copper-on-nitride enhances the stable electrosynthesis of multi-carbon products from CO_2, *Nat. Commun.* **2018,** *9,* 3828.

[258] Zhuang, T.-T.; Liang, Z.-Q.; Seifitokaldani, A.; Li, Y.; De Luna, P.; Burdyny, T.; Che, F.; Meng, F.; Min, Y.; Quintero-Bermudez, R.; Dihn, C. T.; Pang, Y.; Zhong, M.; Zhang, B.; Li, J.; Chen, P.-N.; Zheng, X.-L.; Liang, H.; Ge, W.-N.; Ye, B.-J.; Sinton, D.; Yu, S.-H.; Sargent, E. H. Steering post-C–C coupling selectivity enables high efficiency electroreduction of carbon dioxide to multi-carbon alcohols, *Nat. Catal.* **2018,** *1,* 421–428.

[259] Gao, D.; McCrum, I. T.; Deo, S.; Choi, Y.-W.; Scholten, F.; Wan, W.; Chen, J. G.; Janik, M. J.; Roldan Cuenya, B. Activity and selectivity control in CO_2 electroreduction to multicarbon products over CuO_x catalysts via electrolyte design, *ACS Catal.* **2018,** *8,* 10012–10020.

[260] Dinh, C.-T.; Burdyny, T.; Kibria, M. G.; Seifitokaldani, A.; Gabardo, C. M.; García de Arquer, F. P.; Kiani, A.; Edwards, J. P.; De Luna, P.; Bushuyev, O. S.; Zou, C.; Quintero-Bermudez, R.; Pang, Y.; Sinton, D.; Sargent, E. H. CO_2 electroreduction to ethylene via hydroxide-mediated copper catalysis at an abrupt interface, *Science* **2018,** *360,* 783–787.

[261] Yang, K. D.; Ko, W. R.; Lee, J. H.; Kim, S. J.; Lee, H.; Lee, M. H.; Nam, K. T. Morphology-directed selective production of ethylene or ethane from CO_2 on a Cu mesopore electrode, *Angew. Chem. Int. Ed.* **2017,** *56,* 796–800.

[262] Nam, D.-H.; Bushuyev, O. S.; Li, J.; De Luna, P.; Seifitokaldani, A.; Dinh, C.-T.; García de Arquer, F. P.; Wang, Y.; Liang, Z.; Proppe, A. H.; Tan, C. S.; Todorović, P.; Shekhah, O.; Gabardo, C. M.; Jo, J. W.; Choi, J.; Choi, M.-J.; Baek, S.-W.; Kim, J.; Sinton, D.; Kelley, S. O.; Eddaoudi, M.; Sargent, E. H. Metal–organic frameworks mediate Cu coordination for selective CO_2 electroreduction, *J. Am. Chem. Soc.* **2018,** *140,* 11378–11386.

[263] Wang, L.; Nitopi, S.; Wong, A. B.; Snider, J. L.; Nielander, A. C.; Morales-Guio, C. G.; Orazov, M.; Higgins, D. C.; Hahn, C.; Jaramillo, T. F. Electrochemically converting carbon monoxide to liquid fuels by directing selectivity with electrode surface area, *Nat. Catal.* **2019,** *2,* 702–708.

[264] Ni, W.; Li, C.; Zang, X.; Xu, M.; Huo, S.; Liu, M.; Yang, Z.; Yan, Y.-M. Efficient electrocatalytic reduction of CO_2 on Cu_xO decorated graphene oxides: An insight into the role of multivalent Cu in selectivity and durability, *Appl. Catal. B Environ.* **2019,** *259,* 118044.

[265] Feibelman, P. J. Surface-diffusion mechanism versus electric field: Pt/Pt (001), *Phys. Rev. B* **2001,** *64,* 125403.

Publications

THE JOURNAL OF PHYSICAL CHEMISTRY Letters
Cite This: J. Phys. Chem. Lett. 2018, 9, 7153−7159
Letter
pubs.acs.org/JPCL

Origin of the Selective Electroreduction of Carbon Dioxide to Formate by Chalcogen Modified Copper

Rodrigo García-Muelas,[†] Federico Dattila,[†] Tatsuya Shinagawa,[‡] Antonio J. Martín,[‡] Javier Pérez-Ramírez,*[,‡] and Núria López*[,†]

[†]Institute of Chemical Research of Catalonia, The Barcelona Institute of Science and Technology, Av. Països Catalans 16, 43007 Tarragona, Spain

[‡]Institute for Chemical and Bioengineering, Department of Chemistry and Applied Biosciences, ETH Zürich, Vladimir-Prelog-Weg 1, 8093 Zurich, Switzerland

Supporting Information

ABSTRACT: The electrochemical reduction of atmospheric CO_2 by renewable electricity opens new routes to synthesize fuels and chemicals, but more selective and efficient catalysts are needed. Herein, by combining experimental and first-principles studies, we explain why chalcogen modified copper catalysts are selective toward formate as the only carbon product. On the unmodified copper, adsorbed CO_2 is the key intermediate, yielding carbon monoxide and formate as carbon products. On sulfur, selenium, or tellurium modified copper, chalcogen adatoms are present on the surface and actively participate in the reaction, either by transferring a hydride or by tethering CO_2 thus suppressing the formation of CO. These results highlight the active role of chalcogen centers via chemical steps and point toward basicity as the key descriptor for the stability and selectivity of these catalysts.

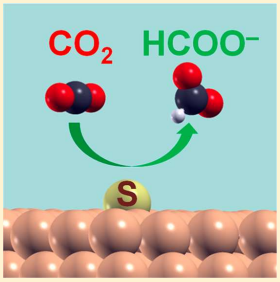

The electrochemical CO_2 reduction reaction (eCO_2RR) driven by renewable electricity can mimic the natural photosynthetic cycle and thus is a key element to meet climate targets.[1,2] In spite of the populated catalogue of catalysts identified, with carbon monoxide, hydrocarbons, and formate as more frequently reported products,[3−5] this technology remains at an incipient stage as existing materials are suboptimal regarding activity, selectivity, stability, and scalability for practical purposes.[6] These complications are related to the lack of robust structure-performance relationships, limited by (i) the complexity of the reaction network, (ii) the challenging application of *in situ* studies in electrochemical environments,[7] and (iii) the simplifications in the models representing electrochemical processes at the molecular scale.

Theoretical attempts to explain the eCO_2RR over well-defined transition metal surfaces[8−11] combine Density Functional Theory (DFT) and the computational hydrogen electrode (CHE) approach.[10,12,13] This strategy allows for solvent contributions to be introduced through approximate models,[14−16] while electric potential and pH effects can be added as linear corrections.[16,17] Neither the effect of the applied potential on adsorption nor the impact of pH on selectivity (known to control methane and ethylene formation[18−22]) are fully included in the simulations, although significant advances have been made lately (see ref 23 and references therein). On clean metals, the reaction starts with the adsorption of CO_2, followed by a succession of proton-coupled electron transfers (PCETs),[17] although decoupled steps have also been proposed;[17,24,25] see Scheme 1. The DFT-CHE model predicts medium-to-high overpotentials for eCO_2RR and describes selectivity trends observed for C_1 and C_2 products on different metals and surface orientations.[8,10,17,23] Carbon monoxide is the key intermediate for most eCO_2RR products, with the exception of formate. The linear scaling relationships (LSRs) between the binding energies of different intermediates on transition metals[26] impose constraints, limiting the optimization of metallic catalysts or alloys.[8,9,27] As we show in the present letter, surface modifiers can break LSRs by adding chemical (potential-independent) steps, thus improving the selectivity control.

Copper is unique in that it reduces CO_2 to compounds demanding more than two electron transfer steps with reasonable selectivity.[2,4] Recent studies have pointed out that p-block elements[5,24,29−34] can act as modifiers and that tiny amounts of sulfur[29,30] and selenium[29] switch the eCO_2RR selectivity toward formate, otherwise a minor product, while largely inhibiting the undesired hydrogen evolution reaction (HER). The aim of our work is to unravel the mechanistic origin of the selectivity switch reported for the sulfur-modified copper catalyst, Cu−S, and illustrate if the effect persists for other chalcogenides. To this end, we have performed DFT

Received: October 21, 2018
Accepted: December 11, 2018
Published: December 11, 2018

DOI: 10.1021/acs.jpclett.8b03212
J. Phys. Chem. Lett. 2018, 9, 7153−7159

Scheme 1. (a) Simplified Reaction Mechanisms for the eCO$_2$RR toward Formate/Formic Acid (Paths 1−2, in Olive and Yellow) and CO (Path 3, Red), and for the Parasitic HER (Path 4, Gray) on Clean Cu;[28, a] (b) Reactions Mechanisms in Which the Chalcogens Act as Active Centers: CO$_2$ Tethering (Path 6, Light Green), Heyrovsky-like Hydride Shuttle (Path 7, Dark Green), and the HER (Path 5, Black).[b]

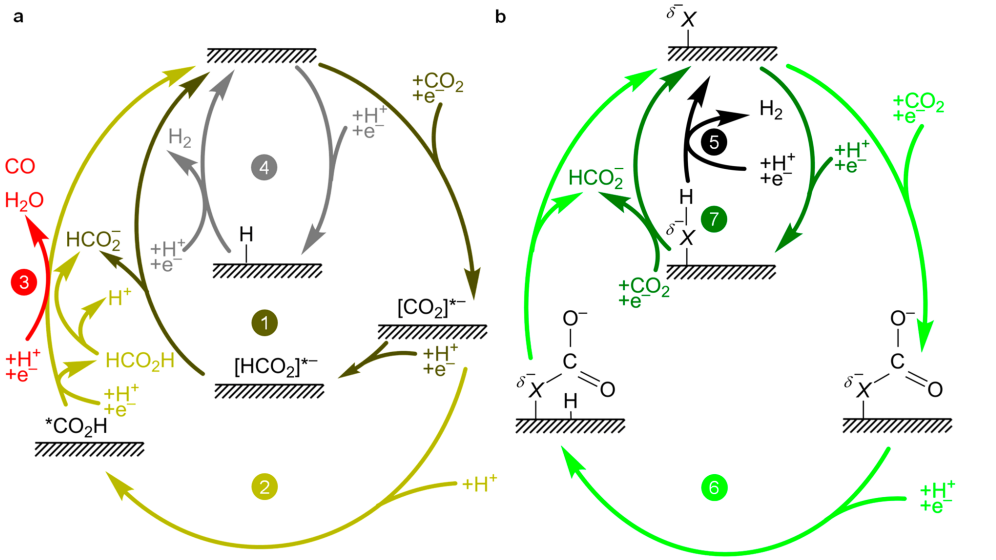

[a]The full mechanism is presented in Scheme S1. [b]The charge of an adsorbed chalcogen, δ^-, depends on the external potential U.

simulations for the systems including O, S, Se, and Te as dopants and compared them to the experimental systems. The true state of O-containing samples is difficult to assess (see below).

We synthesized three copper catalysts from its oxidic Cu$_2$O phase, modified by sulfur (Cu−S), selenium (Cu−Se), or tellurium (Cu−Te) via a solvothermal route.[30] The fresh samples exhibited microsized aggregates containing nanometric particles (Figures S1−S4) with a chalcogen content of 1−3 at. % relative to copper (Table 1). The chalcogens were uniformly distributed, as shown by energy dispersive X-ray spectroscopy coupled to scanning electron microscopy (EDX-SEM, Figure 1a). As for the crystalline structures, Cu−S, Cu−Se, and Cu−Te exhibited X-ray diffraction patterns assigned to Cu$_2$O accompanied by traces of the metallic Cu phase (Figure S2), likely due to the rapid formation of a native oxide layer over the metallic copper particles when exposed to air.[33] The introduction of the chalcogen modifiers did not alter the crystallite size. In addition, as chalcogens are present at low concentrations they likely prevented the identification of any related bulk chalcogen reflections. The presence of chalcogen species on the topmost surface (approximately 1 nm) of the synthesized catalysts was clearly indicated by the time-of-flight secondary ion mass spectroscopy (ToF-SIMS) analysis (Figure S5). X-ray photoelectron spectroscopy (XPS) analysis suggested a very limited presence of surface chalcogenide phases in the as-synthesized materials, as shown for measurements before eCO$_2$RR testing (Figure 1b; see signal at binding energies of ca. 162, 54, and 573 eV for Cu$_x$S, Cu$_x$Se, and Cu$_x$Te, respectively). The chalcogen-free catalyst (Cu−⌀) was prepared by skipping the addition of chalcogen species[29,30] (see Experimental Procedures in Section S1), resulting in unmodified Cu$_2$O particles (see Figure S3).

Table 1. Double-Layer Capacitance, C_{DL} in mF cm^{-2}, and XPS- or EDX-Measured Chalcogen Elemental Content, before and after Electrocatalytic Testing, in Atomic Percentage Relative to Cu[a]

		relative content			
	C_{DL}	XPS_{fresh}	XPS_{used}	EDX_{fresh}	EDX_{used}
Cu−⌀	2.9	78.2 ± 0.1	77.9 ± 0.1	45.8	48.7
Cu−S	1.4	3.4 ± 1.0	1.1 ± 1.1	0.6	0.6
Cu−Se	2.3	2.3 ± 2.2	1.5 ± 1.4	0.2	n.q.[b]
Cu−Te	2.8	n.q.[b]	10.0 ± 8.2	1.1	0.7

[a]For the Cu$_2$O-derived Cu catalyst (Cu−⌀), the percentages refer to oxygen. [b]n.q. nonquantifiable.

Cu−Se and Cu−Te exhibit slightly better catalytic performance than Cu with a mild preference for HCOO$^-$ among the eCO$_2$RR products measured with chronoamperometry (CA) at −0.6 V vs Reversible Hydrogen Electrode (RHE), Figure 1c. In contrast, over Cu-S, HCOO$^-$ is the main carbon product, being in equal proportion with H$_2$ whereas only trace amounts of CO were detected. The Cu−S becomes more selective toward formate at higher overpotentials until the presence of CO and more complex products, typically associated with clean copper, becomes detectable at −0.9 V vs RHE (Figures S6−S7).[35] At −0.8 V, the incipient volcano-like behavior in terms of selectivity observed at −0.6 V manifests now clearly (Figure 1c),suggesting the presence of a general effect modulated by the nature of the chalcogen. Comparison of our

DOI: 10.1021/acs.jpclett.8b03212
J. Phys. Chem. Lett. 2018, 9, 7153−7159

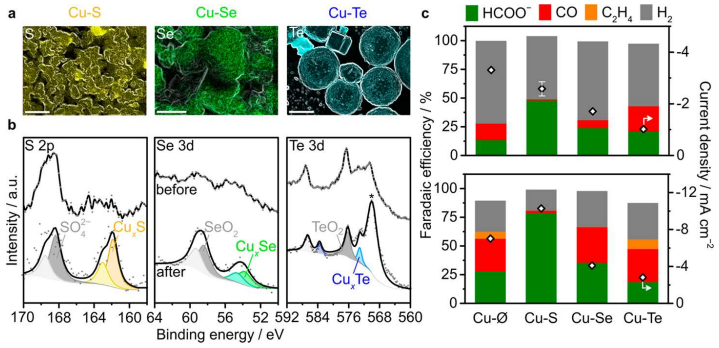

Figure 1. (a) EDX elemental maps of chalcogen elements for the corresponding fresh catalysts. White contours indicating the particle borders are added as a visual aid (see Figure S4). Scale bars: 2 μm. (b) Chalcogen XPS spectra before and after the eCO_2RR testing at −0.6 V vs RHE showing their presence after reaction. The peak indicated by asterisk (*) originates from the Auger emission in the Cu LMM region. (c) Product distribution over the copper-chalcogen catalysts, obtained by chronoamperometry at −0.6 (top) and −0.8 V (bottom) vs RHE for 1.5 h in 0.1 M $KHCO_3$ saturated with CO_2 (pH 6.7). Polycrystalline copper[10] yields around 10% of both $HCOO^-$ and CO at −0.6 V, and 20%/30%, respectively, at −0.8 V. Further tests regarding the electric potential dependence and the role of alkaline cations are presented in Figures S6–S8 and Section S3.

pure Cu (Cu–⌀) with polycrystalline, oxide-derived Cu reveals close similarities in product distribution,[10] suggesting the removal of oxygen atoms from the copper surface under reaction conditions. *In situ* studies on oxide-derived copper catalysts have hinted at the presence of oxygen near the surface.[32,36,37] Nevertheless, the absence of such an oxidic phase has also been suggested[33] and the promotion of carbon products formation was associated with grain boundaries.[33,34,38] Under the eCO_2RR conditions, the surface of the electrocatalysts reconstructs (Figure S1) and the chalcogen content seems to decrease within the limited accuracy at such low concentrations (Table 1). Accordingly, XPS excitations around the Cu 2p peak showed the presence of Cu_2O and Cu^{2+} (Figure S9), whereas peaks compatible with the copper chalcogenide phases built up (Figure 1b; Tables 1, S1).[39] The broad peaks at higher binding energies in Figure 1b are ascribable to oxidic phases,[40] presumably formed upon exposure of the chalcogenides samples to air during characterization.[41] Further ToF-SIMS analysis confirmed the increase in the relative abundance of chalcogen on the topmost layer upon the reaction (Figure S5). Upon the restructuring process, the surface remains populated by chalcogen atoms, although some leaching occurs.[30] We remark that the presence of copper chalcogenide phases after the eCO_2RR testing is not expected from a thermodynamic point of view, because Pourbaix diagrams predict metallic copper as the most stable phase under operation conditions (Figure S10); however, small domains cannot be fully discarded. In summary, the unmodified catalyst (Cu–⌀) can be identified as polycrystalline Cu under operation conditions, since (i) the removal of oxygen atoms or hydroxyl groups is largely favored (Tables S2 and S3) and (ii) the product distribution of Cu–⌀ follows that of polycrystalline Cu (Figure 1c). Therefore, the selectivity patterns observed for Cu–S, Cu–Se, and Cu–Te can be ascribed to the chalcogen modifier.

To unravel the origin of the selectivity patterns, polycrystalline Cu was modeled by the lowest energy Cu(111) surface. Our calculations show that the results of the Cu(211), (110), and (100) facets yield qualitatively the same results, Figure S11. In the model, the chalcogens (X = O, S, Se, Te) are added as adatoms sitting on surface fcc sites (Table S2) leading to a relative composition of 2.7 at. % (X = 1, Cu = 36) mimicking the experimental content, Table 1. Other structural models were tested but found less stable (Table S2). The removal of S, Se, and Te as H_2S, HSe^-, and H_2CO_2Te occurs at more negative potentials than U = −0.92, − 1.06, and −0.87 V vs RHE, respectively (Table 2), explaining why all Cu–X systems

Table 2. Computed Properties of the Chalcogen Modified Cu(111) Surface[a]

system	ΔG_{H_2X}	ΔG_{HX^-}	$\Delta G_{XCO_2H_2}$	q_{X^*}	$\varepsilon_p - \varepsilon_F$	$\Delta(\varepsilon_d - \varepsilon_F)$
Cu–O	−1.28	−0.84	+1.86	−0.93	−2.50	−0.16
Cu–OH	−0.60	−0.16	–	−0.59	−4.22	−0.11
Cu–S	+0.92	+0.94	+2.95	−0.59	−1.61	−0.07
Cu–Se	+1.22	+1.06	+3.74	−0.43	−1.28	−0.05
Cu–Te	+1.71	+1.48	+0.87	−0.21	−0.88	−0.07

[a] ΔG_{H_2X}, ΔG_{HX^-}, $\Delta G_{XCO_2H_2}$: desorption energies for the chalcogens to produce H_2X, HX^-, and XCO_2H_2 (X = O, S, Se, Te), in eV. q_{X^*}: Bader charges of the adsorbed chalcogen, in le$^-$l. $\varepsilon_p - \varepsilon_F$: center of the chalcogen p-band with respect to the Fermi level of the system, in eV. $\Delta(\varepsilon_d - \varepsilon_F)$: d-band center shift for the adjacent Cu atoms upon anchoring of the chalcogen, in eV.

were stable at the working potentials from −0.6 to −0.8 V vs RHE.[30] At more cathodic potentials than −0.90 vs RHE, the Cu–S performance starts resembling that of polycrystalline copper,[10] Table 2 and Figures S6. The stability of the Cu–S system was further tested, Figures S12–S13, suggesting the progressive loss of sulfur from the surface at deeper cathodic potentials.

To understand the mechanistic implications of the eCO_2RR on Cu, we start by analyzing the reactions listed in Scheme 1a where the parasitic hydrogen evolution reaction is also presented. In the reaction network, either coupled or sequential proton and electron transfers appear, and their relative contributions are given by their different dependence on the potential and the interface pH. To elucidate the origin of the selectivity switch imposed by the chalcogen modifier, we modeled CO_2 adsorption as an electron transfer process and

DOI: 10.1021/acs.jpclett.8b03212
J. Phys. Chem. Lett. 2018, 9, 7153–7159

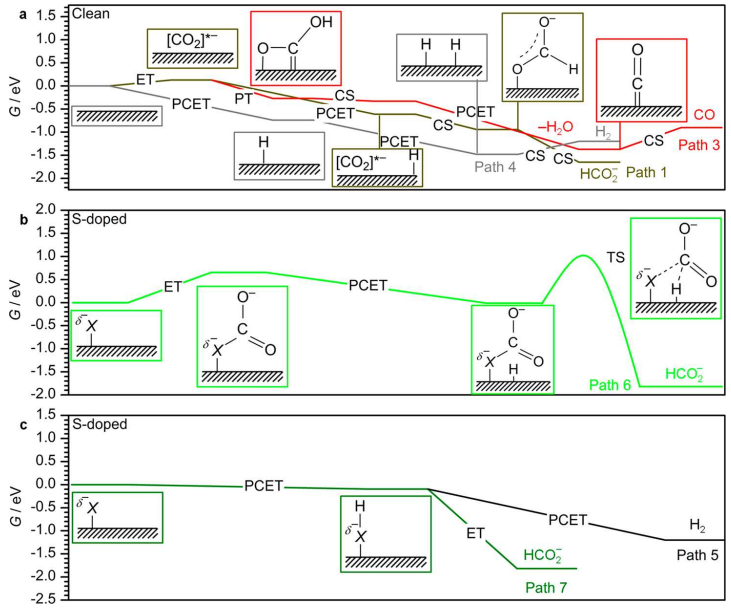

Figure 2. Gibbs free energy profiles on clean and chalcogen modified Cu(111) surfaces at $U = -0.6$ V vs RHE. (a) Electrochemical CO_2 reduction toward formate (path 1, olive), CO (path 3, red), and hydrogen evolution reaction (path 4, gray) on clean Cu(111). Path 2 is also downhill from $CO_2{}^{*-}$ and is omitted for simplicity. For S-modified surfaces (b) presents path 6 starting from tethered $CO_2{}^{*-}$ toward formate and (c) the S-mediated formate path 7 and HER. PCET: proton-coupled electron transfer. ET: electron transfer. PT: proton transfer. CS: chemical step. TS: transition state in CS. The profiles for $U = 0.0$ and -0.8 V vs RHE are shown in Figure S16, and those for other chalcogens, in Figure S17.

decoupled all the other steps along the whole reaction network when possible.[17,42] The rate-determining step in the eCO_2RR process is the difficult CO_2 adsorption both on pure metal electrodes and in molecular catalysts.[3,17,24] Raman spectroscopy has recently evidenced that the resulting carboxylate species is the first intermediate in the CO_2 conversion to formate on copper.[43,44] From a mechanistic perspective, successful CO_2 adsorption and activation imply the endothermic bending of the O−C−O bond, which requires 3.05 eV for the neutral molecule but only 1.23 eV for the negatively charged species, Figure S14. Therefore, its activation implies the electron transfer to its high lying LUMO.[45] On the surface, $CO_2{}^{*-}$ can adopt four possible conformations,[17] depending on the surface potential, Figure S15a. The most stable adsorbed structure at $U = -0.6$ V is $\eta_{2(C,O)}$, where both C and O are bonded to the surface.

Then a proton can be adsorbed onto the copper surface as H* through a PCET step, path 1 in Scheme 1a, reacting with the carboxylate via a chemical step yielding monodentate $HCOO^{*-}$, which desorbs as formate, Figure S15b,[46] similar to CO_2 reduction on PdH_x.[17] A proton from solution is transferred to a terminal oxygen of $CO_2{}^{*-}$, giving rise to a carboxyl intermediate (path 2) that reacts with H* to produce formic acid. Formic acid desorbs spontaneously and converts to formate due to the solution's pH (buffered at 6.7). Alternatively, the COOH* intermediate decomposes to CO* and water through either decoupled or concerted proton−electron transfer, path 3. The desorption of CO from Cu is endergonic,[9] Figure 2a, thus allowing further reduction toward methanol and hydrocarbons.[10] More cathodic potentials can stabilize the $CO_2{}^{*-}$ intermediate, thus simultaneously increasing the Faradaic efficiency or production of $HCOO^-$ and CO, until mild overpotentials are reached.[10] The parasitic HER, by contrast, occurs through either a classical Volmer−Tafel mechanism, path 4, or a Volmer−Heyrovsky mechanism, omitted here for simplicity. As both eCO_2RR and HER have H* as a common intermediate, a mild metal−hydrogen bonding strength promotes both reactions.[47] Applied to other transition metals, the reaction network in Scheme 1a predicts that they are poor formate-producing catalysts.[23,48,49]

The energy profile for Cu shown in Figure 2a at $U = -0.6$ V can be explained as follows: the markedly endergonic CO_2 adsorption, Table S4, requires considerable overpotentials to trigger its reduction. The HER largely predominates at potentials more anodic than −0.8 V. As CO_2 adsorption becomes more exergonic, paths 1 and 2 start competing with the HER (path 4). At higher overpotentials, the increasingly larger $CO_2{}^{*-}$ coverage enhances the production of formate and CO,[50] accounting for the concomitant HER decrease. In our energy profiles, Figure 2a, the HER is preferable over the CO_2 reduction. The larger Faradaic efficiency toward formate could come from mass-transport phenomena[19,51,52] (local pH at the interface, local CO_2 concentration) not included in our model.

Modification of the copper surface with chalcogen (X) adatoms leads to stable configurations with a polarized X−metal bond ($X^{\delta-}$) according to the Bader charges of $\delta = -0.93$, -0.59, -0.43, and -0.21 $|e^-|$ for O, S, Se, and Te respectively, Table S3. Along the series, the bond is more covalent as the partially empty p-states of the chalcogens lie

DOI: 10.1021/acs.jpclett.8b03212
J. Phys. Chem. Lett. 2018, 9, 7153−7159

closer to the highest, unperturbed Cu bands (the d-band is invariant; see Tables 2 and S3). At more negative potentials,[53] the partial charge of the chalcogens, $X^{\delta-}(U)$, increases to δ = −0.98, −0.76, −0.66, and −0.53 |e⁻|. The $X^{\delta-}$ surface site acts as a nucleophile to trap CO_2 concomitant with an electron transfer, producing a chalcocarbonate $X^{\delta-}CO_2{}^{*-}$, path 6 in Scheme 1b. The computed free energies for S-decorated Cu (new paths 5, 6, and 7) are shown in Figure 2. Due to its geometry, $X^{\delta-}CO_2{}^{*-}$ cannot form CO, as it would imply breaking the C−*X* and C−O bonds simultaneously. In parallel, a proton can adsorb on the neighboring Cu from the solution with an electron from Cu to form H*.[42] The reaction proceeds with H* attacking the carbon atom in $X^{\delta-}CO_2{}^{*-}$ to produce formate, as indicated by the inset labeled TS in Figure 2b. This potential-independent chemical step presents an activation energy of 1.02 eV. The $X^{\delta-}$ site can also attract protons to produce $X^{\delta-}H$, paths 5 and 7 in Scheme 1b. This species can attack either a proton or a CO_2 in the solution, to produce hydrogen (HER path 5) or formate (path 7) respectively in Heyrovsky-like mechanisms. Paths 6 and 7 agree with the Tafel plot in Figure S7, which indicates that the rate-determining step for the reaction involves a single electron transfer (slope 120 mV dec^{-1}). Finally, the presence of the chalcogen prevents the adsorption of CO_2 on its neighborhood (destabilizing adsorption by 0.53, 0.27, and 0.12 eV for first, second, and third nearest Cu sites, respectively), blocking unselective paths occuring on Cu-only sites, Figure 2.

The energy profiles in Figure 2 enable the rationalization of the experimental catalytic trends over Cu−S, Cu−Se, and Cu−Te in Figure 1c. Since all steps in path 7 become exergonic from U = −0.6 V vs RHE toward more cathodic potentials and the chalcogen atom destabilizes path 2, the chalcogen centers become highly selective for the eCO_2RR toward formate. As the formation of *X*H* becomes more endergonic for heavier chalcogens, the activity of paths 5 and 7 is reduced along the chalcogen series (Table S4). As already noted, the blocking effect of Se and Te in neighboring Cu atoms is milder than that of S, Table S4, in line with the experimental trends observed in Figure 1.

The differences in activity and selectivity can be traced back to an intrinsic property of the adsorbed chalcogenides as both the tethering of CO_2 (Figure 3a) and the formation of *X*H* (Figure 3b) depend on the donor ability of *X*. Figure 3c−d compile the key energy figures in paths 6 and 7 as a function of the basicity obtained as the p-band center of the chalcogen.[54] In Figure 3c (path 6) the low basicity enhances the stability of the $XCO_2{}^{*-}$ adsorbate, while higher basicity makes $HCOO^-$ formation more exergonic. In Figure 3d (path 7), the limiting factors are the formation of *X*H* and formate, where the former becomes more endergonic at larger basicities. In turn the HER is controlled by H adsorption on Cu (gray) and does not depend on the nature of the adatom. The optimal crossing point between the stability of the key intermediate and formate appears at −2.5 (path 6) and −2.2 eV (path 7), respectively. Thus, in both cases the chalcogen that shows the closest value is sulfur, which is in agreement with its unique catalytic performance among the family of chalcogen modifiers identified in Figure 1. It is also significant that the stability of the chalcogens on the surface correlates with the basicity, Figure S18.

In summary, the selective production of formate upon chalcogen modified copper is due to (i) the presence of basic sites where CO_2 is tethered blocking its dissociation toward CO, (ii) the ability of chalcogens to directly transfer hydrides to CO_2, and (iii) the effective blocking of unselective paths on the surrounding Cu atoms. Our results point out the role of chemical steps in electrochemical processes.

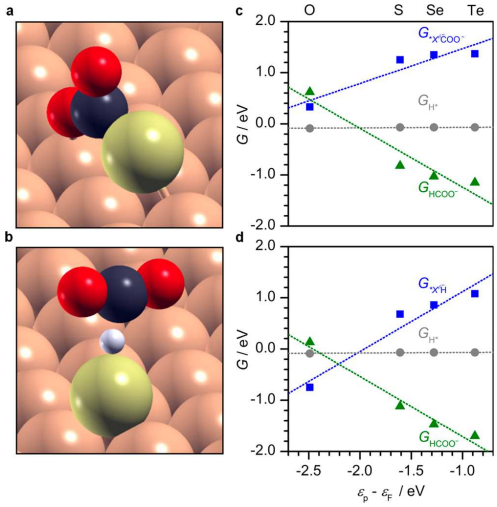

Figure 3. Most important intermediates for formate production (a) via CO_2 tethering on the chalcogen adatom or (b) via the Heyrovsky mechanism (path 6 and 7 in Scheme 1, respectively). (c−d) Gibbs energies (U = 0.0 V vs RHE) of the crucial intermediates as a function of the basicity of the chalcogen, computed as the center of the chalcogen p-band. Blue dots correspond to the energy of the precursors $X^{\delta-}CO_2{}^{*-}$ and $X^{\delta-}H$, respectively shown in the (a−b) panels, while the energy of $HCOO^-$ is shown in green. The largest activity is expected when the green and blue lines cross as the process will be isoenergetic. Gray dots represent the adsorption energy of hydrogen on copper atoms in the vicinity of *X*. Lines were added as a guide to the eye.

■ ASSOCIATED CONTENT

Supporting Information

The Supporting Information is available free of charge on the ACS Publications website at DOI: 10.1021/acs.jpclett.8b03212.

Experimental procedures, computational details, cation effect, supplementary schemes, figures, tables, and references (PDF)

■ AUTHOR INFORMATION

Corresponding Authors

*E-mail: jpr@chem.ethz.ch (J.P.-R.).
*E-mail: nlopez@iciq.es (N.L.).

ORCID

Rodrigo García-Muelas: 0000-0002-2219-5027
Javier Pérez-Ramírez: 0000-0002-5805-7355
Núria López: 0000-0001-9150-5941

Notes

The authors declare no competing financial interest.

The DFT data that support the findings of this study are available in ioChem-BD[55] at DOI 10.19061/iochem-bd-1-92.

DOI: 10.1021/acs.jpclett.8b03212
J. Phys. Chem. Lett. 2018, 9, 7153−7159

■ ACKNOWLEDGMENTS

We are thankful for the financial support from MINECO (Grant Number CTQ2015-68770-R), ETH Zurich, and the European Union under Projects A-LEAF (732840-A-LEAF) and ELCoREL (721624-ELCOREL). The ScopeM of ETH Zurich and the Barcelona Supercomputing Centre (BSC-RES) are thanked for access to their facilities and generous computational resources.

■ REFERENCES

(1) Kondratenko, E. V.; Mul, G.; Baltrusaitis, J.; Larrazábal, G. O.; Pérez-Ramírez, J. Status and Perspectives of CO_2 Conversion into Fuels and Chemicals by Catalytic, Photocatalytic and Electrocatalytic Processes. *Energy Environ. Sci.* **2013**, *6*, 3112−3135.
(2) Raciti, D.; Wang, C. Recent Advances in CO_2 Reduction Electrocatalysis on Copper. *ACS Energy Lett.* **2018**, *3*, 1545−1556.
(3) Gattrell, M.; Gupta, N.; Co, A. A Review of the Aqueous Electrochemical Reduction of CO_2 to Hydrocarbons at Copper. *J. Electroanal. Chem.* **2006**, *594*, 1−19.
(4) Kuhl, K. P.; Cave, E. R.; Abram, D. N.; Jaramillo, T. F. New Insights into the Electrochemical Reduction of Carbon Dioxide on Metallic Copper Surfaces. *Energy Environ. Sci.* **2012**, *5*, 7050−7059.
(5) Larrazábal, G. O.; Martín, A. J.; Krumeich, F.; Hauert, R.; Pérez-Ramírez, J. Solvothermally-Prepared Cu_2O Electrocatalysts for CO_2 Reduction with Tunable Selectivity by the Introduction of p-Block Elements. *ChemSusChem* **2017**, *10*, 1255−1265.
(6) Martín, A. J.; Larrazábal, G. O.; Pérez-Ramírez, J. Towards Sustainable Fuels and Chemicals through the Electrochemical Reduction of CO_2: Lessons from Water Electrolysis. *Green Chem.* **2015**, *17*, 5114−5130.
(7) Choi, Y. W.; Mistry, H.; Roldan Cuenya, B. New Insights into Working Nanostructured Electrocatalysts through Operando Spectroscopy and Microscopy. *Curr. Opin. Electrochem.* **2017**, *1*, 95−103.
(8) Peterson, A. A.; Nørskov, J. K. Activity Descriptors for CO_2 Electroreduction to Methane on Transition-Metal Catalysts. *J. Phys. Chem. Lett.* **2012**, *3*, 251−258.
(9) Hansen, H. A.; Varley, J. B.; Peterson, A. A.; Nørskov, J. K. Understanding Trends in the Electrocatalytic Activity of Metals and Enzymes for CO_2 Reduction to CO. *J. Phys. Chem. Lett.* **2013**, *4*, 388−392.
(10) Peterson, A. A.; Abild-Pedersen, F.; Studt, F.; Rossmeisl, J.; Nørskov, J. K. How Copper Catalyzes the Electroreduction of Carbon Dioxide into Hydrocarbon Fuels. *Energy Environ. Sci.* **2010**, *3*, 1311−1315.
(11) Nie, X.; Esopi, M. R.; Janik, M. J.; Asthagiri, A. Selectivity of CO_2 Reduction on Copper Electrodes: The Role of the Kinetics of Elementary Steps. *Angew. Chem., Int. Ed.* **2013**, *52*, 2459−2462.
(12) Nørskov, J. K.; Rossmeisl, J.; Logadottir, A.; Lindqvist, L.; Kitchin, J. R.; Bligaard, T.; Jónsson, H. Origin of the Overpotential for Oxygen Reduction at a Fuel-Cell Cathode. *J. Phys. Chem. B* **2004**, *108*, 17886−17892.
(13) Hussain, J.; Jónsson, H.; Skúlason, E. Faraday Efficiency and Mechanism of Electrochemical Surface Reactions: CO_2 Reduction and H_2 Formation on Pt(111). *Faraday Discuss.* **2016**, *195*, 619−636.
(14) Chan, K.; Nørskov, J. K. Electrochemical Barriers Made Simple. *J. Phys. Chem. Lett.* **2015**, *6*, 2663−2668.
(15) Xiao, H.; Cheng, T.; Goddard, W. A. Atomistic Mechanisms Underlying Selectivities in C_1 and C_2 Products from Electrochemical Reduction of CO on Cu(111). *J. Am. Chem. Soc.* **2017**, *139*, 130−136.
(16) Xiao, H.; Cheng, T.; Goddard, W. A.; Sundararaman, R. Mechanistic Explanation of the pH Dependence and Onset Potentials for Hydrocarbon Products from Electrochemical Reduction of CO on Cu(111). *J. Am. Chem. Soc.* **2016**, *138*, 483−486.
(17) Kortlever, R.; Shen, J.; Schouten, K. J. P.; Calle-Vallejo, F.; Koper, M. T. M. Catalysts and Reaction Pathways for the Electrochemical Reduction of Carbon Dioxide. *J. Phys. Chem. Lett.* **2015**, *6*, 4073−4082.
(18) Hori, Y.; Takahashi, R.; Yoshinami, Y.; Murata, A. Electrochemical Reduction of CO at a Copper Electrode. *J. Phys. Chem. B* **1997**, *101*, 7075−7081.
(19) Kas, R.; Kortlever, R.; Yılmaz, H.; Koper, M. T. M.; Mul, G. Manipulating the Hydrocarbon Selectivity of Copper Nanoparticles in CO_2 Electroreduction by Process Conditions. *ChemElectroChem* **2015**, *2*, 354−358.
(20) Schouten, K. J. P.; Qin, Z.; Gallent, E. P.; Koper, M. T. M. Two Pathways for the Formation of Ethylene in CO Reduction on Single-Crystal Copper Electrodes. *J. Am. Chem. Soc.* **2012**, *134*, 9864−9867.
(21) Huang, J.; Hörmann, N.; Oveisi, E.; Loiudice, A.; De Gregorio, G. L. Potential-Induced Nanoclustering of Metallic Catalysts during Electrochemical CO_2 Reduction. *Nat. Commun.* **2018**, *9*, 3117.
(22) Ren, D.; Fong, J.; Yeo, B. S. The Effects of Currents and Potentials on the Selectivities of Copper toward Carbon Dioxide Electroreduction. *Nat. Commun.* **2018**, *9*, 925.
(23) Hussain, J.; Jónsson, H.; Skúlason, E. Calculations of Product Selectivity in Electrochemical CO_2 Reduction. *ACS Catal.* **2018**, *8*, 5240−5249.
(24) Li, C. W.; Kanan, M. W. CO_2 Reduction at Low Overpotential on Cu Electrodes Resulting from the Reduction of Thick Cu_2O Films. *J. Am. Chem. Soc.* **2012**, *134*, 7231−7234.
(25) Göttle, A. J.; Koper, M. T. M. Proton-Coupled Electron Transfer in the Electrocatalysis of CO_2 Reduction: Prediction of Sequential vs. Concerted Pathways Using DFT. *Chem. Sci.* **2017**, *8*, 458−465.
(26) Montoya, J. H.; Peterson, A. A.; Nørskov, J. K. Insights into C-C Coupling in CO_2 Electroreduction on Copper Electrodes. *ChemCatChem* **2013**, *5*, 737−742.
(27) Pegis, M. L.; Wise, C. F.; Koronkiewicz, B.; Mayer, J. M. Identifying and Breaking Scaling Relations in Molecular Catalysis of Electrochemical Reactions. *J. Am. Chem. Soc.* **2017**, *139*, 11000−11003.
(28) Yoo, J. S.; Christensen, R.; Vegge, T.; Nørskov, J. K.; Studt, F. Theoretical Insight into the Trends That Guide the Electrochemical Reduction of Carbon Dioxide to Formic Acid. *ChemSusChem* **2016**, *9*, 358−363.
(29) Huang, Y.; Deng, Y.; Handoko, A. D.; Goh, G. K. L.; Yeo, B. S. Rational Design of Sulfur-Doped Copper Catalysts for the Selective Electroreduction of Carbon Dioxide to Formate. *ChemSusChem* **2018**, *11*, 320−326.
(30) Shinagawa, T.; Larrazábal, G. O.; Martín, A. J.; Krumeich, F.; Pérez-Ramírez, J. Sulfur-Modified Copper Catalysts for the Electrochemical Reduction of Carbon Dioxide to Formate. *ACS Catal.* **2018**, *8*, 837−844.
(31) Eilert, A.; Cavalca, F.; Roberts, F. S.; Osterwalder, J.; Liu, C.; Favaro, M.; Crumlin, E. J.; Ogasawara, H.; Friebel, D.; Pettersson, L. G. M.; et al. Subsurface Oxygen in Oxide-Derived Copper Electrocatalysts for Carbon Dioxide Reduction. *J. Phys. Chem. Lett.* **2017**, *8*, 285−290.
(32) Mistry, H.; Varela, A. S.; Bonifacio, C. S.; Zegkinoglou, I.; Sinev, I.; Choi, Y. W.; Kisslinger, K.; Stach, E. A.; Yang, J. C.; Strasser, P.; et al. Highly Selective Plasma-Activated Copper Catalysts for Carbon Dioxide Reduction to Ethylene. *Nat. Commun.* **2016**, *7*, 12123.
(33) Lum, Y.; Ager, J. W. Stability of Residual Oxides in Oxide-Derived Copper Catalysts for Electrochemical CO_2 Reduction Investigated with ^{18}O Labeling. *Angew. Chem., Int. Ed.* **2018**, *57*, 551−555.
(34) Verdaguer-Casadevall, A.; Li, C. W.; Johansson, T. P.; Scott, S. B.; McKeown, J. T.; Kumar, M.; Stephens, I. E. L.; Kanan, M. W.; Chorkendorff, I. Probing the Active Surface Sites for CO Reduction on Oxide-Derived Copper Electrocatalysts. *J. Am. Chem. Soc.* **2015**, *137*, 9808−9811.
(35) The double layer capacitance values obtained by cyclic voltammetry after the eCO_2RR testing (active surface areas) cannot account for the differences in catalytic performance.
(36) De Luna, P.; Quintero-Bermudez, R.; Dinh, C. T.; Ross, M. B.; Bushuyev, O. S.; Todorović, P.; Regier, T.; Kelley, S. O.; Yang, P.;

DOI: 10.1021/acs.jpclett.8b03212
J. Phys. Chem. Lett. 2018, 9, 7153−7159

Sargent, E. H. Catalyst Electro-Redeposition Controls Morphology and Oxidation State for Selective Carbon Dioxide Reduction. *Nat. Catal.* **2018**, *1*, 103−110.
(37) Xiao, H.; Goddard, W. A.; Cheng, T.; Liu, Y. Cu Metal Embedded in Oxidized Matrix Catalyst to Promote CO_2 Activation and CO Dimerization for Electrochemical Reduction of CO_2. *Proc. Natl. Acad. Sci. U. S. A.* **2017**, *114*, 6685−6688.
(38) Feng, X.; Jiang, K.; Fan, S.; Kanan, M. W. A Direct Grain-Boundary-Activity Correlation for CO Electroreduction on Cu Nanoparticles. *ACS Cent. Sci.* **2016**, *2*, 169−174.
(39) The discrimination of chalcogenide phases (Cu*X* and/or Cu_2X, *X* = S, Se) based on XPS is challenging due to the small difference in their binding energies acccording to the experimental determination, 0.2 eV; see ref 40.
(40) The National Institute of Standards and Technology (NIST). X-ray Photoelectron Spectroscopy Database. DOI: 10.18434/T4T88K.
(41) Cho, J. S.; Won, J. M.; Lee, J.-K.; Kang, Y. C. Design and Synthesis of Multiroom-Structured Metal Compounds-Carbon Hybrid Microspheres as Anode Materials for Rechargeable Batteries. *Nano Energy* **2016**, *26*, 466−478.
(42) Schreier, M.; Yoon, Y.; Jackson, M. N.; Surendranath, Y. Competition between H and CO for Active Sites Governs Copper-Mediated Electrosynthesis of Hydrocarbon Fuels. *Angew. Chem., Int. Ed.* **2018**, *57*, 10221−10225.
(43) Chernyshova, I. V.; Somasundaran, P.; Ponnurangam, S. On the Origin of the Elusive First Intermediate of CO_2 Electroreduction. *Proc. Natl. Acad. Sci. U. S. A.* **2018**, *115*, E9261−E9270.
(44) Deng, Y.; Huang, Y.; Ren, D.; Handoko, A. D.; Seh, Z. W.; Hirunsit, P.; Yeo, B. S. On the Role of Sulfur for the Selective Electrochemical Reduction of CO_2 to Formate on CuS_x Catalysts. *ACS Appl. Mater. Interfaces* **2018**, *10*, 28572−28581.
(45) Taifan, W.; Boily, J. F.; Baltrusaitis, J. Surface Chemistry of Carbon Dioxide Revisited. *Surf. Sci. Rep.* **2016**, *71*, 595−671.
(46) Joo, J.; Uchida, T.; Cuesta, A.; Koper, M. T. M.; Osawa, M. Importance of Acid-Base Equilibrium in Electrocatalytic Oxidation of Formic Acid on Platinum. *J. Am. Chem. Soc.* **2013**, *135*, 9991−9994.
(47) Zeradjanin, A. R.; Grote, J. P.; Polymeros, G.; Mayrhofer, K. J. J. A Critical Review on Hydrogen Evolution Electrocatalysis: Re-Exploring the Volcano-Relationship. *Electroanalysis* **2016**, *28*, 2256−2269.
(48) Larrazábal, G. O.; Martín, A. J.; Pérez-Ramírez, J. Building Blocks for High Performance in Electrocatalytic CO_2 Reduction: Materials, Optimization Strategies, and Device Engineering. *J. Phys. Chem. Lett.* **2017**, *8*, 3933−3944.
(49) Hori, Y.; Kikuchi, K.; Suzuki, S. Production of CO and CH_4 in Electrochemical Reduction of CO_2 at Metal Electrodes in Aqueous Hydrogencarbonate Solution. *Chem. Lett.* **1985**, *14*, 1695−1698.
(50) Phillips, K. R.; Katayama, Y.; Hwang, J.; Shao-Horn, Y. Sulfide-Derived Copper for Electrochemical Conversion of CO_2 to Formic Acid. *J. Phys. Chem. Lett.* **2018**, *9*, 4407−4412.
(51) Roberts, F. S.; Kuhl, K. P.; Nilsson, A. Electroreduction of Carbon Monoxide over a Copper Nanocube Catalyst: Surface Structure and pH Dependence on Selectivity. *ChemCatChem* **2016**, *8*, 1119−1124.
(52) Varela, A. S.; Kroschel, M.; Reier, T.; Strasser, P. Controlling the Selectivity of CO_2 Electroreduction on Copper: The Effect of the Electrolyte Concentration and the Importance of the Local pH. *Catal. Today* **2016**, *260*, 8−13.
(53) To simulate a more negative potential on the surface, a spectator K atom was added to the surface to donate electronic density. This was largely transferred to the chalcogen atom.
(54) Torres, D.; López, N.; Illas, F.; Lambert, R. M. Low-Basicity Oxygen Atoms: A Key in the Search for Propylene Epoxidation Catalysts. *Angew. Chem., Int. Ed.* **2007**, *46*, 2055−2058.
(55) Álvarez-Moreno, M.; de Graaf, C.; López, N.; Maseras, F.; Poblet, J. M.; Bo, C. Managing the Computational Chemistry Big Data Problem: The ioChem-BDPlatform. *J. Chem. Inf. Model.* **2015**, *55*, 95−103.

DOI: 10.1021/acs.jpclett.8b03212
J. Phys. Chem. Lett. 2018, 9, 7153−7159

ACS Energy Letters

http://pubs.acs.org/journal/aelccp

Active and Selective Ensembles in Oxide-Derived Copper Catalysts for CO_2 Reduction

Federico Dattila, Rodrigo García-Muelas, and Núria López*

Cite This: *ACS Energy Lett.* 2020, 5, 3176−3184

Read Online

ACCESS | Metrics & More | Article Recommendations | Supporting Information

ABSTRACT: Copper catalysts are unique in CO_2 reduction as they allow the formation of C_{2+} products. Depending on the catalysts' synthesis, product distribution varies significantly: while Cu nanoparticles produce mainly methane and hydrogen, oxide-derived copper leads to ethylene and ethanol. Here, by means of *ab initio* molecular dynamics on oxygen-depleted models, we identified the ensembles controlling catalytic performance. Upon reconstruction and irrespective of the starting structure, recurrent patterns defined by their coordination and charges appear: metallic Cu^0, polarized $Cu^{\delta+}$, and oxidic Cu^+. These species combine to form 14 ensembles. Among them, 4-(6-)coordinated Cu adatoms and $Cu_3^{\delta+}O_3$ are responsible for tethering CO_2, while metastable near-surface oxygens in fcc-(111) or (100)-like Cu domains promote C−C bond formation via glyoxylate species, thus triggering selective C_{2+} production at low onset potentials. Our work provides guidelines for modeling complex structural rearrangements under CO_2 reduction conditions and devising new synthetic protocols toward an enhanced catalytic performance.

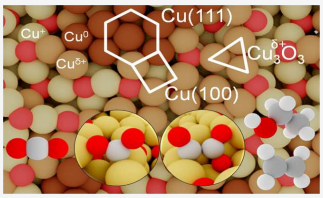

CO_2 reduction (CO_2R) has emerged as a suitable way to store renewable energy as chemical bonds.[1−3] Copper has a unique ability to promote C−C coupling toward C_{2+} products,[4] which are among the most sought-after chemicals.[5] Under reaction conditions, most copper-based catalysts reconstruct because of reaction intermediates and surface polarization caused by the applied electric potential.[6−9] As a consequence, the sample's history affects the activity, selectivity, and stability of the catalyst[6,10,11] (Table S1). In particular, polycrystalline Cu generates mainly CO, HCOOH, $HCOO^-$, H_2, and CH_4 at potentials more reductive than −0.8 V vs RHE,[12−15] while (110) and (111) steps nearby (100) terraces are selective toward C_{2+} products.[12] Instead, oxide-derived Cu catalysts (OD-Cu) show a higher overall activity for producing ethylene,[15−23] ethanol,[17] *n*-propanol,[17,24] *n*-butanol,[25] and traces of acetate and ethane,[17,26] at lower overpotentials than copper nanoparticles.[14,27−29]

To understand and control the key properties of OD-Cu upon reconstruction is crucial to rationally design more active and selective catalysts. It is generally thought that reconstruction boosts activity by increasing the electrochemically active surface area.[2,7,20,30] Regarding selectivity, CO dimerization is considered the crucial selectivity switch toward C_{2+} products.[2,31,32] Several features have been deemed responsible to promote that step, such as low coordinated Cu sites,[11,14,18,33] grain boundaries,[6,17,34] defects,[6,7] open facets,[6,27,35] surface roughness,[7,20] high surface pH,[35−37] cation effects,[2,32] and polarized $Cu^{\delta+}$ sites induced by residual oxygen.[6,15,20,22,23,38,39] However, the specific ensembles which control the selectivity to each product have not yet been identified.

The existence of residual oxygen on OD-Cu catalysts has been strongly debated in the literature, as its presence depends on the history of the material. Thermodynamically, copper oxide is expected to get fully reduced at neutral and alkaline pH for electric potentials lower than −0.1 V vs RHE (Figure S1). However, near-surface oxygen can be trapped kinetically[40] by oxidizing deeply the Cu sample before reduction[41] and by applying high cathodic potentials immediately after oxidation.[23,42] Near-surface oxygen atoms can also be restored by applying pulsed electrolysis[6,30] and by including a co-oxidant.[43] In contrast, materials obtained by shallow air oxidization of mono- or polycrystalline Cu get reduced beyond oxygen detection limits at CO_2 reduction conditions.[44,45] Preoxidation of polycrystalline Cu by mild anodic potentials also results in a low concentration of oxygen sites.[28] When present, residual oxygen atoms do not belong to bulk phases of copper oxide[46] but rather prefer grain boundaries[28] where Cu atoms have an oxidation state intermediate between Cu^0 and Cu^+.[30,39,47] Both residual oxygen and grain boundaries promote C_{2+} products.[34,39] Density functional theory (DFT) models have found

Received: August 17, 2020
Accepted: September 10, 2020
Published: September 22, 2020

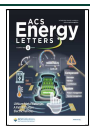

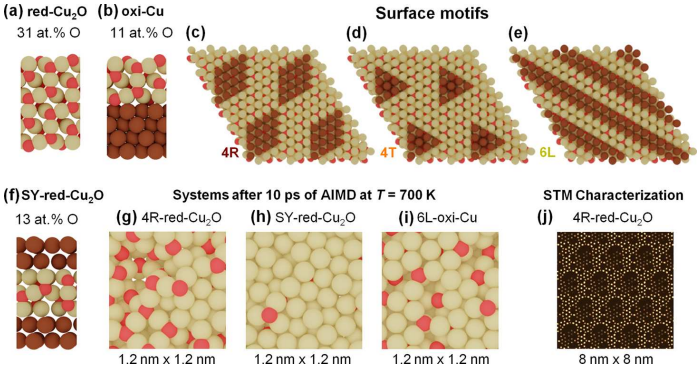

Figure 1. Models for OD-Cu. We considered two systems: (a) a $Cu_2O(111)$ slab to mimic Cu_2O reduction (red-Cu_2O) and (b) a Cu(111)/Cu_2O configuration to resemble Cu oxidation (oxi-Cu) (side views). For each supercell, O atoms were partially removed from the two outermost layers to create three depletion motifs: (c) rhomboidal (4R, patch), (d) triangular (4T, pitting), and (e) linear (6L, strip) (top views). (f) A symmetrical, Cu-terminated system (SY-red-Cu_2O) was included to investigate the influence of stoichiometry and depletion motifs. (g–i) After 10 ps of AIMD at 700 K, the final surfaces present analogous reconstruction (Videos S1–S7[55]) and (j) STM characterization detected similar patterns as experimental Cu/Cu_2O systems[56] (Figure S3). Red-Cu_2O and oxi-Cu systems were labeled *nS*, with *n* number of O atoms removed from the subsurface and *S* the shape of the O depleted region (dark brown). Red-Cu_2O and oxi-Cu suffixes were appended to differentiate both conditions.

that residual oxygen is stable and enhances CO adsorption in highly disordered structures,[48] but not at interstitial sites of crystalline Cu.[49,50] For crystalline phases, DFT simulations have rationalized the selectivities observed for (111), (100), and stepped Cu surfaces toward C_1–C_2 products as a function of CO and H energy descriptors.[3,51] Besides, linear scaling relationships between surface site reactivity and coordination numbers are commonly employed to assess the properties of metals and oxides, in particular for disordered environments.[52,53] However, theoretical models still need to be adapted to the dynamic view of catalytic interfaces, such as OD-Cu under CO_2 reduction conditions.[54]

As DFT-based modeling has focused on rather ideal structures, here we have envisaged an alternative way to understand the reactivity of OD-Cu. Starting from pristine oxides, we have removed oxygen atoms to create oxygen-depleted structures and allow reconstruction upon *ab initio* molecular dynamics. Although several crude approximations have been introduced (see below), we have identified new structural patterns that completely modify our understanding of these materials. In this way, we investigated roughness, coordination, oxidation states, and spectroscopic fingerprints for these structures, showing 14 recurrent ensembles with three chemical species: Cu^0, $Cu^{\delta+}$, and Cu^+. The ensembles characterized by mild polarization are responsible for OD-Cu enhanced activity and C_{2+} selectivity via a newly identified-glyoxylate-like intermediate, Table S2.

OD-Cu catalysts are typically synthesized via oxidation of Cu foils or by electrochemical reduction of copper oxides.[17,45] To mimic changes in OD-Cu morphology under reaction conditions, we built structural models to represent both reduction of Cu_2O (red-Cu_2O) and oxidation of Cu (oxi-Cu) (Figure 1a,b).

In the reduction models, OD-Cu were constructed as a $2\sqrt{3} \times 2\sqrt{3} - R30^\circ$ $Cu_2O(111)$ supercell with about 21 Å lateral size. Then, the oxygens in the outermost layer (12/144) were removed, as suggested by ref 45, along with part of the subsurface sites (4–6/144) to reproduce experimental reports (O content: 10–20 atom %).[19,20] The Cu/O stoichiometry for these systems accounted for an overall oxygen atomic percent of 31–30 atom %, higher than experimental values because of the contribution of the bulk oxide (Table S3). Oxygen depletion followed three different shapes: rhomboidal (R), triangular (T), and linear (L), to promote clustering, pitting, and formation of grain boundaries, respectively (Figures 1c–e and S2). The suboxide formation energies of these initial structures differ only by 0.01 eV/Cu atom (Table S3), proving that they are potentially equivalent starting points. The systems were labeled *nS*: *n* stands for the number of subsurface oxygens removed, and *S* indicates the depletion motif, R, L or T (Figure 1c–e). Deep reduction conditions were simulated through a symmetric slab (SY-red-Cu_2O), $2\sqrt{3} \times 2\sqrt{3} - R30^\circ$ $Cu_2O(111)$ supercell, 7 layers thick. Here, just the two central Cu_2O layers were preserved while removing 120/168 of all the oxygen atoms, leaving 13 atom % of oxygen (Figure 1f). Alternatively, oxidized Cu surfaces were reproduced depositing three Cu_2O layers on $5\sqrt{3} \times 5\sqrt{3} - R30^\circ$ bulk Cu(111) to recreate the geometric stress throughout surface reconstruction. Surface and subsurface oxygens were removed following the same procedure as before: taking the 4R model as reference, the formation energies by copper atom differ by ≤0.01 eV (0.21, 0.21, and 0.22 for the 4R, 4T, and 6L systems; Table S3).

Surface reconstruction was assessed through AIMD with the PBE density functional (ref 57) for 10 ps at 700 K (3 fs time step). Solvent, potential, and electrolyte were not included during AIMD simulations. Although the approximations of our models are severe, our analysis demonstrates the strong structural modifications which occur on these materials under reaction conditions. The assessment of the robustness of our results is summarized in Table S2. Benchmark tests on Hubbard correction and AIMD temperatures were performed on the 4R-red and 4R-oxi systems (Computational Methods in the Supporting Information). Similar surface patterns evolved

https://dx.doi.org/10.1021/acsenergylett.0c01777
ACS Energy Lett. 2020, 5, 3176–3184

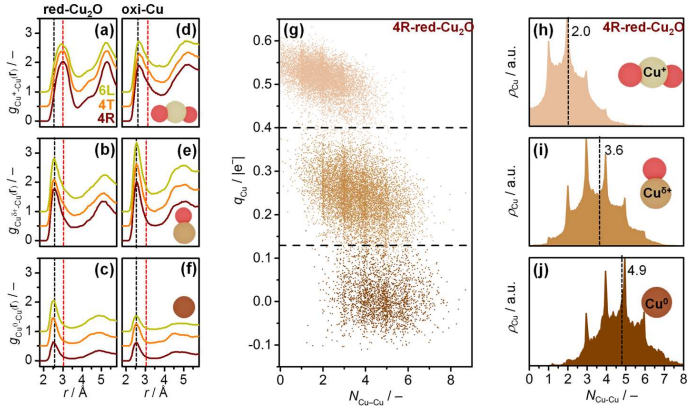

Figure 2. Characterization of Cu species. (a–f) Cu–Cu RDF for Cu atoms coordinated with 0–2 oxygens as shown in the insets. The first (second) coordination shell of bulk Cu (Cu_2O) is shown as black (red) dashed lines. Cu–Cu RDF for the SY-red-Cu_2O system is reported in Figure S12. (g) Cu atoms coordinated to 0–2 oxygens show clear differences in their Bader charges and number of Cu atoms in their first coordination shell. (h–j) Cu–Cu coordination number (N_{Cu-Cu}) cumulative maps show peaks at integer N_{Cu-Cu}, suggesting the existence of recurring ensembles. Average $\bar{N}_{Cu-Cu}$, dashed lines, differ by 1.0 units from metallic to polarized and almost 3.0 to oxidic Cu. Bader charges and N_{Cu-Cu} distributions for the remaining systems are reported in Figures S15 and S17.

upon reconstruction, while their abundance depended on Cu/O stoichiometry (Figure 1g–i). The final structures reproduced the overall disorder characterized by local recurrent features with around 1 nm periodicity and O depletion regions reported as dark areas in STM images of Cu_2O/Cu(111) surfaces under CO autocatalytic reduction[56] (Figure S3). The thermodynamic stability of the models was estimated from their Pourbaix diagrams. The final snapshots of the AIMD simulations were further optimized to their lowest-energy configuration, and solvation contributions were included to the optimized structures through an implicit model.[58,59] Stabilized by configurational entropy and solvation, our disordered systems are metastable.[60] Their formation energy is slightly higher than the thermodynamically stable phase (Cu_2O) by at most 0.1 eV, but significantly, they are more stable than experimentally reported oxidic phases, Cu_8O and $Cu_{64}O$[61] (Tables S4–S7, Figure S1, and eqs S5–S9). Moreover, in our models, O stability on reconstructed surfaces depends on its local coordination: at mild negative potential O desorption is endothermic because of high surface pH,[35−37,62] which may increase up to 14 for high cathodic current densities[63] (Supporting Discussion, Figure S4). Depending on the surface pH, the stability region of residual oxygens extends until −0.84 V vs RHE, in good agreement with recent experimental reports.[6,23,42,64,65] Uncertainty in surface pH determination by 1–2 units and the lack of configuration entropy contribution set the limit for O borderline-stability between −0.6 and −1.0 V vs RHE (Supporting Discussion). Structural characterization was performed on the two outermost layers for the whole AIMD production period. We investigated surface roughness (σ), number of surface sites, radial distribution functions (RDF), Cu coordination numbers (N_{Cu-Cu}), spectroscopic properties, and recurrent ensembles for each of the trajectories (Computational Methods). Final AIMD trajectories show similar Cu 2p and O 1s XPS fingerprints as OD-Cu experimental systems (Figure S5). Analogously, vibrational spectra (eqs S10–S13) qualitatively reproduce Raman shifts detected in experimental reports, as shown in Figures S6 and S7.

OD-Cu activity has been attributed to a higher surface area upon reconstruction.[2,7,20,30] However, previous theoretical simulations did not succeed in quantifying nanostructuring.[39,46,48−51] Through the continuous reorganization induced by AIMD, we were able to assess OD-Cu reconstruction through arithmetic average surface roughness, σ (eqs S14 and S15 and Figure S8). Theoretical atomic roughness was calculated to range within 0.8–1.4 Å for our OD-Cu models (Figure S9); thus, it was significantly higher than experimental values for crystalline Cu, 0.32 Å.[66] For red-Cu_2O systems, surface roughness did not change significantly after equilibration, while oxi-Cu surfaces kept reconstructing until σ = 1.5, 1.1, and 1.0 Å for 4R, 4T, and 6L, respectively, until 8 ps AIMD time, because of the geometric stress between metallic and oxidic layers. The ratio of surface sites of the reconstructed surfaces versus surface sites of crystalline Cu_2O(111) increases by 120% (140%) for red-Cu_2O (oxi-Cu) with regard to pristine oxidic copper (Figure S10 and eq S16), in line with the increased electrochemically active surface area on OD-Cu.[7] 6L-oxi-Cu presents the largest increment of surface sites among all the configurations, albeit showing the lowest atomic surface roughness. Therefore, we identify grain boundaries as minor perturbations of the surface which determine mild surface roughness but large active area, as suggested experimentally.[34] In contrast, reconstruction strongly modified rhomboidal (4R) and triangular configurations (4T), increasing surface roughness (Figure 1c,d and Videos S1–S7[55]).

To determine the local coordination of Cu atoms, we calculated Cu–Cu and Cu–O RDFs, g_{Cu-O} and g_{Cu-Cu} (eqs S17 and S18). For all the systems, g_{Cu-O} shows a well-defined minimum at a Cu–O distance of 2.50 Å, which is between the first and second peaks of bulk Cu_2O: 1.87 and 3.57 Å (Figure S11). Thus, we set d_{Cu-O} = 2.50 Å as threshold for O coordination to Cu. Consequently, we found that Cu exists in three well-defined states according to its coordination to

https://dx.doi.org/10.1021/acsenergylett.0c01777
ACS Energy Lett. 2020, 5, 3176–3184

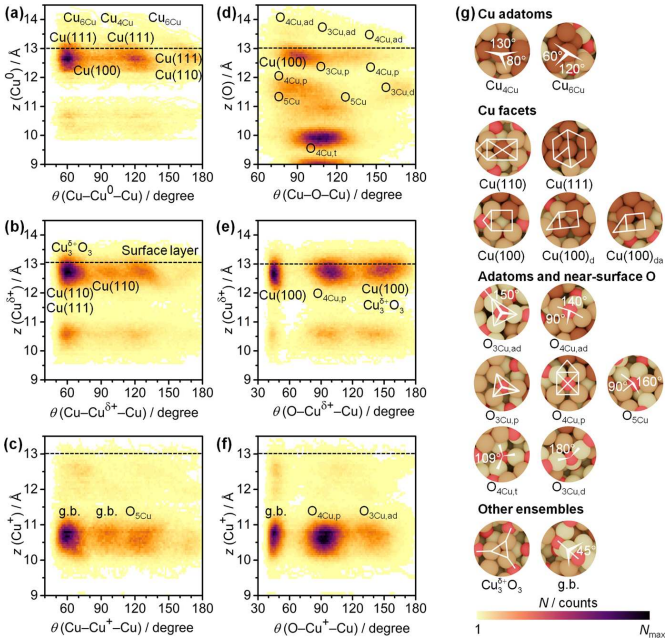

Figure 3. Recurrent ensembles in OD-Cu models. (a–f) Histograms for angles $\theta(A-B-C)$ measured around the first coordination shell of central atom B at different heights $z(B)$ for the 4R-red-Cu_2O system. The ensembles responsible for each feature are labeled and shown in panel g; tetra- and hexa-coordinated Cu adatoms: Cu_{3Cu} and Cu_{4Cu}; reminiscent of crystalline Cu: Cu(100)-like facets, including distorted forms mainly metallic or asymmetric in charge (subscripts "d" and "da"), Cu(110) and Cu(111) facets; $Cu_3^{\delta+}O_3$; Cu/Cu_2O grain boundaries, g.b. (Figure S2); tri- and tetra-coordinated O adatoms: $O_{3Cu,ad}$ and $O_{4Cu,ad}$; tri- and tetra-coordinated planar O: $O_{3Cu,p}$ and $O_{4Cu,p}$; penta-coordinated near-surface O: O_{5Cu}; tetrahedral O: $O_{4Cu,t}$; distorted near-surface O: $O_{3Cu,d}$. Comparison with other models and values of N_{max} are reported in Figures S21 and S22.

nearby oxygen atoms: metallic, suboxidic, and oxidic Cu (Figure 2). Suboxidic $Cu_2O_{0.5}$-like species have been also detected experimentally,[30,47,64] and EXAFS characterization confirmed an average Cu−O coordination number of 1.1 for suboxidic Cu.[64] Despite presenting different stoichiometry (31, 13, and 11 atom % O) and initial configurations (Table S3), all the models gave comparable RDFs upon AIMD, thus reinforcing the general nature of our results (Figures 2a–f and S12).

The first Cu−Cu coordination shell is a combination of crystalline Cu and Cu_2O, somewhat smeared in the intermediate values (Figure 2a–f). To calculate the coordination number of each Cu to neighboring Cu atoms, N_{Cu-Cu}, we counted 1 bond when the Cu−Cu distance was the one of metallic Cu, no bonds for the one of Cu_2O, and applied a Gaussian smearing for the values in between (eqs S19–20 and Figure S13). The distribution of $\bar{N}_{Cu-Cu}$ values averaged over time does not show significant changes for red-Cu_2O models (Figure S14). In contrast, oxi-Cu systems again reveal a continuous reconstruction process until 6 ps, where metallic-like configurations reform from pristine low coordinated Cu. As a general trend, Cu is undercoordinated when compared to typical values for crystalline facets (Table S8). When coordinated to 1 oxygen, copper atoms lose 1 Cu bond; thus, $\bar{N}_{Cu-Cu} \approx 4$ (5) for the two families of models. Finally, double O coordination saturates Cu sites; thus, $\bar{N}_{Cu-Cu}$ further decreases by 2 metallic bonds, ∼2 (3) for red-Cu_2O (oxi-Cu). In agreement with our theoretical predictions of $\bar{N}_{Cu-Cu}$ = 4.9, 3.6, and 2.0 for metallic, suboxidic, and oxidic copper, respectively (Figure 2h–j), $\bar{N}_{Cu-Cu}$ of 6.6, 3.08, 2.21, and 1.84 have been experimentally reported for OD-Cu systems.[64,67]

Moving ahead to address key contributors to OD-Cu performance, we then targeted Cu electronic structure.[6,15,20,22,38] We sampled the Bader charges for the whole simulation period at a time step of 48 fs. Because the seven models feature analogous structural properties (Figures 2a–f and S12) we focused the analysis on the 4R-red-Cu_2O system, whereas the characterization of other models is reported in Figure S15. As shown in Figure 2g, the three Cu species described in the previous section account for well-defined oxidation states. Metallic and oxidic Cu charges are centered at 0.0 and 0.5 |e$^-$|, respectively, akin to bulk Cu and Cu_2O. We labeled these species as metallic, Cu^0, and oxidic copper, Cu^+. Cu atoms coordinated with one oxygen exhibit intermediate positive polarization with a well-defined boundary between 0.1 ≤ q_{Cu} ≤ 0.4 |e$^-$|. Thus, we assign this species to the previously proposed polarized Cu, also called "suboxidic", $Cu^{\delta+}$.[30,47,64]

The relative abundance of these three species depends on the initial configuration and stoichiometry (Figure S16 and

https://dx.doi.org/10.1021/acsenergylett.0c01777
ACS Energy Lett. 2020, 5, 3176−3184

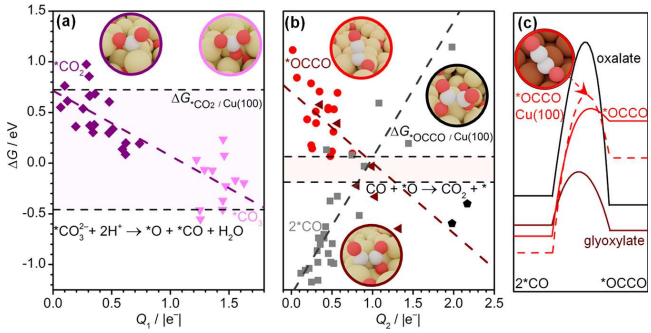

Figure 4. CO_2R activity and C_{2+} selectivity of OD-Cu versus ensemble polarization. (a) OD-Cu can adsorb CO_2 either on a Cu site (purple) or on a near-surface oxygen (magenta) forming a carbonate. CO_2 adsorption energy scales linearly with the polarization of the active sites, Q_1: $\Delta G_{*CO_2} = +0.7(\pm0.1) - 0.6(\pm0.1)Q_1$. Cu^0−$Cu^{\delta+}$ and $Cu^{\delta+}$−$Cu^{\delta+}$ are responsible for enhancing OD-Cu CO_2R (purple area), while activity of O_{ns} sites is limited by carbonate formation. (b) Polarization of active ensembles, Q_2, drives selectivity to C_2 products: $\Delta G_{*OCCO} = +0.7(\pm0.1) - 0.7(\pm0.1)Q_2$. A paired active site, $Cu^{\delta+}$-O_{ns}, stabilizes the CO−CO dimer as a glyoxylate-like intermediate (dark red), enhancing C_2 production. In contrast, for metallic Cu sites (red) CO dimerization is not favored, leading to a higher *CO coverage (gray), $\Delta G_{2*CO} = -1.3(\pm0.1) + 1.3(\pm0.1)Q_2$. For very strong polarization, stable oxalates are generated on the surface (black). Q_1 and Q_2 are defined as the sum of absolute Bader charges of the atoms in the ensemble calculated with implicit solvation (eqs S21 and S22, Figure S27). (c) *OCCO intermediate on both OD-Cu and Cu(100) and oxalate formation on OD-Cu presents a high kinetic barrier of more than 1 eV. The pathway toward the glyoxylate-like intermediate has instead a mild barrier of 0.53 eV. Potential and dipole corrections, here not included, stabilize all intermediates similarly (Table S16). Further details on the linear regressions are shown in Table S17.

Table S9). Red-Cu_2O accounts high abundance of $Cu^{\delta+}/Cu^+$ sites, while the stronger reconstruction occurring on oxi-Cu systems determines an increase of Cu^+ species. Metallic copper is instead favored by low O atomic percentage, as expected for the SY-red-Cu_2O system. The presence of residual Cu^+ species upon reconstruction agrees with recent experimental reports for Cu_2O nanocubes (20% at −0.95 V vs RHE) and Cu(100) under CO_2 pulsed electroreduction (7−11% at −1 V vs RHE).[6,42] N_{Cu-Cu} cumulative maps prove the existence of atomic ensembles for all the three classes: metallic Cu^0 (Figure 2j), polarized $Cu^{\delta+}$ (Figure 2i), and oxidic Cu^+ (Figure 2h). The analysis of the remaining models support this finding (Figure S17).

In addition to averaged properties, a unequivocal identification of recurrent ensembles requires local characterization. Atomic ensembles are defined by their interatomic distances and angles. Therefore, we mapped the occurrence of interatomic angles versus the *z*-coordinate of the central atom to identify its coordination environment. As a result we detected 14 recurrent ensembles which were stable at different AIMD temperatures, Figure S18−S19, and with Hubbard correction, Figure S20. As a 2-dimensional histogram, darker areas represent higher density of atoms with a given angle with neighboring sites at a given *z*-coordinate, within the two outermost layers, Figure 3a-f and Figures S21−S22. For metallic copper, Cu^0, we identified a few 4- and 6-coordinated Cu adatoms, Cu_{4Cu}−Cu_{6Cu}. In addition, surface reconstructs into reminiscent of crystalline domains, such as Cu(100), Cu(110), and Cu(111), either fully metallic or including few polarized $Cu^{\delta+}$. Few surface $Cu^{\delta+}$ species aggregate in triangular $Cu_3^{\delta+}O_3$ ensembles. This ensemble has been characterized experimentally very recently in ref 30, and reconstruction of Cu-based catalysts toward open facets was detected through *operando* electrochemical STM.[9,44] Oxidic Cu^+ is not abundant at the outermost layers, and the interface between Cu^+ and Cu^0−$Cu^{\delta+}$ species mimics the grain boundary motif reported in Figure S2. Regarding the oxygen atoms, their preferred configuration depends on their position. Inner atoms adopt mainly bulk-like tetrahedral shapes, $O_{4Cu,t}$, as well as few distorted configurations with 3-fold or 5-fold coordination, $O_{3Cu,d}$, O_{5Cu}. Besides, there is a strong, narrow signal at 45° which is characteristic of a "grain boundary" ensemble (g.b. in Figure 3g). Near-surface oxygens (O_{ns}) prefer to adopt planar configurations, namely $O_{3Cu,p}$ and $O_{4Cu,p}$. Finally, oxygen adatoms may coordinate with three or four Cu atoms, $O_{3Cu,ad}$ and $O_{4Cu,ad}$. These adatoms give a mild and diffuse signal, meaning that they are less abundant than near-surface configurations and do not have any strong preference to adopt a particular shape. In recent experiments, near-surface oxygen has been found stable in $Cu_2O_{0.5}$ stoichiometry at potentials as reductive as −1.0 V vs RHE,[64] but there is scarce experimental information about the remaining oxygen ensembles.

Previous computational studies assessed the catalytic properties of very ordered systems,[3,51] including O as an impurity in crystalline Cu for modeling OD-Cu catalysts.[39,46,48] Our analysis proves that the landscape of OD-Cu catalysts might be much more complex because of the appearance of several new ensembles. Because metastable states, even if less abundant, can be the active sites which drive the activity and selectivity of metals and oxides,[54] here we investigated the adsorption properties of the identified ensembles to obtain new potential descriptors for CO_2 reduction on OD-Cu. We evaluated *CO_2, *OCCO, and 2*CO adsorption energies, as these molecules are generally reported as the key intermediates for CO_2R activity and C_{2+} selectivity.[2] Because local configurations do not change significantly among red-Cu_2O and oxi-Cu models (Figures S21 and S22), we sampled only the first ones.

Our simulations show that CO_2 adsorbs via Cu−C and Cu−O bonds, $\eta^2_{C,O}$, on Cu sites (Figure 4a, purple), or via a O_{ns}−C bond on near-surface O (Figure 4a, magenta). CO_2 adsorption

https://dx.doi.org/10.1021/acsenergylett.0c01777
ACS Energy Lett. 2020, 5, 3176−3184

energy scales linearly with the polarization of the ensembles, approximated by Q_1, the sum of their Bader charges in absolute value (eqs S21 and S22). $X^{\delta-}-Cu^{\delta+}$ (X = O, Cu^0) asymmetric pairs are strong binding sites for CO_2 because of high polarization. $Cu^0-Cu^{\delta+}$ and $Cu^{\delta+}-Cu^{\delta+}$ pairs in ensembles Cu_{4Cu}, Cu_{6Cu}, and $Cu_3^{\delta+}O_3$ (Figure 3g) can tether CO_2 more favorably than crystalline copper by 0.5 eV (0.2 eV vs 0.7 eV, Table S10). Cu^+ sites, saturated by the 2 neighboring O atoms, do not play a relevant catalytic role (Figure S23). In the literature, the specific role of the $Cu^0_{adatom}-Cu^{\delta+}(Cu^+)$ pair on CO_2 activation has been suggested.[39,68] Here, we provide a generalized model, proposing negative (positive) polarization on C (O) binding sites as a general descriptor for CO_2 activity. As experimental evidence, CO_2 adsorption has been detected *via* SEIRAS spectroscopy at low overpotential for suboxidic and oxidic Cu.[15] High local polarization accounts for the remarkable performance of OD-Cu, along with higher surface roughness and number of active sites (Figures S9 and S10). The high electronic density localized on near-surface $O_{3Cu,p}$ and $O_{4Cu,p}$ oxygens (Figure 3g) saturates the $O_{ns}-C$ bond; thus, it leads to saturation of CO_2 binding energy to high exothermic values (Figure S24). As a consequence, the surface is passivated from carbonate coverage, and it is not active anymore for CO_2 reduction.[38] Carbonate coverage has been reported on OD-Cu under CO_2 reduction conditions via *in situ* and real-time surface-enhanced infrared absorption spectroscopy (SEIRAS) (Table S11).

Because CO_2 reduction activity is promoted by local polarization, we now focus on the CO−CO dimer, whose stability on the surface has been proposed to determine CO_2 selectivity and therefore C_{2+} product distribution.[2,32] In Figure 4b we present the stability of the dimer for the identified local ensembles. Again, the adsorption energy for the dimer depends linearly on the sum of the Bader charges of the ensembles, Q_2, proxy of their polarization (eqs S21 and S22). We can identify 3 types of adsorbed species: CO−CO dimer, *OCCO; glyoxylate-like intermediates, *OCCOO; and oxalate, *OOC-COO. Metal-only domains generate CO−CO dimers (Figure 4b, red inset), which are easily dissociated, therefore leading to similar product distribution as copper foil and nanoparticles (H_2, CH_4).[12,14] Polarized $Cu^0-Cu^{\delta+}$ (100)−(110) facets (Figure 3g) exhibit similar reactivity as crystalline Cu(100) (Table S10), thus confirming the experimental hypotheses on structural and chemical affinity between crystalline open facets and OD-Cu.[27,35] For very high surface polarization, strongly bound oxalates are generated on the surface *via* two near-surface oxygens (Figure 4b, black inset). If formed, oxalates could cause surface passivation and Cu dissolution; however, this process is hindered by the high kinetic barrier associated, 1.51 eV (Figure 4c, black inset). Furthermore, if oxygen sites tether CO too strongly, they may desorb as CO_2 (lower dashed line in Figure 4b and Table S12). Mild surface polarization makes CO−CO formation thermoneutral; therefore, it enables the dimerization reaction.[69,70] Glyoxylate-like species OC*CO-(O_{ns}) triggers OD-Cu selectivity to C_{2+} because of the low kinetic barrier associated to its formation, 0.53 eV (Figure 4b-c, dark red inset). The carbon atoms of this intermediate are separately adsorbed on a bridge position between low coordinated Cu and atop a near-surface oxygen. The local Cu coordination resembles either Cu(111) facets or the $Cu_3^{\delta+}O_3$ ensemble previously reported (ref 71) (Figure S25). Glyoxylate is a well-known intermediate for prebiotic CO_2 reduction,[72] although to the best of our knowledge its dehydrogenated form, OC*CO(O_{ns}), has not yet been reported in electrochemical CO_2 literature.[31,73] We highlight that glyoxylate and oxalate production may occur as well via direct CO_2 reduction (Table S13) and that glyoxylate vibrational frequencies (1630, 1479, and 1145 cm^{-1}; Table S14) are compatible with SEIRAS and IR spectroscopy signals for CO_2 reduction on OD-Cu (Tables S11 and S15). We therefore propose the paired $Cu^{\delta+}-O_{ns}$ active site that stabilizes the glyoxylate-like intermediate to open the pathway for ethanol production on OD-Cu at −0.25 V vs RHE,[17] as a weak metal−oxygen bond has been deemed responsible for alcohol production on Cu.[74]

The product distribution of OD-Cu depends on time and can be attributed to the relative abundance of the different ensembles under CO_2R conditions.[6] Low-coordinated Cu^0 sites (Cu_{6Cu}, Cu_{4Cu}, and $Cu_3^{\delta+}O_3$; Figure 3g) present stronger CO binding energy than crystalline Cu (Figure S23). Therefore, we identify them with the strong binding sites reported on OD-Cu by Verdaguer-Casadevall et al.[75] $Cu^{\delta+}$ coordination tunes significantly its adsorption properties: ΔE_{*CO} ranges from −0.5 to +0.5 eV (Figure S23). Local coordination and oxidation state influences Cu affinity to oxygen: both Cu^0 and $Cu^{\delta+}$ are less oxophilic than Cu(100), and an increasing oxidation state leads to lower O affinity (Figure S23). The rationale of the wide OD-Cu product distribution may then be elucidated by Cu coordination and its affinity to O; thus, those descriptors could be applied in the future to explain the occurrence of specific active sites toward ethylene, ethanol, and *n*-propanol.[10]

We have compiled and identified three key contributions toward OD-Cu activity and C_{2+} selectivity: polarized active sites, open facets, and glyoxylate route. Local charge polarization strengthens CO_2 binding, thus promoting a higher CO_2R activity. This insight provides a solid understanding of the role of $Cu^{\delta+}$ as a privileged site for OD-Cu catalysts.[6,15,20,22,38] Reconstructed open facets resemble crystalline Cu(100), thus motivating ethylene production at high onset potential. The $Cu^{\delta+}-O_{ns}$ pair adsorbs the CO dimer exothermically as a glyoxylate-like intermediate, which accounts for the low onset potential toward C_{2+} products reported experimentally.[17]

In the present work we characterized oxide-derived copper catalysts at different stoichiometries and oxidation stages. After *ab initio* molecular dynamics simulations, the final structures present high surface area and atomic-scale roughness. Independently from the initial model assumed, Cu exists as three species: Cu^0, $Cu^{\delta+}$, and Cu^+, which combine into 14 well-defined ensembles. Among those ensembles, $Cu^{\delta+}$, $Cu^0-Cu^{\delta+}$, and $Cu-O_{ns}$ are the active and selective sites for CO_2 reduction. $Cu^{\delta+}$ and $Cu^0-Cu^{\delta+}$ tether CO_2 actively because of their high polarization, thus promoting CO_2 activation. The $Cu-O_{ns}$ pair stabilizes C−C coupling via a glyoxylate-like intermediate, which opens the reaction pathway toward C_{2+} products from −0.5 V vs RHE because of the low kinetic barrier associated with its formation, 0.53 eV. O_{ns} is here reported stable until −0.84 V vs RHE in good agreement with recent experimental reports.[64] Although our methodology does not include solvent, electrolyte, adsorbates, and electric field during *ab initio* molecular dynamics, the results are qualitatively robust and constitute a step forward in the understanding of the role of new ensembles on oxide-derived copper reactivity. Our study conciliates all the previous experimental observations concerning the nature of OD-Cu

https://dx.doi.org/10.1021/acsenergylett.0c01777
ACS Energy Lett. 2020, 5, 3176−3184

active sites during CO_2 reduction time-scales and the consequent changes in product distribution. As active and selective sites have been characterized, the core of future investigations must be the development of synthetic protocols to stabilize these privileged ensembles.

■ ASSOCIATED CONTENT

Supporting Information

The Supporting Information is available free of charge at https://pubs.acs.org/doi/10.1021/acsenergylett.0c01777.

Computational methods, supporting discussion, eqs S1−S24, Figures S1−S27, and Tables S1−S20 (PDF)

■ AUTHOR INFORMATION

Corresponding Author

Núria López − *Institute of Chemical Research of Catalonia (ICIQ), The Barcelona Institute of Science and Technology (BIST), 43007 Tarragona, Spain;* orcid.org/0000-0001-9150-5941; Email: nlopez@iciq.es

Authors

Federico Dattila − *Institute of Chemical Research of Catalonia (ICIQ), The Barcelona Institute of Science and Technology (BIST), 43007 Tarragona, Spain;* orcid.org/0000-0001-8195-3951

Rodrigo García-Muelas − *Institute of Chemical Research of Catalonia (ICIQ), The Barcelona Institute of Science and Technology (BIST), 43007 Tarragona, Spain;* orcid.org/0000-0002-2219-5027

Complete contact information is available at: https://pubs.acs.org/10.1021/acsenergylett.0c01777

Notes

The authors declare no competing financial interest.

The data sets generated during the current study and the full *ab initio* molecular dynamics trajectories for red-Cu_2O and oxi-Cu systems, Videos S1−S7,[55] are available in the ioChem-BD database[76] at DOI 10.19061/iochem-bd-1-165.

■ ACKNOWLEDGMENTS

The authors acknowledge the financial support from the Spanish Ministry of Science and Innovation (Grant RTI2018-101394−B-I00) and the European Union (projects A-LEAF 732840-A-LEAF and ELCoREL 722614-ELCOREL). The Barcelona Supercomputing Center (BSC-RES) is acknowledged for providing generous computational resources. The authors thank Dr. Marçal Capdevila-Cortada and the Reviewers for fruitful scientific discussions.

■ REFERENCES

(1) Nitopi, S.; et al. Progress and perspectives of electrochemical CO_2 reduction on copper in aqueous electrolyte. *Chem. Rev.* **2019**, *119*, 7610−7672.

(2) Birdja, Y. Y.; Pérez-Gallent, E.; Figueiredo, M. C.; Göttle, A. J.; Calle-Vallejo, F.; Koper, M. T. M. Advances and challenges in understanding the electrocatalytic conversion of carbon dioxide to fuels. *Nat. Energy* **2019**, *4*, 732−745.

(3) Peterson, A. A.; Abild-Pedersen, F.; Studt, F.; Rossmeisl, J.; Nørskov, J. K. How copper catalyzes the electroreduction of carbon dioxide into hydrocarbon fuels. *Energy Environ. Sci.* **2010**, *3*, 1311−1315.

(4) Hori, Y.; Murata, A.; Takahashi, R. Formation of hydrocarbons in the electrochemical reduction of carbon dioxide at a copper electrode in aqueous solution. *J. Chem. Soc., Faraday Trans. 1* **1989**, *85*, 2309−2326.

(5) De Luna, P.; Hahn, C.; Higgins, D.; Jaffer, S. A.; Jaramillo, T. F.; Sargent, E. H. What would it take for renewably powered electrosynthesis to displace petrochemical processes? *Science* **2019**, *364*, 350.

(6) Arán-Ais, R. M.; Scholten, F.; Kunze, S.; Rizo, R.; Roldan Cuenya, B. The role of in situ generated morphological motifs and Cu(I) species in C_{2+} product selectivity during CO_2 pulsed electroreduction. *Nat. Energy* **2020**, *5*, 317−325.

(7) Gao, D.; Arán-Ais, R. M.; Jeon, H. S.; Roldán-Cuenya, B. Rational catalyst and electrolyte design for CO_2 electroreduction towards multicarbon products. *Nat. Catal.* **2019**, *2*, 198−210.

(8) Huang, J.; Hörmann, N.; Oveisi, E.; Loiudice, A.; De Gregorio, G. L.; Andreussi, O.; Marzari, N.; Buonsanti, R. Potential-induced nanoclustering of metallic catalysts during electrochemical CO_2 reduction. *Nat. Commun.* **2018**, *9*, 3117.

(9) Kim, Y. G.; Baricuatro, J. H.; Javier, A.; Gregoire, J. M.; Soriaga, M. P. The evolution of the polycrystalline copper surface, first to Cu(111) and then to Cu(100), at a fixed CO_2RR potential: A study by operando EC-STM. *Langmuir* **2014**, *30*, 15053−15056.

(10) Lum, Y.; Ager, J. W. Evidence for product-specific active sites on oxide-derived Cu catalysts for electrochemical CO_2 reduction. *Nat. Catal.* **2019**, *2*, 86−93.

(11) Auer, A.; Andersen, M.; Wernig, E.-M.; Hörmann, N. G.; Buller, N.; Reuter, K.; Kunze-Liebhäuser, J. Self-activation of copper electrodes during CO electro-oxidation in alkaline electrolyte. *Nat. Catal.* **2020**, DOI: 10.1038/s41929-020-00505-w.

(12) Hori, Y.; Takahashi, I.; Koga, O.; Hoshi, N. Electrochemical reduction of carbon dioxide at various series of copper single crystal electrodes. *J. Mol. Catal. A: Chem.* **2003**, *199*, 39−47.

(13) Kuhl, K. P.; Cave, E. R.; Abram, D. N.; Jaramillo, T. F. New insights into the electrochemical reduction of carbon dioxide on metallic copper surfaces. *Energy Environ. Sci.* **2012**, *5*, 7050−7059.

(14) Reske, R.; Mistry, H.; Behafarid, F.; Roldan Cuenya, B.; Strasser, P. Particle size effects in the catalytic electroreduction of CO_2 on Cu nanoparticles. *J. Am. Chem. Soc.* **2014**, *136*, 6978−6986.

(15) Chou, T.-C.; et al. Controlling the oxidation state of Cu electrode and reaction intermediates for electrochemical CO_2 reduction to ethylene. *J. Am. Chem. Soc.* **2020**, *142*, 2857−2867.

(16) Li, C. W.; Kanan, M. W. CO_2 reduction at low overpotential on Cu electrodes resulting from the reduction of thick Cu_2O films. *J. Am. Chem. Soc.* **2012**, *134*, 7231−7234.

(17) Li, C. W.; Ciston, J.; Kanan, M. W. Electroreduction of carbon monoxide to liquid fuel on oxide-derived nanocrystalline copper. *Nature* **2014**, *508*, 504−507.

(18) Ren, D.; Deng, Y.; Handoko, A. D.; Chen, C. S.; Malkhandi, S.; Yeo, B. S. Selective electrochemical reduction of carbon dioxide to ethylene and ethanol on copper(I) oxide catalysts. *ACS Catal.* **2015**, *5*, 2814−2821.

(19) Kim, D.; Lee, S.; Ocon, J. D.; Jeong, B.; Lee, J. K.; Lee, J. Insights into an autonomously formed oxygen-evacuated Cu_2O electrode for the selective production of C_2H_4 from CO_2. *Phys. Chem. Chem. Phys.* **2015**, *17*, 824−830.

(20) Mistry, H.; et al. Highly selective plasma-activated copper catalysts for carbon dioxide reduction to ethylene. *Nat. Commun.* **2016**, *7*, 12123.

(21) Handoko, A. D.; Ong, C. W.; Huang, Y.; Lee, Z. G.; Lin, L.; Panetti, G. B.; Yeo, B. S. Mechanistic insights into the selective electroreduction of carbon dioxide to ethylene on Cu_2O-derived copper catalysts. *J. Phys. Chem. C* **2016**, *120*, 20058−20067.

(22) De Luna, P.; Quintero-Bermudez, R.; Dinh, C.-T.; Ross, M. B.; Bushuyev, O. S.; Todorović, P.; Regier, T.; Kelley, S. O.; Yang, P.; Sargent, E. H. Catalyst electro-redeposition controls morphology and oxidation state for selective carbon dioxide reduction. *Nat. Catal.* **2018**, *1*, 103−110.

(23) Lee, S. Y.; Jung, H.; Kim, N.-K.; Oh, H.-S.; Min, B. K.; Hwang, Y. J. Mixed copper states in anodized Cu electrocatalyst for stable and

selective ethylene production from CO_2 reduction. *J. Am. Chem. Soc.* **2018**, *140*, 8681−8689.
(24) Li, J.; et al. Copper adparticle enabled selective electrosynthesis of *n*-propanol. *Nat. Commun.* **2018**, *9*, 4614.
(25) Ting, L. R. L.; Garcia-Muelas, R.; Martin, A. J; Veenstra, F. L. P.; Chen, S. T.-J.; Peng, Y.; Per, E. Y. X.; Pablo Garcia, S.; Lopez, N.; Perez-Ramirez, J.; Yeo, B. S. Electrochemical reduction of carbon dioxide to 1-butanol on oxide-derived copper. *Angew. Chem., Int. Ed.* **2020**, *25*, 2−10.
(26) Dutta, A.; Rahaman, M.; Luedi, N. C.; Mohos, M.; Broekmann, P. Morphology matters: tuning the product distribution of CO_2 electroreduction on oxide-derived Cu foam catalysts. *ACS Catal.* **2016**, *6*, 3804−3814.
(27) Loiudice, A.; Lobaccaro, P.; Kamali, E. A.; Thao, T.; Huang, B. H.; Ager, J. W.; Buonsanti, R. Tailoring copper nanocrystals towards C_2 products in electrochemical CO_2 reduction. *Angew. Chem., Int. Ed.* **2016**, *55*, 5789−5792.
(28) Lum, Y.; Ager, J. W. Stability of residual oxides in oxide-derived copper catalysts for electrochemical CO_2 reduction investigated with ^{18}O labeling. *Angew. Chem., Int. Ed.* **2018**, *57*, 551−554.
(29) Zhu, Q.; Sun, X.; Yang, D.; Ma, J.; Kang, X.; Zheng, L.; Zhang, J.; Wu, Z.; Han, B. Carbon dioxide electroreduction to C_2 products over copper-cuprous oxide derived from electrosynthesized copper complex. *Nat. Commun.* **2019**, *10*, 3851.
(30) Lin, S.-C.; Chang, C.-C.; Chiu, S.-Y.; Pai, H.-T.; Liao, T.-Y.; Hsu, C.-S.; Chiang, W.-H.; Tsai, M.-K.; Chen, H. M. Operando time-resolved X-ray absorption spectroscopy reveals the chemical nature enabling highly selective CO_2 reduction. *Nat. Commun.* **2020**, *11*, 3525.
(31) Kortlever, R.; Shen, J.; Schouten, K. J. P.; Calle-Vallejo, F.; Koper, M. T. M. Catalysts and reaction pathways for the electrochemical reduction of carbon dioxide. *J. Phys. Chem. Lett.* **2015**, *6*, 4073−4082.
(32) Pérez-Gallent, E.; Figueiredo, M. C.; Calle-Vallejo, F.; Koper, M. T. M. Spectroscopic observation of a hydrogenated CO dimer intermediate during CO reduction on Cu(100) electrodes. *Angew. Chem., Int. Ed.* **2017**, *56*, 3621−3624.
(33) Cheng, T.; Xiao, H.; Goddard, W. A. Nature of the active sites for CO reduction on copper nanoparticles; Suggestions for optimizing performance. *J. Am. Chem. Soc.* **2017**, *139*, 11642−11645.
(34) Feng, X.; Jiang, K.; Fan, S.; Kanan, M. W. A direct grain-boundary-activity correlation for CO electroreduction on Cu nanoparticles. *ACS Cent. Sci.* **2016**, *2*, 169−174.
(35) Wang, Y.; et al. Catalyst synthesis under CO_2 electroreduction favours faceting and promotes renewable fuels electrosynthesis. *Nat. Catal.* **2020**, *3*, 98−106.
(36) Ringe, S.; Morales-Guio, C. G.; Chen, L. D.; Fields, M.; Jaramillo, T. F.; Hahn, C.; Chan, K. Double layer charging driven carbon dioxide adsorption limits the rate of electrochemical carbon dioxide reduction on Gold. *Nat. Commun.* **2020**, *11*, 33.
(37) Veenstra, F. L.; Ackerl, N.; Martín, A. J.; Pérez-Ramírez, J. Laser-microstructured copper reveals selectivity patterns in the electrocatalytic reduction of CO_2. *Chem.* **2020**, *6*, 1707−1722.
(38) Velasco-Vélez, J.-J.; et al. The role of the copper oxidation state in the electrocatalytic reduction of CO_2 into valuable hydrocarbons. *ACS Sustainable Chem. Eng.* **2019**, *7*, 1485−1492.
(39) Favaro, M.; Xiao, H.; Cheng, T.; Goddard, W. A.; Yano, J.; Crumlin, E. J. Subsurface oxide plays a critical role in CO_2 activation by Cu(111) surfaces to form chemisorbed CO_2, the first step in reduction of CO_2. *Proc. Natl. Acad. Sci. U. S. A.* **2017**, *114*, 6706−6711.
(40) Velasco-Velez, J.-J.; et al. Revealing the active phase of copper during the electroreduction of CO_2 in aqueous electrolyte by correlating *In Situ* X-ray spectroscopy and *In Situ* electron microscopy. *ACS Energy Lett.* **2020**, *5*, 2106−2111.
(41) Zhao, Y.; Chang, X.; Malkani, A. S.; Yang, X.; Thompson, L.; Jiao, F.; Xu, B. Speciation of Cu surfaces during the electrochemical CO reduction reaction. *J. Am. Chem. Soc.* **2020**, *142*, 9735−9743.
(42) Möller, T.; et al. Electrocatalytic CO_2 reduction on CuO_x nanocubes tracking the evolution of chemical state, geometric structure, and catalytic selectivity using Operando Spectroscopy. *Angew. Chem., Int. Ed.* **2020**, DOI: 10.1002/anie.202007136.
(43) He, M.; Li, C.; Zhang, H.; Chang, X.; Chen, J. G.; Goddard, W. A., III; Cheng, M.-j.; Xu, B.; Lu, Q. Oxygen induced promotion of electrochemical reduction of CO_2 via co-electrolysis. *Nat. Commun.* **2020**, *11*, 3844.
(44) Kim, Y. G.; Soriaga, M. P. Cathodic regeneration of a clean and ordered Cu(100)-(1 × 1) surface from an air-oxidized and disordered electrode: An operando STM study. *J. Electroanal. Chem.* **2014**, *734*, 7−9.
(45) Scott, S. B.; et al. Absence of oxidized phases in Cu under CO reduction conditions. *ACS Energy Lett.* **2019**, *4*, 803−804.
(46) Eilert, A.; et al. Subsurface oxygen in oxide-derived copper electrocatalysts for carbon dioxide reduction. *J. Phys. Chem. Lett.* **2017**, *8*, 285−290.
(47) Schedel-Niedrig, T.; Neisius, T.; Böttger, I.; Kitzelmann, E.; Weinberg, G.; Demuth, D.; Schlögl, R. Copper (sub)oxide formation: a surface sensitive characterization of model catalysts. *Phys. Chem. Chem. Phys.* **2000**, *2*, 2407−2417.
(48) Liu, C.; Lourenço, M. P.; Hedström, S.; Cavalca, F.; Diaz-Morales, O.; Duarte, H. A.; Nilsson, A.; Pettersson, L. G. Stability and effects of subsurface oxygen in oxide-derived Cu catalyst for CO_2 reduction. *J. Phys. Chem. C* **2017**, *121*, 25010−25017.
(49) Garza, A. J.; Bell, A. T.; Head-Gordon, M. Is subsurface oxygen necessary for the electrochemical reduction of CO_2 on copper? *J. Phys. Chem. Lett.* **2018**, *9*, 601−606.
(50) Fields, M.; Hong, X.; Nørskov, J. K.; Chan, K. Role of subsurface oxygen on Cu surfaces for CO_2 electrochemical reduction. *J. Phys. Chem. C* **2018**, *122*, 16209−16215.
(51) Bagger, A.; Ju, W.; Varela, A. S.; Strasser, P.; Rossmeisl, J. Electrochemical CO_2 reduction: Classifying Cu facets. *ACS Catal.* **2019**, *9*, 7894−7899.
(52) Calle-Vallejo, F.; Tymoczko, J.; Colic, V.; Vu, Q. H.; Pohl, M. D.; Morgenstern, K.; Loffreda, D.; Sautet, P.; Schuhmann, W.; Bandarenka, A. S. Finding optimal surface sites on heterogeneous catalysts by counting nearest neighbors. *Science* **2015**, *350*, 185−189.
(53) Fung, V.; Tao, F. F.; Jiang, D. E. General structure-reactivity relationship for oxygen on transition-metal oxides. *J. Phys. Chem. Lett.* **2017**, *8*, 2206−2211.
(54) Zhang, Z.; Zandkarimi, B.; Alexandrova, A. N. Ensembles of metastable states govern heterogeneous catalysis on dynamic interfaces. *Acc. Chem. Res.* **2020**, *53*, 447−458.
(55) Dattila, F. Supporting Videos 1−7; https://iochem-bd.iciq.es/browse/handle/100/26145, 2020 (accessed 2020-07-24).
(56) Yang, F.; Choi, Y.; Liu, P.; Hrbek, J.; Rodriguez, J. A. Autocatalytic reduction of a Cu_2O/Cu(111) surface by CO: STM, XPS, and DFT studies. *J. Phys. Chem. C* **2010**, *114*, 17042−17050.
(57) Perdew, J. P.; Burke, K.; Ernzerhof, M. Generalized gradient approximation made simple. *Phys. Rev. Lett.* **1996**, *77*, 3865−3868.
(58) Fishman, M.; Zhuang, H. L.; Mathew, K.; Dirschka, W.; Hennig, R. G. Accuracy of exchange-correlation functionals and effect of solvation on the surface energy of copper. *Phys. Rev. B: Condens. Matter Mater. Phys.* **2013**, *87*, 245402.
(59) Mathew, K.; Sundararaman, R.; Letchworth-Weaver, K.; Arias, T. A.; Hennig, R. G. Implicit solvation model for density-functional study of nanocrystal surfaces and reaction pathways. *J. Chem. Phys.* **2014**, *140*, 084106.
(60) Singh, A. K.; Zhou, L.; Shinde, A.; Suram, S. K.; Montoya, J. H.; Winston, D.; Gregoire, J. M.; Persson, K. A. Electrochemical stability of metastable materials. *Chem. Mater.* **2017**, *29*, 10159−10167.
(61) Guan, R.; Hashimoto, H.; Kuo, K. H. Electron-microscopic study of the structure of metastable oxides formed in the initial stage of copper oxidation. II. Cu_8O. *Acta Crystallogr., Sect. B: Struct. Sci.* **1984**, *B40*, 560−566.
(62) Bohra, D.; Chaudhry, J. H.; Burdyny, T.; Pidko, E. A.; Smith, W. A. Modeling the electrical double layer to understand the reaction

environment in a CO_2 electrocatalytic system. *Energy Environ. Sci.* **2019**, *12*, 3380−3389.
(63) Zhang, F.; Co, A. C. Direct evidence of local pH change and the role of alkali cation during CO_2 electroreduction in aqueous media. *Angew. Chem., Int. Ed.* **2020**, *59*, 1674−1681.
(64) Zhang, W.; Huang, C.; Xiao, Q.; Yu, L.; Shuai, L.; An, P.; Zhang, J.; Qiu, M.; Ren, Z.; Yu, Y. Atypical oxygen-bearing copper boosts ethylene selectivity toward electrocatalytic CO_2 reduction. *J. Am. Chem. Soc.* **2020**, *142*, 11417−11427.
(65) Bai, H.; et al. Controllable CO adsorption determines ethylene and methane productions from CO_2 electroreduction. *Sci. Bull.* **2020**, DOI: 10.1016/j.scib.2020.06.023.
(66) Yu, J.; Namba, Y. Atomic surface roughness. *Appl. Phys. Lett.* **1998**, *73*, 3607−3609.
(67) Xu, H.; et al. Highly selective electrocatalytic CO_2 reduction to ethanol by metallic clusters dynamically formed from atomically dispersed copper. *Nat. Energy* **2020**, *5*, 623−632.
(68) Jiao, J.; et al. Copper atom-pair catalyst anchored on alloy nanowires for selective and efficient electrochemical reduction of CO_2. *Nat. Chem.* **2019**, *11*, 222−228.
(69) Calle-Vallejo, F.; Koper, M. T. M. Theoretical considerations on the electroreduction of CO to C_2 species on Cu(100) electrodes. *Angew. Chem., Int. Ed.* **2013**, *52*, 7282−7285.
(70) Jiang, K.; Sandberg, R. B.; Akey, A. J.; Liu, X.; Bell, D. C.; Nørskov, J. K.; Chan, K.; Wang, H. Metal ion cycling of Cu foil for selective C−C coupling in electrochemical CO_2 reduction. *Nat. Catal.* **2018**, *1*, 111−119.
(71) Dattila, F. *Glyoxylate-like configurations: (O_{ss})OCCO, sites 1−9*. DOI: 10.19061/iochem-bd-1-165, 2020 (accessed 2020-07-24).
(72) Muchowska, K. B.; Varma, S. J.; Moran, J. Synthesis and breakdown of universal metabolic precursors promoted by iron. *Nature* **2019**, *569*, 104−107.
(73) Handoko, A. D.; Wei, F.; Jenndy; Yeo, B. S.; Seh, Z. W. Understanding heterogeneous electrocatalytic carbon dioxide reduction through operando techniques. *Nat. Catal.* **2018**, *1*, 922−934.
(74) Katayama, Y.; Nattino, F.; Giordano, L.; Hwang, J.; Rao, R. R.; Andreussi, O.; Marzari, N.; Shao-Horn, Y. An *in Situ* surface-enhanced infrared absorption spectroscopy study of electrochemical CO_2 reduction: Selectivity dependence on surface C-bound and O-bound reaction intermediates. *J. Phys. Chem. C* **2019**, *123*, 5951−5963.
(75) Verdaguer-Casadevall, A.; Li, C. W.; Johansson, T. P.; Scott, S. B.; McKeown, J. T.; Kumar, M.; Stephens, I. E.; Kanan, M. W.; Chorkendorff, I. Probing the active surface sites for CO reduction on oxide-derived copper electrocatalysts. *J. Am. Chem. Soc.* **2015**, *137*, 9808−9811.
(76) Álvarez-Moreno, M.; de Graaf, C.; López, N.; Maseras, F.; Poblet, J.; Bo, C. Managing the computational chemistry big data problem: The ioChem-BD Platform. *J. Chem. Inf. Model.* **2015**, *55*, 95−103.

https://dx.doi.org/10.1021/acsenergylett.0c01777
ACS Energy Lett. 2020, 5, 3176−3184

UNIVERSITAT ROVIRA I VIRGILI
THEORETICAL MODELS FOR THE ELECTROCHEMICAL REDUCTION OF CO2 ON COPPER CATALYSTS UNDER WORKING CONDITIONS
Federico Dattila

UNIVERSITAT ROVIRA I VIRGILI
THEORETICAL MODELS FOR THE ELECTROCHEMICAL REDUCTION OF CO2 ON COPPER CATALYSTS UNDER WORKING CONDITIONS
Federico Dattila

UNIVERSITAT ROVIRA I VIRGILI
THEORETICAL MODELS FOR THE ELECTROCHEMICAL REDUCTION OF CO2 ON COPPER CATALYSTS UNDER WORKING CONDITIONS
Federico Dattila

UNIVERSITAT ROVIRA I VIRGILI
THEORETICAL MODELS FOR THE ELECTROCHEMICAL REDUCTION OF CO2 ON COPPER CATALYSTS UNDER WORKING CONDITIONS
Federico Dattila

UNIVERSITAT
ROVIRA i VIRGILI